sensors

Special Issue Reprint

Applications of Antenna Technology in Sensors

2nd Edition

Edited by
Pedro Renato Tavares de Pinho

mdpi.com/journal/sensors

MDPI

Applications of Antenna Technology in Sensors: 2nd Edition

Applications of Antenna Technology in Sensors: 2nd Edition

Guest Editor

Pedro Renato Tavares de Pinho

MDPI

Basel • Beijing • Wuhan • Barcelona • Belgrade • Novi Sad • Cluj • Manchester

Guest Editor
Pedro Renato Tavares de Pinho
Departamento de Engenharia
Eletrónica Telecomunicações e
Informática & Instituto de
Telecomunicações
Universidade de Aveiro
Aveiro
Portugal

Editorial Office
MDPI AG
Grosspeteranlage 5
4052 Basel, Switzerland

This is a reprint of the Special Issue, published open access by the journal *Sensors* (ISSN 1424-8220), freely accessible at: https://www.mdpi.com/journal/sensors/special_issues/Antenna_II.

For citation purposes, cite each article independently as indicated on the article page online and as indicated below:

Lastname, A.A.; Lastname, B.B. Article Title. *Journal Name* **Year**, *Volume Number*, Page Range.

ISBN 978-3-7258-4733-4 (Hbk)
ISBN 978-3-7258-4734-1 (PDF)
https://doi.org/10.3390/books978-3-7258-4734-1

Contents

About the Editor

Pedro Renato Tavares de Pinho

Pedro Pinho was born in Vale de Cambra, Portugal, in 1974. He received his Licenciado and Master's degrees in Electrical and Telecommunications Engineering in 1997 and 2000, respectively, and his Ph.D. in Electrical Engineering in 2004, all from the University of Aveiro, Portugal. He is currently an Associate Professor in the Department of Electronics, Telecommunications and Informatics at the University of Aveiro, where he also serves as Director of the Doctoral Program in Electrical Engineering. He is a Senior Researcher at the Instituto de Telecomunicações (IT) and a Senior Member of both IEEE and URSI.

Dr. Pinho has edited four books published by Intech and MDPI and co-authored *Guided Propagation of Electromagnetic Waves* (LTC Editora, 2015), in addition to 12 book chapters. He is the author or co-author of over 300 scientific publications in international journals and conferences and is a co-inventor of three patents.

He serves as Associate Editor for *IET Microwaves, Antennas & Propagation*, regularly participates in technical program committees of international conferences, and acts as a reviewer for several IEEE journals.

To date, he has supervised or co-supervised more than 80 MSc theses and 15 PhD students. His research interests include antenna design, wireless power transmission, and electromagnetic wave propagation.

Preface

Advances in antenna technology are a cornerstone of modern wireless communication, underpinning the connectivity and sensing capabilities of our increasingly digital world. As wireless systems evolve toward 5G, 6G, and the Internet of Things (IoT), antenna engineers face the challenge of designing antennas that are not only more efficient and broadband but also compact, adaptive, and integrable into diverse platforms. High-capacity MIMO and phased array antennas enable smart beamforming and spatial multiplexing to meet ever-growing data demands, while innovations in materials and fabrication (from flexible substrates to 3D printing) open the door for antennas embedded in everyday objects, wearables, and sensors. Advanced antenna systems thus play a pivotal role in connecting billions of devices and in facilitating new applications—from remote health monitoring to satellite mega-constellations, making this a vibrant field of research and development.

This edited volume, **Applications of Antenna Technology in Sensors: 2nd Edition**, is a compilation of ten state-of-the-art papers originally published in the MDPI *Sensors* journal's Special Issue of the same name. The collected papers exemplify the scope of current antenna research, spanning novel designs for IoT sensors, high-performance arrays for extreme environments, and innovative techniques for improving antenna array efficiency. Below, we outline the structure of the reprint and summarize the contributions of each chapter.

Abounasr et al. introduces a flexible inkjet-printed loop resonator designed as a sensor for food quality monitoring. Operating at 2.4 GHz, this antenna-based sensor detects spoilage in meat by tracking shifts in its resonance frequency caused by dielectric changes during storage. The authors demonstrate high sensitivity, observing a clear frequency drift (from ~2.14 GHz to 1.29 GHz over five days) correlating with meat degradation. This compact, low-cost device illustrates the potential of printable antennas in real-time, non-invasive IoT food monitoring systems.

Sreang and Chung present miniaturized helical antennas for a passive wireless temperature sensor based on surface acoustic wave (SAW) technology. Two small helical antenna designs—a cylindrical helix and a hemispherical helix—are developed to excite a 915 MHz SAW resonator, achieving resonance within the 902–928 MHz ISM band. Despite their tiny size, these antennas provide sufficient bandwidth (22–30 MHz) for the sensor and facilitate entirely battery-less temperature monitoring: the SAW device's resonant frequency shifts with temperature, by about 66.7 kHz per 10 C, which the antenna system can detect remotely.

Continuing the theme of antenna-enabled sensing, Yeo and Lee describes a compact wideband tapered slot antenna (TSA) tailored for chipless RFID sensor tags. The authors tackle the challenge of reducing the size of TSAs while maintaining ultra-wide bandwidth: they introduce fan-shaped and stepped geometrical structures appended to the TSA's ground plane to achieve size miniaturization and bandwidth enhancement. Two design iterations are detailed. The first uses appended quarter- and half-circular slot structures, yielding a measured impedance bandwidth of approximately 2.53–13.38 GHz with a 39% size reduction compared to a conventional TSA. The second design combines fan-shaped slots with stepped cuts, further extending the bandwidth to about 2.31–13.80 GHz and achieving nearly a 46% size reduction. The chapter includes prototype measurements confirming over 140% fractional bandwidth and stable gain (3–8 dBi) across the range, making this antenna well-suited for next-generation chipless RFID sensors that require wideband operation in compact formats.

Frazao et al. offer a comprehensive review of radar-based cardiac monitoring techniques. Motivated by the rise in smart healthcare and contactless vital sign monitoring, this review examines how Doppler radar and related microwave sensors can measure heart rate (HR) and heart rate variability (HRV) without

physical contact. The authors survey various system architectures (from continuous wave to FMCW radars), operating frequencies, antenna configurations, and signal processing algorithms. A key insight is that system architecture and signal processing choices have the greatest impact on measurement accuracy, with FMCW radar systems emerging as particularly effective for detecting heart activity. By contrast, the choice of carrier frequency (within the microwave bands commonly used) did not substantially affect performance. This finding suggests that lower-frequency, cost-effective radar hardware can be employed without sacrificing accuracy, provided that optimal signal processing is used. The review concludes by noting recent advances and challenges, providing a timely resource for researchers developing next-generation wireless health monitoring devices.

Yahya et al. develop a reconfigurable triple-band monopole antenna for long-range IoT (LoRa) applications. This planar antenna, fabricated on an FR-4 substrate, can switch between three distinct sub-GHz ISM bands (centered at 433 MHz, 868 MHz, and 915 MHz) commonly used in Europe, Asia, and the Americas for LoRa networks. By incorporating PIN diodes in the radiating structure, the antenna dynamically reconfigures its operating band without changing its physical dimensions. The design achieved compact size (80×50 mm), an omnidirectional radiation pattern, and measured gains of roughly 2 dBi in each band with high radiation efficiency (>90%).

Molins-Benlliure et al. addresses the challenge of integrating efficient antennas into extremely compact IoT devices by designing a very low-profile 2.4 GHz chip antenna using low-temperature co-fired ceramic (LTCC) technology. The proposed antenna is a planar inverted-F antenna (PIFA) embedded in a ceramic block ($\varepsilon r \approx 7.1$) with an "accordion"-style corrugated geometry. Remarkably, the antenna occupies a volume of only $0.075\lambda \times 0.056\lambda \times 0.019\lambda$ at 2.4 GHz (where λ is the free-space wavelength), and it does not require any clearance area on the hosting circuit board's ground plane. Even with its miniature size, the antenna achieves about 25 MHz bandwidth (for S11 < –6 dB), which is acceptable for 2.4 GHz ISM applications. This chapter's results provide valuable design guidelines for engineers looking to embed high-performance antennas into the ever-shrinking form factors of IoT devices.

Sánchez-Sevilleja et al. present the design and space qualification of a broadband S-band antenna for a CubeSat constellation. Developed for the Spanish INTA ANSER program, the antenna will serve as the primary space-to-ground communications link for a Leader-Follower CubeSat system. The design features dual circular polarization over a wide bandwidth in the 2–4 GHz range, achieved without the need for an external polarizing network or bulky phase shifters. This not only makes the antenna compact and lightweight (crucial for CubeSat integration) but also ensures stable gain patterns across the band, improving link reliability. The authors discuss the use of space-grade materials and processes, since the antenna had to be qualified to survive launch and the space environment. The performance is benchmarked against the previous generation UHF monopole used in earlier satellites, with the new S-band antenna markedly improving data throughput and link margin due to its higher gain and polarization diversity. By the time of publication, the antenna had been integrated into the 3U CubeSat "Leader" platform and successfully passed all environmental tests, with a scheduled launch (January 2025).

By Li et al. addresses another demanding scenario: high-gain antennas that remain operational over extreme temperature ranges. The chapter introduces a novel microstrip patch array design intended for environments with large temperature swings (such as aerospace, industrial, or defense systems). The authors propose a 4×4 patch antenna array where each radiating element is a double-H-shaped slot patch, chosen to broaden the bandwidth and reduce thermal sensitivity. The array operates in the Ku-band, covering approximately 12 GHz to 18.25 GHz with a 41% fractional bandwidth, and delivers a peak gain of ~19 dBi at 15.5 GHz. Importantly, both simulation and measurement confirm that the antenna's performance is robust against temperature variations: when tested from –50 C up to +150 C in a temperature chamber, the array retained a wide bandwidth (~39%

measured, 11.4–17 GHz) and high gain (~18.7 dBi at 15.5 GHz at 150°C) with minimal degradation. This resilience is attributed to the careful choice of materials and a stable design of the feed network.

Sanchez et al. apply the CORPS concept to the feed network of a concentric ring antenna array. The idea is to exploit the intrinsic phase progression of specially arranged periodic delay networks so that fewer phase shifters are needed to steer the beam of a circular phased array. The authors design CORPS networks (using 2×3 and 4×7 sub-blocks) to feed a concentric ring array and demonstrate that this configuration can scan the beam over ±25° in elevation with significantly fewer phase shifter components than a conventional fully equipped array. A differential evolution algorithm is used to optimize the amplitude weights for low sidelobe levels. Full-wave simulations show that the CORPS-fed array achieves comparable radiation performance (beam shape and sidelobe levels) to a standard design, and a prototype built for validation confirms the scanning capability and low sidelobes across the intended scan angles.

Calvillo et al. builds on a similar theme but for linear arrays, introducing a new feed network scheme that combines CORPS with microwave crossover networks (analogous to a Butler matrix) to minimize phase shifter count. The authors interleave two stages of 2×3 CORPS networks in a clever way that yields the required progressive phase shifts for beam steering while also shaping the amplitude taper for low sidelobes. The result is a linear array design that requires only one-third of the phase shifters of a conventional approach—a 66% reduction in complexity. Despite this drastic simplification, the measured prototype maintains a peak sidelobe level around –22 dB and can scan the main beam to ±25° with negligible performance loss compared to a fully equipped array. This chapter highlights an elegant technique to design "smart" feed networks, which can be pivotal for future large antenna arrays (for example, in mm-wave 5G or satellite broadband) where minimizing hardware is key to feasibility.

In summary, the ten chapters in this volume provide a rich overview of contemporary research in advanced antennas and their myriad applications. The contributions span from fundamental advances in antenna designs, such as novel miniaturization and reconfiguration techniques, to applied innovations addressing real-world communication needs in IoT networks, space missions, and sensing systems. Antenna engineers and researchers will find in these chapters not only specific technical solutions (e.g., a new wideband array architecture or a flexible sensing antenna) but also broader methodologies and design principles that can inspire future work.

The editor and the authors would like to express their gratitude to the publisher for the assigned time, invaluable experience, efforts, and staff that successfully contribute to enriching the final overall quality of the reprint. To Isabel Nunes—Thank you for your vision and teaching. To Íris Pinho and Petra Pinho.

Pedro Renato Tavares de Pinho
Guest Editor

sensors

MDPI

Article

A High-Sensitivity Inkjet-Printed Flexible Resonator for Monitoring Dielectric Changes in Meat

Jamal Abounasr *, Mariam El Gharbi, Raúl Fernández García and Ignacio Gil

Department of Electronic Engineering, Universitat Politècnica de Catalunya, 08222 Terrassa, Spain; mariam.el.gharbi2@upc.edu (M.E.G.); raul.fernandez-garcia@upc.edu (R.F.G.); ignasi.gil@upc.edu (I.G.)
* Correspondence: jamal.abounasr@upc.edu

Abstract: This paper introduces a flexible loop antenna-based sensor optimized for real-time monitoring of meat quality by detecting changes in dielectric properties over a six-day storage period. Operating within the 2.4 GHz ISM band, the sensor is designed using CST Microwave Studio 2024 to deliver high sensitivity and accuracy. The sensing mechanism leverages resonance frequency shifts caused by variations in permittivity as the meat degrades. Experimental validation across five samples showed a consistent frequency shift from 2.14 GHz (Day 0) to 1.29 GHz (Day 5), with an average sensitivity of 0.173 GHz/day. A strong correlation was observed between measured and simulated results, as evidenced by linear regression ($R^2 = 0.984$ and $R^2 = 0.974$ for measured and simulated data, respectively). The sensor demonstrated high precision and repeatability, validated by low standard deviations and minimal frequency deviations. Compact, printable, and cost-effective, the proposed sensor offers a scalable solution for food quality monitoring. Its robust performance highlights its potential for integration into IoT platforms and extension to other perishable food products, advancing real-time, non-invasive, RF-based food safety technologies.

Keywords: flexible loop antenna; inkjet-printed sensor; microwave resonance; meat freshness monitoring; dielectric property analysis; real-time food quality assessment; permittivity-based sensing; non-invasive monitoring; 2.4 GHz ISM band; printed electronics

1. Introduction

Food safety and quality are critical aspects of global public health and food security. The increasing complexity of food supply chains, coupled with growing consumer demand for fresh, high-quality products, requires robust monitoring systems [1]. Ensuring that food, especially perishable items such as meat, remains safe and of high quality throughout its storage and distribution is essential to preventing foodborne illness, reducing economic losses, and building consumer confidence [2,3]. Contaminated or substandard food creates serious health risks to consumers leading to illnesses associated with ingestion of food, which include acute bowel disorders, chronic illness, and mortality [4]. It is reported by the World Health Organization (WHO) that millions of people across the globe suffer from foodborne diseases every year with, contamination by pathogenic organisms such as Salmonella, Listeria, and *E. coli* as key factors. It is also important to realize that the spoilage of meat leads to the generation of poisonous by-products as well as the growth of pathogens, thus warranting the need for stringent supervision [5]. On a worldwide scale, food safety and food quality are important issues of food security. Spoilage and waste

appear as a challenge to food security, especially in underdeveloped countries with very little cold chain facilities. A developed means of supervision may help to manage food waste by tracing the most susceptible products dressed to be lost in the chain, which will help to take proper measures as early as possible.

Technological advances in radio frequency (RF) and microwave technologies transform food safety and quality assurance by providing real-time, non-invasive monitoring solutions [6]. These techniques leverage the interaction between electromagnetic waves and food materials to detect certain key quality parameters such as spoilage. RF-based systems, including antenna-based sensors and RFID sensors, allow for continuous monitoring of environmental conditions and dielectric property changes in food [7]. By offering a sophisticated and scalable approach to food monitoring, RF and microwave techniques pave the way for safer and more efficient food quality management. In the context of food safety and quality assurance, dielectric properties, particularly permittivity, serve as reliable indicators of structural and compositional changes in perishable foods [8]. As food ripens or spoils, its chemical composition undergoes significant alterations, leading to measurable changes in its dielectric properties. These changes make permittivity a cornerstone of radio frequency (RF)- and microwave-based sensing and monitoring technologies [9]. By accurately measuring these properties, advanced systems can deliver real-time insights into food freshness, enhancing safety, reducing waste, and ensuring better quality control throughout the supply chain.

A trained individual, such as a store manager, can assess the quality of meat by sight, smell, and touch. However, this approach poses potential health risks to the inspector. In addition, relying solely on subjective judgment leads to the possibility of errors that are not supported by objective data. Furthermore, when touch and smell are used in the inspection process, it becomes impossible to assess the packaged products [10]. The existing meat quality monitoring systems are costly to implement and not widely utilized. Despite their presence, cases of health issues and fatalities resulting from the consumption of spoiled meat are still occur.

To address these challenges, several studies have demonstrated the effectiveness of RF and microwave techniques for monitoring perishable foods such as meat, dairy, and seafood [11–13]. These methods offer advantages over traditional approaches, including faster processing times, non-destructive analysis, and improved scalability. For example, a UHF RFID system was used to monitor frozen meat using received signal strength indicator (RSSI) data, as reported in [14]. This method demonstrated monotonic relationships between RSSI values, temperature, and hardness during defrosting, enabling effective cold chain monitoring and safety. Another technique was introduced in [15], where dielectric measurements were used to assess meat freshness by monitoring changes in permittivity and conductivity over storage intervals. Using capacitance and conductance data measured with an LCZ meter across frequencies from 10 kHz to 1 MHz, the study demonstrated a decline in these dielectric properties with increasing storage time. In addition, an IoT-based system combining cameras and air quality sensors, using deep learning models to analyze color changes and predict meat freshness in real time, was reported in [16]. This system requires complex calibration for different types and conditions of meat, and its applicability may be limited to specific use cases. However, all of the studies mentioned above rely primarily on rigid substrates, and these kinds of substrates may not be ideal for applications that require flexibility, such as integration into smart packaging or wearable systems for real-time monitoring.

This paper presents a flexible antenna-based sensor for monitoring meat (beef) freshness over six days using microwave signals. The sensor, a circular loop antenna printed on a flexible polyamide substrate, detects shifts in resonance frequency caused by changes in

the meat's dielectric properties as it degrades. These shifts alter the antenna's resonance characteristics, enabling non-invasive freshness detection. Measurements were conducted using a Vector Network Analyzer (VNA) to observe resonance frequency shifts over time.

The analysis was limited to six days because the meat was visibly rotten beyond this period, making further investigation unnecessary. Additionally, resonance frequency results on subsequent days showed no significant changes compared to Day 6, confirming complete spoilage, which is evident through visual and sensory inspection. Extending the analysis further was, thus, unnecessary for food quality assessment.

2. Sensor Design and Working Principle

2.1. Sensor Design and Manufacturing

The sensor, based on a loop antenna design, was developed to operate within the 2.4 GHz ISM band and optimized using CST Microwave Studio 2024. The geometrical parameters of the proposed antenna are detailed in Table 1 and illustrated in Figures 1 and 2.

These parameters were tuned to achieve optimal performance and ensure efficient electromagnetic coupling with the target samples. Polyimide (PI) films, commonly known by the brand name Kapton, were selected as the substrate material due to their excellent dielectric properties ($\epsilon_r = 3.5$, loss tangent = 0.0027), lightweight structure, and durability under extreme environmental conditions. To ensure consistency for high-performance microwave applications, the electrical properties of the substrate were verified using a Q-meter, as shown in Figure 1a.

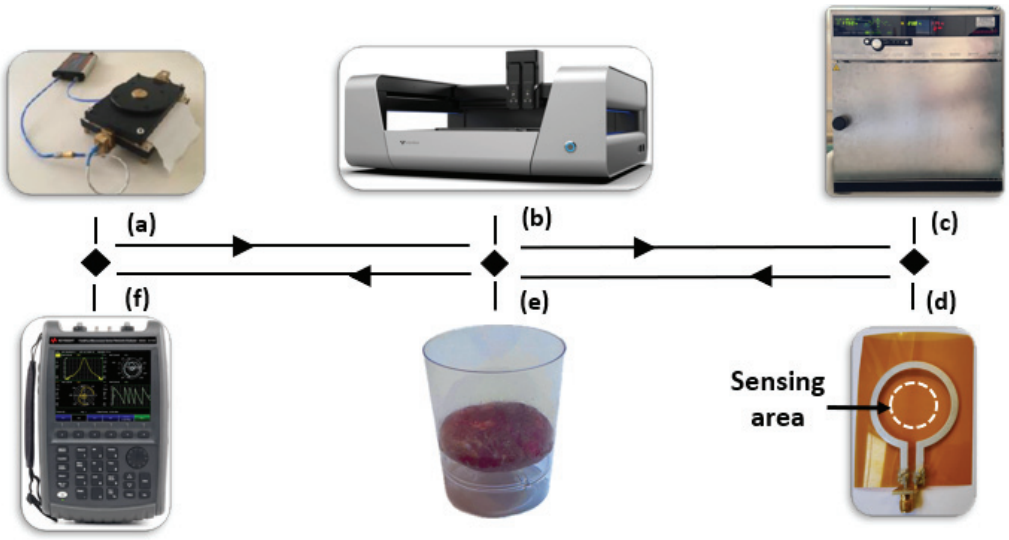

Figure 1. Overview . of the experimental setup and fabrication process: (**a**) Q-meter used for extracting electrical properties of the substrate; (**b**) Voltera NOVA inkjet and extrusion printer used for antenna fabrication; (**c**) Memmert oven for drying and curing the printed ink to ensure proper adhesion and distribution; (**d**) final fabricated loop antenna; (**e**) 10 g of meat sample; (**f**) vector network analyzer (VNA) for antenna performance validation.

The conductive traces of the loop antenna were fabricated using an inkjet and extrusion printer (Voltera NOVA, Figure 1b) with a 225 µm nozzle. This system simplifies the calibration process by automating parameters such as dispensing height, ink pressure, and temperature, making it highly user-friendly and efficient. The printing process typically requires less than 15 min to complete. Inkjet printing was chosen for its rapid prototyping capabilities, minimal material waste, and suitability for flexible substrates, making it an ideal technique for disposable and scalable food quality sensors.

After printing, the antennas were dried in a Memmert oven (Figure 1c) at 50 °C for 15 min to ensure proper ink adhesion and uniform distribution. This step is critical for maintaining reliable conductivity and achieving stable sensor performance. The final fabricated loop antenna is shown in Figure 1d, and it demonstrated excellent electrical matching to the standard 50 Ω impedance. This performance was validated using a vector network analyzer (VNA, Figure 1f).

To assess its functionality, the sensor was tested with a meat sample (Figure 1e) placed directly on the loop in the sensing area illustrated in Figure 2. Measurements were collected over multiple days to analyze the impact of permittivity variations on the reflection coefficient (S_{11}) and resonance frequency behavior. This robust and systematic design ensures the sensor's reliability for dielectric sensing applications in meat quality evaluation.

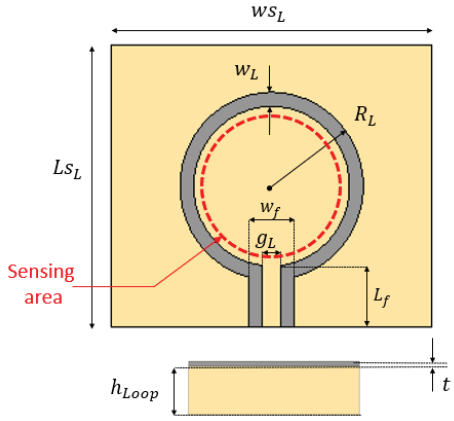

Figure 2. The geometrical parameters of the proposed antenna.

Table 1. Geometrical parameters of the proposed sensor.

Parameter	Value (mm)	Description
WS_L	50	Width of the substrate
LS_L	60	Length of the substrate
W_L	3	Width of the loop
R_L	20	Radius of the loop
W_f	10	Width of the feedline
g_L	4	Gap between loop and feedline
L_f	13	Length of the feedline
h_{Loop}	0.19	Substrate thickness
t	0.008	Conductor thickness

2.2. Working Principle

The proposed loop antenna sensor operates by generating a localized electromagnetic (EM) field in its near-field region. When a material, such as meat, is placed within this field, the electromagnetic waves interact with the dielectric properties of the material, such as its relative permittivity (ϵ_r). This interaction modifies the antenna's impedance by either absorbing or reflecting the EM energy, resulting in measurable changes in the reflection coefficient (S_{11}) and a shift in the resonance frequency (f_r).

At the resonance frequency, the antenna's impedance is minimized, enabling strong energy coupling with the surrounding medium. This occurs when the inductive reactance (X_L) of the loop antenna matches the capacitive reactance (X_C) of the surrounding system. The two reactances cancel each other out, leaving only the resistive component in the total impedance:

$$Z_{\text{tot}} = R + j(X_L - X_C) \quad (1)$$

At resonance, since $X_L = X_C$, the impedance simplifies to

$$Z_{\text{tot}} = R \tag{2}$$

This purely resistive impedance results in the lowest impedance value, allowing maximum current flow in the loop. The strong current flow enhances the interaction between the antenna and the surrounding material, amplifying the sensor's sensitivity to dielectric changes. As the dielectric properties of the material affect the EM field distribution, the resonance frequency and reflection coefficient shift accordingly.

The interaction between the loop antenna and the material is illustrated in Figure 3, which highlights how the loop antenna generates a localized EM field that interacts with the material. The highest intensity regions, shown in red and orange, are concentrated near the loop antenna edges, while the field weakens radially outward. The meat sample perturbs the field, as evidenced by the redistribution of field lines, confirming the antenna's sensitivity to dielectric variations in the sample.

The specific composition of the meat, along with the effective dielectric properties used in this study, is detailed in the following subsection. These properties were carefully selected to ensure accurate simulation and analysis of the interaction between the loop antenna and the meat samples.

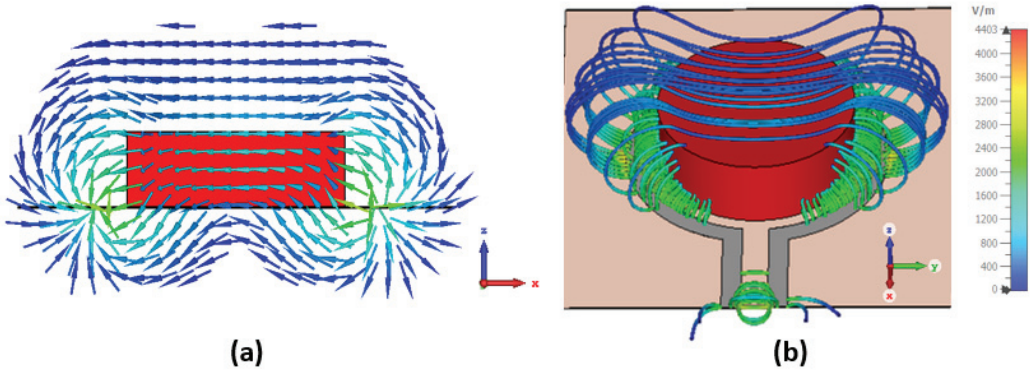

Figure 3. Simulated electric field highlighting the interactions between the loop antenna and the meat sample: (**a**) side view and (**b**) 3D view of the E field.

3. Experimental Setup and Measurement Workflow

To investigate the dielectric properties of beef samples and their interaction with the loop antenna, a systematic experimental workflow was implemented. Each sample was carefully prepared to weigh exactly 10 g, with a composition of 80% muscle and 20% fat, reflecting a typical profile for evaluating meat quality. The samples were cylindrical in shape, with a radius of 1.5 cm and a height of 1.5 cm, corresponding to a volume of approximately 10.61 cm^3. These geometric and compositional parameters were used for both experimental measurements and simulation models to ensure consistency and accuracy in the analysis. Five samples were prepared and tested daily over a six-day period, providing a robust dataset for analysis. The relative permittivity (ϵ_r) and loss tangent ($\tan\delta$) of the meat were calculated using a weighted average approach based on the dielectric properties of muscle and fat, ensuring accurate modeling and analysis. These properties were derived using the following equations [17,18]:

$$\epsilon_{\text{eff}} = f_{\text{muscle}} \cdot \epsilon_{\text{muscle}} + f_{\text{fat}} \cdot \epsilon_{\text{fat}} \tag{3}$$

$$\tan\delta = \frac{\sigma}{\omega\epsilon_0\epsilon_r} \tag{4}$$

where the variables are as follows:

- ϵ_{eff}: effective relative permittivity of the mixture.
- $f_{\text{muscle}} = 0.8$ and $f_{\text{fat}} = 0.2$: weight fractions of muscle and fat.
- ϵ_{muscle} and ϵ_{fat}: relative permittivities of muscle and fat.
- σ: conductivity of the mixture.
- $\omega = 2\pi f$: angular frequency, where $f = 2.4\,\text{GHz}$.
- $\epsilon_0 = 8.854 \times 10^{-12}\,\text{F/m}$: permittivity of free space.

Using these equations and the dielectric properties of muscle ($\epsilon_{\text{muscle}} \approx 49, \sigma_{\text{muscle}} \approx 1.3\,\text{S/m}$) and fat ($\epsilon_{\text{fat}} \approx 5.2, \sigma_{\text{fat}} \approx 0.05\,\text{S/m}$), the effective properties of the mixture were calculated as follows:

$$\epsilon_{\text{eff}} = (0.8 \cdot 49) + (0.2 \cdot 5.2) \approx 40.96 \tag{5}$$

$$\tan\delta = \frac{1.048}{2\pi \cdot 2.4 \times 10^{9} \cdot 8.854 \times 10^{-12} \cdot 40.96} \approx 0.020 \tag{6}$$

These calculated values were used to simulate the electromagnetic interaction between the loop antenna and the meat sample.

The storage conditions were carefully controlled to simulate realistic handling scenarios while minimizing environmental disturbances. Each sample was stored for 12 h at 7 °C (refrigerated) to slow degradation, followed by 8 h at 25 °C (room temperature) to mimic typical exposure conditions. This cycle was repeated daily to reflect practical storage variations. To mitigate the influence of ambient humidity and temperature fluctuations, all measurements were performed immediately after removing the samples from refrigeration, ensuring consistency in dielectric behavior and minimizing external interference.

The experimental setup included a loop antenna designed to operate within the 2.4 GHz ISM band and a vector network analyzer (VNA) to measure the reflection coefficient (S_{11}) over a frequency range of 1–3 GHz, as presented in Figures 4 and 5. Each sample was carefully positioned on the loop antenna to ensure proper coupling with the electromagnetic field. The placement of the sample on the loop antenna allowed direct interaction between the localized electromagnetic field and the dielectric properties of the meat.

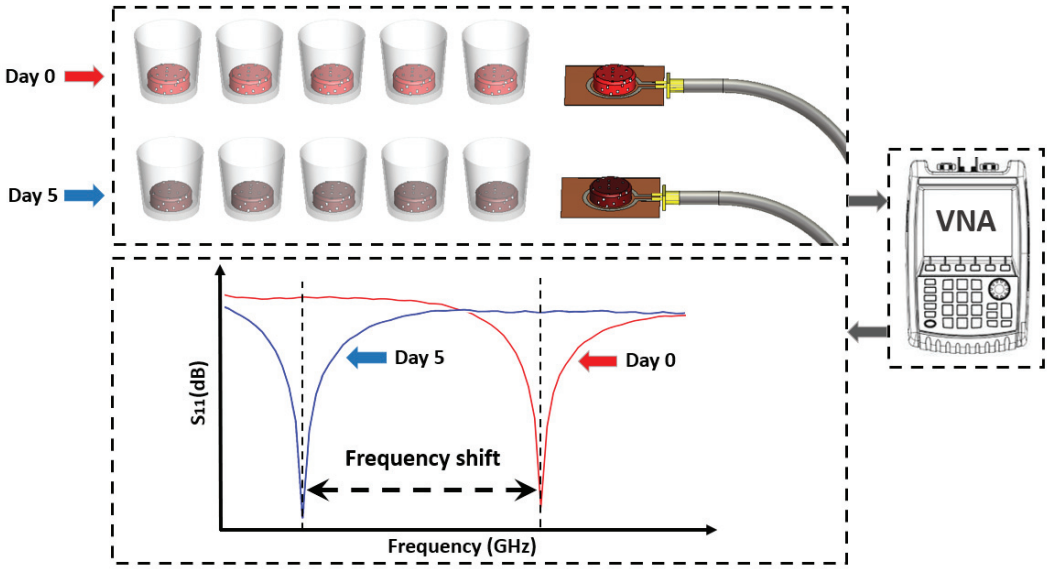

Figure 4. Three-dimensional model representation of the experimental protocol for assessing meat quality using microwave sensing. The model depicts fresh samples (Day 0) and aged samples (Day 5) placed in containers, connected to a microwave sensing setup and a vector network analyzer (VNA).

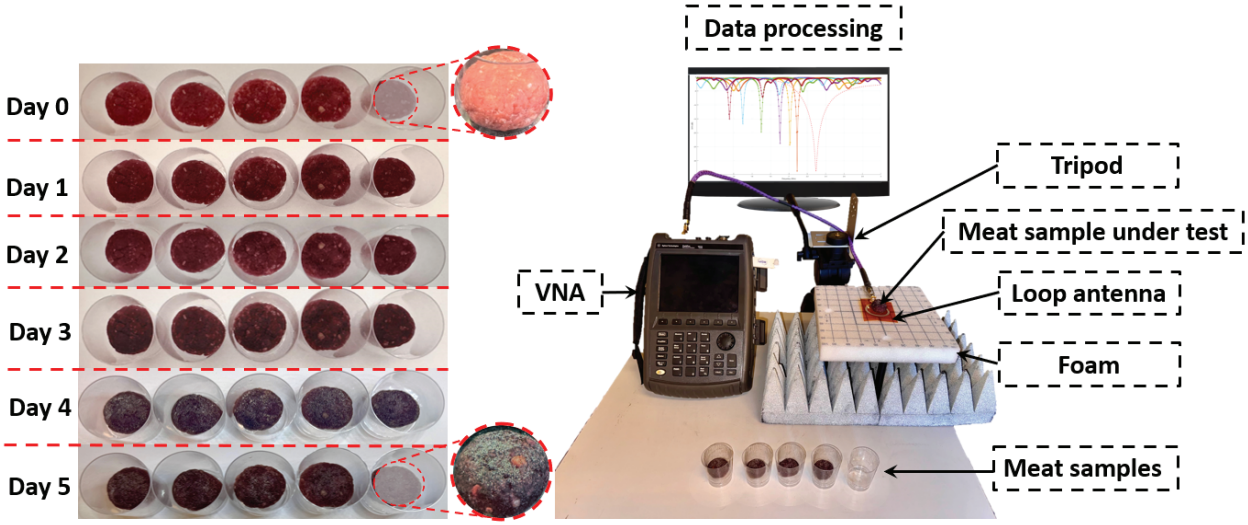

Figure 5. Comprehensive experimental setup for analyzing dielectric property variations in meat samples from Day 0 to Day 5.

For data collection, S_{11} measurements were recorded across the frequency band for each sample. Five samples were measured daily, starting from Day 0 (fresh meat) to Day 5 (stored meat). Measurements were repeated under identical conditions each day to track trends in resonance frequency over time. Data acquisition and analysis were performed using MATLAB 2024B, which facilitated the comparison of S_{11} variations across frequencies and the statistical analysis of all samples.

Data processing involved analyzing the shifts in resonance frequency, identifying changes in the reflection coefficient, and performing statistical comparisons across all days, as described in Figure 4. This comprehensive approach enabled precise monitoring of changes in the dielectric properties of the meat over time, providing valuable insights into the relationship between meat quality and its electromagnetic response.

4. Results and Discussion

The experimental results in this section present the capability of the loop antenna to detect variations in the dielectric properties of meat samples stored under controlled conditions, as shown in Figure 5. By monitoring changes in the reflection coefficient (S_{11}) and resonance frequency over time, the antenna's sensitivity to changes in permittivity caused by meat aging, storage, and environmental variations is assessed. The measurements were benchmarked against simulated data to confirm consistency and establish a correlation between experimental and theoretical observations.

Additionally, statistical analyses were performed to evaluate the repeatability of the measurements and quantify the observed frequency shifts resulting from the effects of aging, storage, and environmental factors on the meat samples. The results are discussed with a focus on the sensor's performance, the influence of material properties on measurement accuracy, and potential applications in food quality assessment.

4.1. Antenna Sensor Evaluation in Free Space

The reflection coefficient (S_{11}) of the loop antenna was evaluated both experimentally and through simulation to benchmark the antenna's performance in free-space conditions. Figure 6 presents a comparative analysis of the measured and the simulated S_{11} as a function of frequency within the 1 GHz to 3 GHz range. The simulated response exhibits a sharp resonance dip at 2.4 GHz, which corresponds to the antenna's design frequency in the ISM

band. The measured response closely follows the simulation, showing a resonance dip at approximately 2.14 GHz. This corresponds to a frequency shift of approximately 10.83%.

The measured response is slightly lower in frequency than the simulated response, which can be attributed to fabrication tolerances and variations in material properties. Factors such as the actual permittivity and thickness of the substrate, which may deviate slightly from simulation inputs, could lead to this shift. Additionally, environmental conditions during measurement might contribute to further deviations.

Despite this shift, the close agreement between the simulated and measured data validates the design process and highlights the effectiveness of the fabrication method. The minimum reflection at resonance confirms good impedance matching to the standard 50 Ω system, ensuring efficient energy coupling and minimal power loss at the operational frequency. This benchmark establishes a reliable reference for subsequent experiments involving varying permittivity conditions caused by meat samples.

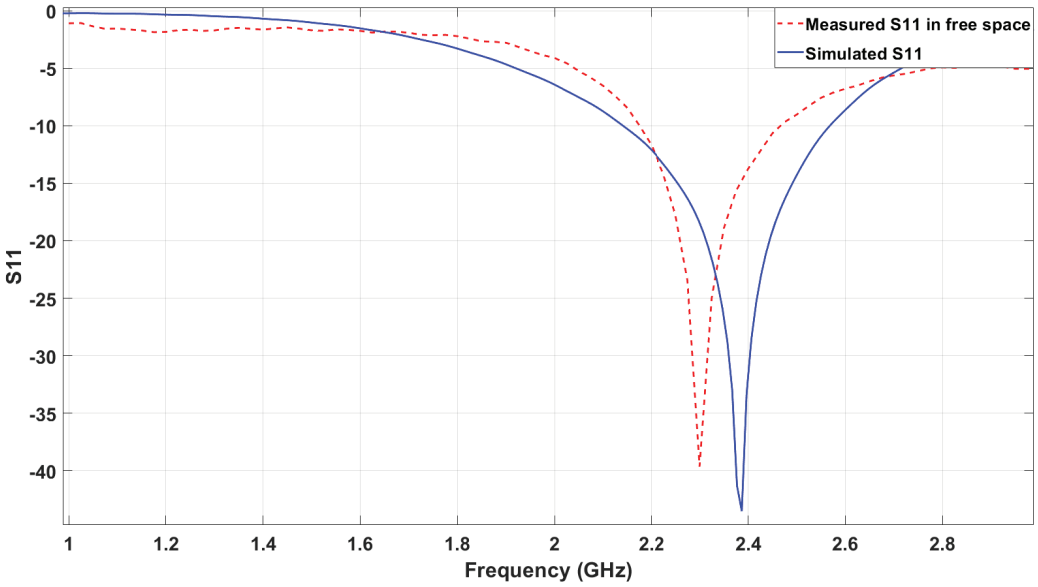

Figure 6. Comparison of measured and simulated S_{11} in free space.

4.2. Permittivity Variation Over Days

To validate the hypothesis regarding the influence of permittivity variation on resonance frequency shifts, a parametric sweep simulation was conducted in CST Studio Suite. This simulation utilized a cylindrical meat model with a radius of 1.5 cm, a height of 1.5 cm, and a volume of approximately 10.61 cm^3, consistent with the experimentally prepared samples. The relative permittivity (ϵ_r) of the modeled meat sample was varied, with initial and final values ranging from $\epsilon_r = 37$ to $\epsilon_r = 91$, as derived and justified in earlier calculations. The goal of this simulation was to observe and quantify the impact of changing dielectric properties on the resonance frequency behavior of the antenna system.

Figure 7 illustrates the results of the simulation, showing a clear trend in the frequency response: as the relative permittivity of the material increased, the resonance frequency consistently shifted towards lower values. For the initial permittivity value ($\epsilon_r = 37$), the simulated resonance frequency was approximately 2.1 GHz, corresponding to a state where electromagnetic coupling with the material was relatively low.

However, as the permittivity increased to its maximum value of $\epsilon_r = 91$, the resonance frequency decreased significantly to approximately 1.3 GHz. This marked shift reflects the increased energy storage capacity of higher-permittivity materials, which modifies the electromagnetic field distribution and results in a reduced resonance frequency.

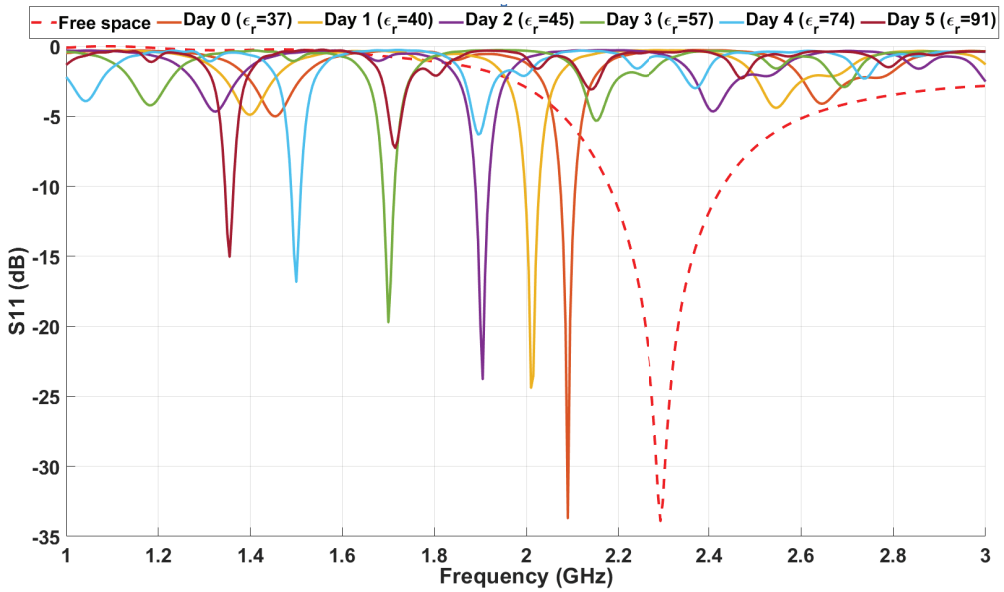

Figure 7. Simulated S_{11} response over the frequency range for various permittivity values corresponding to different days.

The observed trend presented in Figure 8 aligns closely with theoretical predictions, where materials with higher permittivity are expected to exhibit stronger electromagnetic coupling due to increased polarization. This effect reduces the antenna's operating frequency as the system's inductive and capacitive reactance components adjust to the new material properties. Such behavior is indicative of the sensor's sensitivity to the dielectric properties of the surrounding medium and highlights its potential for detecting subtle variations in material composition.

By performing a comprehensive parametric sweep simulation, the permittivity values were strategically selected to align with the frequencies observed in the measurement results (discussed in later sections). This approach ensures that the simulated frequency shifts correspond closely to the experimentally obtained data, thereby validating the reliability of the proposed sensing mechanism. The consistency between the simulation and measurement outcomes highlights the antenna's capability to effectively monitor dielectric changes over time.

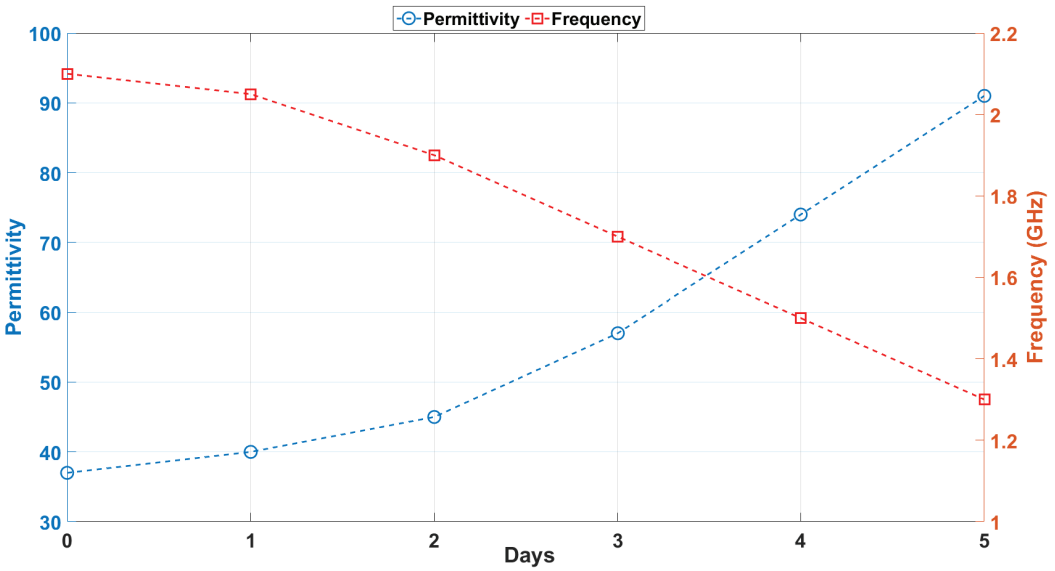

Figure 8. Dynamic relationship between simulated permittivity and frequency across days.

In addition, the selected permittivity values cover a broad range, from low-loss materials ($\epsilon_r = 37$) to highly lossy materials ($\epsilon_r = 91$), reflecting realistic variations in biological tissues. This comprehensive range demonstrates the sensor's adaptability for diverse applications where dielectric property variations are critical.

4.3. Experimental Observations

4.3.1. Average S_{11} Measurements over Six Days

The reflection coefficient (S_{11}) was measured daily for five beef samples over a six-day period to investigate how the dielectric properties of the samples evolved during storage and were impacted by environmental conditions. Each measurement covered a frequency range of 1 GHz to 3 GHz, with the goal of identifying shifts in the resonance frequency and overall trends in the reflection behavior. These measurements were averaged across all five samples for each day, providing a generalized representation of the changes in S_{11} over time while minimizing sample-specific variability.

Figure 9 presents the average S_{11} response for each day, starting from Day 0 (representing fresh samples) to Day 5 (representing aged samples). A distinct downward shift in the resonance frequency is observed over the storage period. On Day 0, the resonance frequency was approximately 2.1 GHz, closely matching the simulated values under initial conditions. By Day 5, the resonance frequency had decreased to approximately 1.3 GHz, reflecting the impact of storage-induced changes on the dielectric properties.

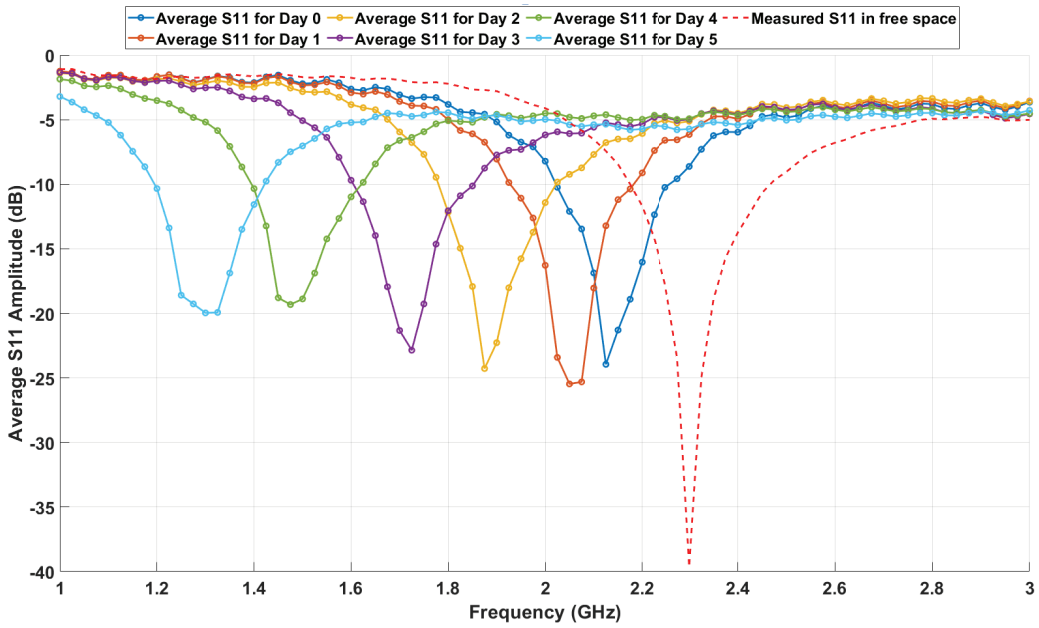

Figure 9. Average (S_{11}) measurements over six days.

Importantly, the bandwidth remained consistent over the six-day period, indicating that the antenna's quality factor (Q-factor) and energy coupling characteristics were unaffected. This stability ensures reliable sensitivity to resonance frequency shifts without distortion.

The environmental conditions—specifically, the 8-hour exposure to room temperature (25 °C) after 12 h of refrigerated storage (7 °C)—accelerated the aging process. This is evident from the resonance frequency shifts and increased energy dissipation, as reflected in the broadening and shallowing of the S_{11} dips over time. These changes are attributed to enzymatic activity, microbial growth, and moisture redistribution, which collectively increase the effective permittivity and conductivity of the meat samples.

The free-space S_{11} curve, represented by a red dashed line in Figure 9, serves as a baseline measurement. It represents the loop antenna's resonance behavior in the absence of any dielectric loading. Compared to the free-space baseline, the curves for Days 0 through 5 exhibit significant shifts in the resonance frequency, highlighting the impact of the meat's dielectric properties on the antenna's performance.

These observations confirm the strong correlation between permittivity changes in the meat samples and the measured resonance frequency shifts. The gradual downward frequency trend aligns with theoretical predictions, where materials with higher permittivity values lead to increased energy storage and a corresponding reduction in resonance frequency. Furthermore, the environmental exposure significantly influences this trend by enhancing the dielectric property changes.

It is important to note that the measurements were conducted over six days because, beyond this period, the results began to show a stabilized trend. Measurements taken on Days 7 and 8 showed similar results to Day 6, indicating stabilization in the dielectric behavior of the samples. On day 9, the meat samples had deteriorated to the point of spoilage, making further analysis impractical. This observation underscores the six-day window as critical for assessing changes in meat quality using this sensing approach.

4.3.2. Resonant Frequency Trends over Time

To assess the uniformity of the experimental process and the consistency of the prepared meat samples, the resonance frequency was analyzed across five identical samples over a period of six days. Figure 10 illustrates the resonance frequency trend for each sample, demonstrating that despite minor fluctuations, all samples exhibited highly consistent resonance frequency behavior throughout the storage period. This consistency validates the preparation process and ensures that the samples were homogeneous in composition and structure, resulting in nearly identical electromagnetic responses.

The overlapping trends confirm the reliability of the experimental procedure and eliminate concerns of variability due to differences in individual samples. These results highlight the effectiveness of the sensing mechanism in delivering reproducible and precise measurements, reflecting the loop antenna's sensitivity and reliability in detecting dielectric property changes in meat samples.

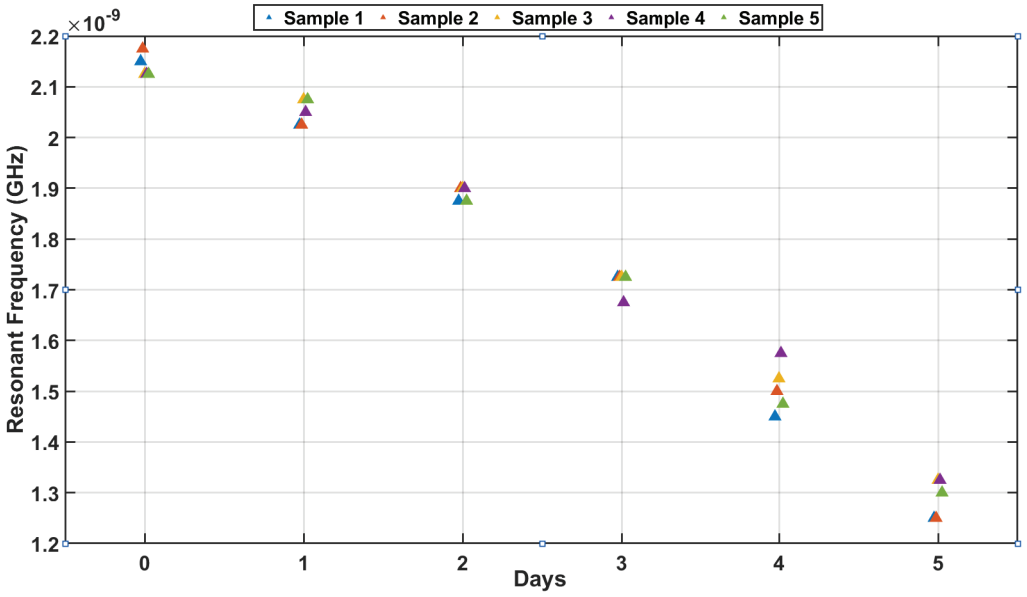

Figure 10. Trend of measured resonance frequencies across individual samples over six days.

4.3.3. S_{11} Amplitude Comparison Across All Samples

The evaluation of the minimum S_{11} amplitude over six days offers valuable insights into the sensitivity and consistency of the proposed antenna-based sensing system. As depicted in Figure 11, the bar plots demonstrate that the minimum S_{11} amplitude values for the five identical meat samples remain consistent throughout the six-day period, with only minor variability observed. This consistency highlights the reliability of the experimental setup and confirms that the prepared samples exhibit comparable dielectric properties, ensuring uniform electromagnetic responses across measurements.

The red squares in Figure 11, representing the average S_{11} amplitude, shows a slight upward trend over the storage period. This trend reflects the impact of meat degradation on the reflection coefficient, which aligns with theoretical expectations. As the meat ages, changes in its dielectric properties, such as increased permittivity and conductivity due to spoilage, result in higher energy absorption. This behavior leads to a gradual reduction in the reflection magnitude, further confirming the sensor's ability to monitor the dielectric property changes associated with meat spoilage.

The error bars in the figure indicate minimal variability among the samples, underscoring the homogeneity of the meat preparation process and the robustness of the antenna's sensing mechanism. Notably, the slightly higher variability observed on Day 2 could be attributed to environmental factors or initial sample-specific conditions. These factors, however, are mitigated in subsequent days as the samples degrade more uniformly, resulting in reduced variability. Overall, the observations confirm the antenna's capability to consistently and accurately detect changes in the dielectric properties of the samples over time.

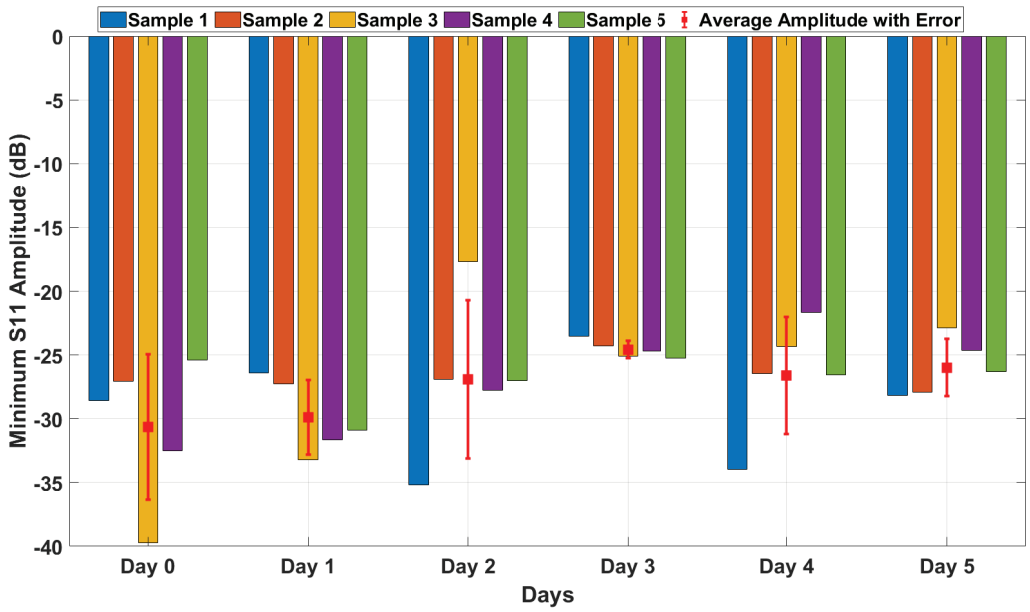

Figure 11. Measured minimum S_{11} amplitudes with average and error bars over days.

4.4. Simulated and Measured Data Comparison

Figure 12 presents the comparison between the simulated and measured resonant frequencies for Days 0 through to 5. The simulated frequencies, derived from permittivity values (ϵ_r), exhibit strong agreement with the measured data, as illustrated by the close alignment of the points and regression lines. The maximum observed error between the simulated and measured frequencies is 0.04 GHz, confirming the high accuracy of the measurement system.

The standard deviations (σ) of the measured data remain consistently low across all days, as shown in Table 2. The largest standard deviation (0.048 GHz) was observed on Day 4, which could be attributed to minor environmental variations or handling differences. However, this variability is well within acceptable limits, demonstrating the robustness of the measurement setup.

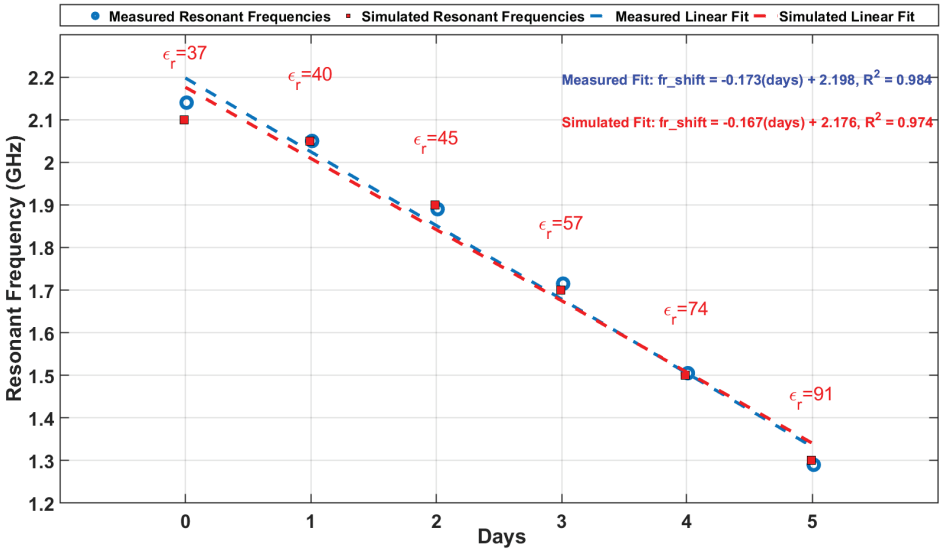

Figure 12. Linear regression analysis of measured and simulated resonant frequencies over time.

Table 2. Summary of simulated and measured resonant frequencies.

Day	ϵ_r	Simulated Frequency (GHz)	Measured Avg Frequency (GHz)	Std. Dev (σ) (GHz)	Error (GHz)
0	37	2.10	2.14	0.022	0.04
1	40	2.05	2.05	0.025	0.00
2	45	1.90	1.89	0.014	0.01
3	57	1.70	1.72	0.022	0.02
4	74	1.50	1.51	0.048	0.01
5	91	1.30	1.29	0.038	0.01

The linear regression analysis further validates the correlation between the simulated and measured data, with the regression equations and R^2 values displayed in Figure 12. These high R^2 values indicate a very strong linear relationship between the resonant frequency and the number of storage days, reflecting the sensor's sensitivity to changes in dielectric properties.

The absolute error (Error) between the simulated (f_{sim}) and measured (f_{meas}) resonant frequencies is calculated as

$$\text{Error} = |f_{\text{meas}} - f_{\text{sim}}| \tag{7}$$

The standard deviation (σ) of the measured resonant frequencies across five samples for a specific day is given by

$$\sigma = \sqrt{\frac{1}{n}\sum_{i=1}^{n}\left(f_i - \overline{f}\right)^2} \tag{8}$$

where

- f_i is the resonant frequency of sample i,
- $\overline{f}$ is the mean resonant frequency,

- n is the number of samples (5 in this study).

The trend of decreasing resonant frequency with increasing permittivity aligns with theoretical expectations. As the meat degrades, spoilage-related changes in its composition lead to an increase in permittivity, causing a downward shift in the resonance frequency. This frequency shift was observed to decrease consistently from 2.14 GHz on Day 0 to 1.29 GHz on Day 5, corresponding to an average sensitivity of 0.173 GHz/day. This behavior underscores the loop antenna's suitability for real-time, non-invasive monitoring of food quality, while the consistently low standard deviations demonstrate the repeatability and reliability of the system.

Comparative Analysis with Existing Technologies

Table 3 summarizes the current sensor technologies for food quality monitoring, comparing their detection methods, measured parameters, target samples, sizes, and fabrication complexities. Existing technologies such as RF energy harvesting, dielectric characterization, VOC detection, and RSSI-based systems are tailored for measuring parameters like color values, temperature, and frequency shifts. However, most of these solutions are complex and non-printable, which restricts their scalability and ease of implementation.

In contrast, the proposed loop antenna sensor presents significant advantages. It is simple, printable, and compact (50 × 70 mm), providing a cost-effective and scalable solution for monitoring meat freshness through resonant frequency shifts. Despite its reduced size, the sensor maintains high sensitivity to dielectric changes, delivering accurate and reliable results.

This work bridges the gap between advanced sensing technologies and practical applications, positioning the proposed loop antenna sensor as an ideal candidate for real-time food quality monitoring in supply chains to ensure freshness and minimize waste.

Table 3. Overview of sensor types and their characteristics.

Ref.	Sensor Type	Detection Method	Samples	Measuring Parameters	Size (mm)	Fabrication Complexity
[19]	Collinear antenna	RF energy harvesting	Pork	RGB [1] color values	149 × 36	Simple/ Not-printable
[20]	Microwave antenna sensor	Dielectric characterization	Duck	Frequency shift	60 × 60	Simple/ Not-printable
[21]	Colorimetric sensor array	Detection of VOCs [2]	Beef, chicken, fish, pork, shrimp	Concentration of VOCs [2] related to spoilage	787.4 × 279.4	Complex/ Not-printable
[14]	RFID [3] Tag antenna	RSSI [4] data	Frozen meat	Temperature	98 × 27	Complex/ Not-printable
[22]	Patch antenna	Dielectric characterization	Meat curing	Frequency shift	80 × 80	Simple/ Not-printable
[23]	Smart sensor tag	RF energy harvesting	Pork	Temperature, humidity	57.62 × 78.93	Complex/ Not-printable
This work	Loop antenna	Dielectric properties	Meat	Frequency shift	50 × 70	Simple/ Printable

[1] Red, Green, and Blue; [2] Volatile Organic Compounds; [3] Radio Frequency Identification; [4] Received Signal Strength Indicator.

5. Conclusions

This study presents a flexible loop antenna-based sensor designed for real-time monitoring of meat freshness through dielectric property changes over a six-day period. The sensor demonstrated a sensitivity of 0.173 GHz/day, with the resonance frequency shifting from 2.14 GHz to 1.29 GHz as the meat degraded. However, beyond Day 6, no significant frequency shifts were observed, indicating that the sensor's detection limit for spoilage assessment had been reached. The experimental results aligned closely with simulations, showing minimal errors (maximum 0.04 GHz) and low standard deviations, confirming the system's accuracy and repeatability.

While the sensor is compact (50 mm × 70 mm), printable, and cost-effective, it is most effective for monitoring thin meat cuts or surface-level freshness due to the need for the meat to be within the electromagnetic (EM) field to detect changes. This limits the sensor's current application for larger meat portions and requires further research into multi-sensor or extended-range solutions to address these limitations.

Despite these constraints, the sensor holds significant potential for scalable food quality monitoring applications. However, since this is a proof-of-concept study, the sensor is intended to provide a relative, rather than absolute, assessment of freshness.

Future work may involve integrating the sensor into IoT platforms for automated real-time data collection, as well as exploring its application for other perishable foods and environmental factors. These developments could advance RF-based food safety solutions, offering an affordable and efficient tool to monitor food quality in various contexts.

Author Contributions: Conceptualization, J.A.; methodology, J.A and M.E.G.; software, J.A.; validation, I.G. and J.A.; formal analysis, J.A. and I.G.; investigation, J.A.; resources, I.G. and R.F.G.; data curation, J.A.; writing—original draft preparation, J.A.; writing—review and editing, J.A., I.G. and R.F.G.; visualization, I.G. and R.F.G.; supervision, I.G. and R.F.G.; project administration, I.G. and R.F.G.; funding acquisition, I.G. and R.F.G. All authors have read and agreed to the published version of the manuscript.

Funding: This research was funded by AGAUR (FI Joan Oró), grant number (2023 FI-1 00453). The APC was funded by Spanish Government-MICINN under Projects TED2021-131209B-I00 and PID2021-124288OB-I00.

Institutional Review Board Statement: Not applicable.

Informed Consent Statement: Not applicable.

Data Availability Statement: Data are unavailable due to privacy restrictions.

Conflicts of Interest: The authors declare no conflicts of interest.

References

1. Darwish, A.; Ricci, M.; Zidane, F.; Vasquez, J.A.T.; Casu, M.R.; Lanteri, J.; Migliaccio, C.; Vipiana, F. Physical contamination detection in food industry using microwave and machine learning. *Electronics* **2022**, *11*, 3115. [CrossRef]
2. Ahmed, I.; Lin, H.; Zou, L.; Li, Z.; Brody, A.L.; Qazi, I.M.; Lv, L.; Pavase, T.R.; Khan, M.U.; Khan, S.; et al. An overview of smart packaging technologies for monitoring safety and quality of meat and meat products. *Packag. Technol. Sci.* **2018**, *31*, 449–471. [CrossRef]
3. Kutsanedzie, F.Y.H.; Guo, Z.; Chen, Q. Advances in nondestructive methods for meat quality and safety monitoring. *Food Rev. Int.* **2019**, *35*, 536–562. [CrossRef]
4. Wang, X.; Bouzembrak, Y.; Lansink, A.G.J.M.O.; Van Der Fels-Klerx, H.J. Application of machine learning to the monitoring and prediction of food safety: A review. *Compr. Rev. Food Sci. Food Saf.* **2022**, *21*, 416–434. [CrossRef] [PubMed]
5. Bhalla, T.C. International laws and food-borne illness. In *Food Safety and Human Health*; Elsevier: Amsterdam, The Netherlands, 2019; pp. 319–371.
6. Jeong, N.; Gan, Y.; Kong, L. Emerging non-invasive microwave and millimeter-wave imaging technologies for food inspection. *Crit. Rev. Food Sci. Nutr.* **2024**, 1–12.. [CrossRef]

7. Bibi, F.; Guillaume, C.; Gontard, N.; Sorli, B. A review: RFID technology having sensing aptitudes for food industry and their contribution to tracking and monitoring of food products. *Trends Food Sci. Technol.* **2017**, *62*, 91–103. [CrossRef]
8. El Khaled, D.; Novas, N.; Gazquez, J.A.; Garcia, R.M.; Manzano-Agugliaro, F. Fruit and vegetable quality assessment via dielectric sensing. *Sensors* **2015**, *15*, 15363–15397. [CrossRef] [PubMed]
9. Kim, S. Inkjet-printed electronics on paper for RF identification (RFID) and sensing. *Electronics* **2020**, *9*, 1636. [CrossRef]
10. VanOverbeke, D. *Handbook of Beef Safety and Quality*; CRC Press: Boca Raton, FL, USA, 2024.
11. Wang, M.; Yang, Y.; Mu, B.; Nikitina, M.A.; Xiao, X. Millimeter wave-based non-destructive biosensor system for live fish monitoring. *Biosensors* **2022**, *12*, 541. [CrossRef] [PubMed]
12. Wang, D.; Zhang, M.; Jiang, Q.; Mujumdar, A.S. Intelligent system/equipment for quality deterioration detection of fresh food: Recent advances and application. *Foods* **2024**, *13*, 1662. [CrossRef] [PubMed]
13. Beshai, H.; Sarabha, G.K.; Rathi, P.; Alam, A.U.; Deen, M.J. Freshness monitoring of packaged vegetables. *Appl. Sci.* **2020**, *10*, 7937. [CrossRef]
14. Marindra, A.M.J.; Pratama, B.M.; Suroso, D.J. Non-invasive frozen meat monitoring system using UHF RFID tag antenna-based sensing and RSSI. *Int. J. Adv. Sci. Eng. Inf. Technol.* **2023**, *13*, 1–7. [CrossRef]
15. Ghatass, Z.F.; Soliman, M.M.; Mohamed, M.M. Dielectric technique for quality control of beef meat in the range 10 kHz–1 MHz. *Am.-Eurasian J. Sci. Res.* **2008**, *3*, 62–69.
16. Kim, D.-E.; Mai, N.-D.; Chung, W.-Y. AIoT-based meat quality monitoring using camera and gas sensor with wireless charging. *IEEE Sens. J.* **2023**, *24*, 7317–7324. [CrossRef]
17. Sihvola, A.H. *Electromagnetic Mixing Formulas and Applications*; IET: Stevenage, UK, 1999; Volume 47.
18. Pozar, D.M. *Microwave Engineering*, 4th ed.; University of Massachusetts at Amherst, John Wiley & Sons, Inc.: Hoboken, NJ, USA, 2012; pp. 26–30.
19. Kim, D.-E.; Nando, Y.A.; Chung, W.-Y. Battery-free pork freshness estimation based on colorimetric sensors and machine learning. *Appl. Sci.* **2023**, *13*, 4896. [CrossRef]
20. Calvet-Chautard, M.; Jaque Gonzalez, P.; Véronèse, T.; Dubuc, D.; Grenier, K. Microwave-based sensor dedicated to the characterization of meat freshness. In Proceedings of the 2020 IEEE MTT-S International Microwave Biomedical Conference (IMBioC), Toulouse, France, 14–17 December 2020 ; pp. 1–4.
21. Li, Z.; Suslick, K.S. Portable optoelectronic nose for monitoring meat freshness. *ACS Sens.* **2016**, *1*, 1330–1335. [CrossRef]
22. Muradov, M.; Cullen, J.; Mason, A. Real-time monitoring of meat drying process using electromagnetic wave sensors. In *Next Generation Sensors and Systems*; Springer: Berlin/Heidelberg, Germany, 2016; pp. 221–233.
23. Nguyen, N.H.; Lam, M.B.; Chung, W.-Y. Battery-less pork freshness monitoring based on high-efficiency RF energy harvesting. *J. Sens. Sci. Technol.* **2020**, *29*, 293–302. [CrossRef]

sensors

MDPI

Article

Design, Development, and Qualification of a Broadband Compact S-Band Antenna for a CubeSat Constellation

Saray Sánchez-Sevilleja [1,*], David Poyatos [1], José Luis Masa-Campos [2], Víctor Miguel Aragón [1], José Antonio Rodríguez [1] and Amaia Santiago [1]

[1] INTA National Institute of Aerospace Technology, Ajalvir Road, km 4, 28850 Torrejón de Ardoz, Spain; poyatosmd@inta.es (D.P.); aragonfvm@inta.es (V.M.A.); rodriguezpja@inta.es (J.A.R.); santiagopa@inta.es (A.S.)
[2] E.T.S.I. Telecommunication, Department of Signals, Systems and Radiocommunications, Universidad Politécnica de Madrid (UPM), C/Ramiro de Maeztu 7, 28040 Madrid, Spain; joseluis.masa@upm.es
* Correspondence: ssansev@inta.es

Abstract: An S-band antenna has been designed, developed, measured, space-qualified, and integrated into the INTA ANSER satellite constellation and the future ANSER-AT mission. This antenna will be part of the space-to-ground communication link for the constellation, which consists of one Leader and two Followers. The novel antenna, mounted on the Leader, has been designed and manufactured with materials and processes specifically tested for space. It features dual circular polarization over a wide band without requiring a phase-shifting network, making it very compact and straightforward. Additionally, its gain patterns are highly stable within the desired band, improving its link capacity compared to the UHF monopole alternative used in the previous Leader. Currently, the antenna has been qualified and installed on INTA's Leader-S, set to launch in January 2025, as well as on the future ANSER-AT mission.

Keywords: constellation; cluster; CubeSat; antenna; MPA; polarization; axial ratio

1. Introduction

The number of space missions that are based on CubeSat is continuously increasing [1–3]. Indeed, this class of nanosatellites is particularly attractive because it enables access to space at a low cost, allowing small countries, universities, or even minor private companies to gain experience in the aerospace sector. In addition, thanks to modern technologies, relatively complex missions can be planned, e.g., for earth observation, remote sensing, communication technology experiments, hardware validation, and other scientific missions, as well as educational purposes. These satellites must satisfy strict requirements not only to ensure their successful operation in the harsh environment of space but also to comply with the safety requirements imposed by the launcher company or organization. In the case of CubeSat nanosatellites, they also must comply with the CubeSat standard [4], which imposes stringent limitations on satellite dimensions and weight, which makes the design of each subsystem a challenge [5].

In this scenario, INTA (National Institute for Aerospace Technology) has launched ANSER, an ad hoc constellation of clusters, where each cluster is formed of several CubeSat nanosatellites flying in formation, with one Leader (which could not be launched due to technical issues with the launcher) and two Followers (currently in orbit since 2023 and operational) [6].

The objective of ANSER is to develop and demonstrate technologies that will enable efficient earth observation missions in the future, making use of four main novel concepts: constellations of nanosatellites, formation flying, fractionated instruments, and miniaturized technologies. The ANSER flight segment consists of three 3U CubeSats (a Leader and two Followers), each with nearly identical physical characteristics, i.e., size, mass, moment of inertia, etc. There was an attempt to launch the three 3U CubeSats, using a Vega-C rocket, into an orbit at an altitude of 550 km in October 2023. Once there, the satellites, which do not have an on-board propulsion system, should maneuver themselves to establish and maintain a formation using the aerodynamic drag generated by the Earth's atmosphere. But an anomaly occurred during the launch of ANSER, preventing the deployment of the Leader satellite. The two mission satellites successfully deployed by the launcher, Follower 1 and Follower 2, are currently operating normally, with their subsystems already validated in orbit. Consequently, the decision has been made to reassemble the lost satellite, now called Leader-S, and seize the opportunity to introduce some enhancements to the system, given the validated in-orbit performance of the remaining subsystems of the Follower satellites, which are identical to those of the Leader [7].

Leader-S relies on UHF communication systems with deployable monopole antennas for low-bit-rate uplinks and downlinks (telecommands and telemetry), while, for high bit rates, the S-band is among the best choices [8]. As a result, one of the key components of the Leader-S is the design of a new S-band communication subsystem, as this ensures a link with the ground station for the uplink of telecommands and the downlink of telemetry and payload data. In particular, the design of this new antenna system is a fundamental step as it must take into account aspects of the mission (e.g., satellite attitude) [9,10] and comply with the CubeSat size constraints while, of course, ensuring good performance [11].

In this scenario, the S-band antenna to be included in Leader-S and in the future ANSER-AT satellites can provide gain, versatility, and reliable up/downlinks and inter-satellite links in a wide operating bandwidth, with its focus on aspects such as miniaturization, radiation efficiency, bandwidth, and improved polarization capability using dual circular polarization [12]. This circular dual polarization is essential in satellite communications, as it enables better signal reception and transmission regardless of the orientation of the satellite or the ground receiving antenna [5]. Furthermore, in the case of the Leader-S CubeSat, the antenna's size and profile must be kept within certain dimensions to adhere to the CubeSat standards. The cost and complexity of the antenna and its technique must also be considered for CubeSat integration [13].

A popular candidate for such advanced antenna systems is multilayer microstrip patch antennas. The flexibility of printed planar antennas lies in their low profile, light weight, and low fabrication cost [12,14–16].

Regarding this, this paper is organized as follows: Section 2 presents the applications for which the S-band antenna has been developed (ANSER and ANSER-AT). Section 3 describes the geometry of the designed antenna, while Section 4 outlines a parametric study considering the effects of its notches and its parasitic element. Section 5 presents the results and compares them with the existing literature, and finally, the paper concludes with Section 6, which shows the qualification and acceptance test results.

2. Satellite Constellations: ANSER and ANSER-AT

ANSER is an ad hoc constellation of clusters, where each cluster is formed by several CubeSat nanosatellites flying in formation. The higher the number of clusters in the constellation, the shorter the mission revisit time, and the higher the number of elements in any cluster, the wider the swath on the ground [6,7,16]. This concept of mission, when applied to Earth observation, shall be supported by five key technologies: stable and

efficient formation flying control, highly accurate pointing control, precise guiding and navigation, inter-satellite communications, and high-performance payloads compatible with very small platforms.

Each cluster will consist of one Leader and two Followers (Figure 1a) placed in a cross-track configuration with respect to the original orbital plane. The three observation nanosatellites will work together as if they were a single platform, monitoring the water quality of reservoirs and dams on the peninsula (Figure 1b). To this end, the Leader controls the cluster operation, distributing the tele-commands received from the Mission Control Centre placed in INTA. Each follower carries a miniature spectrometer with a spectral resolution better than 8 nm and a spatial resolution of at least 50 m. The whole cluster acts as a distributed EO instrument, with scientific and housekeeping data being collected by the Leader from the observing Followers via an inter-satellite link (ISL). The ideal distance between the followers, about 10 km, is estimated as a function of the swath capability of each individual observer.

(**a**) (**b**)

Figure 1. ANSER constellation: (**a**) ANSER Leader + Followers; (**b**) formation flight simulation.

The three satellites, devoid of an onboard propulsion system, are required to maneuver in order to establish and maintain a formation utilizing the aerodynamic drag generated by the Earth's atmosphere. The capacity to generate differential aerodynamic drag between the satellites by altering their attitude forms the foundation for controlling the formation in the absence of a propulsion system. The operations plan stipulates that each satellite should be commissioned in sequence and then maneuvered to establish a distant formation that cancels any drift. Thereafter, the satellites would gradually approach each other to enable inter-satellite communications and even explore more advanced formations. The constellation was defined using one of the satellites (Leader) as a reference, with the other two (Followers) working with its coordinates.

At this moment, the two ANSER Followers are maneuvering to approach a distance of 100 km and wait together for the reintroduction of Leader-S. Its launch, initially scheduled for 1 November, has been postponed by SpaceX to 14 January 2025. It has, therefore, been decided that both Followers will wait for the third element at an altitude of around 520 km [6,7].

In addition to the ANSER mission, the ANSER-AT (6U CubeSats) mission enhances Earth observation by focusing on formation control and resilience within a satellite constellation. This additional mission employs aerodynamic forces, such as lift and drag, for maintaining formation in low Earth orbit, instead of traditional propulsion. This innovative technique, employed by ANSER-AT, supports the broader objectives of the ANSER mission, which include the monitoring of environmental factors such as water quality and atmospheric conditions. Additionally, it aims to enhance cost efficiency and mitigate the risks associated with propulsion-based control [16].

3. Design and Geometry of the Proposed Antenna

3.1. S-Band Antenna Design

In order to enhance communication capabilities for the satellite–ground link without compromising the already qualified payload, a lightweight, flat, wideband, and compact S-band antenna is required. The requirements that the S-Band antenna must meet are defined in Table 1.

Table 1. S-Band antenna requirements.

Frequency	2.03 GHz $\pm$ 10 MHz and 2.205 GHz $\pm$ 25 MHz
Reflection coefficient	≤ -12 dB
Gain	≥ -10 dBi
Polarization	Circular dual
Axial ratio	<4 dB
Maximum size	80 $\times$ 80 mm
Maximum height	6.6 mm
Connector	SMP

In addition, due to the special environment in space and the requirements of the ANSER program, the antenna design has many other environmental challenges to consider [8,9]:

- The antenna must be mechanically robust and able to survive both random vibration and shock during the launch. The thermal design of the antennas must be carefully evaluated; therefore, antennas are designed to perform over a wide temperature variation, from -50 °C to +90 °C.
- In addition, materials for the antenna need to be chosen carefully, considering the effects of vacuum and micro-gravity without losing sight of EMC and mutual coupling amongst the payloads, circuits, and other antennas fitted in a small space.
- A major consideration for antenna design is the interaction between antennas and the modem CubeSat structures. The spacecraft's structure can cause electromagnetic scattering, as well as have blockage effects on the antenna's radiation patterns. The scattering can interfere with the antenna's radiation pattern and can cause severe degradation in gain performance and sidelobes. This degradation will have a major influence on the communication-link system's performance and needs to be assessed. For that reason, a study was conducted on the most suitable positions to place the antenna in terms of link budget and coverage (Figure 2).

Taking all this into account, a multilayer microstrip antenna has been designed, developed, integrated, and measured. The choice of microstrip technology is based on the advantages such as being lightweight, low-profile, cost-effective, and flexible for integration, which is particularly crucial in space applications. Microstrip antennas can be used either as single elements when the gain requirements are low or in an array configuration such as microstrip patch antenna arrays, phased arrays, or reflect arrays in order to boost their gain, beamforming, and beam scanning performance [12]. However, the main limitation of microstrip patch antennas (MPAs) is their narrowband characteristics due to their high Q nature [14,16]. A number of wideband approaches have been proposed to enhance the impedance bandwidth of microstrip patch antennas, such as the use of shorting pins or walls [17,18], parasitic elements attached either to the radiating or non-radiating edge of the patch [19,20], stacked multiple patches on different substrate layers [21], aperture-coupled feeding techniques [22–24], metamaterial-based antennas and increasing the substrate

thickness relative to the free space wavelength or using substrates with dielectric constants close to unity. However, when using any of the aforementioned techniques, a trade-off must be performed between the bandwidth performance of the antenna and its radiating characteristics [9,14,16,25,26]. Despite that, in this work, a wideband S-band multilayer antenna has been developed, qualified, and integrated for Leader-S satellite, maintaining optimal radiation characteristics.

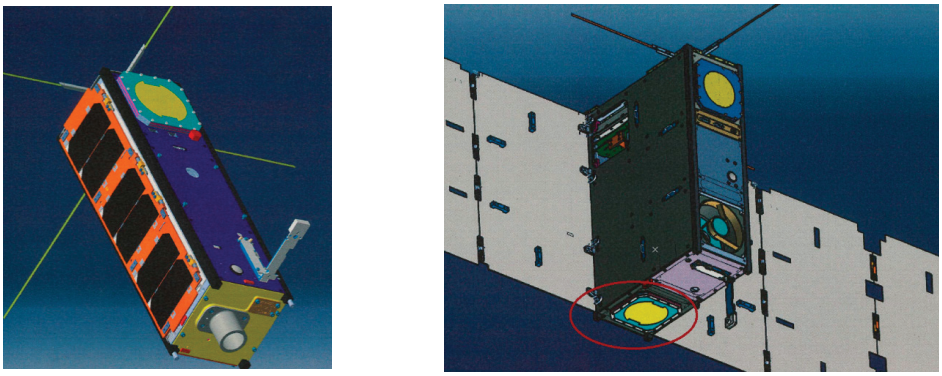

(**a**) (**b**)

Figure 2. S-Band antenna model placed on ANSER cubeSats: (**a**) ANSER; (**b**) ANSER—AT (final position marked with a red circle).

In addition, the unique environment of space and the requirements of the ANSER program impose numerous environmental challenges on antenna design [8,9].

- The antenna must be mechanically robust and capable of withstanding both random vibrations and shocks during launch. The thermal design of the antennas must be meticulously evaluated, with the antennas themselves designed to function over a wide temperature range, from −50 °C to +90 °C.
- Furthermore, the selection of materials for the antenna must be made with great care, taking into account the effects of vacuum and micro-gravity without compromising considerations of EMC and mutual coupling amongst the payloads, circuits, and other antennas when fitted within a confined space.
- A significant aspect of antenna design is the interaction between antennas and the modem CubeSat structures, as the spacecraft's structure can induce electromagnetic scattering and result in blockage effects on the antenna's radiation patterns. The interaction of this scattering with the antenna's radiation patterns can lead to significant degradation in gain performance and sidelobes, which, in turn, can have a substantial impact on the performance of the communication-link system. Consequently, a study was conducted to ascertain the most optimal positioning of the antenna, taking into account the link budget and coverage (see Figure 2).

The design, development, integration, and measurement of a multilayer microstrip antenna has been undertaken, taking all these factors into account. The selection of microstrip technology is based on the advantages of being lightweight, low-profile, cost-effective, and flexible for integration, which is particularly crucial in space applications. Microstrip antennas can be used either as single elements when the gain requirements are low or in an array configuration such as microstrip patch antenna arrays, phased arrays, or reflect arrays in order to boost their gain, beamforming, and beam scanning performance [12]. However, the main limitation of microstrip patch antennas (MPAs) is their narrowband characteristics due to their high Q nature [14,16]. A number of wideband approaches have been proposed to enhance the impedance bandwidth of microstrip patch antennas, such as the use of shorting pins or walls [17,18], parasitic elements attached either to the radiating

or non-radiating edge of the patch [19,20], stacked multiple patches on different substrate layers [21], aperture-coupled feeding techniques [22–24], metamaterial-based antennas and increasing the substrate thickness relative to the free space wavelength or using substrates with dielectric constants close to unity. However, when employing any of the aforementioned techniques, a trade-off must be maintained between the bandwidth performance of the antenna and its radiating characteristics [9,14,16,25,26]. Notwithstanding this, in the present work, a wideband S-band multi-layer antenna has been developed, qualified, and integrated for Leader-S satellite, maintaining optimal radiation characteristics.

Furthermore, the compact antenna design, with dimensions of 80 mm × 80 mm × 6.53 mm and a weight of 30 g, features dual circular polarization, a highly recommended characteristic in satellite communications. This provides increased mobility and freedom in the orientation angle between a transmitter and a receiver in comparison with a linearly polarized antenna [25]. The antenna's flat and compact design, facilitated by a single feed rather than multiple feeding points with phase-shifting networks, enables dual circular polarization without the need for additional components. This approach simplifies the antenna's design, reduces its weight and complexity, minimizes loss, and enhances aperture efficiency, making it particularly well-suited for space applications. However, it should be noted that the challenge of achieving dual circular polarization over a wide bandwidth remains significant despite the advantages offered by single-point feeding. This aspect, therefore, represents the primary strength of the antenna [26].

Firstly, the 8% impedance bandwidth has been achieved by placing a parasitic patch in a stacked patch configuration. In this setup, the lower patch is fed through a co-axial pin, while the upper patch is electromagnetically coupled to the lower patch. This configuration enables the lower frequency to be determined by the lower patch while the upper patch sets the upper frequency, thereby increasing the bandwidth [19–21]. Additionally, to generate circular polarization, the coaxial pin is rotated by an angle of 45° with respect to the center line, thereby establishing the orthogonal components of the field with equal magnitude and a 90° phase shift, resulting in circular polarization but with a narrow bandwidth [27]. By incorporating sufficiently large slots or notches in both patches, the axial ratio (AR) bandwidth is enhanced without compromising the radiation characteristics. Consequently, the antenna achieves a bandwidth of 8%, encompassing both uplink (2.03 GHz) and downlink (2.205 GHz) frequencies, thereby ensuring robustness in gain and polarization vs. frequency. This guarantees the link's viability under any conditions that may cause a deviation in the antenna's operating frequency.

In consideration of the aforementioned factors, the proposed circularly polarized antenna is to be constructed from a multilayer stack-up. In order to minimize manufacturing costs and in accordance with the principles of CubeSat development, a low-cost substrate will be utilized HF Rohacell [28] and Rogers 4360 [29] (Figure 3). The layers of this multilayer stack-up are divided into three RO4360 dielectric boards separated by two Rohacell spacers, which provide structural integrity while behaving almost like air: a lower board formed by two layers consisting of a RO4360 dielectric layer (H2) covered with a copper layer on one of its sides (H1). The copper layer H1 functions as a ground plane, upon which the SMP connector is soldered, while the primary function of the RO4360 is to provide rigidity while reducing weight compared to a metallic board. The central board comprises an additional layer of RO4360 dielectric featuring copper metallization on one side, which is partially removed to create the lower patch. The pins of the SMP connectors are soldered to this patch. Finally, a third board is constructed using an additional layer of RO4360 with copper metallization on the top side, which is partially removed to create the parasitic patch. The excitation of this parasitic patch is facilitated through electromagnetic coupling from the lower patch, with the coupling strength being determined by the thickness of the

Rohacell spacers. Additionally, two miniature coaxial 50 ohm SMP connectors (right and left polarizations) are employed to feed the lower patch, ensuring the integration of the antenna without interfering with other functional units inside the satellite (see Figure 4).

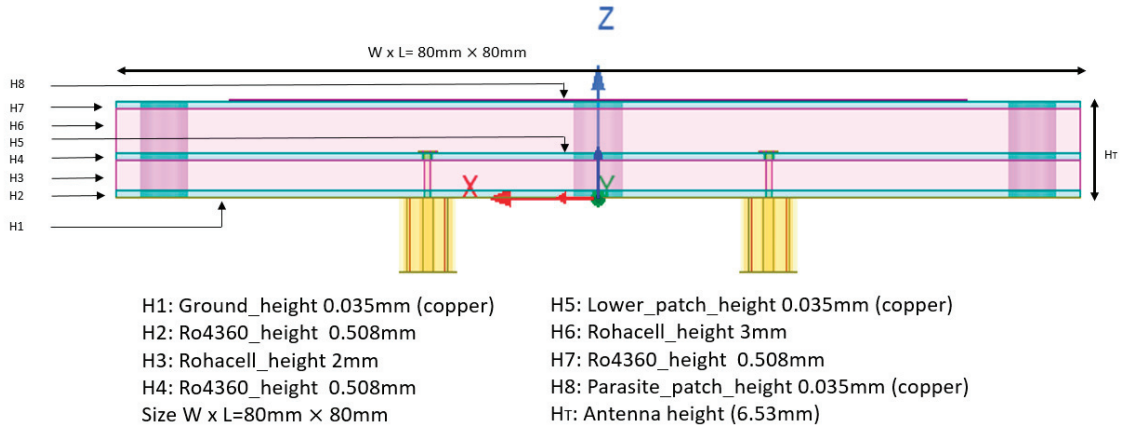

Figure 3. S—Band antenna stack-up.

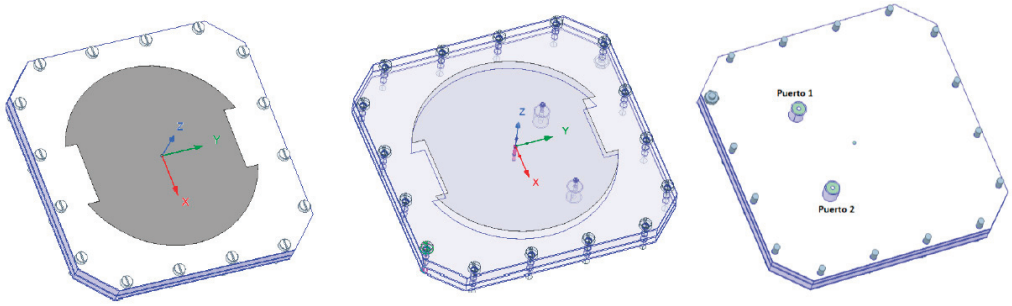

Figure 4. General overview of S—Band antenna design.

The subsequent investigation in Section 4 will entail a parametric analysis of the parasitic element and the presence of notches, with the objective of achieving circular polarization across a broad frequency range. Additionally, the gain bandwidth performance will be assessed and contrasted with the impedance bandwidth of the proposed antenna.

3.2. Manufacturing and Assembly

Two prototypes have been developed based on the same electromagnetic design, with the objective of qualifying them with space levels prior to integration within the Leader-S structure. It is noteworthy that both prototypes are functionally identical: the Engineering Qualification Model (QM), which will be qualified with values and duration of qualification, and the flight model (FM), which will be qualified with duration and values of acceptance. It is anticipated that the FM will be the antenna that will fly placed on Leader-S. The design, integration and measurement of these prototypes have been conducted at INTA facilities, yielding identical results. With regard to the assembly, the layers are manufactured separately: a first plate containing the ground plane, to which the connector flanges are soldered (see Figure 5c); a second plate containing the lower patch, to which the connector pins are soldered (see Figure 5b); and a third plate containing the parasitic patch (see Figure 5a). These plates are separated by two Rohacell spacers, which provide structural rigidity. In order to adjust the antenna to the available slot in the CubeSat, the corners of each layer are chamfered and a central pin has been included to avoid unwanted discharges. Finally, only 12 nylon screws are required for fastening the multilayer, and two miniaturized SMP connectors for right and left polarizations feed the antenna.

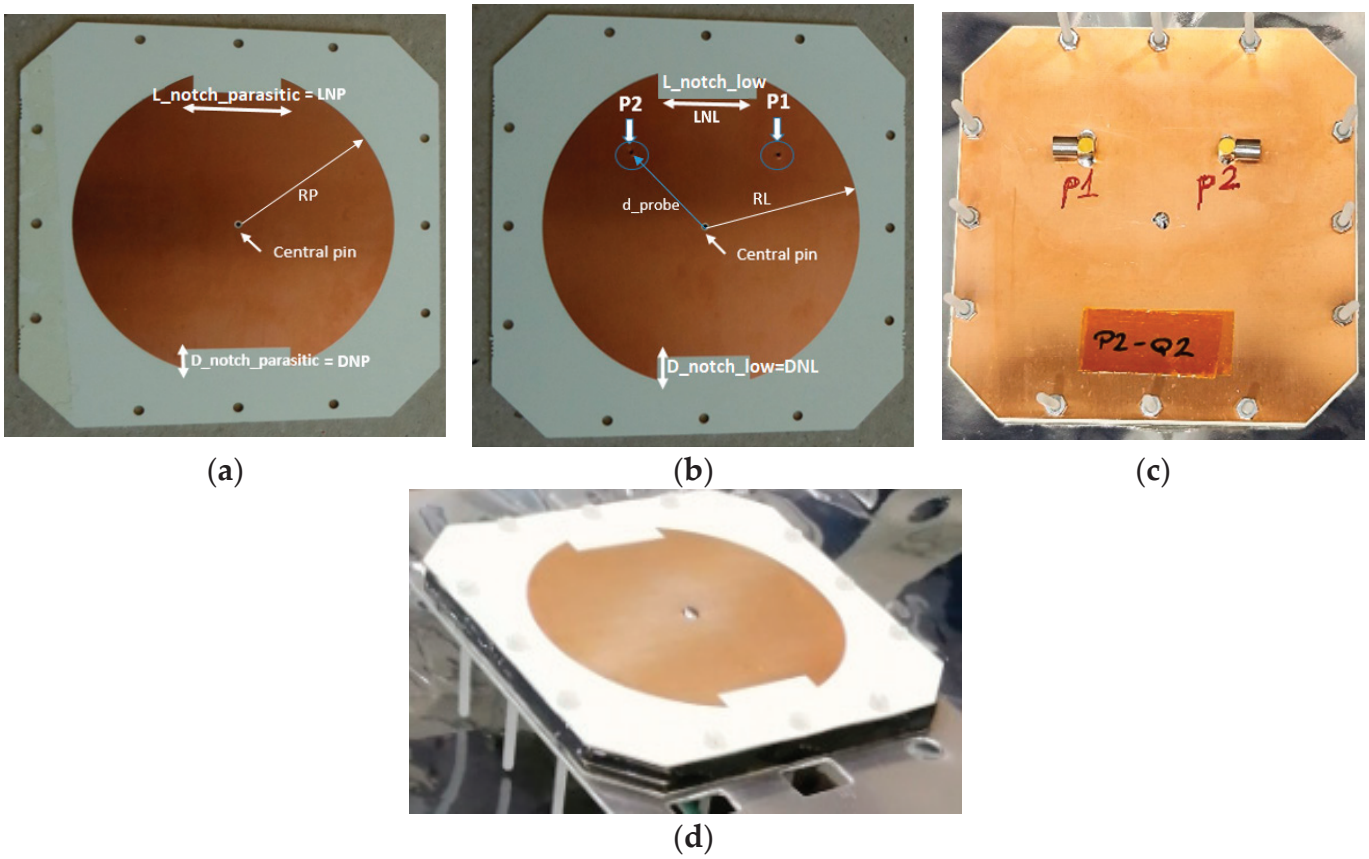

Figure 5. S-Band QM Antenna Design: (**a**) upper parasitic patch; (**b**) lower patch; (**c**) back part with SMP connectors (**d**) S-band antenna.

Once the antenna has been assembled with materials that have undergone a bakeout process, it is bordered with an adhesive (SCOTCH WELD 2216 A + B. Batch EGE 208 [30]), which is applied to both antennas to prevent the intermediate layers forming the antenna from releasing unwanted particles in space. Following the application of the adhesive, the ANSER QM S Band antenna undergoes a complete qualification test campaign.

Due to space specifications, the manufacturing process, material handling, assembly, and antenna measurements are carried out in the clean rooms of the INTA facilities, following a written, predefined procedure.

4. Parametric Study of S-Band Antenna

In a stacked microstrip patch antenna fed by a single point, the size of the lower and parasitic patches affects several performance parameters, including the resonant frequency, bandwidth, axial ratio (circular polarization), and radiation pattern [31]. In fact, the lower frequency is determined by the larger patch, which is usually the lower one, while the higher frequency is determined by the smaller patch, which typically corresponds to the parasitic one. Furthermore, it has been demonstrated that altering the dimensions (length and depth) and positioning of the notches in both patches of the antenna can have a substantial impact on the axial ratio bandwidth and, consequently, on the polarization characteristics of the antenna [32–35]. As a result, a parametric study was conducted to ensure a suitable design was achieved. The final design parameters following optimization are presented in Table 2.

Table 2. Parameters values of designed antenna.

RP (radius_parasitic_patch)	30.6 mm
RL (radius_lower_patch)	30.7 mm
LNP (L_notch_parasitic)	20 mm
LNL (L_notch_low)	18 mm
DNP (D_notch_parasitic)	5.6 mm
DNL (L_notch_low)	4.35 mm
d_probe	20 mm
Size	80 mm × 80 mm

As demonstrated in Figure 6a, the dimensions of the lower patch (RL) within the stacked microstrip antenna have a significant impact on critical parameters such as resonant frequency, bandwidth, and impedance matching. It is observed that increasing the size of the lower patch leads to a decrease in resonant frequency and a concomitant reduction in bandwidth. Conversely, a reduction in the size of the lower patch results in an increase in resonant frequency and an enhancement in bandwidth. It is also noteworthy that the change in size can impact the antenna's efficiency due to weaker coupling between stacked patches.

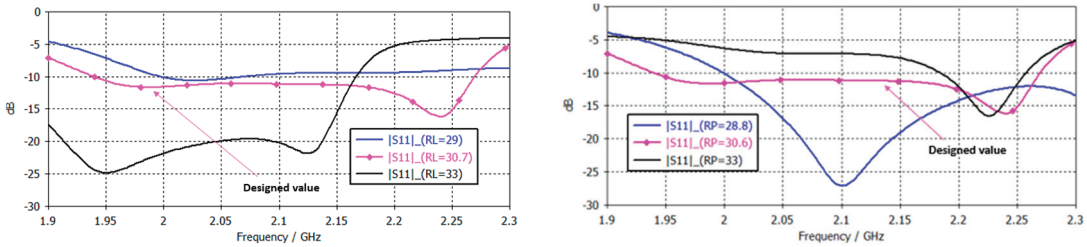

(**a**) (**b**)

Figure 6. |S11| as a function of patches size: (**a**) lower patch; (**b**) parasitic patch.

Conversely, an augmentation in the dimensions of the parasitic patch (RP) has been observed to result in a shift towards lower frequencies of the lower resonant frequency, thereby enhancing the impedance bandwidth through an improvement in coupling between the patches. However, this augmentation can potentially lead to a degradation in the axial ratio (circular polarization), resulting in diminished efficiency of the polarization. Moreover, an inadequate sizing of the parasitic patch can give rise to inefficient coupling and an escalation in return loss. Lastly, changes in patch size can alter the radiation pattern, potentially affecting directivity and side lobes. Therefore, the size of the lower and parasitic patches plays a crucial role in optimizing antenna performances [14,16,31]. The separation thickness between two stacked microstrip patches significantly influences the antenna's performance (H3 and H6) [26,27]. Increasing the separation leads to a reduction in the coupling between the patches, resulting in a decrease in the resonance frequency and an increase in the bandwidth as the effective interaction between the patches becomes weaker. Conversely, although reducing the separation enhances the coupling, increases the resonant frequency, and improves impedance matching, the bandwidth decreases, and it can also lead to greater cross-talk (undesired coupling of signals between the two orthogonal polarizations) or undesirable radiation characteristics. Furthermore, the separation affects the overall efficiency, with optimal spacing ensuring efficient power transfer between the patches without excessive loss. It is, therefore, crucial to fine-tune the separation in order to control the antenna's radiation pattern and optimize its performance since there is always

an optimal separation suitable for the resonant size of the two patches, the lower and the parasitic.

The shape, depth, and positioning of the notches influence the current distribution on the patches, thus affecting the impedance matching, AR bandwidth, and polarization characteristics. The introduction of lateral slots or notches on the edges of the patch modifies the surface currents and fields generated on the antenna [32]. These slots affect the patch's symmetry, and with proper placement and size, they generate a current distribution that facilitates the excitation of orthogonal field modes. It has been established that these two orthogonal modes possess a 90-degree phase difference and that when these two modes are of equal magnitude, circular polarization is achieved [14,16]. Furthermore, it has been demonstrated that the axial ratio (AR) bandwidth for circular polarization improves when the size of the slots is increased. The incorporation of notches along the edges of the patch results in the creation of additional electromagnetic coupling points between regions of the lower and parasitic patches, thereby enhancing the coupling between the orthogonal modes within the patches. This, in turn, enables the antenna to maintain circular polarization efficiently over a broader frequency range [33,34].

As demonstrated in Figure 7b, an enhancement in impedance matching capability is observed with an increase in notch depth (DNP), leading to an expansion in the frequency response. However, when the depth exceeds a certain threshold, these notches have a detrimental effect on the coupling between the patches, necessitating the calculation of design values through fine optimization. The AR bandwidth (Figure 8b) also improves with increasing depth (DNP and DNL), but only up to a certain notch depth value, after which it worsens, reducing the bandwidth. Finally, increasing notch length (LNP and LNL) improves the AR bandwidth (Figure 8a), and therefore, notches with a high length are chosen. Consequently, the length of the notches of the designed antenna is considerably larger than that of conventional circular patches based on lateral slots.

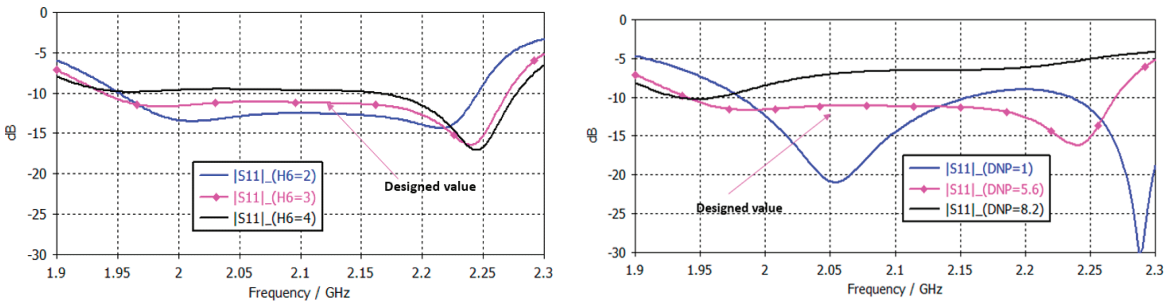

Figure 7. |S11| variation: (**a**) H6 (h—rohacel2); (**b**) depth notch parasitic (DNP).

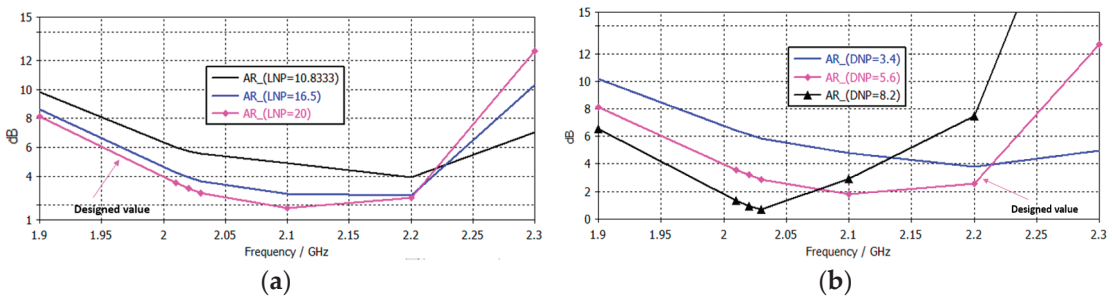

Figure 8. Variation in axial ratio with the size of the notches; (**a**) LNP (length); (**b**) DNP (depth).

The variation in the size and position of the notches, the size of patches, and the thickness of the dielectrics in a stacked patch antenna can have a significant effect on the

axial ratio and the impedance matching and, therefore, on the polarization characteristics of the antenna. As a result, a thorough optimization process is imperative to ascertain the optimal values of the antenna parameters, thereby ensuring low axial ratios, optimal circular polarization, and the attainment of the desired bandwidth and resonant frequency (see Table 1).

5. Isolated S-Band Antenna Results

Following the design of both the QM and the FM models, individual measurements were conducted to validate the simulated model in the electromagnetic software CST Microwave Studio 2023. Measurements of the S-parameters and radiation characteristics, including gain patterns and axial ratio, were conducted for the frequencies of interest in both models. These measurements were carried out in the compact range chamber at INTA facilities (see Figure 9).

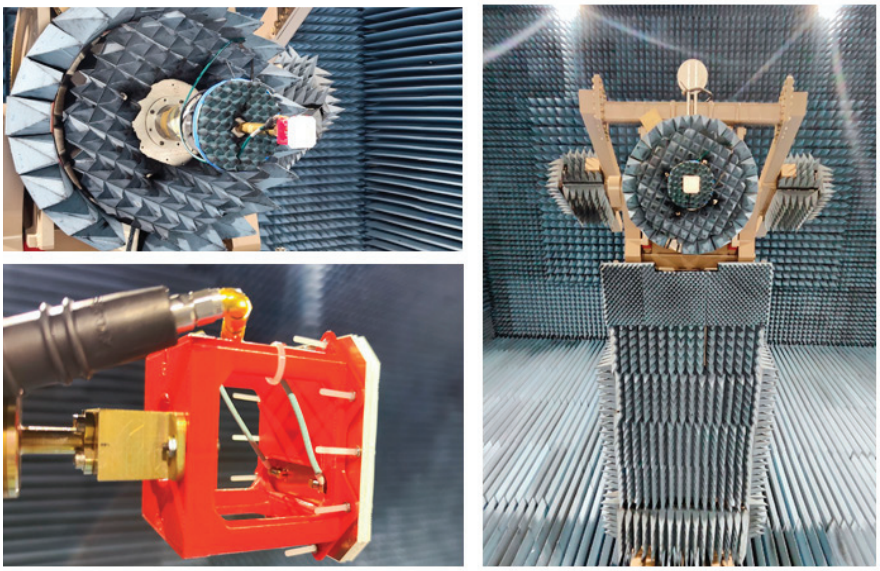

Figure 9. Measurement setup of the QM antenna in INTA's compact range chamber.

As demonstrated in Figure 10, the S-parameter simulation exhibited a high degree of correlation with the actual measurements, thereby validating the design. Furthermore, the excellent reproducibility observed in the manufacturing, assembly, and measurement processes resulted in two S Band Antenna models demonstrating identical functionality, both in terms of S-parameter measurement and radiation measurement. Consequently, these antennas are to be qualified for space mounting on dummies, with the understanding that QM and FM models will be subjected to divergent qualification and acceptance test levels.

The following measurements versus simulations of the axial ratio at the two frequencies of interest (uplink and downlink) are presented below, as well as the comparison of the gain in the copolar and cross-polar components for both left-hand and right-hand polarization. As the comparison between measurements and simulations of the QM antenna shows high coincidence, the designed model is validated.

As demonstrated in Figure 11, the comparison between measurements (solid line) and simulations (dashed line) of the co-polar and cross-polar gain for both principal cuts of each polarization and for the uplink and downlink frequencies is shown. It is evident that the gain difference between simulations and measurements is minimal.

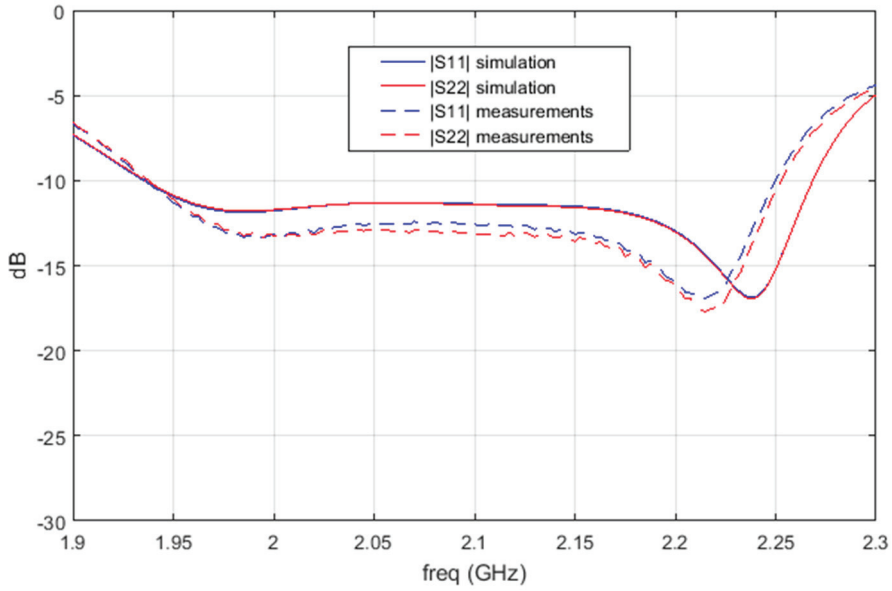

Figure 10. Measurements vs. simulations of S—parameters amplitude of QM S Band Antenna.

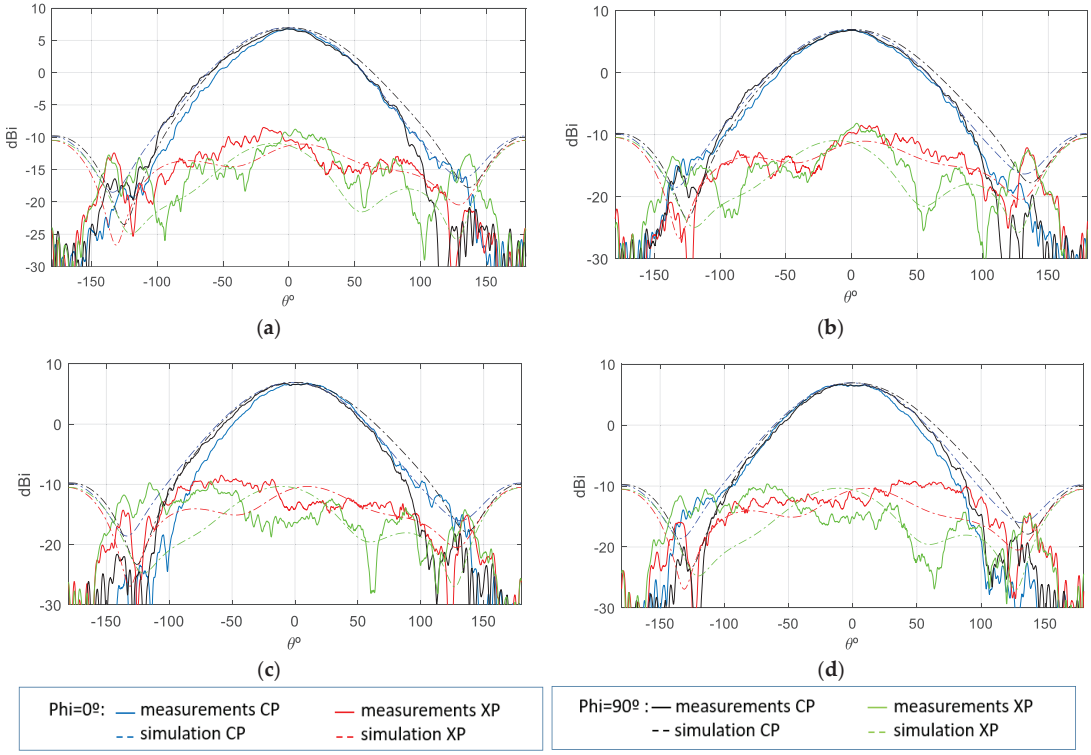

Figure 11. Gain measurement vs. simulation of isolated antenna; (**a**) f = 2.03 GHz—Port 1; (**b**) f = 2.03 GHz—Port 2; (**c**) f = 2.205 GHz—Port 1; (**d**) f = 2.205 GHz—Port 2.

The gain values demonstrate notable stability across theta, with peak gain ranging from [6.5–7] dBi. Additionally, the back radiation exhibits minimal interference, contributing to the prevention of disruption in the inter-satellite link. Concerning the axial ratio (AR), the objective is to preserve dual circular polarization over a substantial frequency bandwidth and over the widest possible angular range of theta from both ports. This ensures uninterrupted communication with the ground station even in the event of satellite rotation. As demonstrated in Figures 12 and 13, the AR remains below the requisite 4 dB level within the designated angular range [$\pm 50^{\circ}$], thereby ensuring uninterrupted ground communication. As with the gain outcomes, the dashed lines represent simulations,

while the solid lines represent measurements. The close agreement between these lines substantiates the efficacy of the designed antenna model.

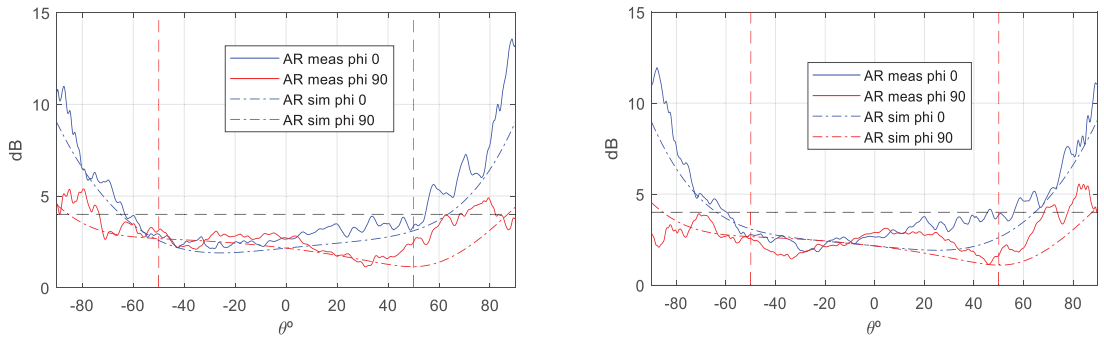

Figure 12. AR measurement vs. simulation isolated antenna, f = 2.03 GHz: (**a**) Port 1; (**b**) Port 2.

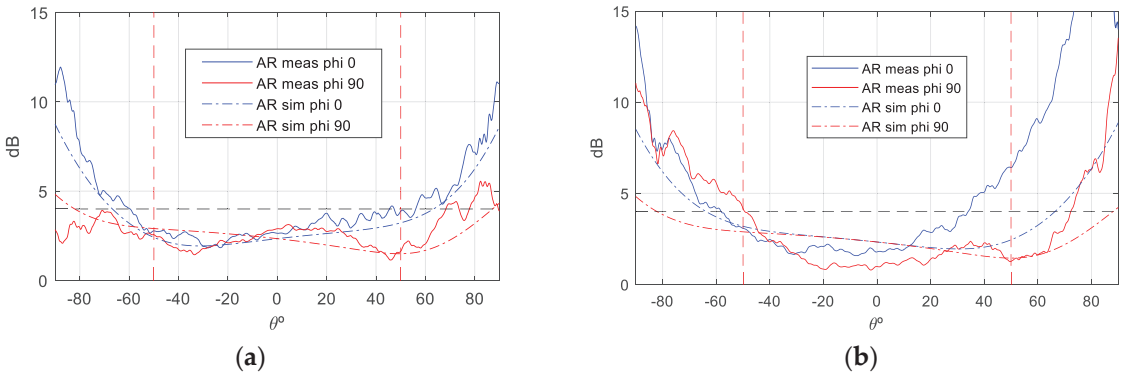

Figure 13. AR measurement vs. simulation of isolated antenna, f = 2.205 GHz: (**a**) Port 1; (**b**) Port2.

Figure 14 compares the AR bandwidth as a function of frequency (boresight direction) between simulated and measured results when the antenna is isolated, demonstrating that the antenna meets the AR bandwidth requirements of 8%. The dashed lines represent simulations, the solid lines represent measurements, and the green dotted lines represent the margins in which AR must meet the requirement of <4 dB.

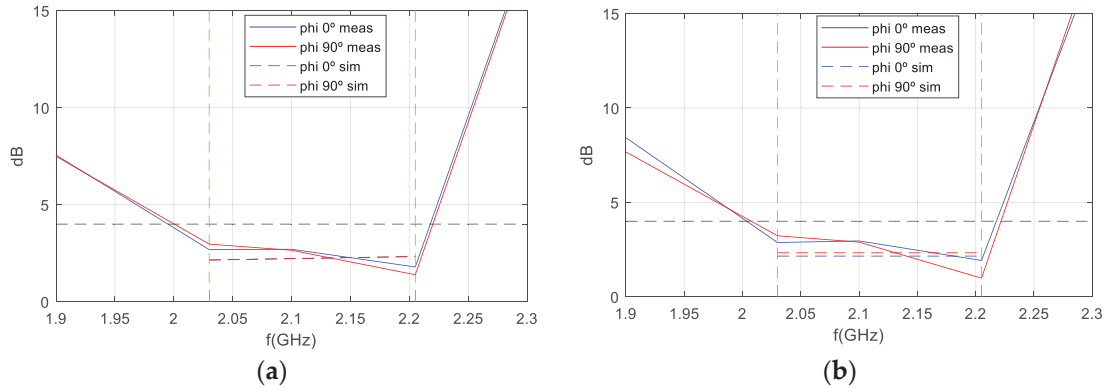

Figure 14. AR measurement vs. simulation of isolated antenna varying with frequency. (**a**) Port1; (**b**) Port 2.

Finally, as presented in Table 3, a comparison is made between the proposed design in this article and other designs mentioned in the references. While the text cites numerous references to antennas deployed on satellites, the comparison is specifically limited to those

operating within the same frequency band, utilizing circular polarization, and employing microstrip patch technology.

Table 3. Comparison of the parameters of the referenced antennas.

Ref	Frequency (GHz)	Polarization	AR Bandwidth (%)	Gain (dBi)	Size (mm)	Weight (gr)	Space Qualification	Feeding Type
[5]	S-Band (2.4)	CP	2	7.3	$96 \times 96 \times 7$	--	no	Multiple points
[9]	S-Band (2.4)	CP	4	2.3	$100 \times 100 \times 11$	120	yes	Dual feed
[10]	S-Band (2.43)	CP	3.5	4.89	$68.5 \times 59.4 \times 6$	75	no	Single feed
[21]	S-Band (2.43)	CP	6	8.07	$42 \times 55 \times 4.8$	145	no	Dual feed
[22]	S-Band (2.2)	CP	16	5.9	$78 \times 75 \times 10$	97	no	Dual feed
[35]	S-Band (2.4)	CP	2.45	4.8	$19 \times 20 \times 7.2$	--	no	Dual feed
Designed Antenna	S-Band (2.2)	CP	8	7.2	$80 \times 80 \times 6.5$	30	yes	Single feed

The analysis in Table 3 demonstrates that the designed antenna operates in circular polarization within the S-band, aligning with most references, yet it exhibits several advantages over alternative designs. Firstly, it is highly compact, with a total height of only 6 mm and a weight of 30 g. It provides a relatively high gain (7 dBi) for a single antenna, maintaining wide angular coverage. However, its key innovation lies in achieving impedance bandwidth and axial ratio (AR) bandwidth greater than 8% (better than the referenced antennas) despite being fed from a single point, which simplifies the structure and minimizes height. This is made possible through a stacked dual-patch configuration with integrated notches, a feature not achieved in the referenced works.

In addition to that, the antenna has been space-qualified, demonstrating no degradation in its electromagnetic performance after rigorous environmental tests. It was successfully integrated and launched into space aboard the Falcon 9 launcher by SpaceX on January 14 as part of the Leader-S CubeSat mission within the ANSER constellation.

6. Results of Antenna Deployed on Satellite

Following the validation of the QM antenna model through radiofrequency measurements, it is placed on a mockup (RF dummy) that replicates the actual Leader-S platform, including solar panels, a UHF antenna, and a magnetometer (see Figure 15a). In this new setup, the antenna is measured again in the anechoic chamber at INTA facilities, with the results of these measurements then being compared with those of the isolated antenna in order to assess how polarization and gain are affected by its deployment.

The S-parameters of the antenna exhibit slight variations when mounted on the RF dummy, particularly on one of the ports, primarily due to the proximity of the S-band antenna to the UHF antenna (four monopoles). However, this variation is minimal and does not compromise the requirements, as it remains below -15 dB within the band.

The gain pattern of the mounted antenna (see Figure 16) exhibits a slight narrowing compared to the isolated case while maintaining the peak gain value without incurring additional losses. With regard to the cross-polarization pattern, a slight deterioration is observed in the angular region closest to the UHF antenna. However, this does not have a significant impact on the final requirements, as the system employs dual-polarization operation to select the optimal received pattern from both polarizations.

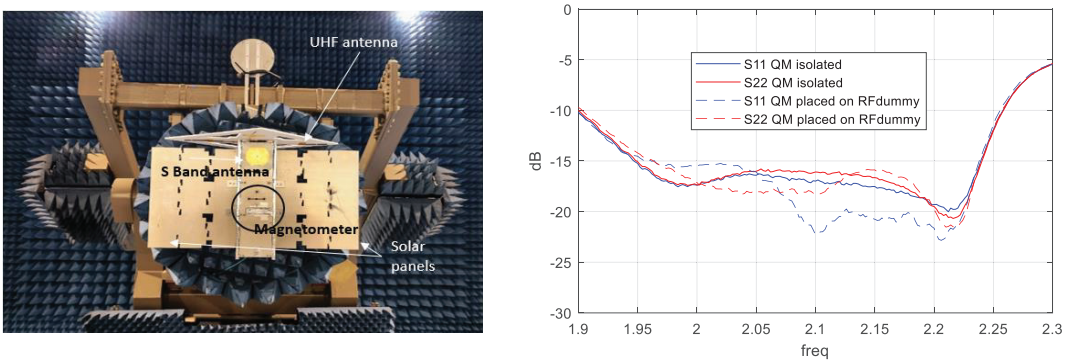

Figure 15. (**a**) QM S Band antenna on RF dummy (measurements set—up); (**b**) |S11| and |S22| measurements of isolated QM antenna vs. placed on RF dummy.

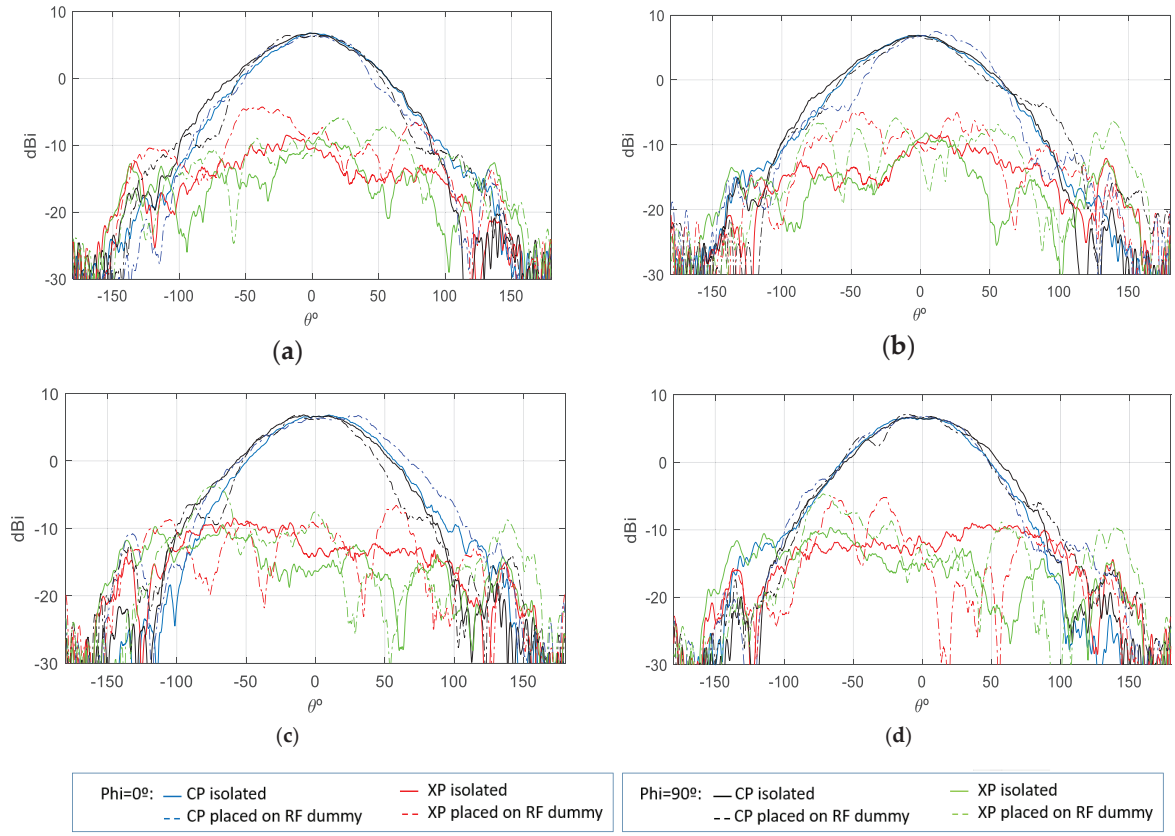

Figure 16. Gain measurement of S—band antenna isolated vs. placed on RF dummy; (**a**) f = 2.03 GHz—Port 1; (**b**) f = 2.03 GHz—Port 2; (**c**) f = 2.205 GHz—Port 1; (**d**) f = 2.205 GHz—Port 2.

The mounted antenna on the RF dummy exhibits gain values with no losses in comparison to the isolated antenna. Indeed, at lower frequencies, the maximum gain through port P1 is 7 dBi, while through port P2, it reaches 7.6 dBi. At higher frequencies, the gain through port P1 is 7.1 dBi, and through port P2, it is 7.2 dBi. This variation in the maximum gain values of the S-band antenna is attributable to its position relative to the UHF antenna, which comprises four monopoles positioned asymmetrically with respect to P1 and P2. Consequently, the gain is influenced in a slightly different manner on each port by that UHF antenna. Given that the antenna is based on a multi-layer stacked patch structure, the gain achieved once the antenna is mounted on the satellite and measured is excellent. Furthermore, the gain remains highly stable, with a rate of decline of only 0.14 dB per degree.

Although the axial ratio (Figures 17 and 18) is the parameter most affected when the antenna is mounted on the satellite, it shows minimal distortion within the area of interest (boresight) at all frequencies measured, especially on port 2. However, the axial ratio at Port 1 and f = 2.03 GHz is more affected due to its proximity to the monopoles of the UHF antenna, which reduces the angular range to −20/+40 degrees. Despite this effect, the antenna maintains its circular polarization characteristics within the relevant band (8.8%), especially in the boresight region, making it particularly suitable for this type of application (Figure 14).

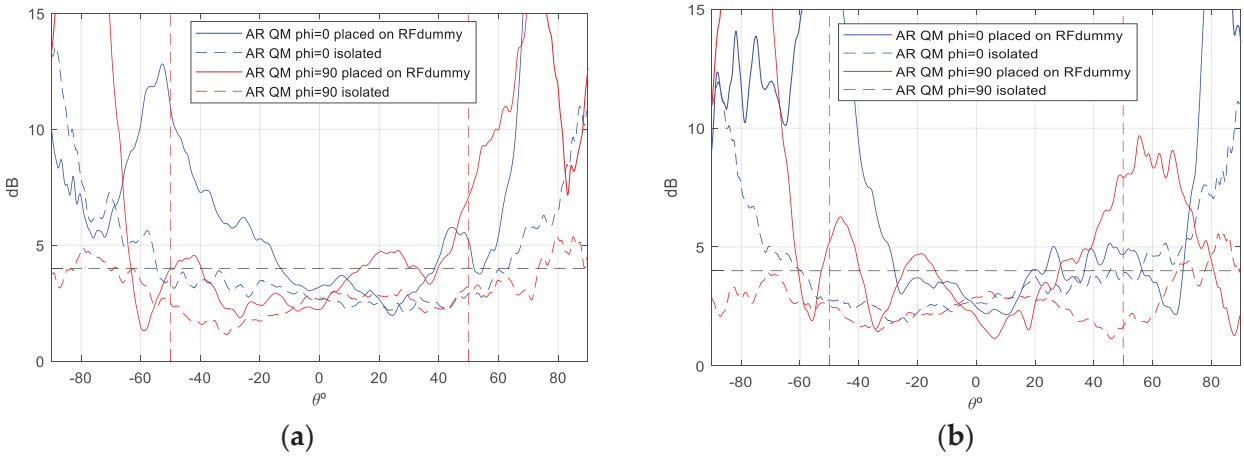

Figure 17. AR measurement of S—band antenna isolated vs. placed on RF dummy, f = 2.03 GHz: (**a**) Port 1; (**b**) Port 2.

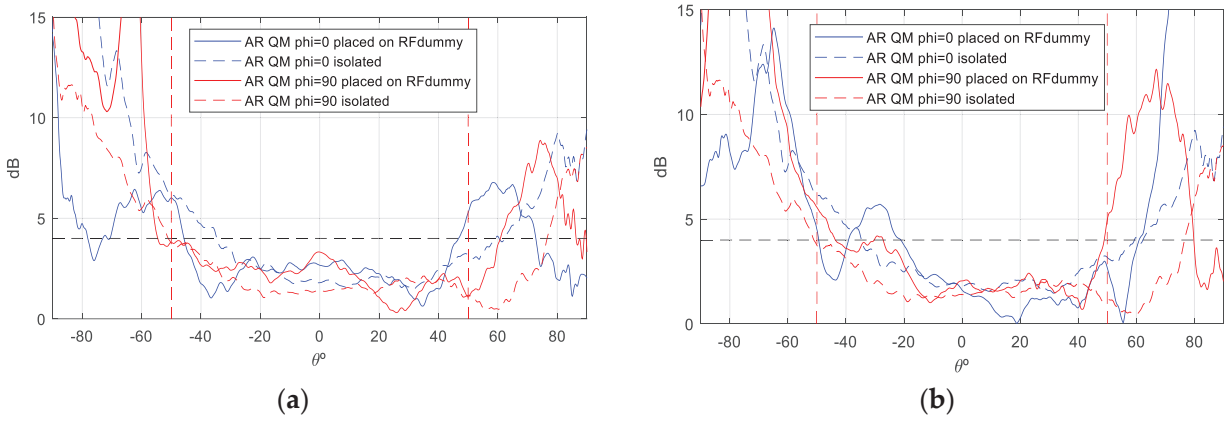

Figure 18. AR measurement of S—band antenna isolated vs. placed on RF dummy, f = 2.205 GHz: (**a**) Port 1; (**b**) Port 2.

7. Antenna Qualification and Acceptance Test

Following the successful validation of the antenna, both in isolation and in deployment on the satellite, space qualification and acceptance tests are conducted. The qualification (QM unit) and acceptance (FM unit) levels will be those specified by ISI-LAUNCH, as Leader-S is scheduled for launch on a SpaceX Falcon 9 rocket [36]. Qualification tests are performed on the QM S-Band antenna. This model has been submitted to a comprehensive qualification test campaign, encompassing various stages (Figure 19), with specific qualification durations and levels designated for the environmental tests.

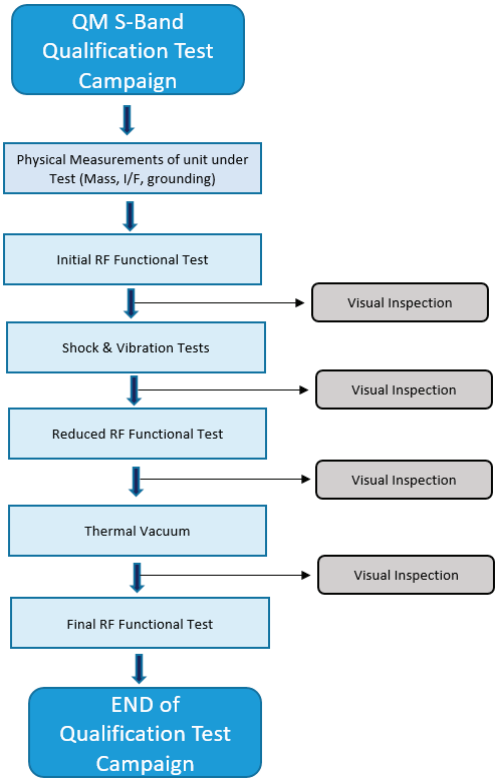

Figure 19. QM S-band qualification test flow.

7.1. Physical Measurements of Unit Under Qualification

In this step, the thicknesses of the plates forming the antenna stack-up are verified, as are the size and dimensions of the integrated antenna, the grounding, the conductivity of the connectors, and the interfaces with the satellite Leader-S. These verifications are conducted prior to the commencement of the functional tests. The antenna has a total height of 7 mm and a weight of 30 g.

7.2. Initial and Final RF Functional Test

Prior to the initiation of vibration, thermal vacuum, and shock tests (Initial RF Functional Test), and upon completion of these environmental tests (Final RF Functional Test), full RF tests are conducted. The Initial RF Functional measurements (see Figures 15–18) act as a reference point for comparison with measurements taken after the completion of these tests, thereby ensuring the continued functionality of the AUT. The RF functional measurements (initial and final) are conducted by means of the QM S-Band antenna positioned on an RF dummy (see Figure 15a). The primary distinction between the isolated QM measurements depicted in Figure 9 and the QM integrated within the RF-dummy configuration illustrated in Figure 15a pertains to the presence of a UHF antenna affixed to the test antenna, based on metal rods, which directly interferes with the radiated field lines of the QM antenna. Additionally, a magnetometer, a metallic component that the QM antenna also perceives, is employed. The combined effect of these elements on the radioelectric characteristics of the QM antenna is a consequence of these interferences, and; therefore, it is important to characterize this effect (Section 4).

7.3. Visual Inspection

Subsequent to the execution of each environmental test, a visual inspection is conducted to ensure that there are no noticeable changes. The validity criteria for this visual inspection are as follows: The absence of color change in the dielectric, which could in-

dicate material degradation, is to be noted. Furthermore, the lateral adhesive SCOTCH WELD 2216 A + B, Batch EGE 208 [30], must not be detached. Additionally, the two SMP connectors must not be displaced or broken, and no visible marks or cracks must be present on the copper plates or the dielectric.

7.4. Vibration Test

The detailed test flow for the vibration test is shown in Figure 20. The QM S-Band antenna is installed on a mass dummy for the purpose of conducting shock, thermal vacuum, and vibration tests (see Figure 21a). Subsequent to the installation of the antenna on the mass dummy, new measurements of S-parameters are taken prior to and following each mechanical or environmental test. This procedure is undertaken in order to ensure the functionality of the antenna. Vibration tests are conducted within the Environmental Test Laboratory at INTA, utilizing pneumatic pyroshock systems (Shaker LDS 824LSC, serial number 527) and Shaker LDS V9-MKII 440, N/S 9033-001), both situated in a cleanroom class ISO 8. The INTA's Testing laboratories have a quality system that meets the requirements of UNE-EN ISO/IEC 17025:2005 [37] for testing laboratories. In this scenario, the mass dummy of the satellite (with QM antenna) is mounted inside the ISIS TEST POD following the procedure issued by the supplier. The TEST POD is then fixed to the vibration I/F plate (Figure 21b). This plate is mechanically characterized (low-level sine/random) in each axis test. The vibration test was performed in the three axes: X, Y, and Z.

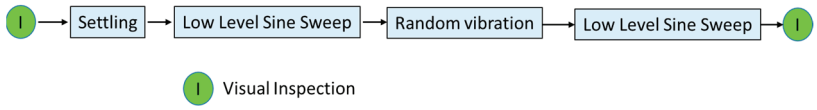

Figure 20. Vibration test flow for each axis.

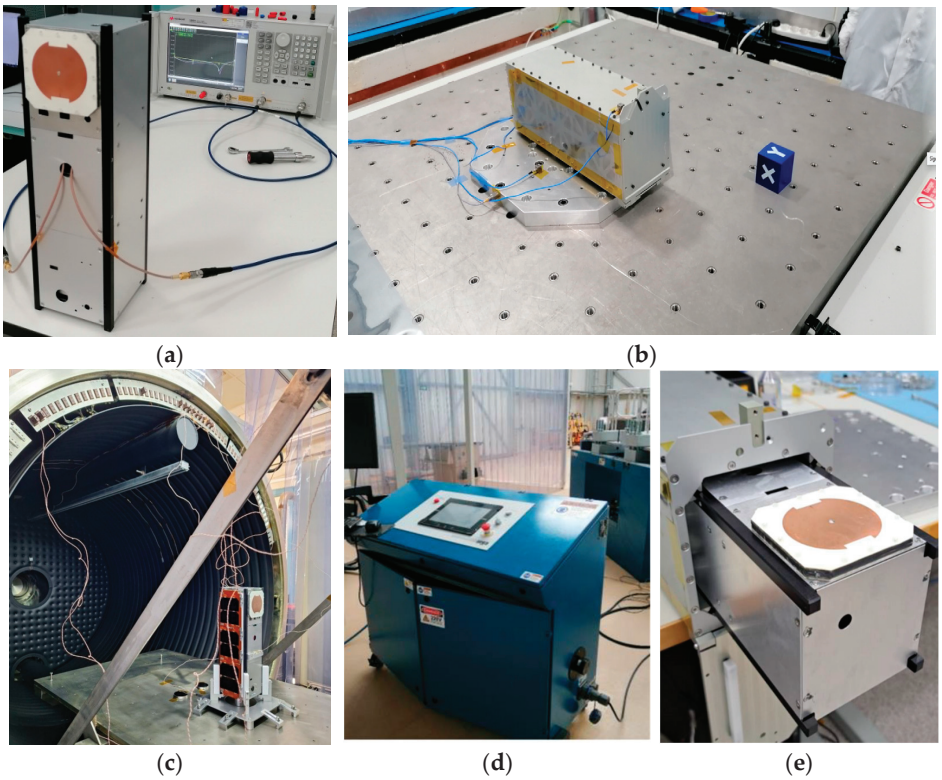

Figure 21. Environmental tests set—up: (**a**) antenna placed on mass dummy; (**b**) vibration I/F plate; (**c**) Thermal Chamber TVC-2 (INTA); (**d**) pneumatic pyroshock system (NTA); (**e**) mass dummy inside test pod.

7.5. Thermovacuum Test (TVAC)

The primary objective of the TVAC is to elevate the temperature of the QM S Band antenna beyond the levels attained in the thermal analysis, thereby demonstrating the subsystem's capacity to function effectively in pertinent thermal-vacuum circumstances and to withstand thermal cycles in such conditions without compromising its operational capabilities. For the purposes of this test, the antenna is to be mounted on the mass dummy and undergo eight cycles in two operating modes (hot and cold) so that the unit reaches temperature levels according to the specification limits (Table 4).

Table 4. Temperatures range in TVAC cycles.

FreqHz	Maximum Predicted Environment Induced by Launch Vehicle and Co-Payload (s) SRS (g)
100	30
1000	1000
10,000	1000

TVAC tests are carried out in the Test Laboratory at INTA (TVC-2 thermal chamber COSMOS 02), and the equipment for testing is located in a cleanroom class ISO 8 (see Figure 21c).

7.6. Shock Test

The objective of the final mechanical test is to ascertain the capacity of the Leader-S QM S Band antenna to withstand mechanical shock requirements and thereby bring the mechanical tests performed on the QM unit to a conclusion. Once again, the QM unit antenna remains mounted on the mass dummy and is now mounted inside the ISIS TESTPOD in the same manner as in the vibration tests (see Figure 21e). The g-acceleration values to which the antenna is subjected are described in Table 5, and a safety factor of +6 dB is applied to this profile for qualification tests (as required by the launcher, SpaceX's Falcon 9). Finally, three actions on each axis are performed, and the equipment for testing is located in a cleanroom class ISO 8.

Table 5. Profile of g-acceleration values in shock tests.

Environment	Shroud Temperature
Hot (Tmax)	+85 °C [0, +8 °C]
Cold (Tmin)	−40 °C [−8 °C, 0]

S-parameter measurements are taken after each of the environmental tests to ensure there is no distortion of the S-parameters and, therefore, to guarantee that the antenna maintains its electrical functionality.

7.7. Verification of Results After Qualification Tests

Once the environmental and mechanical qualification tests for the space antenna are completed, and the measurements taken between each test have validated the antenna's functionality final RF measurements are conducted (Figures 22–26). For these measurements, the antenna is removed from the mass dummy and reinstalled on the RF dummy, where not only the S-parameters but also the gain and radiation pattern are measured (final RF functional test).

During the qualification tests, the antenna was found to exceed its designated parameters. Specifically, during the TVAC tests, the antenna was subjected to temperatures that

exceeded the required ranges (Table 4) for eight complete cycles without any discernible modification to its physical characteristics or S-parameters. To verify this, a combination of visual inspections and S-parameter measurements was employed. These measurements were conducted before, during, and after each cycle while the antenna was inside the chamber. A subsequent filtration process was deemed necessary in order to remove any reflections that had been introduced by the chamber into the aforementioned graphs. Furthermore, the antenna underwent both vibration and shock tests in accordance with the envelope values defined by the Falcon 9 launcher from SpaceX, with the results of these tests even exceeding the standard qualification requirements. It was only subsequent to the shock tests that a slight variation in the S-parameter response was observed when compared with the reference measurements (Figure 22a). No significant changes were observed in the gain and AR measurements (see Figures 23–26).

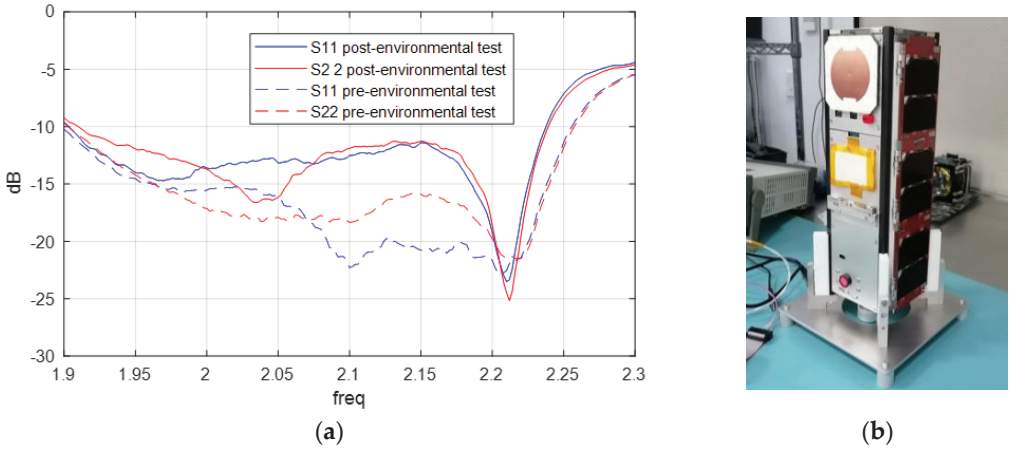

Figure 22. Final RF test: (**a**) S—parameters; (**b**) FM S−band antenna placed on FM Leader−S.

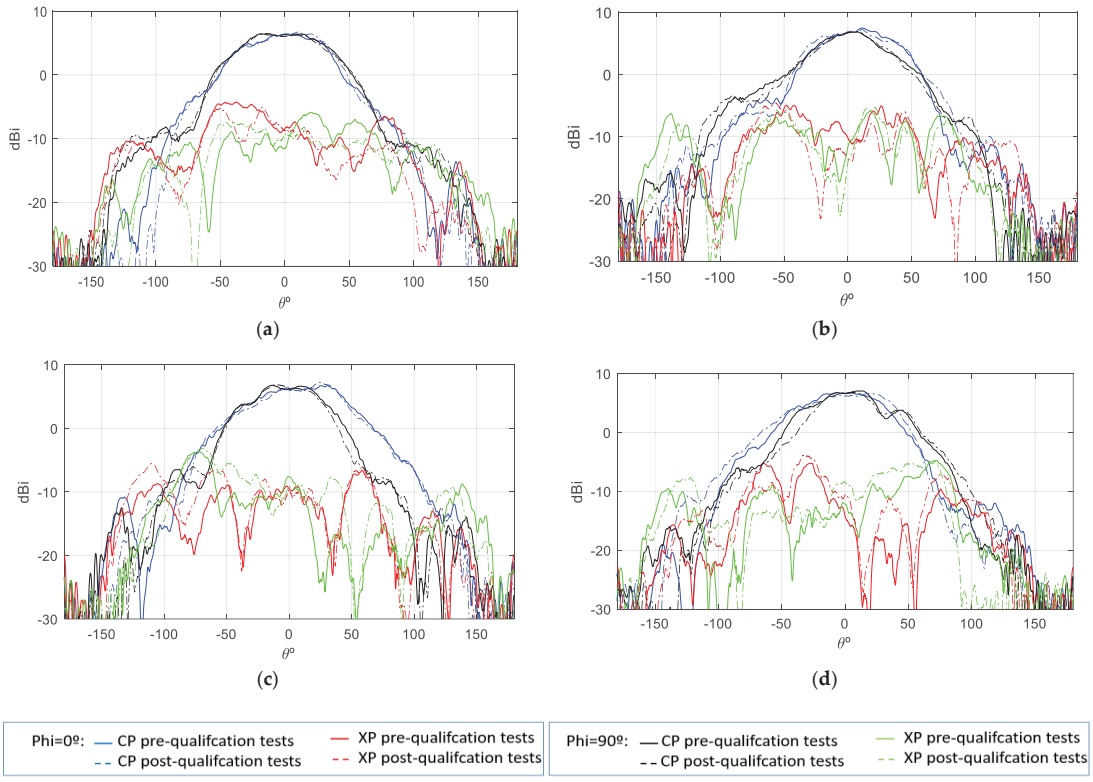

Figure 23. Gain measurement of S-band isolated antenna before and after qualification tests campaign; (**a**) f = 2.03 GHz—Port 1; (**b**) f = 2.03 GHz−Port 2; (**c**) f = 2.205 GHz−Port 1; (**d**) f = 2.205 GHz−Port 2.

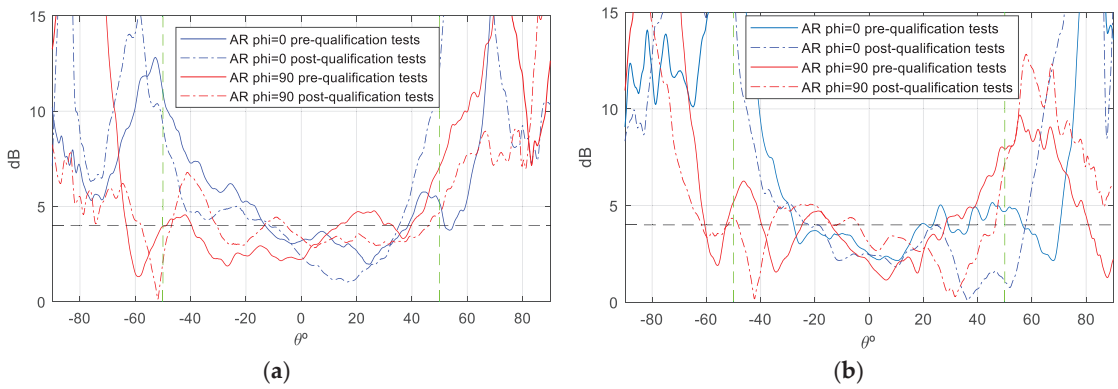

Figure 24. AR measurement S—band antenna before and after qualification tests campaign. f = 2.03 GHz (the green dotted lines represent the margins in which AR must meet the requirement of <4 dB): (**a**) Port 1; (**b**) Port 2.

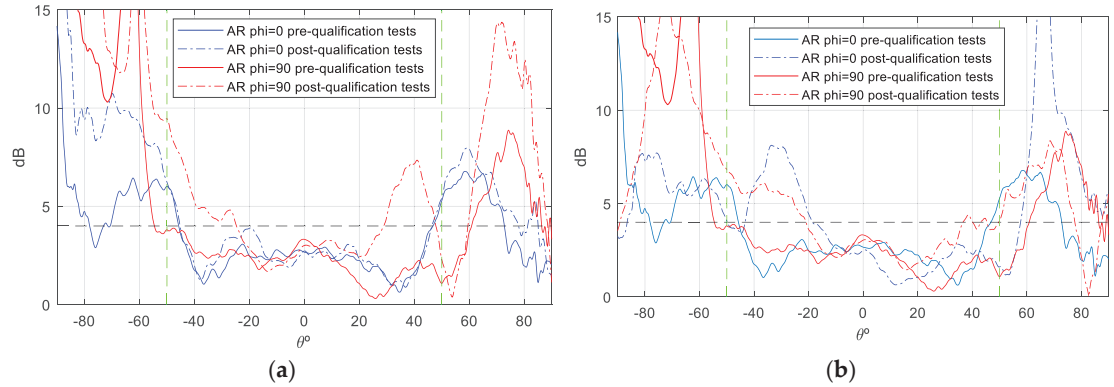

Figure 25. AR measurement S—band antenna before and after qualification tests campaign, f = 2.205 GHz (the green dotted lines represent the margins in which AR must meet the requirement of <4 dB): (**a**) Port 1; (**b**) Port 2.

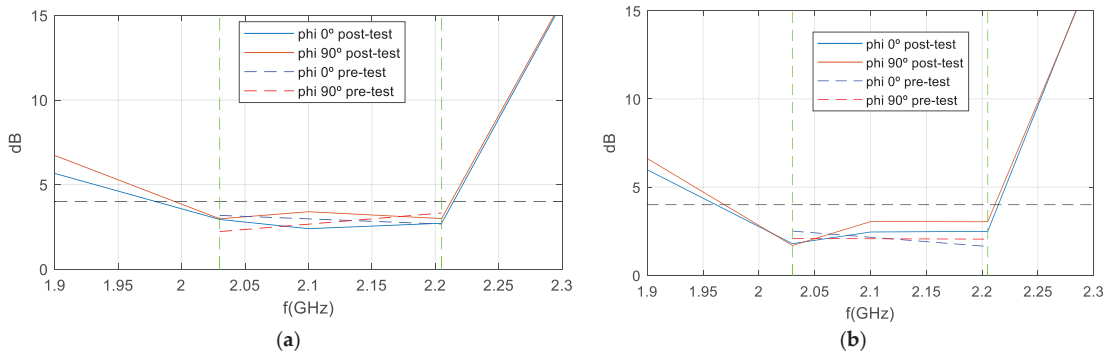

Figure 26. AR measurement vs. frequency of S-band antenna before and after qualification tests: (**a**) Port 1; (**b**) Port 2.

As a demonstration that the antenna maintains a bandwidth greater than 8% in both impedance matching and axial ratio (AR), Figure 26 is presented. The green dotted lines represent the margins in which AR must meet the requirement of <4 dB. This figure shows the AR as a function of frequency (in boresight) for the antenna mounted on the RF dummy, with measurements taken in an anechoic chamber before and after the qualification process. Although the pre-test measurements were taken only at the up-link and down-link frequencies, a comparison is represented, and the figure clearly shows how the pre- and post-test curves are very close to each other. Therefore, it is demonstrated that the

AR bandwidth, as well as the impedance matching bandwidth of the antenna, is 8%, as required by the ANSER program specification, even after being qualified for space.

It is, therefore, concluded that the antenna is qualified for space, with its physical and functional characteristics remaining intact. This is evidenced by the maintenance of its gain pattern characteristics and axial ratio after undergoing all qualification tests (see Figures 22–26). Following the completion of antenna qualification tests, the flight model of the antenna (FM) is integrated into the Leader-S satellite (see Figure 22b), which has passed all acceptance tests. The Leader-S satellite is scheduled for integration and launch aboard a SpaceX Falcon rocket [36] in January 2025.

8. Conclusions

This paper presents the design, implementation, measurement, integration, and space qualification of an S-band antenna as part of the ground communication system of one of the three nanosatellites forming the ANSER constellation (INTA). The antenna is ultra-lightweight (30 g) and compact (6.7 mm in height), featuring dual circular polarization while achieving wideband AR, setting it apart from the existing literature. The antenna functions by being fed from a single point for both polarizations, thus eliminating the necessity for 0–90° phase-shifting networks. It achieves an 8% bandwidth in the S-band, encompassing both uplink and downlink frequencies. The technological challenges posed by the antenna's size, its wideband axial ratio, and the maintenance of stable radiation characteristics with minimal back radiation have been successfully overcome. The antenna has been qualified and integrated into Leader-S, which was launched aboard SpaceX's Falcon rocket in January 2025.

Author Contributions: Conceptualization, S.S.-S. and D.P.; methodology, S.S.-S. and D.P.; software, S.S.-S. and V.M.A.; validation, S.S.-S. and V.M.A., D.P. and A.S., formal analysis, S.S.-S. and D.P.; investigation, S.S.-S.; resources, D.P.; data curation, S.S.-S.; writing—original draft preparation, S.S.-S.; writing—review and editing, J.L.M.-C., D.P. and J.A.R.; visualization, S.S.-S., J.L.M.-C. and D.P.; supervision, J.L.M.-C. and D.P.; project administration, D.P.; funding acquisition, J.L.M.-C. All authors have read and agreed to the published version of the manuscript.

Funding: This work was supported by the Spanish Government under grant TED2021-130650B-C21 (ANT4CLIM) funded by MCIN/AEI/10.13039/501100011033 (Agencia Estatal de Investigación) and by UE (European Union) "NextGenerationEU"/PRTR.

Institutional Review Board Statement: Not applicable.

Informed Consent Statement: Not applicable.

Data Availability Statement: Data are contained within the article.

Acknowledgments: Since this article describes the entire process, from the design and optimization of the antenna to its measurement, functional validation, and final space qualification, we would like to express our gratitude to the radiofrequency team for the measurements carried out in the INTA anechoic chambers (Helena Palacios, José R. Rodríguez and José A. Luque), as well as to the environmental testing team. I would also like to thank the integration team, including José M. Encinas and Victor M. Ortuño, and the quality assurance team led by Mª del Rosario Chandal, whose contributions were invaluable. Finally, we would like to thank the ANSER (Santiago Rodriguez) for giving us the opportunity to be part of his team and the Radiation Group (UPM) for financing the cost of the APC.

Conflicts of Interest: The authors declare no conflicts of interest.

References

1. Swartwout, M. The first one hundred CubeSats: A statistical look. *J. Small Satell.* **2014**, *2*, 213–233.
2. Toorian, A.; Lee, K.D.S. The CubeSat approach to space access. In Proceedings of the 2008 IEEE Aerospace Conference, Sky, MT, USA, 1–8 March 2008; pp. 1–14.
3. Heidt, H.; Puig-Suari, J.; Moore, A.; Nakasuka, S.; Twiggs, R. CubeSat: A new generation of picosatellite for education and industry low-cost space experimentation. In Proceedings of the 14th Annual AIAA/USU Conference on Small Satellites, Logan, UT, USA, 21–24 August 2000.
4. Nugent, R.; Munakata, R.; Chin, A.; Puig-Suari, R.C.J. The CubeSat: The picosatellite standard for research and education. *Aerosp. Eng.* **2008**, *805*, 756–5087.
5. ANascetti EPittella, P. Teofilatto and S. Pisa. High-Gain S-band Patch Antenna System for Earth-Observation CubeSat Satellites. *IEEE Antennas Wirel. Propag. Lett.* **2015**, *14*, 434–437.
6. Information on the ANSER Programme on the ESA Website. Available online: https://www.esa.int/Enabling_Support/Space_Engineering_Technology/Vega_s_fuel-free_CubeSats_to_keep_formation_with_wings (accessed on 9 February 2025).
7. Information on the ANSER Programme on the INTA Website. Available online: https://www.inta.es/INTA/es/blogs/ceit/?valor=/INTA/es/blogs/ceit/crear-comentario/&valor2=/.content/bs-blog/ceit/comentarios/&valor3=/INTA/es/blogs/ceit/BlogEntry_1727699955681 (accessed on 9 February 2025).
8. Gao, S.; Clark, K.; Unwin, M.; Zackrisson, J.; Shiroma, W.A.; Akagi, J.M.; Maynard, K.; Garner, P.; Boccia, L.; Amendola, G.; et al. Antennas for Modern Small Satellites. *IEEE Antennas Propag. Mag.* **2009**, *51*, 40–56. [CrossRef]
9. Abulgasem, S.; Tubbal, F.; Raad, R.; Theoharis, P.I.; Lu, S.; Iranmanesh, S. Antenna designs for cubesats: A review. *IEEE Access* **2021**, *9*, 45289–45324. [CrossRef]
10. Yao, Y.; Liao, S.; Wang, J.; Xue, K.; Balfour, E.A.; Luo, Y. A New Patch Antenna Designed for CubeSat: Dual feed, LVS dual-band stacked, and circularly polarized. *IEEE Antennas Propag. Mag.* **2016**, *58*, 16–21. [CrossRef]
11. Rather, N.N.; Suganthi, S. Electrically small S-band antenna for CubeSat applications. In Proceedings of the 2017 International Conference on Wireless Communications, Signal Processing and Networking (WiSPNET), Chennai, India, 22–24 March 2017; pp. 1687–1691.
12. Liu, S.; Theoharis, P.I.; Raad, R.; Tubbal, F.; Theoharis, A.; Iranmanesh, S.; Abulgasem, S.; Khan, M.U.A.; Matekovits, L. A Survey on CubeSat Missions and Their Antenna Designs. *Electronics* **2022**, *11*, 2021. [CrossRef]
13. Hammoumi, M.E.; Idrissi, N.E.A.E.; Raad, R.; Theoharis, P.I.; Tubbal, F. A Wideband Compact Patch Antenna for Ka-band and CubeSat Applications. In Proceedings of the 2021 15th International Conference on Signal Processing and Communication Systems (ICSPCS), Sydney, Australia, 13–15 December 2021; pp. 1–5.
14. James, J.R.; Hall, P.S. *Handbook of Microstrip Antenna*; Peter Peregrinus Ltd.: London, UK, 1989; Volume 1.
15. Balanis, C.A. *Antenna Theory: Analysis and Design*; Wiley-Interscience: Hoboken, NJ, USA, 2005.
16. Bandyopadhyay, S.; Foust, R.; Subramanian, G.P.; Chung, S.-J.; Hadaegh, F.Y. Review of Formation Flying and Constellation Missions Using Nanosatellites. *J. Spacecr. Rocket.* **2016**, *53*, 567–578. [CrossRef]
17. Abulgasem, S.; Tubbal, F.; Raad, R.; Theoharis, P.I.; Liu, S.; Khan, M.U.A. A Wideband Metal-Only Patch Antenna for CubeSat. *Electronics* **2021**, *10*, 50. [CrossRef]
18. Fong, L.K.; Chair, R. On the use of Shorting Pins in the Design of Microstrip Patch Antennas. *HKIE Trans.* **2004**, *11*, 31–38. [CrossRef]
19. Kumar, G.; Gupta, K. Broad-band microstrip antennas using additional resonators gap-coupled to the radiating edges. *IEEE Trans. Antennas Propag.* **1984**, *32*, 1375–1379. [CrossRef]
20. Cao, Y.; Cai, Y.; Cao, W.; Xi, B.; Qian, Z.; Wu, T.; Zhu, L. Broadband and High-Gain Microstrip Patch Antenna Loaded with Parasitic Mushroom-Type Structure. *IEEE Antennas Wirel. Propag. Lett.* **2019**, *18*, 1405–1409. [CrossRef]
21. Sarin, V.P.; Nishamol, M.S.; Tony, D.; Aanandan, C.K.; Vasudevan, P.M.K. A Wideband Stacked Offset Microstrip Antenna with Improved Gain and Low Cross Polarization. *IEEE Trans. Antennas Propag.* **2011**, *59*, 1376–1379. [CrossRef]
22. Veljovic, M.J.; Skrivervik, A.K. Aperture-Coupled LowProfile Wideband Patch Antennas for CubeSat. *IEEE Trans. Antennas Propag.* **2019**, *67*, 3439–3444. [CrossRef]
23. Byrne, B.; Capet, N.; Romier, M. Compact S-band and X-band antennas for CubeSats. *CEAS Space J.* **2020**, *12*, 587–596. [CrossRef]
24. Bountzioukas, P.; Kikas, G.; Tsiolakis, C.; Stoupis, D.; Chatziargyriou, E.; Hatzopoulos, A.; Mavropoulos, A.; Komis, I.-N.; Kita, A.; Palma, D.; et al. The Evolution from Design to Verification of the Antenna System and Mechanisms in the AcubeSAT mission. In Proceedings of the 74th International Astronautical Congress, Baku, Azerbaijan, 2–6 October 2023.
25. Iqbal, J.; Illahi, U.; Khan, M.A.; Rauf, A.; Ali, E.M.; Bari, I.; Ali, H.; Khan, M.A.; Alibakhshikenari, M.; Dalarsson, M. A Novel Single-Fed Dual-Band Dual-Circularly Polarized Dielectric Resonator Antenna for 5G Sub-6GHz Applications. *Appl. Sci.* **2022**, *12*, 5222. [CrossRef]
26. Tang, Z.; Liu, J.; Cai, Y.-M.; Wang, J.; Yin, Y. A wideband differentially fed dual-polarized stacked patch antenna with tuned slot excitations. *IEEE Trans. Antennas Propag.* **2018**, *66*, 2055–2060. [CrossRef]

27. AbuTarboush, H.F.; Al-Raweshidy, H.S.; Nilavalan, R. Bandwidth enhancement for microstrip patch antenna using stacked patch and slot. In Proceedings of the 2009 IEEE International Workshop on Antenna Technology, Santa Monica, CA, USA, 2–4 March 2009; pp. 1–4.
28. HF Rohacell: Evonik Operations GmbH. Smart Materials. High Performance Polymers. Performance Foams. HF Rohacell: Evonik Operations GmbH: Darmstadt, Germany.
29. Rogers 4360: 100 S. Roosevelt Avenue, Chandler, AZ, USA. Available online: www.rogerscorp.com (accessed on 12 January 2025).
30. SCOTCH WELD 2216 A + B, Batch EGE 208: Industrial Adhesives and Tapes Division. 3M Center, Building 225-3S-06 St. *Paul, MN, USA.* Available online: www.3M.com/industrial (accessed on 12 January 2025).
31. Tubbal, F.; Raad, R.; Chin, K.-W.; Matekovits, L.; Butters, B. A high gain s-band CPW-fed slot antenna for cubesat. *Ann. Telecommun.* **2019**, *74*, 223–237. [CrossRef]
32. Zhang, Y.; Hong, W.; Yu, C.; Kuai, Z.Q.; Don, Y.D.; Zhou, J.Y. Planar ultrawideband antennas with multiple notched bands based on etched slots on the patch and/or split ring resonators on the feed line. *IEEE Trans. Antennas Propag.* **2008**, *56*, 3063–3068. [CrossRef]
33. Chang, D.-C.; Lien, H.-C. Enhancing AR bandwidth of circularly polarization microstrip antenna. In Proceedings of the IWAT 2005. IEEE International Workshop on Antenna Technology: Small Antennas and Novel Metamaterials, Singapore, 7–9 March 2005; pp. 270–273.
34. Varshney, G.; Pandey, V.S.; Yaduvanshi, R.S. Axial ratio bandwidth enhancement of a circularly polarized rectangular dielectric resonator antenna. *Int. J. Microw. Wirel. Technol.* **2018**, *10*, 984–990. [CrossRef]
35. Podilchak, S.K.; Comite, D.; Montgomery, B.K.; Li, Y.; Buendía, V.G.-G.; Antar, Y.M.M. Solar-panel integrated circularly polarized meshed patch for cubesats and other small satellites. *IEEE Access* **2019**, *7*, 9656096566. [CrossRef]
36. Falcon 9 Launcher. Available online: https://www.spacex.com/vehicles/falcon-9/ (accessed on 9 February 2025).
37. General Requirements for the Competence of Testing and Calibration Laboratories. Available online: https://www.iasonline.org/wp-content/uploads/2021/02/ISO-IEC-17025-2017-IAS.pdf (accessed on 1 December 2024).

sensors

MDPI

Article

Miniaturized Antenna Design for Wireless and Powerless Surface Acoustic Wave Temperature Sensors

Naranut Sreang and Jae-Young Chung *

Department of Electrical and Information Engineering, Seoul National University of Science and Technology, Nowon-gu, Seoul 01811, Republic of Korea; naranut.sreang@gmail.com
* Correspondence: jychung@seoultech.ac.kr

Abstract: This paper presents the introduction, design, and experimental validation of two small helical antennae. These antennae are a component of the surface acoustic wave (SAW) sensor interrogation system, which has been miniaturized to operate at 915 MHz and aims to improve the performance of wireless passive SAW temperature-sensing applications. The proposed antenna designs are the normal-mode cylindrical helical antenna (CHA) and the hemispherical helical antenna (HSHA); both designed structures are developed for the ISM band, which ranges from 902 MHz to 928 MHz. The antennae exhibit resonance at 915 MHz with an operational bandwidth of 30 MHz for the CHA and 22 MHz for the HSHA. A notch occurs in the operating band, caused by the characteristics of the SAW sensor. The presence of this notch is crucial for the temperature measurement by aiding in calculating the frequency shifting of that notch. The decrement in the resonance frequency of the SAW sensor is about 66.67 kHz for every 10 °C, which is obtained by conducting the temperature measurement of the system model across temperature environments ranging from 30 °C to 90 °C to validate the variation in system performance.

Keywords: hemispherical helical antenna (HSHA); temperature sensor; surface acoustic wave (SAW); miniaturized antenna

1. Introduction

Wireless temperature monitoring has emerged as a pivotal technology that has significantly enhanced operational efficiencies across multiple sectors through its capability for real-time remote observations. This technology has been widely used in several fields to assure adherence to essential requirements for the safety and effectiveness of products and services [1–3]. Healthcare is one of the primary sectors where wireless temperature monitoring is crucial. Monitoring the conditions within vaccine and drug storage facilities is crucial for preserving the integrity of pharmaceuticals. A specialized wireless health-monitoring system was developed to accurately measure internal body temperature [4,5]. The technology has a significant influence in the field of agriculture, specifically in monitoring greenhouse temperatures to enhance the optimal circumstances for plant growth, and a wireless temperature monitoring system using an infrared sensor was explored to ensure the consistent and accurate monitoring of plant canopy temperatures in agricultural environments [6]. Within the food sector, food quality and safety are ensured throughout the processing and storage stages. To facilitate this, a wireless energy-efficient temperature probe was built to monitor food processes. The system was designed to accurately monitor processes in low-temperature environments, specifically in pharmaceutical and food processing plants [7]. Furthermore, these systems play a vital role in building and home environments, energy sector, data centers, and aerospace engines [8–10].

A temperature sensor is an important part of a temperature-monitoring system. Various types of high- and low-temperature sensors, such as LC-based resonator sensors, radio frequency identification (RFID) sensors, resistance temperature detectors (RTDs) sensors,

and wireless surface acoustic wave (SAW) sensors, have been studied and developed [11–14]. Among the temperature sensors, the SAW sensor has garnered increased interests in research due to its compact size, high sensitivity, rapid and fast response, and ability to function effectively in harsh environments, which have been consistently advancing, leading to improvements across all facets of the technology [15]. Several studies have shown that the SAW temperature device can be integrated with the antenna to perform well in challenging environments [16,17]. A SAW temperature sensor that utilizes a delay line was explicitly designed to function at 440 MHz and 2.4 GHz center frequencies, allowing it to effectively measure temperature in high-temperature settings [18]. The initial proof of concept system, which started at 250 MHz, progressed to the present at 915 MHz [19]. Most wireless passive SAW sensor systems are being developed and utilized at a frequency of 915 MHz for certain applications because of the advantages offered by the 915 MHz operating frequency ISM band. These advantages include less interference, extended communication range, and improved penetration compared to higher frequencies such as 2.4 GHz. This frequency is also considered optimal due to favorable device and compact antenna sizes and the widespread availability of compatible wireless RF components [20]. Wireless SAW sensors are designed to operate on 915 MHz; they have also been integrated with a disk monopole antenna with a size of 0.110λ and provide a broad band of 30 MHz [21]. A novel approach to temperature measurement using a wireless temperature sensor that depends on SAW technology was studied. Both the reader antenna, PIFA, and a normal-mode helical antenna were developed to operate at 915 MHz. The impedance matching network is required for efficient transmission, and the helical antenna size is about 0.070λ, which is relatively large [22].

Therefore, this work presents a miniaturized antenna design for this wireless passive and powerless SAW temperature sensor that operates at a central frequency of 915 MHz. We employed the High-Frequency Simulation Software (HFSS) for the simulations and optimization to achieve a compact size for two different types of normal-mode helical antennae: the non-uniform-pitch Cylindrical Helical Antenna (CHA) with a size of 0.055λ and the Hemispherical Helical Antenna (HSHA) with a size of 0.015λ. The antenna is mounted onto a coplanar waveguide (CPW), and the SAW sensor is directly installed next to the antenna without requiring a matching circuit. To verify the design, a low-temperature test was conducted to ensure optimal functionality of the system, as described in the following section.

2. Antenna Design

2.1. Non-Uniform-Pitch Cylindrical Helical Antenna (CHA) Design

The proposed system design configuration is composed of a surface acoustic wave sensor, which is a blue square box implemented on the shorted coplanar waveguide (CPW) structure with an FR-4 substrate material, a thickness of 1 mm, and a size of 24×24 mm^2, as shown in Figure 1a. The top perspective view of the proposed system design is displayed in Figure 1b. When the antenna receives the signal from the reader, it transmits the electromagnetic wave to the coplanar waveguide (CPW) and SAW sensor. The CPW provides a low-loss pathway for the signal, ensuring efficient transmission. The SAW sensor, implemented on the CPW, interacts with the incoming electromagnetic wave. It is sensitive to changes in the surrounding environment, such as temperature fluctuations. When these alterations occur, they affect the properties of the acoustic wave produced within the sensor. The surface acoustic wave (SAW) sensor reflects the altered signal back through the CPW. The alterations in the reflected signal serve as an indication of the environment or temperature changes that have been noticed by the SAW sensor.

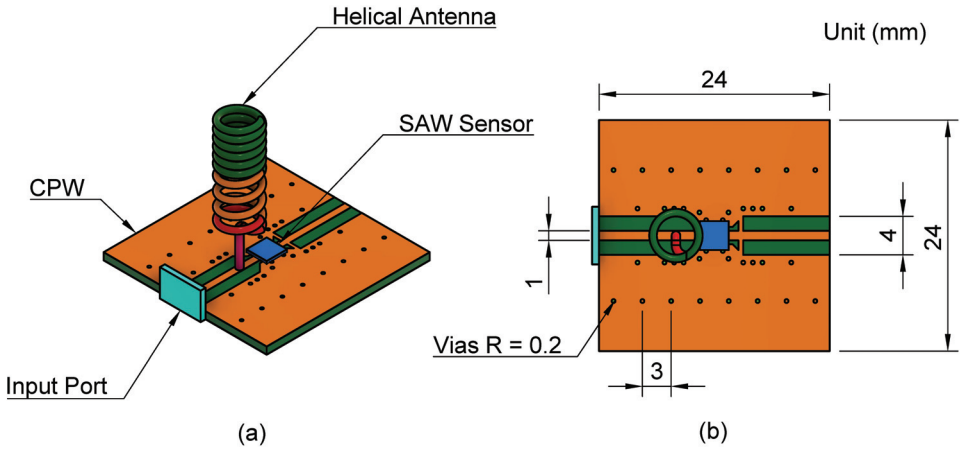

Figure 1. Proposed system design configuration. (**a**) Side view; (**b**) Top view and substrate dimension.

The essential factors to consider for an optimal helical antenna typically encompass helical length (l); pitch length (S), which is the distance between each successive coil of the helix; number of turns (N); the helix's cross-section (A); and the most important parameter, which is the helix's diameter (D). The equation below defines the relationship between these parameters and their influence on the antenna's resonant frequency (f_c) [23,24].

$$f_c = \frac{\sqrt{S}}{2\pi D\sqrt{\pi\mu_0\mu_r CN}} \tag{1}$$

where C is the capacitance of the helical antenna system; based on the equation provided above, the length of the helix and pitch length has a proportional relationship with the resonant frequency. In contrast, the diameter and number of turns are inversely proportional to the resonant frequency of the helix. Designing the normal-mode helical antenna using a uniform pitch distance may result in a larger size. The incorporation and use of a helical antenna with a non-uniform pitch have been suggested in the design since it is a notable benefit by offering a bandwidth improvement of about 18% and offers a smaller size as described in [25].

The diameter (D) selection is of utmost importance when designing a helical antenna since it directly impacts its resonant frequency and overall performance. The diameter of the helix has to be significantly smaller than the wavelength to achieve this normal mode. Our proposed design for a normal-mode non-uniform-pitch helical antenna is chosen to be $D \approx \frac{1}{50}\lambda$. The antenna consists of 3 different pitch lengths as described in Figure 2a and Table 1.

Table 1. Design parameters of the initial proposed non-uniform Cylindrical Helical Antenna (CHA).

Helix Stage	*S* (mm)	*N* (turns)
First Stage	$S1 = 1$	$N1 = 1.0$
Second Stage	$S2 = 3$	$N2 = 3.5$
Third Stage	$S3 = 1$	$N3 = 6.5$

A parametric study of the antenna diameter was conducted by varying the value from the initial value $D = 4$ mm to $D = 5.8$ mm. From Equation (1), the diameter of the helix and the resonance frequency are inversely proportional to each other, which matches the simulation study depicted in Figure 2b. When the antenna diameter value increases, the resonance frequency decreases. The study shows the trade-off between the antenna's target resonance frequency and the return loss level, which results in a narrow bandwidth while achieving the target operating frequency. As shown in Figure 2c, the variation of antenna pitch distance at the second stage was also monitored. The initial second-stage pitch distance (S2) was set to 3 mm and decreased to 2.5 mm and 1.5 mm sequentially. The

simulation result indicates that the resonance frequency of the antenna changed towards a lower frequency, which means it has a proportional relationship with the pitch length. Looking at Figure 2d, the helix's third-stage number of turns increased from 6.5 turns to 7.5 and 8.5 turns. This study shows the inversely proportional relationship between the central frequency of the CHA antenna and the number of turns. As we increase the value of the number of turns, the resonance frequency decreases while providing a good return loss at a lower frequency.

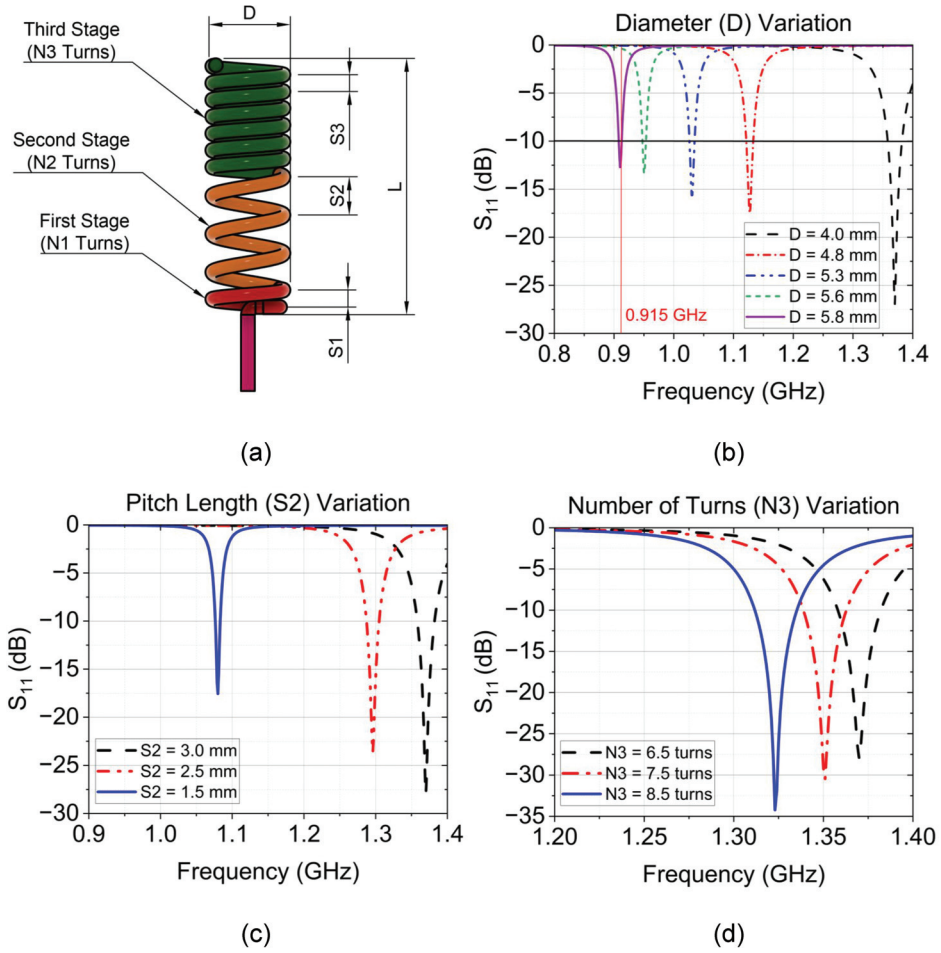

Figure 2. Parametric study of the CHA antenna. (**a**) Antenna dimension, (**b**) Simulation result for diameter variations, (**c**) Pitch length variation, (**d**) Change in number of turns.

Based on this simulation study and according to Equation (1), we obtained the optimal design model of the non-uniform-pitch helical antenna with a diameter $D = 5$ mm and length $L = 16.8$ mm, which is approximately equal to 0.055λ. The optimized antenna exhibits resonance at 0.917 GHz with a return loss of -20.750 dB in the bandwidth range of 0.913 GHz to 0.920 GHz, as depicted in Figure 3. The antenna provides a gain of 1 dBi omnidirectional radiation pattern. The optimal model design parameters are described in Table 2, including each stage's pitch length and number of turns.

Table 2. Design parameters of the optimal design of non-uniform Cylindrical Helical Antenna (CHA).

Stage	*S* (mm)	*N* (turns)
First Stage	$S1 = 1.2$	$N1 = 1.0$
Second Stage	$S2 = 2.5$	$N2 = 3.0$
Third Stage	$S3 = 1.1$	$N3 = 6.5$

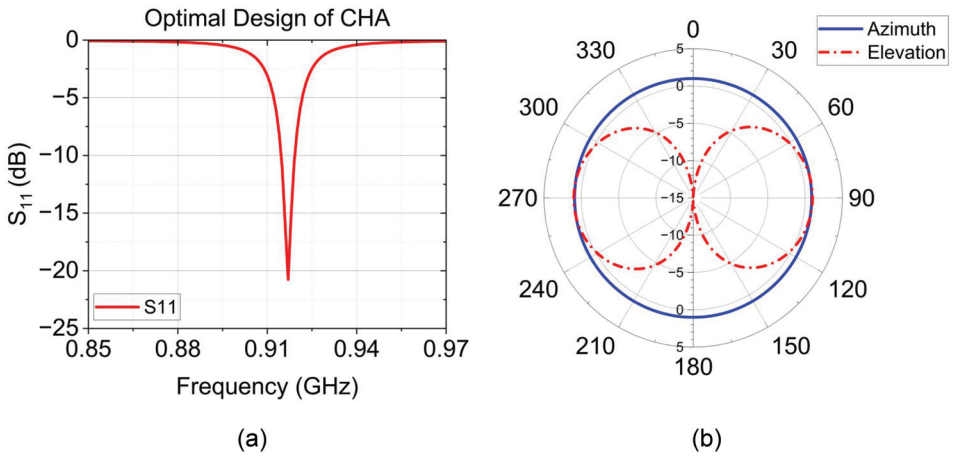

Figure 3. Simulation result of the optimal design of the non-uniform-pitch Cylindrical Helical Antenna (CHA). (**a**) Return loss (dB); (**b**) Radiation pattern.

2.2. Hemispherical Helical Antenna (HSHA) Design

In the previous design, the non-uniform-pitch helical antenna is well-suited for wireless surface acoustic wave (SAW) temperature sensor applications. Nevertheless, the objective of this effort is to minimize the size of the system as much as feasible. Therefore, we suggest utilizing a hemispherical helical structure to evaluate the trade-offs and drawbacks of both designs and obtain a more compact system. The hemispherical helical antenna has benefits in terms of size reduction and enhanced performance. It has a more durable and compact structure compared to other helical antenna structures like cylindrical and spherical antennae, making it more suitable for applications that demand compact designs [26–28]. The pitch distance (p) of the hemispherical helical antenna is constant, with N turns of the hemispherical shape, while $N_t = 2N$ is the full-sphere number of turns. The resonance of the antenna itself can be controlled or adjusted by changing the value of the spherical radius (r) or diameter (D). The hemispherical helical antenna structure's geometry in each axis can be obtained as below [28]:

$$x(n) = \sqrt{r^2 - (r-n)^2} \times \cos\left(\frac{2\pi n}{p}\right) \tag{2}$$

$$y(n) = \sqrt{r^2 - (r-n)^2} \times \sin\left(\frac{2\pi n}{p}\right) \tag{3}$$

$$z(n) = -n + r \tag{4}$$

where $n \in [0, r]$ and $p = \frac{2\pi r}{N_t} = \frac{\pi r}{N}$.

As illustrated in Figure 4, the proposed design consists of a hemispherical helical antenna and a SAW sensor mounted on a coplanar waveguide (CPW) with an FR-4 substrate material, having a thickness of 1 mm and dimensions of 24×15 mm^2. The system operates as described in the previous section.

The initial design features an antenna wire's cross-section diameter of $d = 1$ mm. To fully conform to the hemisphere, 3 to 5 turns are suitable for achieving an omnidirectional radiation pattern and ensuring the wire fully winds around the spherical shape; increasing the number of turns can enhance the axial ratio bandwidth [29,30]. The diameter of the hemispherical helix is chosen as $D = 0.036\lambda$, approximately 12 mm. To analyze the characteristics of the Hemispherical Helical Antenna (HSHA), we first mounted the HSHA on the CPW, which has exact dimensions as the CPW used to feed the Cylindrical Helical Antenna (CHA). The simulation results, depicted in Figure 5a and noted with a black solid curve, show that the antenna system exhibits resonance at 0.592 GHz with a return loss of -11.7 dB. The resonance frequency of the HSHA can be controlled by physical parameters such as the number of turns (N) and diameter (D).

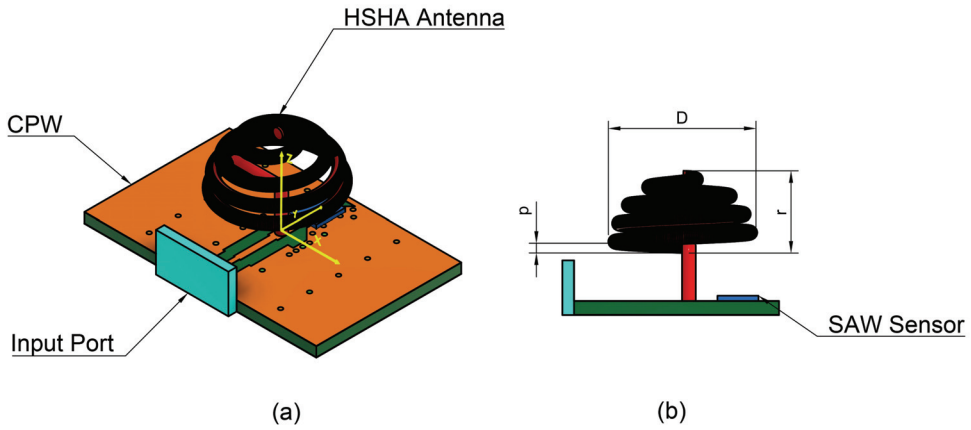

Figure 4. Proposed design of the Hemispherical Helical Antenna (HSHA). (**a**) Side view of system configuration; (**b**) Antenna geometry.

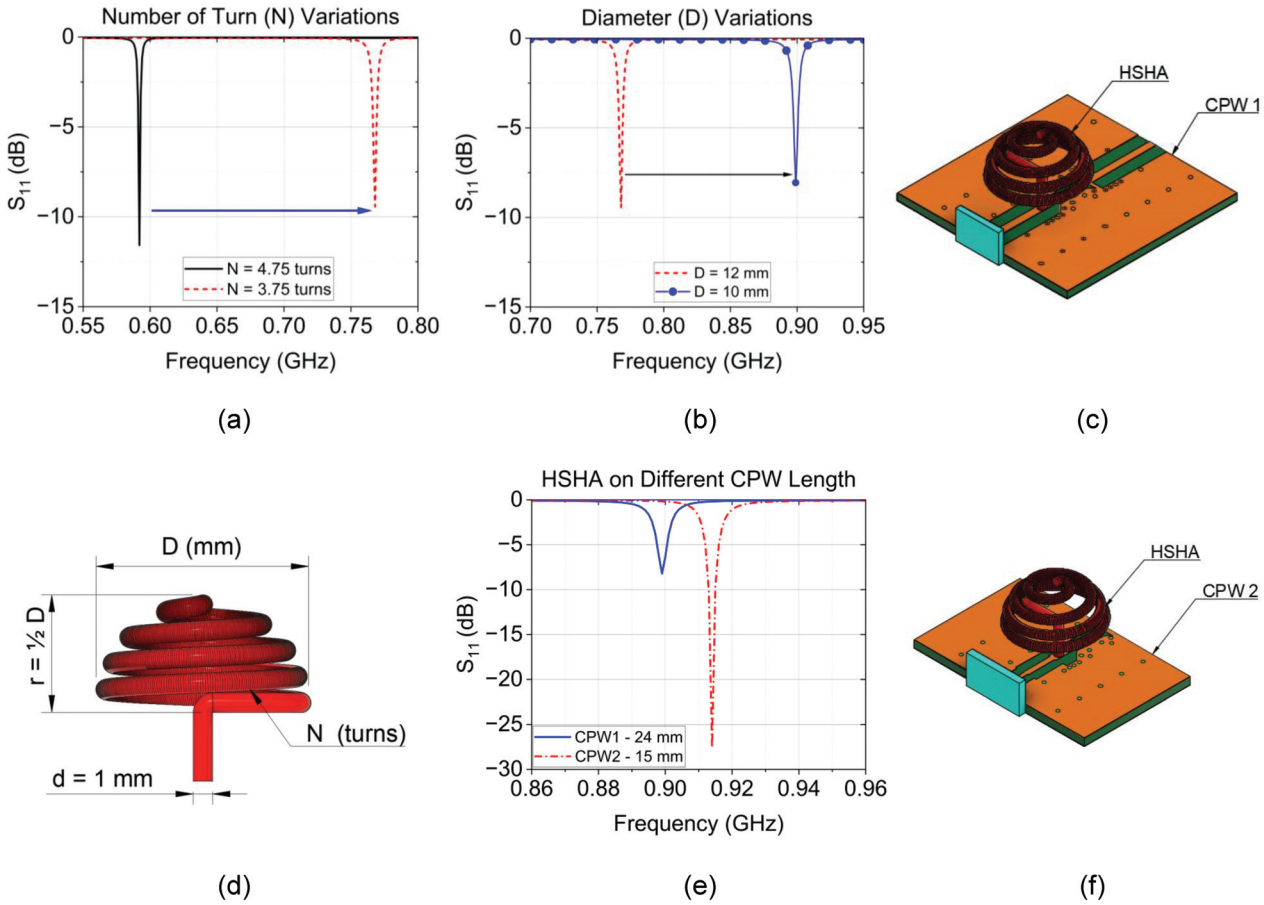

Figure 5. Study of Hemispherical Helical Antenna (HSHA). (**a**) Simulation result of HSHA of the number of turn variations; (**b**) Antenna diameter variations; (**c**) HSHA on CPW1 with a length of 24 mm; (**d**) HSHA dimension; (**e**) HSHA performance on different lengths of CPW; (**f**) HSHA mounted on CPW2 with 15 mm length.

Following Equation (1), we shift the resonance frequency to a higher value by changing the number of turns from $N1 = 4.75$ to $N2 = 3.75$ turns. This adjustment results in resonance at approximately 0.768 GHz, indicated by a red dashed curve in Figure 5a, where a significant loss is also observed. Since the number of turns reaches the minimum value for the wire to maintain a hemispherical shape, the next consideration is the antenna

diameter, which is inversely proportional to the resonance frequency. By decreasing the diameter from $D1 = 12$ mm to $D2 = 10$ mm, we further analyze the impact on resonance. As seen in Figure 5b, the antenna exhibits resonance at 0.889 GHz while providing poor matching at the operating band. The CPW length of the antenna is reduced from CPW1 in Figure 5c, with a length of 24 mm, to the CPW2 as illustrated in Figure 5f, having a smaller length. Decreasing the length of a CPW resonator often leads to an increased resonance frequency [31]. So, the length reduction was studied, and the antenna system resonance shifted to a higher frequency, which was very close to the targeted value at 0.914 GHz with a CPW2 length of 15 mm and providing a lower return loss, as depicted in Figure 5e.

We successfully designed two suitable antennae for wireless SAW temperature sensors as compared in Table 3, in which the antenna height and PCB dimension are described. The HSHA model provides an advantage in terms of a smaller size than the CHA model. In contrast, as shown in Figure 6a, the HSHA antenna model provides a smaller bandwidth in the desired operating band of 0.915 GHz. Additionally, the HSHA tends to have a smaller gain than the CHA model as illustrated in Figure 6b. However, both antennae achieve an omnidirectional radiation pattern appropriate for the ideal wireless SAW temperature sensor application.

Table 3. Design parameters of the optimal design of non-uniform Cylindrical Helical Antenna (CHA) and Hemispherical Helical Antenna (HSHA).

Antenna Type	PCB Size (mm^3)	Antenna Height (mm)	Diameter (mm)
CHA	$24 \times 24 \times 1$	16.8	5
HSHA	$24 \times 15 \times 1$	5	10

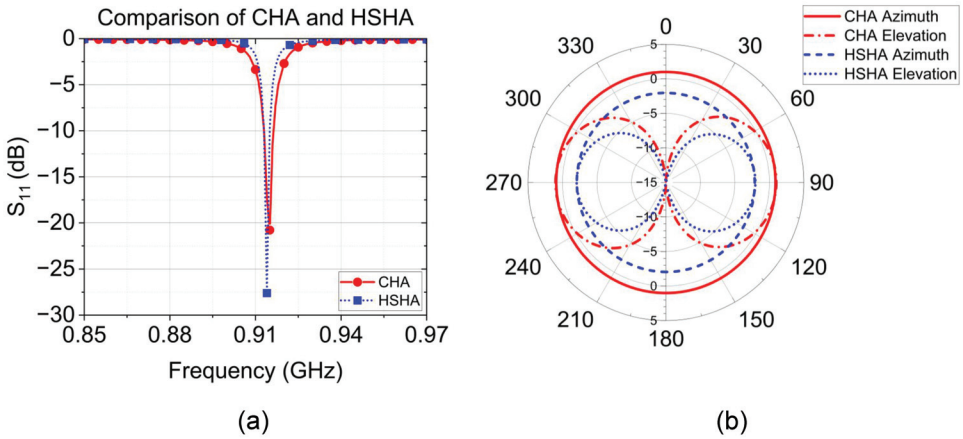

Figure 6. Simulation comparison of the proposed design of CHA and HSHA. (**a**) Return loss. (**b**) Radiation pattern.

3. Antenna Fabrication and Measurement

3.1. Return Loss

Photographs of the manufactured non-uniform-pitch Cylindrical Helical Antenna (CHA) and Hemispherical Helical Antenna are shown in Figure 7. To conduct experimental measurements, we needed to connect each of our fabricated antenna systems with a VNA using an SMA connector. The MS46122B VNA model was used, and this belongs to Anritsu's ShockLine series. As seen in Figure 8, the fabricated models were studied using two types of measurement, which have the CHA and HSHA antennae only on the CPW1 and CPW2, respectively, without the SAW temperature sensor mounted on the PCB and vice versa. Without the SAW sensor, we can see that both antennae exhibit resonance at the desired operating band, which is 0.915 GHz. As with the simulation results above, the HSHA antenna can be a compact size or smaller than the CHA model, but we observed a drawback in terms of bandwidth after measuring the return loss of

the antenna. The SAW sensor alone was also measured, and a small resonance at around 0.915 GHz was observed. Based on this SAW sensor's performance, when we combined the SAW sensors with the antennae together and measured the return loss using a vector network analyzer, the measurement of the antenna with the presence of a SAW sensor was obtained. It had an initial central frequency of 0.915 GHz and could be changed by the surrounding temperature; we observed a notch occurring at around 0.914.45 GHz for CHA and 0.915 GHz for HSHA.

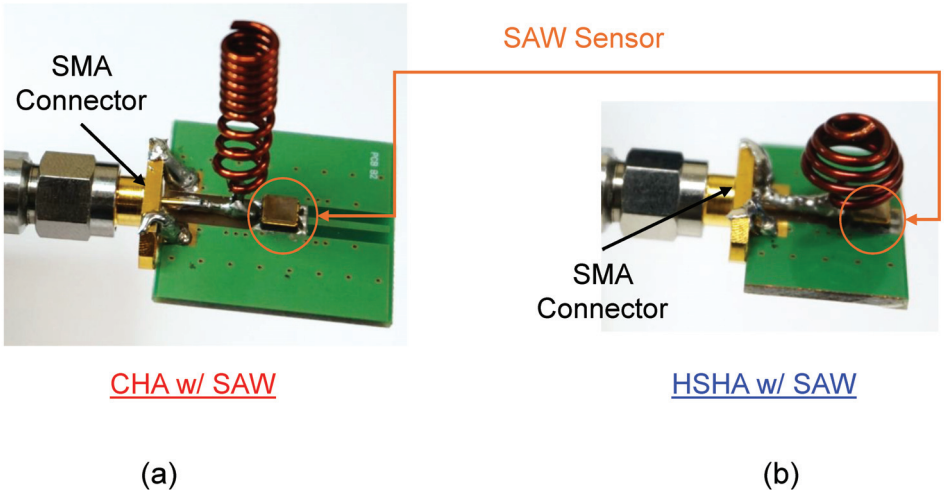

Figure 7. Measurement of the antenna system. (**a**) Fabricated model of CHA with SAW sensor model. (**b**) Fabricated HSHA model with SAW sensor.

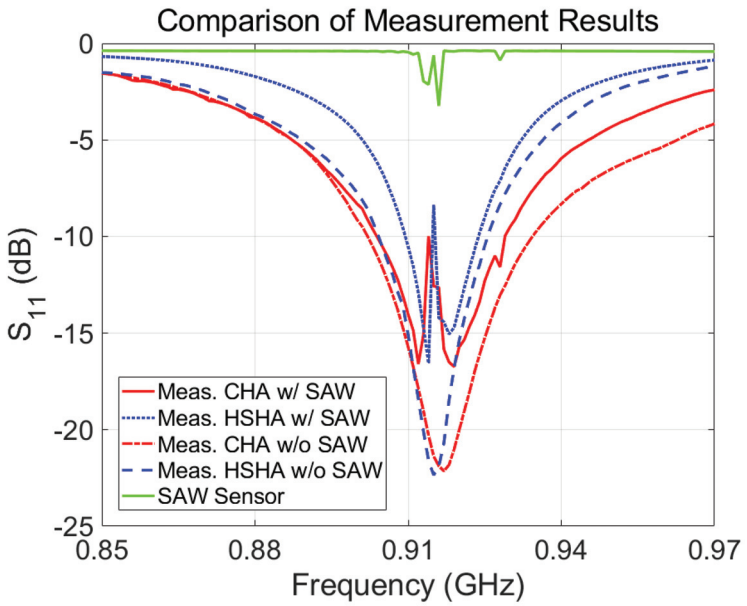

Figure 8. Comparison measurement result of the antenna system with the case of not having the SAW sensor mounted and with the case of the SAW sensor mounted.

3.2. Received Power Test

The efficacy of the helical antenna was further assessed by conducting free space path loss (FSPL) and received power measurements. The free space path loss measures the attenuation of signal power as it propagates over unobstructed space. This statistic substantially facilitates the comprehension of the efficiency and scope of wireless sensing networks.

The FSPL can be calculated using the following equation [32]:

$$\text{FSPL} = 20\log_{10}(d) + 20\log_{10}(f) + 20\log_{10}\left(\frac{4\pi}{c}\right) \quad (5)$$

Here, d represents the distance between the transmitter and receiver, measured in (m), and f represents the frequency of the signal in Hz. The symbol c represents the velocity of light when it is traveling through a vacuum.

The receive power test involves measuring and analyzing the power received by the helical antenna. The power received by the antenna (P_r) can be determined by applying the following equation:

$$P_r = P_t + G_t + G_r - \text{FSPL} \quad (6)$$

where P_t is the transmitted power (dBm). G_t (dBi) is the gain of the transmitting antenna. G_r is the gain of the receiving antenna in dBi.

In this experiment, we placed the transmitting helical antenna at a constant distance of 1 m from the receiving source, which is the TX900-PB-23223 model, which had a gain of 10.0 dBi, operating from 850 MHz to 930 MHz. We quantified the received power using a spectrum analyzer. The measurements were conducted in a room, as depicted in Figure 9. The antenna was installed vertically. The CHA and HSHA were placed as DUT for the test in 3 different transmit power P_t values, and we observed that the HSHA model provided a lower received signal level at the receiver. It is proof that the result of the simulated gain of both models is acceptable based on the comparison of the received power test data plotted in Figure 10. The comparison between the actual received power test and the calculated power is also described in Table 4. We can see that the actual measurement is around 10 dB different from the ideal calculated one due to the other loss that we did not include in the calculation.

Table 4. Measured and calculated Rx. power for different Tx values. Power levels at 915 MHz.

Tx. Power (dBm)	Measured Rx. Power (dBm) CHA	Measured Rx. Power (dBm) HSHA	Calculated Rx. Power (dBm) CHA	Calculated Rx. Power (dBm) HSHA
0	−31.88	−38.63	−22.36	−24.7
10	−22.88	−27.52	−12.36	−14.7
20	−13.5	−20.06	−2.36	−4.7

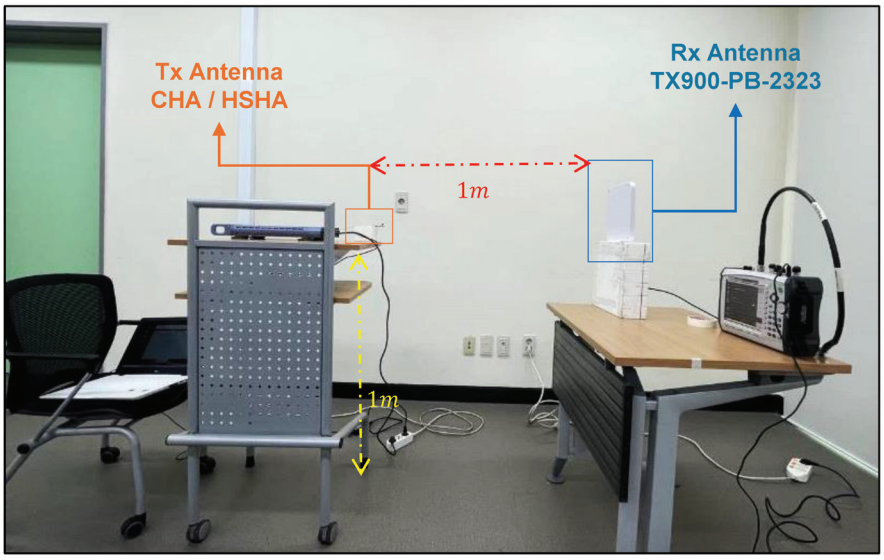

Figure 9. Received Power Test Setup and Configuration.

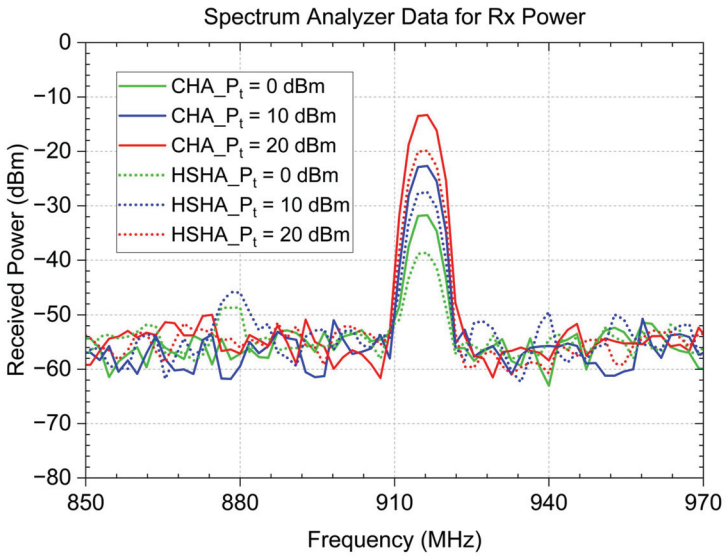

Figure 10. Comparison of received power measurements with different frequency and transmit power levels.

3.3. Temperature Test

In this temperature measurement, we established the test configuration based on the arrangement shown in Figure 11a,b. The Device Under Test (DUT) is linked to the Vector Network Analyzer (VNA)—model Anritsu MS2038C—via the wire connector. At the same time, the temperature controller regulates the heating plate positioned approximately 2 cm below the DUT. The Digital Thermometer is positioned adjacent to the heating plate to detect and measure the temperature surrounding the testing environment. The temperature test was performed two times, initially using the non-uniform-pitch Cylindrical Helical Antenna (CHA) and subsequently with the Hemispherical Helical Antenna (HSHA). The testing of both models was conducted with temperature in a range of 30 °C to 90 °C, which is the highest possible ambient temperature that could be achieved using the test equipment.

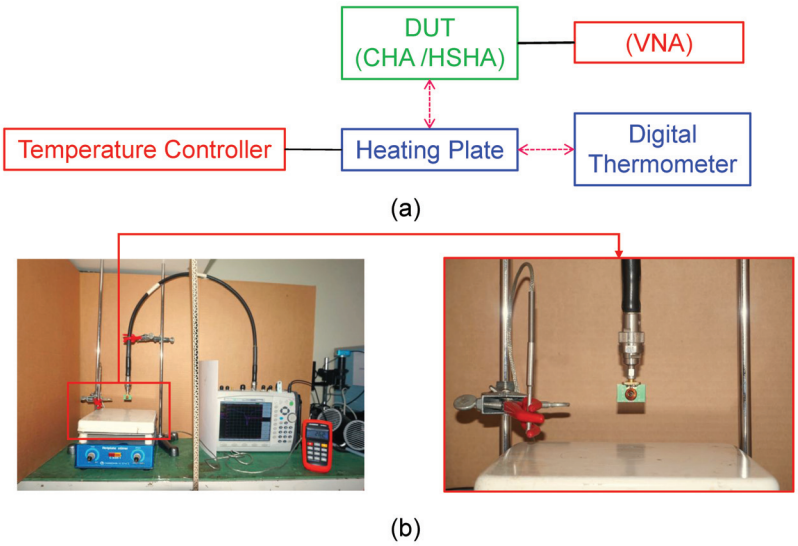

Figure 11. Antenna system temperature test. (**a**) Test configuration diagram; (**b**) Test setup photograph.

Figure 12a,c show the measured return loss of the CHA and HSHA antenna models, respectively. On the other side, Figure 12b,d show a closer look at the antenna performances. They emphasize the notches that were formed at the central frequency of 915 MHz due to the SAW temperature sensor effect. It was discovered that both system's resonance frequencies

shifted to lower values as the temperature increased. The measured data were recorded every 10 °C, and the frequency changes based on the test environment temperature are depicted in Figure 13. Within the test range of 30 °C to 90 °C, both CHA and HSHA systems need a 400 KHz bandwidth of the operating band for the decrement of the resonance frequencies. The linear fitting curve provides the characteristic of the antenna resonance frequency decrement with temperature. The linear fitting equation of the CHA is $f_{cha} = 0.0071t + 914.9$ while $f_{hsha} = 0.0066t + 914.35$ is the linear fitting equation for the HSHA model.

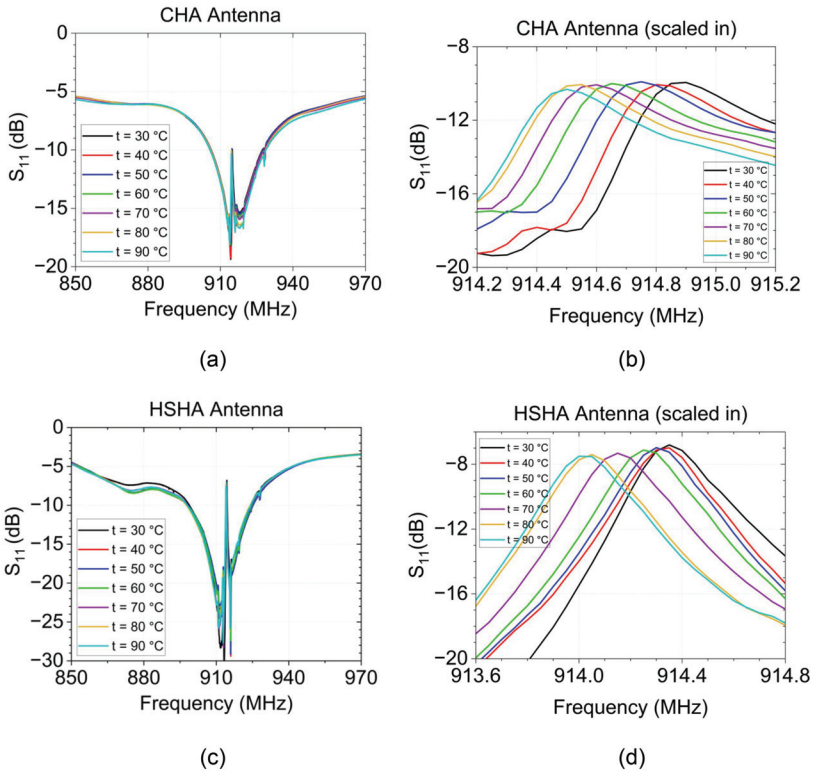

Figure 12. Temperature test result; changes in return loss based on temperature. (**a**) CHA antenna; (**b**) Scale-in of CHA test result; (**c**) HSHA antenna; (**d**). Scale-in of HSHA test results.

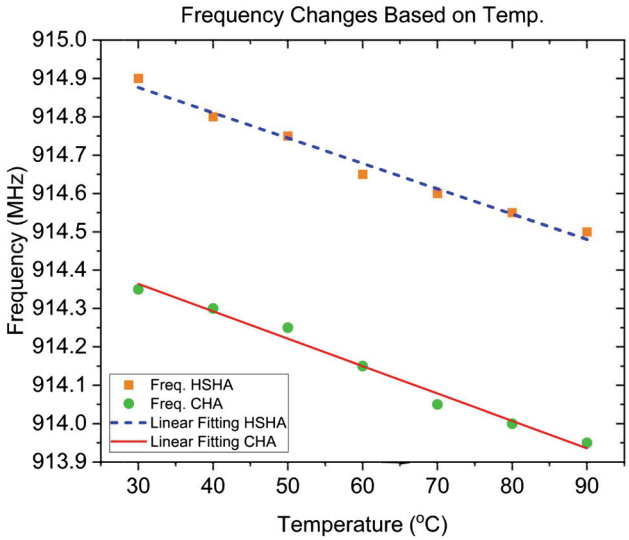

Figure 13. SAW sensor system frequency changes based on temperature.

4. Conclusions

A comparison between the proposed design of a miniaturized non-uniform-pitch Cylindrical Helical Antenna (CHA) and Hemispherical Helical Antenna (HSHA) with the other existing antenna designed for a wireless temperature sensor is presented in Table 5. The antenna's electrical size is compared, and the gain and bandwidth of each work are also included. Besides having a compact size, the CHA antenna also exhibits 915 MHz over a bandwidth of 30 MHz, which can cover a range of 902 MHz to 932 MHz. The maximum gain value that it can achieve is 1 dBi, and it exhibits an omniradiation pattern, which is the same as the HSHA model, which achieves a smaller and more compact size and length. However, it provides a smaller gain of −2 dB and operates over a smaller bandwidth of 22 MHz, covering 904 MHz to 926 MHz.

Table 5. Comparison of various existing wireless temperature sensors with antenna systems.

References	Frequency (MHz)	Bandwidth (MHz)	Ant. Length	Gain (dBi)	Ant. Volume (mm^3)
[18]	434	20	0.029λ	2	$45 \times 45 \times 0.2$
[21]	915	30	0.110λ	2	$36 \times 20 \times 14$
[22]	915	20	0.070λ	1.4	$30 \times 30 \times 20$
This Work	915 (CHA)	30	0.055λ	1	$24 \times 24 \times 21.8$
	915 (HSHA)	22	0.015λ	−2	$24 \times 15 \times 9$

In conclusion, we successfully designed two compact antennae suitable for wireless SAW temperature sensor applications; the antennae include a non-uniform-pitch Cylindrical Helical Antenna (CHA) and a Hemispherical Helical Antenna operating at 915 MHz with a bandwidth of 30 MHz and 22 MHz, respectively. From the CHA system design to the HSHA system model, including feeding CPW, the overall system is deduced to be compact at around 70% smaller. The temperature test was conducted from 30 °C to 90 °C using the test set up described above, and the frequency shift was such that for every 10 °C change, the SAW sensor frequency decreased by an average of 66.67 kHz. However, the system exhibited inadequate amplification, resulting in a received power that fell short of theoretical projections. Additionally, the utilization of wire presents obstacles in the manufacturing process. A new system model is being built for future development to improve resilience and enhance gain and return loss.

Author Contributions: Conceptualization, N.S. and J.-Y.C.; methodology, N.S. and J.-Y.C.; software, N.S.; validation, N.S. and J.-Y.C.; formal analysis, N.S.; investigation, N.S.; resources, N.S.; data curation, N.S.; writing—original draft preparation, N.S.; writing—review and editing, N.S. and J.-Y.C.; visualization, N.S. and J.-Y.C.; supervision, J.-Y.C.; project administration, J.-Y.C.; funding acquisition, J.-Y.C. All authors have read and agreed to the published version of the manuscript.

Funding: This research was supported by Seoul National University of Science and Technology.

Data Availability Statement: Data are contained within the article.

Conflicts of Interest: The authors declare no conflicts of interest.

Abbreviations

The following abbreviations are used in this manuscript:

SAW	Surface Acoustic Wave
CHA	Cylindrical Helical Antenna
HSHA	Hemispherical Helical Antenna
RTDs	Resistance Temperature Detectors

RFID	Radio Frequency Identification
CPW	Coplanar Waveguide
Tx	Transmitter
Rx	Receiver
DUT	Device Under Test
VNA	Vector Network Analyzer
PCB	Printed Circuit Board
FSPL	Free Space Path Loss

References

1. Singh, R.; Singh, S.P. Development of a Low Cost Wireless Temperature Monitoring System for Industrial & Research Application. *Int. J. Curr. Eng. Technol.* **2015**, *5*, 355–361.
2. Park, D.; Jung, H.-S.; Cho, H.-J.; Sul, S.-K. Design of wireless temperature monitoring system for measurement of magnet temperature of IPMSM. In Proceedings of the 2018 IEEE Transportation Electrification Conference and Expo (ITEC), Long Beach, CA, USA, 13–15 June 2018; pp. 656–661.
3. Khairi, N.A.; Jambek, A.B.; Boon, T.W.; Hashim, U. Design and analysis of a wireless temperature monitoring system. In Proceedings of the RSM 2013 IEEE Regional Symposium on Micro and Nanoelectronics, Langkawi, Malaysia, 25–27 September 2013; pp. 105–108.
4. Wei, Q.; Park, H.-J.; Lee, J.H. Development of a wireless health monitoring system for measuring core body temperature from the back of the body. *J. Healthc. Eng.* **2019**, *2019*, 8936121. [CrossRef]
5. Mansor, H.; Shukor, M.H.A.; Meskam, S.S.; Rusli, N.Q.A.M.; Zamery, N.S. Body temperature measurement for remote health monitoring system. In Proceedings of the 2013 IEEE International Conference on Smart Instrumentation, Measurement and Applications (ICSIMA), Kuala Lumpur, Malaysia, 25–27 November 2013; pp. 1–5.
6. Mahan, J.R.; Conaty, W.; Neilsen, J.; Payton, P.; Cox, S.B. Field performance in agricultural settings of a wireless temperature monitoring system based on a low-cost infrared sensor. *Comput. Electron. Agric.* **2010**, *71*, 176–181. [CrossRef]
7. Raghunathan, N.; Jiang, X.; Peroulis, D.; Ganguly, A. Wireless low-power temperature probes for food/pharmaceutical process monitoring. In Proceedings of the 2015 IEEE SENSORS, Busan, Republic of Korea, 1–4 November 2015; pp. 1–4.
8. Saha, S.; Majumdar, A. Data centre temperature monitoring with ESP8266 based Wireless Sensor Network and cloud based dashboard with real time alert system. In Proceedings of the 2017 Devices for Integrated Circuit (DevIC), Kalyani, India, 23–24 March 2017; pp. 307–310.
9. Monteleone, S.; Sampaio, M.; Maia, R.F. A novel deployment of smart Cold Chain system using 2G-RFID-Sys temperature monitoring in medicine Cold Chain based on Internet of Things. In Proceedings of the 2017 IEEE International Conference on Service Operations and Logistics, and Informatics (SOLI), Bari, Italy, 18–20 September 2017; pp. 205–210.
10. Li, C.; Feng, Q.; Jia, M.; Gao, L.; Jia, P.; Fang, Z.; Lu, H.; Xiong, J. Accurate real-time temperature measurement method in ultra-high temperature rotational environments for aero engines/turbines. *IEEE Sens. J.* **2022**, *22*, 6482–6490. [CrossRef]
11. Bhar, I.; Mandal, N. A review on advanced wireless passive temperature sensors. *Measurement* **2022**, *187*, 110255. [CrossRef]
12. Idhaiam, K.S.V.; Pozo, P.D.; Sabolsky, K.; Sabolsky, E.M.; Sierros, K.A.; Reynolds, D.S. All-ceramic LC resonator for chipless temperature sensing within high temperature systems. *IEEE Sens. J.* **2021**, *21*, 19771–19779. [CrossRef]
13. Ji, Y.; Tan, Q.; Lu, X.; Zhang, G.; Zhang, W.; Xiong, J. Wireless passive separated LC temperature sensor based on high-temperature co-fired ceramic operating up to 1500 °C. *J. Micromech. Microeng.* **2019**, *29*, 035015. [CrossRef]
14. Qian, Y.; Luo, Z.; Liu, Z.; Zhao, H.; Li, C.; Song, Y.; Nan, D.; Wei, J. Application of RTD sensor in the real-time measurement and wireless transmission. In Proceedings of the 2014 Fourth International Conference on Instrumentation and Measurement, Computer, Communication and Control, Harbin, China, 18–20 September 2014; pp. 658–662.
15. Gao, X.; Cheng, L.; Xue, X.; Zhai, S.; Liang, Y.; Wang, W.; Liu, M.; Zhu, J.; Li, Z. Development of wireless and passive SAW temperature sensor with very high accuracy. *Appl. Sci.* **2021**, *11*, 7422. [CrossRef]
16. Stevens, D.S.; Andle, J.C.; Sabah, S.; Jumani, S.J.; Wall, B.W.A.; Baier, M.; Martens, T.; Gruenwald, R. Applications of wireless temperature measurement using SAW resonators. In Proceedings of the Fourth International Symposium on Acoustic Wave Devices for Future Mobile Communication Systems, Chiba, Japan, 3–5 March 2010.
17. Reindl, L.; Shrena, I.; Kenshil, S.; Peter, R. Wireless measurement of temperature using surface acoustic waves sensors. In Proceedings of the IEEE International Frequency Control Symposium and PDA Exhibition Jointly with the 17th European Frequency and Time Forum, Tampa, FL, USA, 4–8 May 2003; pp. 935–941.
18. Lee, K.; Wang, W.; Kim, T.; Yang, S. A novel 440 MHz wireless SAW microsensor integrated with pressure–temperature sensors and ID tag. *J. Micromech. Microeng.* **2007**, *17*, 515. [CrossRef]
19. Gallagher, M.W.; Santos, B.C.; Malocha, D.C. Wireless wideband SAW sensor-antenna design. In Proceedings of the 2010 IEEE International Frequency Control Symposium, Newport Beach, CA, USA, 1–4 June 2010; pp. 291–296.
20. Sandoval, R.M.; Garcia-Sanchez, A.-J.; Garcia-Sanchez, F.; Garcia-Haro, J. Evaluating the more suitable ISM frequency band for IoT-based smart grids: A quantitative study of 915 MHz vs. 2400 MHz. *Sensors* **2016**, *17*, 76. [CrossRef]
21. Malocha, D.C.; Humphries, J.; Figueroa, J.A.; Lamothe, M.; Weeks, A. 915 MHz SAW wireless passive sensor system performance. In Proceedings of the 2016 IEEE International Ultrasonics Symposium (IUS), Tours, France, 18–21 September 2016; pp. 1–4.

22. Han, Y.; Qi, B.; Tan, J. Antenna design of passive wireless temperature sensor based on surface acoustic wave. In Proceedings of the 2017 IEEE 9th International Conference on Communication Software and Networks (ICCSN), Guangzhou, China, 6–8 May 2017; pp. 713–717.
23. Balanis, C.A. *Antenna Theory: Analysis and Design*; John Wiley & Sons: Hoboken, NJ, USA, 2016; pp. 549–555.
24. Stutzman, W.L.; Thiele, G.A. *Antenna Theory and Design*; John Wiley & Sons: Hoboken, NJ, USA, 2012.
25. Zhao, S.; Fumeaux, C.; Coleman, C. Miniaturised high-frequency and very-high-frequency antennas based on optimised non-uniform helical structures. *IET Microw. Antennas Propag.* **2012**, *6*, 603–610. [CrossRef]
26. Hui, H.T.; Chan, K.Y.; Yung, E.K.N. The low-profile hemispherical helical antenna with circular polarization radiation over a wide angular range. *IEEE Trans. Antennas Propag.* **2003**, *51*, 1415–1418. [CrossRef]
27. Rayhana, A.I.; Alaaudeen, K.M. A conformable design of hemispherical helical antenna for ocean monitoring. In *SSRG International Journal of Electronics and Communication Engineering (SSRG-IJECE)*; Seventh Sense Research Group: Tiruchirappalli, India, 2019; pp. 49–53, ISSN 2348-8549.
28. Alsawaha, H.W.; Safaai-Jazi, A. Ultrawideband hemispherical helical antennas. *IEEE Trans. Antennas Propag.* **2010**, *58*, 3175–3181. [CrossRef]
29. Zhang, Y.; Hui, H.T. A printed hemispherical helical antenna for GPS receivers. *IEEE Microw. Wirel. Compon. Lett.* **2005**, *15*, 10–12. [CrossRef]
30. Hui, H.T.; Yung, E.K.N.; Law, C.L.; Koh, Y.S.; Koh, W.L. Design of a small and low-profile 2 $\times$ 2 hemispherical helical antenna array for mobile satellite communications. *IEEE Trans. Antennas Propag.* **2004**, *52*, 346–348. [CrossRef]
31. Görlür, A.; Karpuz, C. Influence of narrow transverse slit in CPW resonator on its resonance characteristics. *Electron. Lett.* **2000**, *36*, 49–50. [CrossRef]
32. Rappaport, T.S. *Wireless Communications: Principles and Practice*; Cambridge University Press: Cambridge, UK, 2024; pp. 70–77

sensors

MDPI

Article

Compact Wideband Tapered Slot Antenna Using Fan-Shaped and Stepped Structures for Chipless Radio-Frequency-Identification Sensor Tag Applications

Junho Yeo [1,*] and Jong-Ig Lee [2]

[1] Department of Artificial Intelligence, Daegu University, 201 Daegudae-ro, Gyeongsan 38453, Republic of Korea
[2] Department of Electrical and Electronics Engineering, Dongseo University, Busan 47011, Republic of Korea; leeji@gdsu.dongseo.ac.kr
* Correspondence: jyeo@daegu.ac.kr; Tel.: +82-53-850-6642

Abstract: In this paper, two kinds of miniaturization methods for designing a compact wideband tapered slot antenna (TSA) using either fan-shaped structures only or fan-shaped and stepped structures were proposed. First, a miniaturization method appending the fan-shaped structures, such as quarter circular slots (QCSs), half circular slots (HCSs), and half circular patches (HCPs), to the sides of the ground conductor for the TSA was investigated. The effects of appending the QCSs, HCSs, and HCPs sequentially on the input reflection coefficient and gain characteristics of the TSA were compared. The compact wideband TSA using the first miniaturization method showed the simulated frequency band for a voltage standing wave ratio (VSWR) less than 2 of 2.530–13.379 GHz (136.4%) with gain in the band ranging 3.1–6.9 dBi. Impedance bandwidth was increased by 29.7% and antenna size was reduced by 39.1%, compared to the conventional TSA. Second, the fan-shaped structures combined with the stepped structures (SSs) were added to the sides of the ground conductor to further miniaturize the TSA. The fan-shaped structures based on the HCSs and HCPs were appended to the ground conductor with the QCSs and SSs. The compact wideband TSA using the second miniaturization method had the simulated frequency band for a VSWR less than 2 of 2.313–13.805 GHz (142.6%) with gain in the band ranging 3.0–8.1 dBi. Impedance bandwidth was increased by 37.8% and antenna size was reduced by 45.9%, compared to the conventional TSA. Therefore, the increase in impedance bandwidth and the size reduction effect of the compact wideband TSA using the second miniaturization method were better compared to those using the first method. In addition, sidelobe levels at high frequencies decreased while gain at high frequencies increased. A prototype of the compact wideband TSA using the second miniaturization method was fabricated on an RF-35 substrate to validate the simulation results. The measured frequency band for a VSWR less than 2 was 2.320–13.745 GHz (142.2%) with measured gain ranging 3.1–7.9 dBi.

Keywords: compact wideband tapered slot antenna (TSA); miniaturization method; fan-shaped structures; stepped structures; chipless radio frequency identification (RFID)

1. Introduction

As the era of the fourth industrial revolution progresses to realize a hyper-connected intelligent information society in which both people and objects are connected, and collected data are analyzed and utilized based on artificial intelligence, the demand of wideband wireless communication technology is extensively increasing in order to satisfy the need to support more users and to provide more information with higher data rates [1,2]. The design of a wideband antenna is necessary to support the wideband wireless communication technology [3]. Wideband antennas can be divided into omni-directional and directional antennas depending on radiation patterns or directivity of the antenna. The types of directional wideband antennas include Yagi-Uda antennas, quasi-Yagi antennas, log-periodic dipole array antennas, spiral antennas, tapered slot antennas (TSAs), horn

antennas, and reflector antennas [4]. Among various directional wideband antennas, TSAs have been widely used because they are thin with a planar structure, are easy to manufacture, and have relatively high gain characteristics over a wide band [5]. The concept of the TSAs began in the late 1950s as a flared slot antenna with the slot width gradually increasing [6]. TSAs with an exponentially tapered slot were introduced by Gibson as the Vivaldi antenna in 1979 [7] and have been actively studied in the fields of ultra-wideband (UWB) communications, radar, and imaging. TSAs can be classified into constant width, linear, stepped, elliptical, exponential (Vivaldi), and double exponential, depending on the shape of the slot [5].

Compact wideband directional antennas are required in application fields, such as a UWB communication for wearable devices, UWB radar and imaging systems, wireless body area networks, and retransmission-based chipless radio frequency identification (RFID) systems [8–10]. Miniaturization methods to reduce the dimensions of the TSAs found in the literature can be classified as follows: an addition of the slots with various shapes to the sides of the ground conductor, an insertion of the corrugations to the sides of the ground conductor, and a modification of the shape of the tapered slot [11]. Firstly, the slots with various shapes, such as exponential, triangular, anti-spiral, quarter circular, half circular, eye-shaped, eye-shaped combined with a circle, modified exponential, fractal-shaped, and hook-shaped, were appended to the edges or sides of the ground conductor for the miniaturization of the TSAs. When the slots were etched on the sides of the ground conductor, the outer electrical length of the TSAs was increased, and this, in turn, moved the lower limit of the frequency band, which has a size-reduction effect. A bunny-ear-shaped TSA with an exponentially tapered ground conductor operating in the frequency range from 0.5 GHz to 18 GHz was proposed to reduce the size of the TSA [12]. A compact, linear TSA with a combination of a triangular slot on the left side and corrugations on the right side of the ground conductor was introduced to operate from 3.1 GHz to 11 GHz [13]. However, the frequency bandwidth was somewhat limited by the coplanar waveguide feed to a delay slotline transition. A compact sheep-horn-shaped TSA with a pair of anti-spiral-shaped structure loadings at the ends and two lumped resistors at the half path of the spirals covering a frequency band of 1.2–9.8 GHz was reported [14]. In this case, the gain of the TSA was not provided and the lumped resistors might reduce antenna gain. A pair of quarter circular slots and nonuniform corrugations were added on the sides of the ground conductor of an elliptical TSA to cover a frequency band of 3.1–10.6 GHz, but the antenna performance was similar to the TSA with the triangular slot and corrugations [15]. A miniaturized TSA with a combination of quarter circular slots and stepped structures for further size reduction was proposed to cover 2.35–11 GHz [16]. However, the frequency bandwidth might be extended by using curved structures instead of linear structures. A compact TSA using a pair of half circular slots operating in a frequency band of 4.5–50 GHz with large bandwidth was also reported, but the antenna width was quite large compared to other compact TSAs in the literature because of the circular patches appended to the upper part of the TSA [17]. Two pairs of eye-shaped slots were added on the sides of the ground conductor for designing a compact TSA with an operating frequency band ranging from 3 GHz to 12.6 GHz [18]. More pairs of slots can be used for size reduction if the ground conductor has enough space to add them. Resonant cavities consisting of an eye-shaped slot and a circular slot were introduced to the edges of the ground conductor to make a compact TSA covering 0.5–6 GHz [19]. However, gain at low-frequency regions was less than 1 dBi, so a tradeoff between the size reduction and lowest gain in the band should be considered. A miniaturized dual-layer TSA with a pair of modified exponential slots operating in the frequency range from 2.5 GHz to 11 GHz was reported, but the antenna height was doubled due to the dual-layer structure [20]. A comparison of performance and dimensions based on using either exponential slots or circular slots might need to be investigated. The slots using the third generation of Koch fractal curve with a combination of circular slots were used to make a compact TSA operating from 4.87 GHz to 11 GHz, but the Koch fractal curve-based slots would be very difficult to design in practice because

of their complex structure and time-consuming geometry calculation [21]. Hook-shaped slots were appended to the sides of the ground conductor for a compact linear TSA with a frequency band of 2.83–11.31 GHz [22]. In this case, a new design using a different taper shape and slots using the curve-based structures instead of straight line-based structures might need to be investigated for further miniaturization. Four sequentially rotated Vivaldi elements were bent into the antenna aperture for the miniaturization of the wideband directional circularly polarized antenna operating in the frequency band from 1.6 GHz to 2.9 GHz using a 1-to-4-integrated feeding network with identical amplitudes and an orthogonal phase [23]. However, the antenna height was quite large due to the bent Vivaldi structures. Four cascaded circular cavity structures based on several circular holes in tandem with different curvatures were appended on the sides of the ground conductor of a Vivaldi antenna to cover the 0.45–10 GHz frequency band, but gain at low-frequency regions was less than 0 dBi and the antenna size was very large [24].

Secondly, corrugations were inserted on the sides of the ground conductor to miniaturize the TSAs. Corrugations are a periodic arrangement of uniform or nonuniform slits (narrow rectangular, triangular, trapezoidal or arbitrary-shaped slots). They can also be used for different purposes, such as gain enhancement and radiation pattern improvement. A compact coplanar waveguide-fed TSA using three pairs of trapezoidal slots was proposed to operate on a frequency band from 3 GHz to 11.4 GHz [25]. Effects of adding more pairs of the slots on the size reduction and gain enhancement need to be investigated systematically. The miniaturization performance of rectangular, cosine, and sawtooth (triangular) corrugations added to the TSA with multi-section binomial transformers were compared for UWB applications [26]. When 42 pairs of corrugations with three different types were appended, the TSA with the rectangular corrugations showed the lowest operating frequency with a frequency band of 2.92–11.91 GHz. However, the antenna size was quite large compared to other compact TSAs in the literature. Six pairs of corrugations using slanted elliptical rectangular slots were used to miniaturize an antipodal TSA operating in the 4.5–50 GHz band, but the antenna size was also quite large [27].

Thirdly, the shape of the tapered slot was modified nonuniformly by varying the width of the tapered slot using a sinusoidal modulated Gaussian or a truncated Fourier series. A sinusoidal modulated Gaussian tapered slot with exponential slots on the ground conductor was proposed for a compact TSA operating from 2 GHz to 12 GHz [28]. A nonuniform tapered slot using a truncated Fourier series with cosine functions was introduced to design a miniaturized TSA with a frequency band of 2.9–13.55 GHz [29]. However, the tapered slot using a sinusoidal modulated Gaussian or a truncated Fourier series would also be very difficult to design in practice due to a complex structure.

To increase the gain of the miniaturized TSAs, directive materials using a parasitic metallic patch, a dielectric lens/cover with high relative permittivity, and a metamaterial loading/lens with periodic unit cells were added above the tapered slot aperture as a director [22]. Firstly, for the gain enhancement method using a parasitic metallic patch, various patch shapes, such as an elliptical, a diamond-shaped, or in multiple strips, were appended either inside the tapered slot or above the tapered slot [30–33]. Secondly, a dielectric lens/cover with different shapes, such as a half-elliptical shaped, a trapezoidal shaped, an exponential shaped, or a combination of two fan-shaped and a half-circular-shaped slots, was applied to enhance gain [34–40]. Thirdly, for a metamaterial loading/lens, different unit cell shapes, such as a meander-line, a modified split ring, a modified parallel line, or a rectangular patch, were used [41–48]. In addition to adding directive materials, methods of adding a horn structure and increasing the number of tapered slots were attempted to enhance gain of the compact TSAs. A pyramidal horn structure was combined with the TSA as an exterior surrounding structure to increase gain [49]. Two metallic plates can also be used instead of the horn structure with four plates to alleviate the cost and complexity of the fabrication [50,51]. A double-slot structure excited in uniform amplitude and phase by using a T-junction power divider was proposed to increase the gain of the TSA [52].

Meanwhile, RFID technologies, which use identification information transmitted from a tag attached to an object using electromagnetic waves to automatically recognize the attached object without contact using various frequencies, have been developed as a next-generation automatic recognition technology and have been widely used in various fields of everyday life, such as goods (asset) management, access control, food waste management, electronic passport, transportation card, highway electronic toll collection, clothing and book theft prevention, and medicine management [53,54]. To solve the problem of the high price for chip-based RFID tags, various studies have been conducted on chipless RFID tags [55]. Among the various methods realizing chipless RFID tags, a microwave resonator-based method has been actively investigated. The microwave resonator-based method can be divided into time domain, frequency domain, and hybrid methods depending on the domain in which electromagnetic wave signals are used [56,57]. Frequency domain methods can be divided into a retransmission-based method using transmitting and receiving antennas combined with resonators and a back scattering-based method using only resonators. As mentioned earlier, a compact wideband directive antenna with moderate gain is required for the retransmission-based method in order to receive the interrogation electromagnetic wave of the reader and transmit the spectral signature of the tag for identification (ID) or sensing information back to the reader [10,58].

In this paper, two design methods for a compact wideband TSA using fan-shaped and stepped structures for chipless RFID sensor tag applications were proposed. First, a miniaturization of the TSA by sequentially appending the fan-shaped structures using quarter circular slots, half circular slots, and half circular patches to the sides of the ground conductor was proposed. Next, to further miniaturize the TSA, the fan-shaped structures combined with the stepped structures were added to the sides of the ground conductor. The variations in the input reflection coefficient and gain of the TSA were systematically compared when the fan-shaped slots or patches were added at each stage during the design process. In addition, the operating characteristics of the final-designed compact wideband TSAs using the two miniaturization methods were analyzed using the surface current density distributions and radiation patterns at several frequencies in the band. The proposed compact wideband antenna with the slots combined with the fan-shaped and stepped structures was fabricated on an RF-35 substrate to compare with the simulation results. All the simulated results in this paper were obtained using CST Studio Suite (Dassault Systèmes Co., Vélizy-Villacoublay, France) [59].

2. Miniaturization Using Fan-Shaped Structures

The geometry of a compact wideband TSA using the fan-shaped structures is shown in Figure 1. On the top side of the substrate, a ground conductor consisting of an exponentially tapered slot terminated with a circular slot cavity and side slots using fan-shaped structures was printed, whereas a 50-ohm microstrip transmission line consisting of a circular termination stub and two-stage transmission lines of different widths was printed on the bottom side. An RF-35 substrate with a relative permittivity of $\varepsilon_r = 3.5$, a loss tangent of $\tan\delta = 0.0018$, and a thickness of $h = 0.76$ mm was used.

The tapered slot was designed using Equation (1). In the equation, x is the distance from the x-axis to the end of the exponential slot when the horizontal axis of the substrate is the x-axis and its origin is the center of the lower edge for the substrate. For instance, when y increases from 6 mm ($l_{off1} + 2 \times r_s$) to 36 mm (L), x increases from 0.16 mm to 5.85 mm exponentially, using the design parameters in Table 1.

$$x = \pm\left\{c_1 exp(r_1(y - (l_{off1} + 2 \times r_s))) - c_1 + \frac{w_{s1}}{2}\right\}, \ (l_{off1} + 2 \times r_s) \le y \le L \qquad (1)$$

The quarter circular slots (QCSs) with a radius of r_{g1}, the half circular slots (HCSs) with a radius of r_{g2}, the half circular patches (HCP1s) with a radius of r_{g3}, and the half circular patches (HCP2s) with a radius of r_{g4} were sequentially added on the sides of the ground conductor to miniaturize the TSA. We note that the QCSs are the fan-shaped structures

with an angle of 90°, whereas the HCSs and HCPs are the fan-shaped structures with an angle of 180°. Table 1 shows the final design parameters of the compact wideband TSA using fan-shaped structures consisting of the QCSs, HCSs, HCP1s, and HCP2s.

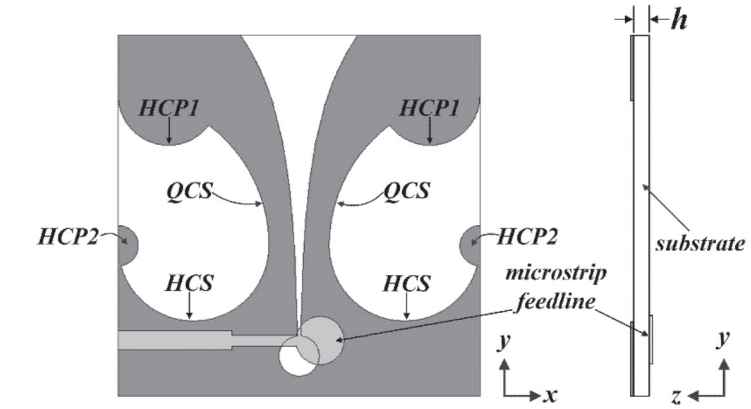

(**a**)

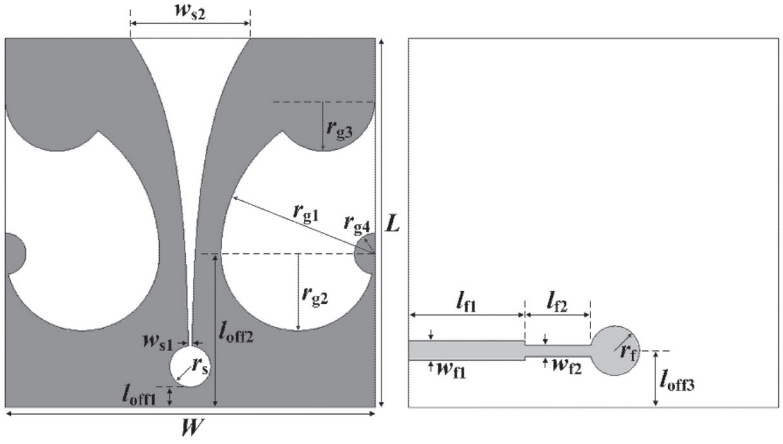

(**b**)

Figure 1. Geometries of the compact wideband TSA using fan-shaped structures (quarter circular slots (QCSs), half circular slots (HCSs), and half circular patches (HCP1s and HCP2s)): (**a**) whole structure and (**b**) top and bottom sides with design parameters.

Table 1. Design parameters of the compact wideband TSA using fan-shaped structures.

Parameter	Value (mm)	Parameter	Value (mm)
W	36	w_{f2}	1.1
L	36	r_f	2.4
w_{s1}	5	r_{g1}	16
w_{s2}	11.7	r_{g2}	8
l_{off1}	2	r_{g3}	5
l_{off2}	15	r_{g4}	2
l_{off3}	5.6	r_s	2
l_{f1}	11.3	c_1	0.17
l_{f2}	6.5	r_1	0.118
w_{f1}	1.9	h	0.76

Figure 2 shows the antenna structures considered when the QCSs, HCSs, HCP1s, and HCP2s are added sequentially during the design process of the compact wideband TSA

using the fan-shaped structures. Figure 2a is the geometry of a conventional TSA without the slots on the sides of the ground conductor, whereas Figure 2b shows the TSA with the QCSs with a radius of r_{g1} appended to the sides of the ground conductor. Figure 2c is the geometry of the TSA with the QCSs with a radius of r_{g1} and the HCSs with a radius of r_{g2}, whereas Figure 2d shows the TSA with the QCSs with a radius of r_{g1}, the HCSs with a radius of r_{g2}, and the HCP1s with a radius of r_{g3}. Figure 2e shows the final compact TSA with the QCSs with a radius of r_{g1}, the HCSs with a radius of r_{g2}, the HCP1s with a radius of r_{g3}, and the HCP2s with a radius of r_{g4}.

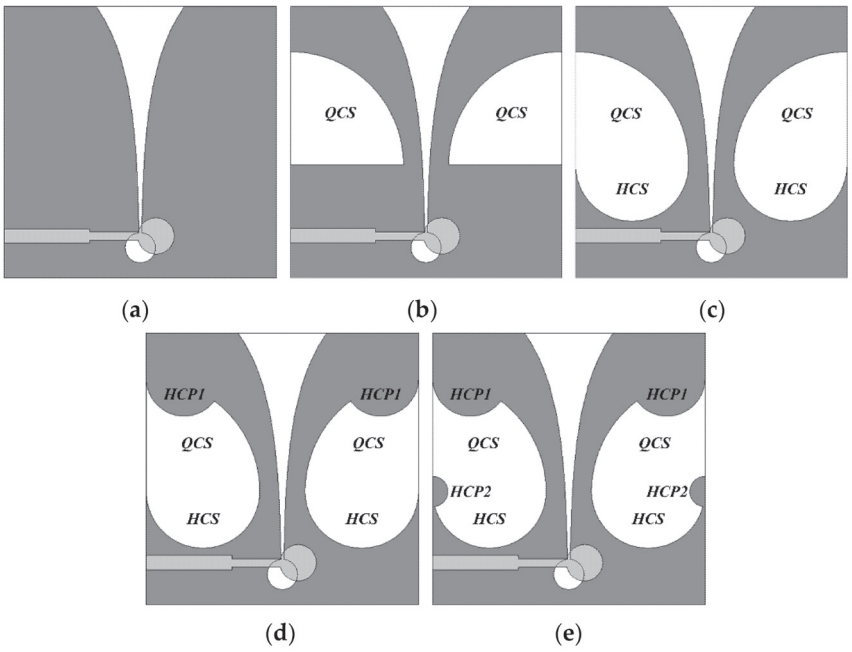

Figure 2. Design process of the compact wideband TSA using the fan-shaped structures: (**a**) conventional TSA without slots, (**b**) the TSA with the QCSs, (**c**) the TSA with the QCSs and HCSs, (**d**) the TSA with the QCSs, HCSs, and HCP1s, and (**e**) the TSA with the QCSs, HCSs, HCP1s, and HCP2s.

Figure 3 compares the input reflection coefficient and gain characteristics of the five antenna structures shown in Figure 2. In the case of the conventional TSA shown in Figure 2a without the slots on the sides of the ground conductor, the frequency band for a voltage standing wave ratio (VSWR) less than 2 was 4.157–13.670 GHz (106.7%), and gain in the band was 3.2–7.7 dBi. When the QCSs with a radius of r_{g1} = 16 mm were added to the sides of the ground conductor as shown in Figure 2b, the frequency band for a VSWR less than 2 was increased to 2.894–13.589 GHz (129.8%) and gain in the band was 4.0–8.3 dBi. Therefore, impedance bandwidth was increased by 23.1% and antenna size was reduced by 30.4%, compared to the conventional TSA in Figure 2a. Next, as the HCSs with a radius of r_{g2} = 8 mm were appended below the QCSs as shown in Figure 2c, the frequency band for a VSWR less than 2 was 2.754–13.605 GHz (132.7%), and gain in the band was 3.1–7.1 dBi. In this case, impedance bandwidth was increased by 26.0% and antenna size was reduced by 33.8%, compared to the conventional TSA. When the HCP1s with a radius of r_{g3} = 5 mm were added to the upper corners of the QCSs, as shown in Figure 2d, the frequency band for a VSWR less than 2 was 2.704–13.391 GHz (132.8%) and gain in the band was 3.1–6.8 dBi. Hence, impedance bandwidth was increased by 26.1% and antenna size was reduced by 35.0%, compared to the conventional TSA. Finally, when the HCP2s with a radius of r_{g4} = 2 mm were appended to the lower corners of the QCSs as shown in Figure 2e, the frequency band for a VSWR less than 2 was 2.530–13.379 GHz (136.4%) and gain in the band was 3.1–6.9 dBi. Therefore, impedance bandwidth of the compact wideband TSA with the QCSs, HCSs, HCP1s, and HCP2s was increased by 29.7% and antenna size was reduced by 39.1%, compared to the conventional TSA.

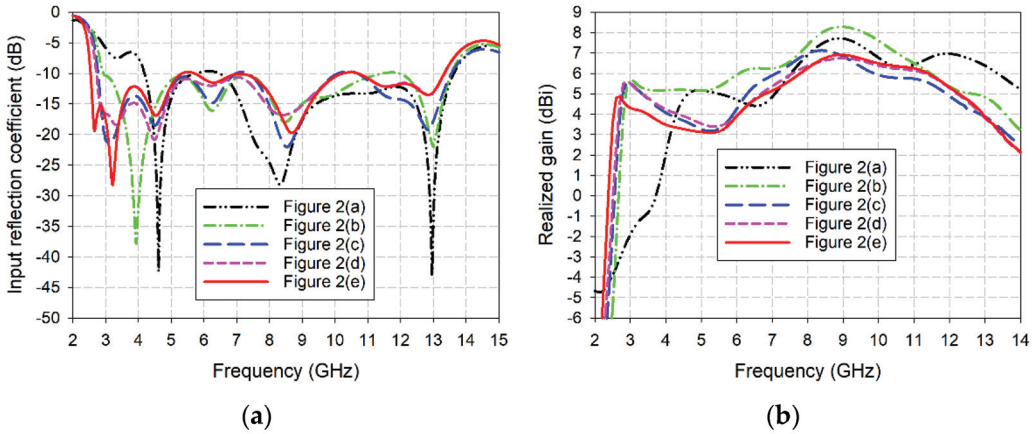

Figure 3. Performance comparison of the five antenna structures considered in the design process for the compact wideband TSA using the fan-shaped structures: (**a**) input reflection coefficient and (**b**) realized gain.

Figure 4 shows a comparison of the effects of varying the radius r_{g1} of the QCSs and the radius of r_{g3} of the HCP1s on the input reflection coefficient and realized gain characteristics of the compact wideband TSA with fan-shaped structures. For varying r_{g1}, it was varied from 14 mm to 16 mm with a step of 1 mm and other design parameters were fixed at the values in Table 1. For varying r_{g3}, it was varied from 1 mm to 5 mm with a step of 2 mm, and other design parameters were fixed at the values in Table 1. It turned out that the frequency band of the input reflection coefficient moved toward low frequency, and the bandwidth slightly increased as r_{g1} increased from 14 mm to 16 mm. However, gain in the band decreased slightly due to the effect of size reduction. For r_{g1} = 14 mm, the frequency band for a VSWR less than 2 was 2.708–13.687 GHz (133.9%), and gain in the band was 3.6–7.2 dBi. As r_{g1} increased to 15 mm, the frequency band for a VSWR less than 2 shifted toward low frequency, i.e., 2.616–13.586 GHz (135.4%), and gain in the band was 3.3–7.0 dBi. When r_{g1} increased further to 16 mm, the frequency band for a VSWR less than 2 moved further toward low frequency, i.e., 2.530–13.379 GHz (136.4%), and gain in the band was 3.1–6.9 dBi.

The effects of varying r_{g3} also showed a similar trend to the r_{g1} results with relatively smaller variations in the frequency bandwidth and gain characteristics. For r_{g3} = 1 mm, the frequency band for a VSWR less than 2 was 2.584–13.595 GHz (136.1%) with some deteriorated middle-frequency regions, and gain in the band was 2.2–7.1 dBi with reduced gain in the high-frequency region. As r_{g3} increased to 3 mm, the frequency band for a VSWR less than 2 shifted toward low frequency, i.e., 2.552–13.432 GHz (136.1%) with some deteriorated middle-frequency regions, and gain in the band was 2.6–6.8 dBi with reduced gain in the middle- and high-frequency regions. When r_{g3} increased further to 5 mm, the frequency band for a VSWR less than 2 moved further toward low frequency, i.e., 2.530–13.379 GHz (136.4%), and gain in the band was 3.1–6.9 dBi. Therefore, the value of r_{g3} needs to be carefully determined by looking at impedance matching and gain variations in the band.

Figure 5 shows the simulated surface current distributions of the compact wideband TSA using the fan-shaped structures with r_{g1} = 16 mm at 2.53 GHz, 3.1 GHz, 6 GHz, 9 GHz, and 12 GHz. The surface currents at low frequencies, such as 2.53 GHz and 3.1 GHz, were distributed on the whole structure of the TSA, including the slots on the ground conductor and the tapered slot. As the frequency increased, the surface currents were mainly distributed on the tapered slot. For high frequencies at 9 GHz and 12 GHz, the length of the tapered slot is larger than one guided wavelength at these frequencies, and the sidelobe levels were increased.

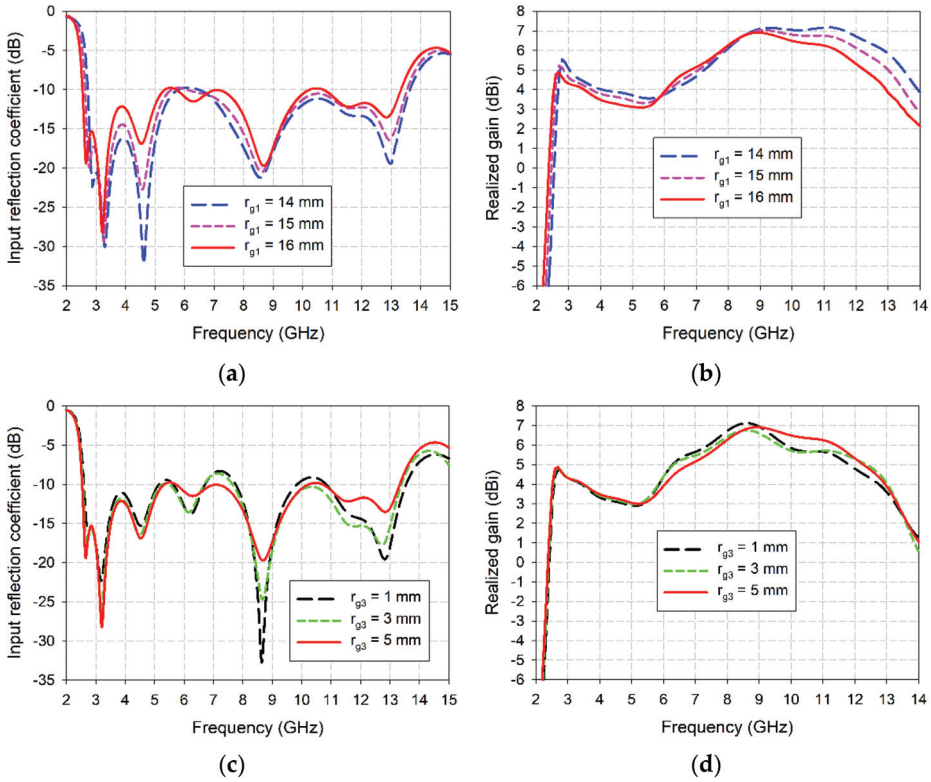

Figure 4. Effects of varying the radius r_{g1} of the QCSs and the radius r_{g3} of the HCP1s on the performance of the compact wideband TSA with fan-shaped structures: (**a**) input reflection coefficient for varying r_{g1}, (**b**) realized gain for varying r_{g1}, (**c**) input reflection coefficient for varying r_{g3}, and (**d**) realized gain for varying r_{g3}.

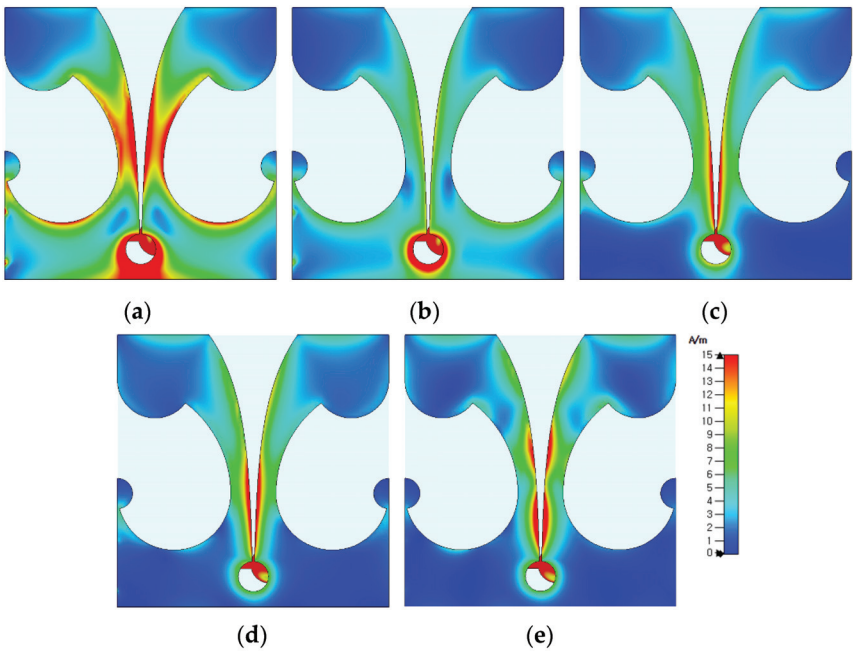

Figure 5. Surface current distributions of the compact wideband TSA using the fan-shaped structures at (**a**) 2.53 GHz, (**b**) 3.1 GHz, (**c**) 6 GHz, (**d**) 9 GHz, and (**e**) 12 GHz.

Three-dimensional radiation patterns of the compact wideband TSA using the fan-shaped structures at 2.53 GHz, 3.1 GHz, 6 GHz, 9 GHz, and 12 GHz are compared in Figure 6, whereas Figure 7 shows the co-pol. (polarization) and cross-pol. radiation

patterns on the E-plane (*x*-*y* plane) and H-plane (*y*-*z* plane) at 2.53 GHz, 3.1 GHz, 6 GHz, 9 GHz, and 12 GHz. It can be seen that the sidelobe and cross-pol. levels increased as the frequency increased.

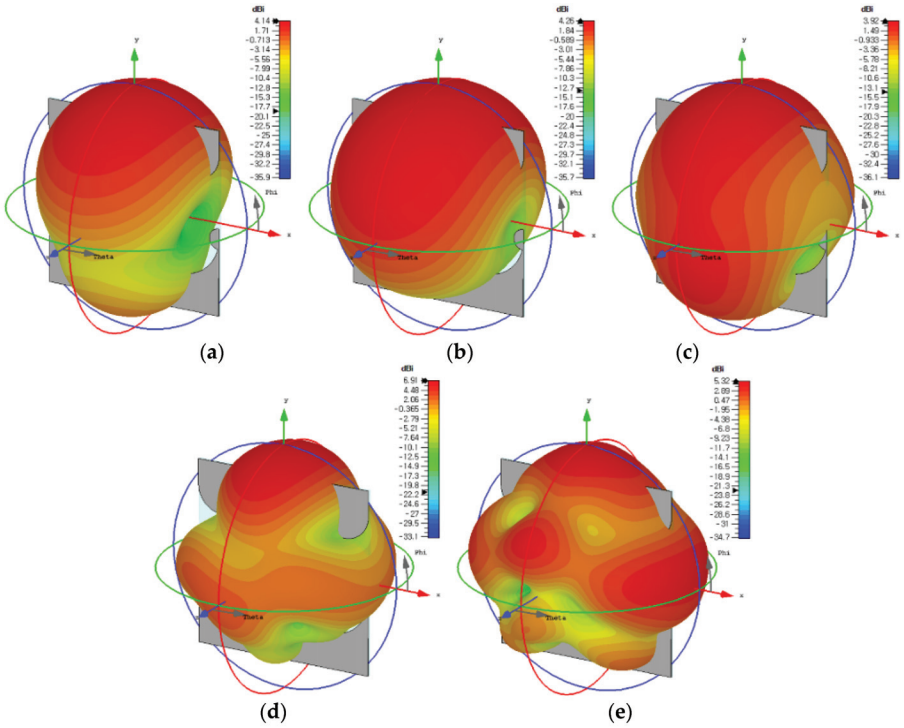

Figure 6. Three-dimensional radiation patterns of the compact wideband TSA using the fan-shaped structures at (**a**) 2.53 GHz, (**b**) 3.1 GHz, (**c**) 6 GHz, (**d**) 9 GHz, and (**e**) 12 GHz.

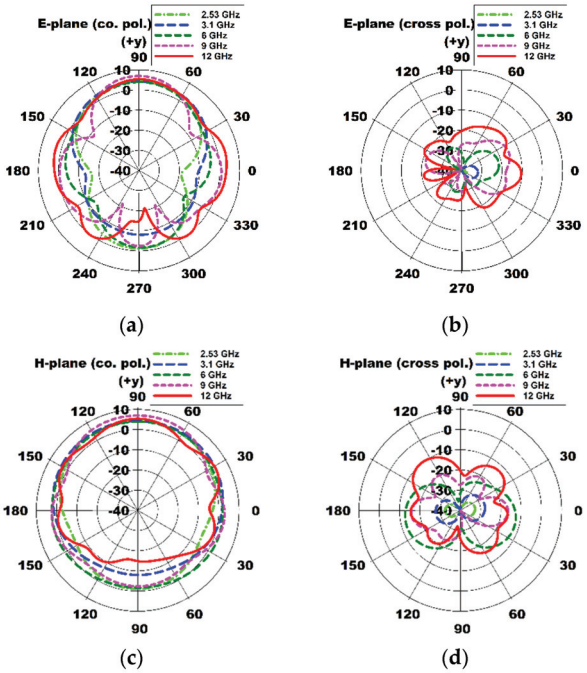

Figure 7. Comparison of E- and H-plane radiation patterns of the compact wideband TSA using the fan-shaped structures at 2.53 GHz, 3.1 GHz, 6 GHz, 9 GHz, and 12 GHz: (**a**) E-plane co-pol. (*x*-*y* plane), (**b**) E-plane cross-pol. (*x*-*y* plane), (**c**) H-plane co-pol. (*y*-*z* plane), and (**d**) H-plane cross-pol. (*y*-*z* plane).

3. Miniaturization Using Fan-Shaped and Stepped Structures

This section deals with a method of combining the fan-shaped structures and a stepped structure to further decrease the size of the TSA. An attempt to miniaturize the TSA by combining the quarter circular slots and a stepped structure has been studied in [16]. For further miniaturization, we investigated appending the half circular slots and half circular patches on the stepped structure. Figure 8 shows the geometry of the compact wideband TSA using a combination of the fan-shaped and stepped structures.

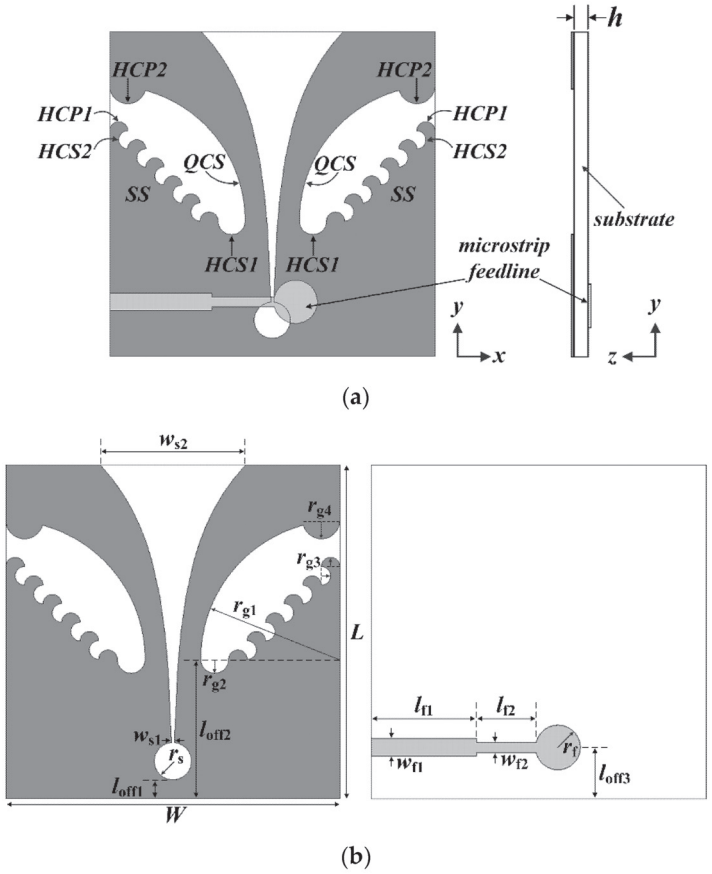

Figure 8. Geometries of the compact wideband TSA using the fan-shaped and stepped structures: (**a**) whole structure and (**b**) top and bottom sides with design parameters.

The configuration of the compact wideband TSA using the fan-shaped and stepped structures is similar to that of the compact wideband TSA using the fan-shaped structures. For the miniaturization of the TSA, the quarter circular slots (QCSs) with a radius of r_{g1}, the stepped structures (SSs) with five steps, the half circular slots (HCS1s) with a radius of r_{g2}, the half circular patches (HCP1s) and half circular slots (HCS2s) with a radius of r_{g3}, and the half circular patches (HCP2s) with a radius of r_{g4} were sequentially appended on the sides of the ground conductor. Table 2 shows the final design parameters of the compact wideband TSA using the fan-shaped and stepped structures consisting of the quarter circular slots, stepped structures, half circular slots, and half circular patches. Note that c_1 slightly increased to 0.23 compared to that of the compact wideband TSA using the fan-shaped structures.

The antenna structures considered when the QCSs, SSs, HCS1s, HCP1s, HCS2s, and HCP2s are added sequentially during the design process of the compact wideband TSA using the fan-shaped and stepped structures are shown in Figure 9. Figure 9a is the geometry of a conventional TSA without the slots on the sides of the ground conductor, whereas Figure 9b shows the TSA with the QCSs with a radius of r_{g1} appended to the sides of the ground conductor. Figure 9c is the geometry of the TSA with the QCSs with a radius

of r_{g1} and the SSs with five steps, whereas Figure 9d shows the TSA with the QCSs with a radius of r_{g1}, the SSs with five steps, the HCS1s with a radius of r_{g2}, and the HCP1s and HCS2s with a radius of r_{g3}. Figure 9e shows the final compact TSA with the QCSs with a radius of r_{g1}, the SSs with five steps, the HCS1s with a radius of r_{g2}, the HCP1s and HCS2s with a radius of r_{g3}, and the HCP2s with a radius of r_{g4}.

Table 2. Design parameters of the compact wideband TSA using the fan-shaped and stepped structures.

Parameter	Value (mm)	Parameter	Value (mm)
W	36	w_{f2}	1.1
L	36	r_f	2.4
w_{s1}	5	r_{g1}	16
w_{s2}	11.7	r_{g2}	2
l_{off1}	2	r_{g3}	1
l_{off2}	15	r_{g4}	2
l_{off3}	6.1	r_s	2
l_{f1}	11.3	c_1	0.23
l_{f2}	7	r_1	0.118
w_{f1}	1.9	h	0.76

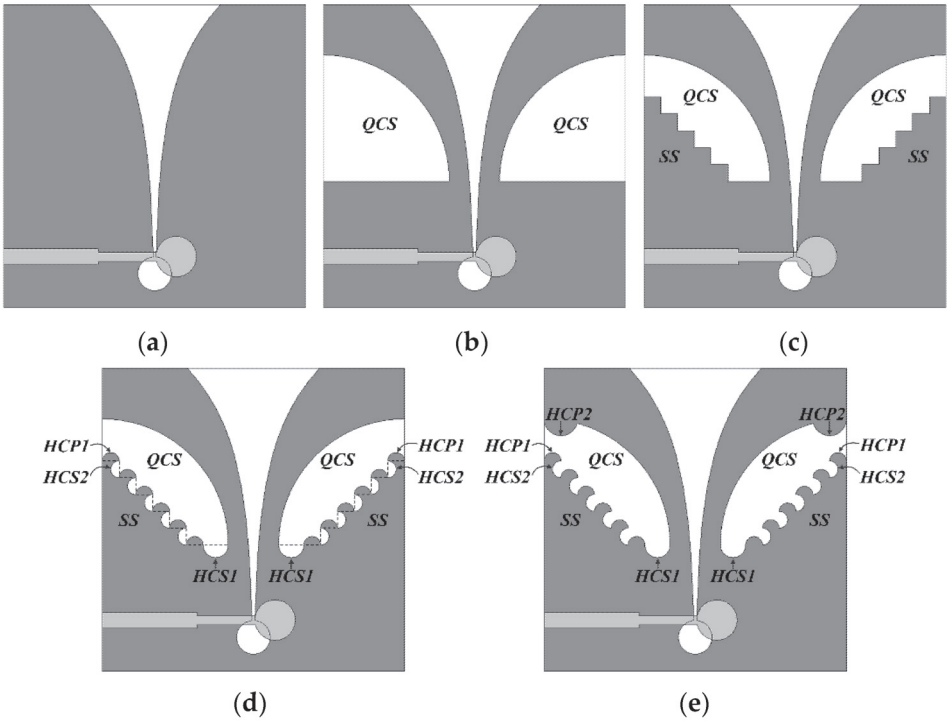

Figure 9. Design process of the compact wideband TSA using the fan-shaped and stepped structures: (**a**) conventional TSA without slots; (**b**) the TSA with the QCSs; (**c**) the TSA with the QCSs and SSs; (**d**) the TSA with the QCSs, SSs, HCS1s, HCS2s, and HCP1s; and (**e**) the TSA with the QCSs, SSs, HCS1s, HCS2s, HCP1s, and HCP2s.

The performances such as input reflection coefficient and gain characteristics of the five antenna structures shown in Figure 9 were compared in Figure 10. The frequency band of the conventional TSA in Figure 9a without the slots for a VSWR less than 2 was 4.276–13.691 GHz (104.8%), and gain in the band was 3.7–8.0 dBi. The frequency band for a VSWR less than 2 was increased to 3.178–13.711 GHz (124.7%) and gain in the band was 5.1–8.5 dBi when the QCSs with a radius of r_{g1} = 16 mm were added to the sides of the ground conductor as shown in Figure 9b. In this case, impedance bandwidth was increased by 19.9% and antenna size was reduced by 25.7%, compared to the conventional

TSA in Figure 9a. Next, as the SSs with five steps having a step length of 2 mm ($2 \times r_{g3}$) were appended in the center of the QCSs as shown in Figure 9c, the frequency band for a VSWR less than 2 was 2.483–13.671 GHz (138.5%) and gain in the band was 3.5–8.5 dBi. Hence, impedance bandwidth was increased by 33.7.0% and antenna size was reduced by 41.9%, compared to the conventional TSA. When the HCS1s with a radius of r_{g2} = 2 mm were added to the lower corners of the QCSs, and the HCP1s and HCS2s with a radius of r_{g3} = 1 mm were added in the steps of the SSs, as shown in Figure 9d, the frequency band for a VSWR less than 2 was 2.360–13.767 GHz (141.5%) and gain in the band was 3.1–8.6 dBi. In this case, impedance bandwidth was increased by 36.7% and antenna size was reduced by 44.8%, compared to the conventional TSA.

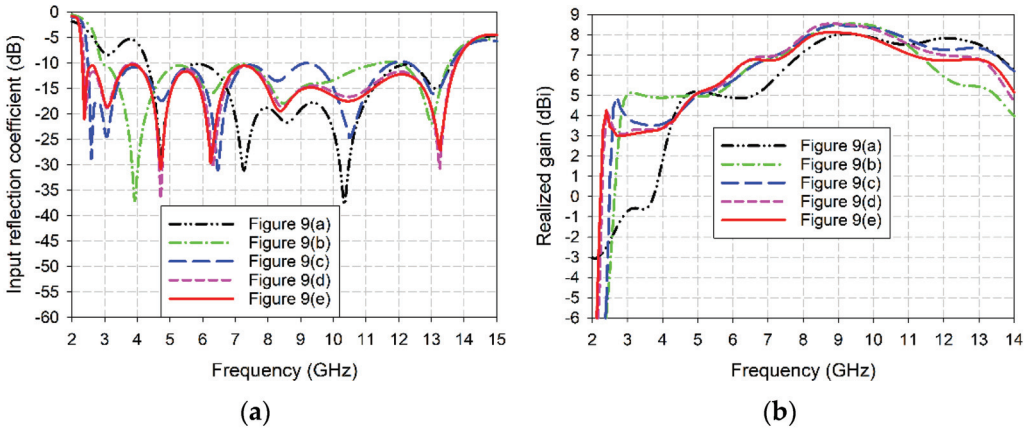

Figure 10. Performance comparison of the five antenna structures considered in the design process for the compact wideband TSA using the fan-shaped and stepped structures: (**a**) input reflection coefficient and (**b**) realized gain.

Finally, when the HCP2s with a radius of r_{g4} = 2 mm were appended to the upper corners of the QCSs as shown in Figure 9e, the frequency band for a VSWR less than 2 was 2.313–13.805 GHz (142.6%) and gain in the band was 3.0–8.1 dBi. Therefore, impedance bandwidth of the compact wideband TSA with the QCSs, SSs, HCS1s, HCP1s, HCP2s, and HCP2s was increased by 37.8% and antenna size was reduced by 45.9%, compared to the conventional TSA. In addition, when compared to the TSA with the QCSs and SSs in Figure 9c, impedance bandwidth was increased by 4.1% and antenna size was reduced by 6.9%.

Figure 11 shows the simulated surface current distributions of the compact wideband TSA using the fan-shaped and stepped structures at 2.313 GHz, 3.1 GHz, 6 GHz, 9 GHz, and 12 GHz. Similar to the compact wideband TSA using the fan-shaped structures only, the surface currents at low frequencies such as 2.313 GHz and 3.1 GHz were distributed on the whole structure of the TSA, including the slots on the ground conductor and the tapered slot. As the frequency increased, the surface currents were mainly distributed on the tapered slot.

Three-dimensional radiation patterns of the compact wideband TSA using the fan-shaped and stepped structures at 2.313 GHz, 3.1 GHz, 6 GHz, 9 GHz, and 12 GHz are compared in Figure 12. The co-pol. and cross-pol. radiation patterns in the E-plane (x-y plane) and H-plane (y-z plane) at 2.313 GHz, 3.1 GHz, 6 GHz, 9 GHz, and 12 GHz are shown in Figure 13. We note that the sidelobe levels at high frequencies such as 9 GHz and 12 GHz decreased compared to those of the compact wideband TSA using the fan-shaped structures only. It is conjectured that the ground slots using the fan-shaped and stepped structures were finished far above the feed line compared to when only the fan-shaped structures were used, and this lowered the sidelobe levels.

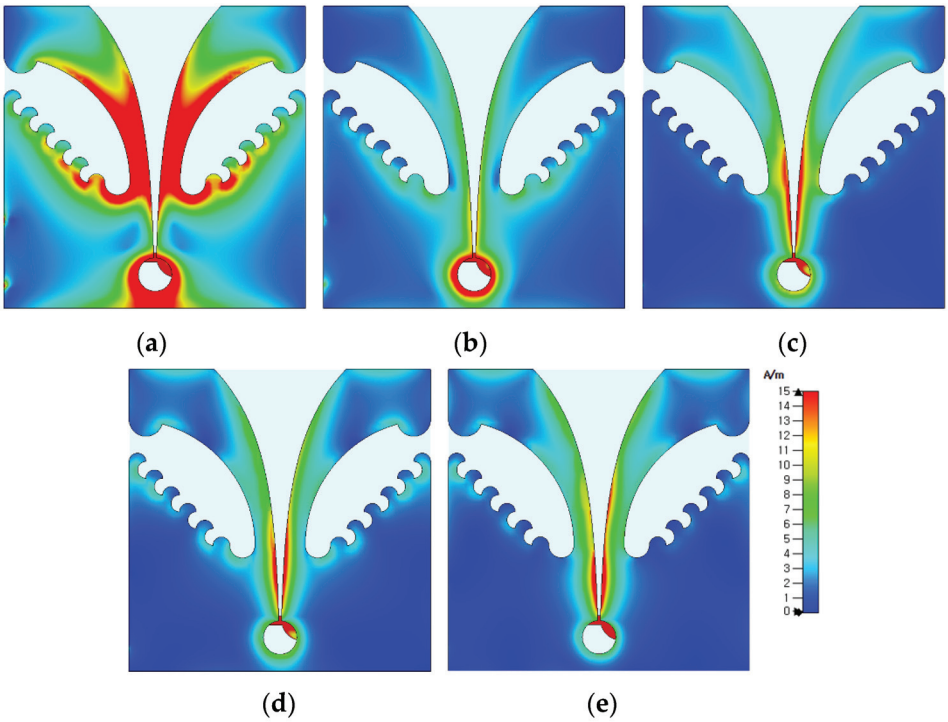

Figure 11. Comparison of the surface current distributions of the compact wideband TSA using the fan-shaped and stepped structures at (**a**) 2.313 GHz, (**b**) 3.1 GHz, (**c**) 6 GHz, (**d**) 9 GHz, and (**e**) 12 GHz.

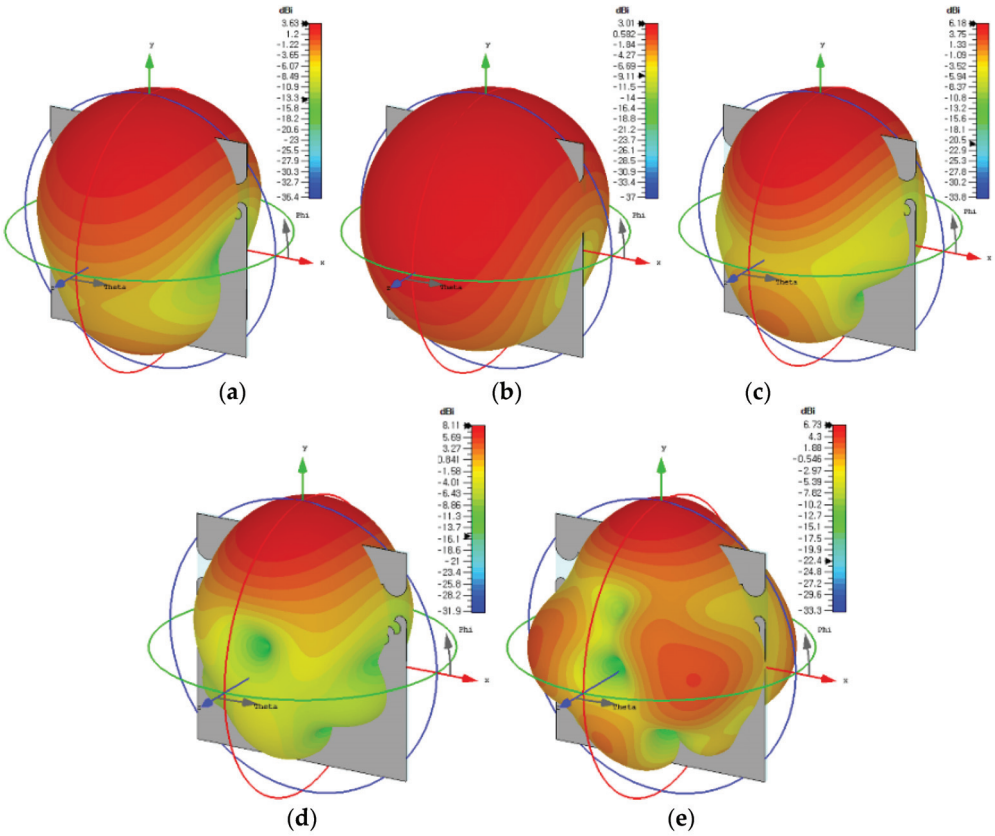

Figure 12. Three-dimensional radiation patterns of the compact wideband TSA using the fan-shaped and stepped structures at (**a**) 2.313 GHz, (**b**) 3.1 GHz, (**c**) 6 GHz, (**d**) 9 GHz, and (**e**) 12 GHz.

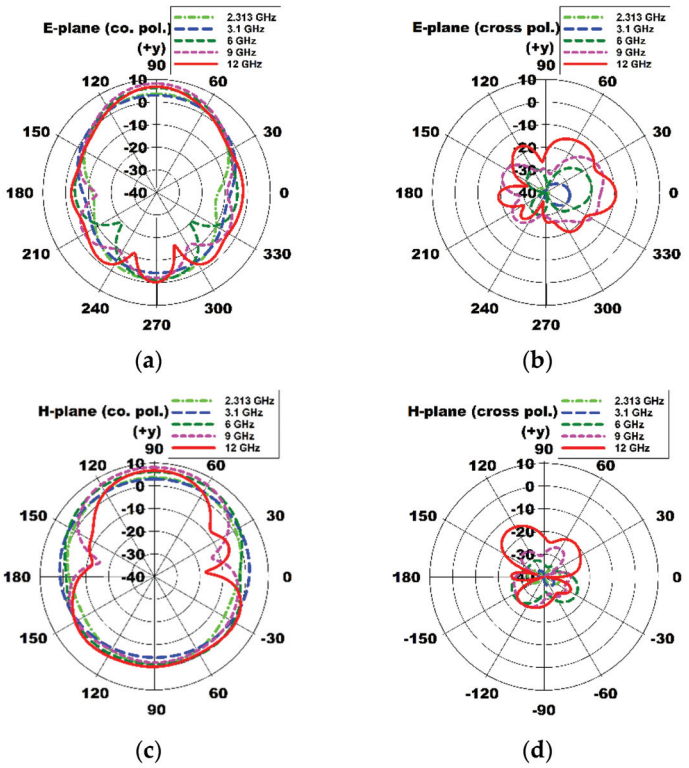

Figure 13. Comparison of E- and H-plane radiation patterns of the compact wideband TSA using the fan-shaped and stepped structures at 2.313 GHz, 3.1 GHz, 6 GHz, 9 GHz, and 12 GHz: (**a**) E-plane co-pol. (*x*-*y* plane), (**b**) E-plane cross-pol. (*x*-*y* plane), (**c**) H-plane co-pol. (*y*-*z* plane), and (**d**) H-plane cross-pol. (*y*-*z* plane).

4. Experiment Results and Discussion

A prototype of the compact wideband TSA using the fan-shaped and stepped structures was fabricated on an RF-35 substrate to validate the simulation results, as shown in Figure 14. Input reflection coefficient characteristic of the fabricated compact wideband TSA using the fan-shaped and stepped structures was measured using an Agilent N5230 (Agilent Technologies Inc., Santa Clara, CA, USA) vector network analyzer. The measured frequency band for a VSWR less than 2 was 2.320–13.745 GHz (142.2%), whereas it was 2.313–13.805 GHz (142.6%) for the simulated result, as shown in Figure 15a. The lower limit of the measured frequency band slightly increased, and the upper limit decreased. Therefore, the measured frequency band slightly decreased compared to the simulated one.

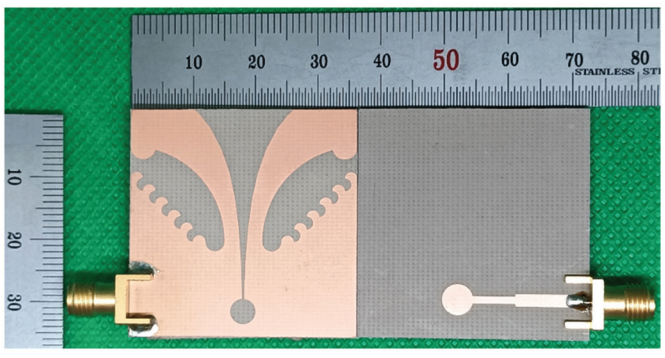

Figure 14. Photographs of the fabricated compact wideband TSA using the fan-shaped and stepped structures: (**a**) top view and (**b**) bottom view.

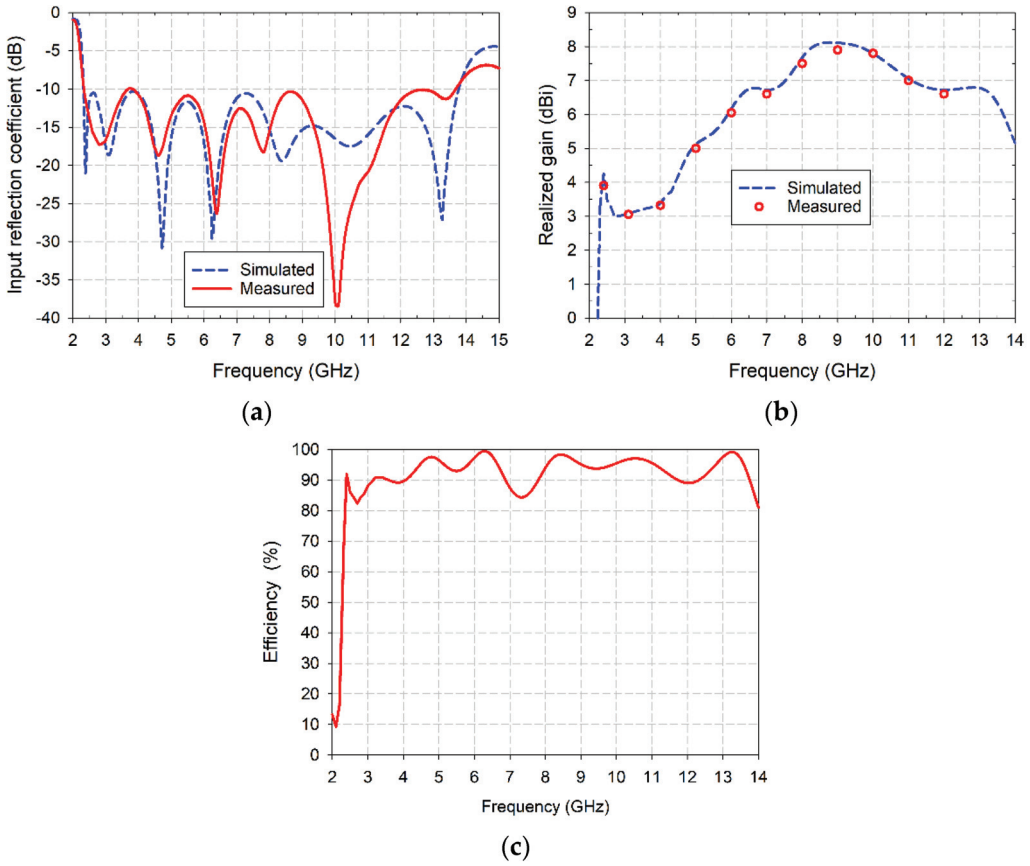

Figure 15. Measured performance of the fabricated compact wideband TSA using the fan-shaped and stepped structures: (**a**) input reflection coefficient, (**b**) realized gain, and (**c**) simulated efficiency.

Measured gain of the fabricated compact wideband TSA using the fan-shaped and stepped structures was compared in Figure 15b. It ranged from 3.1 dBi to 7.9 dBi, which is similar to the simulated one. A simulated total efficiency of the fabricated compact wideband TSA using the fan-shaped and stepped structures is plotted in Figure 15c. Total efficiency ranged from 80% to 99.5% in the band.

Figure 16 shows the comparison of the measured and simulated radiation patterns in the E- and H-planes at 2.35 GHz, 3.1 GHz, 6 GHz, 9 GHz, and 12 GHz. The measured and simulated radiation patterns agreed well with each other for both planes, but the measured cross pol. levels were increased due to the effects of the coaxial cable used for measurement. Cross pol. levels can be suppressed by using a double-layer structure instead of a single-layer one [20] or an antipodal structure with increased height.

Table 3 compares the dimensions and performances of the proposed compact wideband TSA using the fan-shaped and stepped structures with other compact wideband TSAs in the literature. Electrical dimensions of the antennas were calculated using the free-space wavelength of the lower limit frequency (λ_L) for each antenna. We can see that the frequency bandwidth of the proposed compact wideband TSA using the fan-shaped and stepped structures is the largest among the antennas except [14,17,19,24,27], but the electrical dimensions considering the lower limit frequency are smaller than these. In addition, the electrical dimensions of the proposed TSA are the smallest among the antennas except [14,16,23,29], but the lowest gain is larger compared to them. In this regard, tradeoff between the lowest gain in the band and impedance frequency bandwidth must be necessary for designing the compact TSA considering minimum antenna size. Figure 17 shows the general design procedure of the compact wideband TSA. Firstly, determine the length and width of the TSA considering minimum antenna size and substrate material. The longer the TSA's length, the lower the lowest limit frequency and the wider the fre-

quency bandwidth with increased gain. Secondly, determine a taper shape among constant width, linear, stepped, elliptical, exponential (Vivaldi), and double exponential. Thirdly, choose a proper wideband feeding structure, such as a microstrip-to-slotline transition or a coplanar waveguide-to-slotline transition. The shapes and sizes of the open conductor stub and slot cavity should be optimized for wideband operation. Fourthly, select a proper miniaturization method among an addition of the slots with various shapes to the sides of the ground conductor, an insertion of the corrugations to the sides of the ground conductor, and a modification of the shape of the tapered slot.

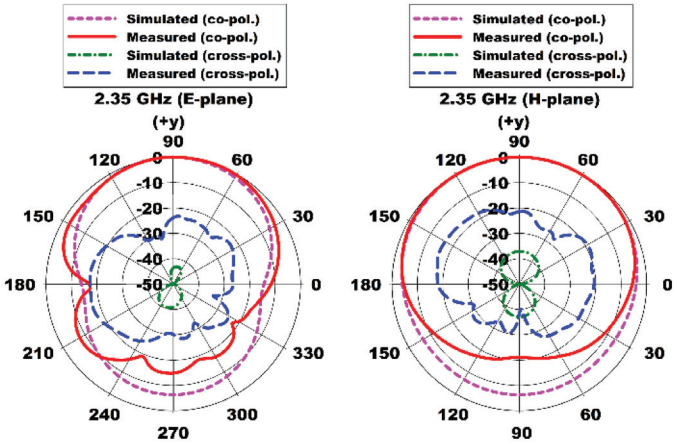

(a)

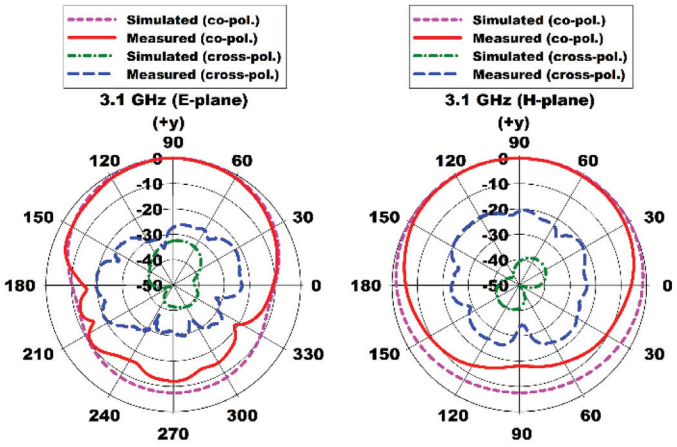

(b)

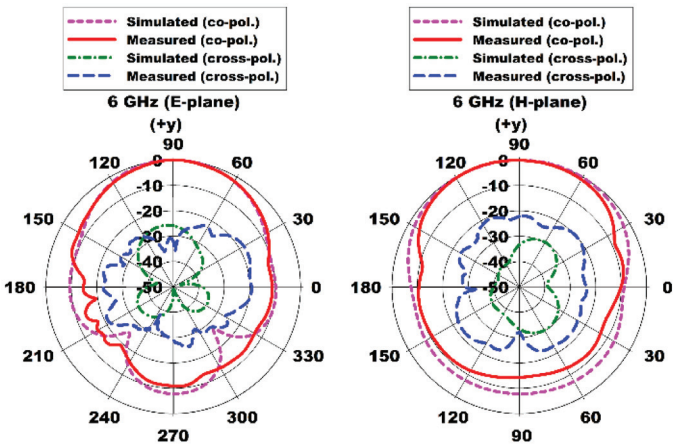

(c)

Figure 16. *Cont.*

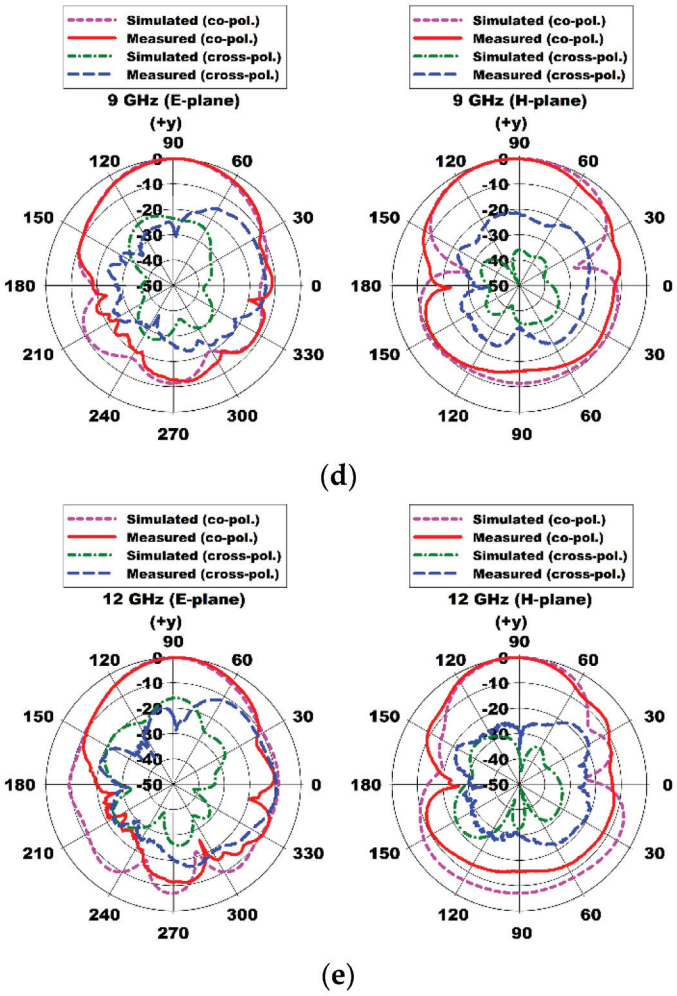

Figure 16. Measured radiation patterns in the E- and H-planes of the compact wideband TSA using the fan-shaped and stepped structures at (**a**) 2.35 GHz, (**b**) 3.1 GHz, (**c**) 6 GHz, (**d**) 9 GHz, and (**e**) 12 GHz.

Table 3. Comparison of the dimensions and performances of the compact wideband TSA using the fan-shaped and stepped structures with other compact wideband TSAs in the literature.

References	Miniaturization Methods	Physical Dimensions (mm^3)	Electrical Dimensions ($\lambda_L{}^3$)	Bandwidth for VSWR < 2 (GHz)	Gain (dBi)
[13]	Triangular slot and corrugations	35 × 36 × 0.8	0.362 × 0.372 × 0.008	3.1–10.6 (109.5%)	2–8.5
[14]	Anti-spiral shape and lumped resistors	63.5 × 53 × -	0.254 × 0.212 × -	1.2–9.8 (156.4%)	-
[15]	Quarter circular slots and nonuniform corrugations	37 × 34 × 0.8	0.382 × 0.351 × 0.008	3.1–10.6 (109.5%)	1.5–8.1
[16]	Quarter circular slots and stepped structures	36 × 30 × 1.0	0.282 × 0.235 × 0.008	2.35–11.0 (129.6%)	3.0–7.8
[17]	Half circular slots	44 × 62 × 0.254	0.66 × 0.93 × 0.004	4.5–50.0 (167.0%)	3.0–12.0
[18]	Two pairs of eye-shaped slots	36 × 36 × 0.8	0.36 × 0.36 × 0.008	3.0–12.8 (124.1%)	3.7–8.3

Table 3. *Cont.*

References	Miniaturization Methods	Physical Dimensions (mm^3)	Electrical Dimensions ($\lambda_L{}^3$)	Bandwidth for VSWR < 2 (GHz)	Gain (dBi)
[19]	Resonant cavities consisting of an eye-shaped slot and a circular slot	150 × 258 × 0.8	0.25 × 0.43 × 0.001	0.5–6.0 (169.2%)	0.8–8.0
[20]	Modified exponential slots	36 × 32 × 2	0.3 × 0.267 × 0.017	2.5–11.0 (125.9%)	3.5–8.0
[21]	Third generation of Koch fractal curves and circular slots	36 × 60 × 0.64	0.584 × 0.974 × 0.01	4.87–11.0 (77.3%)	-
[22]	Hook-shaped slots	30 × 32 × 0.8	0.283 × 0.302 × 0.008	2.83–11.31 (119.9%)	3.2–7.5
[23]	Bent Vivaldi elements	48 × 48 × 22.5	0.256 × 0.256 × 0.12	1.6–2.9 (57.8%)	1.7–5.7 (dBic)
[24]	Four cascaded circular cavity structures based on several circular holes in tandem with different curvatures	195 × 244.2 × 1.57	0.295 × 0.366 × 0.0024	0.45–10 (182.8%)	−1–10.8
[25]	Corrugations using three pairs of trapezoidal slots	35 × 30 × 1	0.35 × 0.3 × 0.01	3.0–11.4 (116.7%)	3.0–7.4
[26]	42 pairs of rectangular corrugations	50 × 100 × 0.8	0.487 × 0.973 × 0.008	2.92–11.91 (121.2%)	3.9–10.5
[27]	6 pairs of corrugations using slanted elliptical rectangular slots	30 × 40 × 0.51	0.45 × 0.6 × 0.008	4.5–50 (167.0%)	3.0–10.0
[28]	Sinusoidal modulated Gaussian tapered slot	50 × 56 × 0.8	0.333 × 0.373 × 0.005	2.0–12.0 (142.9%)	1.5–5.2
[29]	Nonuniform tapered slot using a truncated Fourier series with cosine functions	30 × 20.3 × 0.8	0.288 × 0.196 × 0.008	2.9–13.55 (129.5%)	1.8–6.9
This Work	Fan-shaped and stepped structures	36 × 36 × 0.76	0.278 × 0.278 × 0.006	2.320–13.745 (142.2%)	3.1–7.9

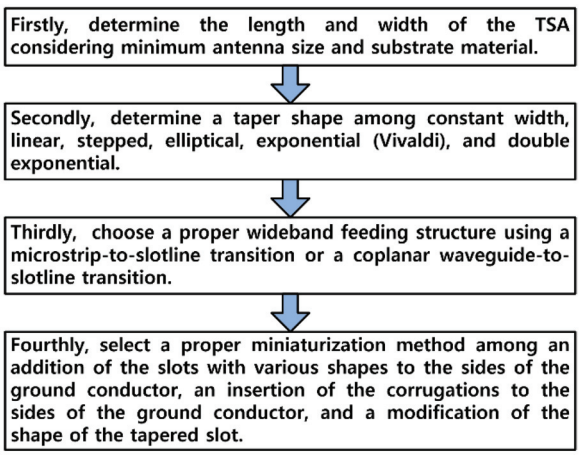

Figure 17. General design procedure of compact wideband TSA.

5. Conclusions

We proposed two miniaturization methods for a compact wideband TSA either using the fan-shaped structures only or using a combination of the fan-shaped and stepped structures. The first miniaturization method was an addition of the fan-shaped structures to the sides of the ground conductor of the TSA. The quarter circular slots, the half circular slots, and the half circular patches were sequentially appended to the sides of the ground conductor, and their effects on the input reflection coefficient and gain characteristics of the TSA were compared. The frequency band of the compact wideband TSA with the fan-shaped structures using the QCSs, HCSs, HCP1s, and HCP2s for a VSWR less than 2 was 2.530–13.379 GHz (136.4%) and gain in the band was 3.1–6.9 dBi. In this case, impedance bandwidth was increased by 29.7% and antenna size was reduced by 39.1%, compared to the conventional TSA. The second miniaturization method to further reduce the antenna size was a combination of the fan-shaped and stepped structures. Similar to the first miniaturization method, the quarter circular slots, the stepped structures, the half circular slots, and the half circular patches were sequentially appended to the sides of the ground conductor, and their effects on the input reflection coefficient and gain characteristics of the TSA were compared. The frequency band of the compact wideband TSA with the fan-shaped and stepped structures using the QCSs, SSs, HCS1s, HCP1s, HCP2s, and HCP2s for a VSWR less than 2 was 2.313–13.805 GHz (142.6%) and gain in the band was 3.0–8.1 dBi. Impedance bandwidth was increased by 37.8% and antenna size was reduced by 45.9%, compared to the conventional TSA. The operating characteristics of the compact wideband TSAs using the two miniaturization methods were also analyzed using the surface current density distributions and radiation patterns at several frequencies in the band. It turned out that the sidelobe levels at high frequencies such as 9 GHz and 12 GHz of the compact wideband TSA with the second miniaturization method using the fan-shaped and stepped structures decreased compared to those of the compact wideband TSA with the first miniaturization method using the fan-shaped structures only.

A prototype of the compact wideband TSA using the fan-shaped and stepped structures was fabricated on an RF-35 substrate to validate the simulation results. The measured frequency band for a VSWR less than 2 was 2.320–13.745 GHz (142.2%), and the measured frequency band slightly decreased compared to the simulated result. Measured gain ranged from 3.1 dBi to 7.9 dBi, which is similar to the simulated one. The measured and simulated radiation patterns agreed well with each other for both E- and H-planes.

The proposed compact wideband TSAs using the fan-shaped and stepped structures can be used for designing compact wideband directive antennas for retransmission-based chipless RFID sensor tag applications in real-life scenarios. They might also be used for UWB radar and imaging applications, such as the through-wall human detection and identification of movements, human vital signal monitoring, and breast cancer detection imaging system.

As part of future work, we plan to study a new method with a wider bandwidth and miniaturization rate by combining the various miniaturization methods analyzed in this paper.

Author Contributions: J.Y. contributed the idea, the simulation, the analysis, and the overall research. J.-I.L. contributed fabrications and measurements. All authors have read and agreed to the published version of the manuscript.

Funding: This research was supported by Daegu University Research Grant 2020.

Institutional Review Board Statement: Not applicable.

Informed Consent Statement: Not applicable.

Data Availability Statement: Data are contained within the article.

Conflicts of Interest: The authors declare no conflicts of interest.

References

1. Jabbar, A.; Jamshed, M.A.; Shawky, M.A.; Abbasi, Q.H.; Imran, M.A.; Rehman, M.U. Multi-gigabit millimeter-wave industrial communication: A solution for industry 4.0 and beyond. In Proceedings of the GLOBECOM 2022—2022 IEEE Global Communications Conference, Rio de Janeiro, Brazil, 4–8 December 2022; pp. 5001–5006.
2. Turab, M.; Jamil, S. A comprehensive survey of digital twins in healthcare in the era of metaverse. *BioMedInformatics* **2023**, *3*, 563–584. [CrossRef]
3. Schantz, H. *The Art and Science of Ultra-Wideband Antennas*; Artech House: Norwood, MA, USA, 2005; pp. 30–32.
4. Denidni, T.A.; Augustin, G. *Ultrawideband Antennas for Microwave Imaging Systems*; Artech House: Norwood, MA, USA, 2014; pp. 45–47.
5. Waterhouse, R. *Printed Antennas for Wireless Communications*; John Wiley & Sons Ltd.: Chichester, UK, 2007; pp. 162–165.
6. Eberle, J.; Levis, C.; McCoy, D. The flared slot: A moderately directive flush-mounted broad-band antenna. *IRE Trans. Antennas Propag.* **1960**, *8*, 461–468. [CrossRef]
7. Gibson, P.J. The Vivaldi aerial. In Proceedings of the 9th European Microwave Conference, Brighton, UK, 17–21 September 1979; pp. 101–105.
8. Wu, B.; Ji, Y.; Fang, G. Design and measurement of compact tapered slot antenna for UWB microwave imaging radar. In Proceedings of the 2009 9th International Conference on Electronic Measurement & Instruments, Beijing, China, 16–19 August 2009; pp. 2226–2229.
9. Yadav, A.; Kumar Singh, V.; Kumar Bhoi, A.; Marques, G.; Garcia-Zapirain, B.; de la Torre Díez, I. Wireless body area networks: UWB wearable textile antenna for telemedicine and mobile health systems. *Micromachines* **2020**, *11*, 558. [CrossRef] [PubMed]
10. Ashraf, M.A.; Alshoudokhi, Y.A.; Behairy, H.M.; Alshareef, M.R.; Alshebeili, S.A.; Issa, K.; Fathallah, H. Design and analysis of multi-resonators loaded broadband antipodal tapered slot antenna for chipless RFID applications. *IEEE Access* **2017**, *5*, 25798–25807. [CrossRef]
11. Saleh, S.; Jamaluddin, M.H.; Razzaz, F.; Saeed, S.M.; Timmons, N.; Morrison, J. Compactness and performance enhancement techniques of ultra-wideband tapered slot antenna: A comprehensive review. *Alex. Eng. J.* **2023**, *74*, 195–229. [CrossRef]
12. Lee, J.J.; Livingston, S. Wide band bunny-ear radiating element. In Proceedings of the IEEE Antennas and Propagation Society International Symposium, Ann Arbor, MI, USA, 28 June–2 July 1993; pp. 1604–1607.
13. Zhu, F.; Gao, S.; Ho, A.; Chan, H.; Alhameed, R.A.; Li, J.; Xu, J. Compact-size linearly tapered slot antenna for portable ultra-wideband imaging systems. *Int. J. RF Microw. Comput. Aided Eng.* **2013**, *23*, 290–299. [CrossRef]
14. Li, X.-P.; Xu, G.; Duan, C.-J.; Ma, M.-R.; Shi, S.-E.; Li, W. Compact TSA with anti-spiral shape and lumped resistors for UWB applications. *Micromachines* **2021**, *12*, 1029. [CrossRef] [PubMed]
15. Zhu, F.; Gao, S. Compact elliptically tapered slot antenna with nonuniform corrugations for ultra-wideband applications. *Radioengineering* **2013**, *22*, 276–280.
16. Geng, D.; Yang, D.; Xiao, H.; Chen, Y.; Pan, J. A novel miniaturized Vivaldi antenna for ultra-wideband applications. *Prog. Electromagn. Res. C* **2017**, *77*, 123–131. [CrossRef]
17. Bai, J.; Shi, S.; Prather, D.W. Modified compact antipodal Vivaldi antenna for 4–50-GHz UWB application. *IEEE Trans. Microw. Theory Tech.* **2011**, *59*, 1051–1057. [CrossRef]
18. Ma, K.; Zhao, Z.; Wu, J.; Ellis, S.M.; Nie, Z.P. A printed Vivaldi antenna with improved radiation patterns by using two pairs of eye-shaped slots for UWB applications. *Prog. Electromagn. Res.* **2014**, *148*, 63–71. [CrossRef]
19. Liu, Y.; Zhou, W.; Yang, S.; Li, W.; Li, P.; Yang, S. A novel miniaturized Vivaldi antenna using tapered slot edge with resonant cavity structure for ultrawideband applications. *IEEE Antennas Wirel. Propag. Lett.* **2016**, *15*, 1881–1884. [CrossRef]
20. Yang, D.; Liu, S.; Geng, D. A miniaturized ultra-wideband Vivaldi antenna with low cross polarization. *IEEE Access* **2017**, *5*, 23352–23357. [CrossRef]
21. de Oliveira, A.M.; Justo, J.F.; Perotoni, M.B.; Kofuji, S.T.; Neto, A.G.; Bueno, R.C.; Baudrand, H. A high directive Koch fractal Vivaldi antenna design for medical near-field microwave imaging applications. *Microw. Opt. Technol. Lett.* **2017**, *59*, 337–346. [CrossRef]
22. Yeo, J. Compact, gain-enhanced, linearly tapered slot antenna with a combined director using a strip director and double-sided metamaterial loading for UWB applications. *Prog. Electromagn. Res. C* **2022**, *127*, 263–277. [CrossRef]
23. Liu, X.; Zhu, Y.; Xie, W. A miniaturized wideband directional circularly polarized antenna based on bent Vivaldi antenna structure. *IEEE Antennas Wirel. Propag. Lett.* **2023**, *22*, 298–302. [CrossRef]
24. Hossain, A.; Pham, A.V. A novel gain-enhanced miniaturized and lightweight Vivaldi antenna. *IEEE Trans. Antennas Propag.* **2023**, *71*, 9431–9439. [CrossRef]
25. Fei, P.; Jiao, Y.C.; Ding, Y.; Zhang, F.S. A compact coplanar waveguide fed wide tapered slot ultra-wideband antenna. *Prog. Electromagn. Res.* **2011**, *25*, 77–85. [CrossRef]
26. Chareonsiri, Y.; Thaiwirot, W.; Akkaraekthalin, P. Design of ultra-wideband tapered slot antenna by using binomial impedance transformer. *Frequenz* **2017**, *71*, 251–260. [CrossRef]
27. Liu, J.; Xu, C.; Yu, H.; Su, J. Design of a miniaturized ultrawideband and low scattering antipodal vivaldi antenna array. *Sci. Rep.* **2021**, *11*, 12499. [CrossRef]
28. Pandey, G.; Verma, H.; Meshram, M. Compact antipodal Vivaldi antenna for UWB applications. *Electron. Lett.* **2015**, *51*, 308–310. [CrossRef]

29. Saleh, S.; Ismail, W.; Abidin, I.S.Z.; Bataineh, M.H.; Alzoubi, A.S. Novel Compact UWB vivaldi non-uniform slot antenna with enhanced bandwidth. *IEEE Trans. Antennas Propag.* **2022**, *70*, 6592–6603. [CrossRef]
30. Nassar, I.T.; Weller, T.M. A novel method for improving antipodal Vivaldi antenna performance. *IEEE Trans. Antennas Propag.* **2015**, *63*, 3321–3324. [CrossRef]
31. Samsuzzaman, M.; Islam, M.T.; Shovon, A.A.S.; Faruque, R.I.; Misran, N. A 16-modified antipodal Vivaldi antenna array for microwave-based breast tumor imaging applications. *Microw. Opt. Technol. Lett.* **2019**, *61*, 2110–2118. [CrossRef]
32. Li, Z.; Kang, X.; Su, J.; Guo, Q.; Yang, Y.; Wang, J. A wideband end-fire conformal Vivaldi antenna array mounted on a dielectric cone. *Int. J. Antennas Propag.* **2016**, *2016*, 9812642. [CrossRef]
33. Gao, C.; Li, E.; Zhang, Y.; Guo, G. A directivity enhanced structure for the Vivaldi antenna using coupling patches. *Microw. Opt. Technol. Lett.* **2018**, *60*, 418–424. [CrossRef]
34. Bourqui, J.; Okoniewski, M.; Fear, E.C. Balanced antipodal Vivaldi antenna with dielectric director for near-field microwave imaging. *IEEE Trans. Antennas Propag.* **2010**, *58*, 2318–2326. [CrossRef]
35. Molaei, A.; Kaboli, M.; Abrishamian, M.S.; Mirtaheri, S.A. Dielectric lens balanced antipodal Vivaldi antenna with low cross-polarisation for ultra-wideband applications. *IET Microw. Antennas Propag.* **2014**, *8*, 1137–1142. [CrossRef]
36. Moosazadeh, M.; Kharkovsky, S.; Case, J.T.; Samali, B. Miniaturized UWB antipodal Vivaldi antenna and its application for detection of void inside concrete specimens. *IEEE Antennas Wirel. Propag. Lett.* **2017**, *16*, 1317–1320. [CrossRef]
37. Moosazadeh, M.; Kharkovsky, S. A compact high-gain and front-to-back ratio elliptically tapered antipodal Vivaldi antenna with trapezoid-shaped dielectric lens. *IEEE Antennas Wirel. Propag. Lett.* **2016**, *15*, 552–555. [CrossRef]
38. Amiri, M.; Tofigh, F.; Ghafoorzadeh-Yazdi, A.; Abolhasan, M. Exponential antipodal Vivaldi antenna with exponential dielectric lens. *IEEE Antennas Wirel. Propag. Lett.* **2017**, *16*, 1792–1795. [CrossRef]
39. Huang, D.; Yang, H.; Wu, Y.; Zhao, F.; Liu, X. A high-gain antipodal Vivaldi antenna with multi-layer planar dielectric lens. *J. Electromagn. Waves Appl.* **2017**, *32*, 403–412. [CrossRef]
40. Li, X.X.; Pang, D.W.; Wang, H.L.; Zhang, Y.M.; Lv, G.Q. Dielectric slabs covered broadband Vivaldi antenna for gain enhancement. *Prog. Electromagn. Res. C* **2017**, *77*, 69–80. [CrossRef]
41. Zhou, B.; Cui, T.J. Directivity enhancement to Vivaldi antennas using compactly anisotropic zero-index metamaterials. *IEEE Antennas Wirel. Propag. Lett.* **2011**, *10*, 326–329. [CrossRef]
42. Pandey, G.K.; Singh, H.S.; Meshram, M.K. Meander-line-based inhomogeneous anisotropic artificial material for gain enhancement of UWB Vivaldi antenna. *Appl. Phys. A* **2016**, *122*, 134. [CrossRef]
43. Boujemaa, M.A.; Herzi, R.; Choubani, F.; Gharsallah, A. UWB antipodal Vivaldi antenna with higher radiation performances using metamaterials. *Appl. Phys. A* **2018**, *124*, 714. [CrossRef]
44. Zhu, S.; Liu, H.; Wen, P.; Du, L.; Zhou, J. A miniaturized and high gain double-slot Vivaldi antenna using wideband index-near-zero metasurface. *IEEE Access* **2018**, *6*, 72015–72024. [CrossRef]
45. Islam, M.T.; Samsuzzaman, M.; Kibria, S.; Misran, N.; Islam, M.T. Metasurface loaded, high gain antenna based microwave imaging using iteratively corrected delay multiply and sum algorithm. *Sci. Rep.* **2019**, *9*, 17317. [CrossRef] [PubMed]
46. Chen, L.; Lei, Z.; Yang, R.; Fan, J.; Shi, X. A broadband artificial material for gain enhancement of antipodal tapered slot antenna. *IEEE Trans. Antennas Propag.* **2015**, *63*, 395–400. [CrossRef]
47. Li, X.X.; Liu, G.; Zhang, Y.; Sang, L.; Lv, G. A compact multi-layer phase correcting lens to improve directive radiation of Vivaldi antenna. *Int. J. RF Microw. Comput. Aided Eng.* **2017**, *27*, e21109. [CrossRef]
48. Li, X.; Zhou, H.; Gao, Z.; Wang, H.; Lv, G. Metamaterial slabs covered UWB antipodal Vivaldi antenna. *IEEE Antennas Wirel. Propag. Lett.* **2017**, *16*, 2943–2946. [CrossRef]
49. Lim, T.H.; Park, J.E.; Choo, H. Design of a Vivaldi-fed hybrid horn antenna for low-frequency gain enhancement. *IEEE Trans. Antennas Propag.* **2018**, *66*, 438–443. [CrossRef]
50. Boas, E.C.V.; Ferrero, M.A.S.; Nasri, A.; Mittra, R.; Sodré, A.C. 31 dBi-gain slotted waveguide antenna array using wing-based reflectors. *IEEE Access* **2022**, *10*, 57327–57338. [CrossRef]
51. Yeo, J.; Lee, J.-I. Gain enhancement of microstrip patch array antennas using two metallic plates for 24 GHz radar applications. *Electronics* **2023**, *12*, 1512. [CrossRef]
52. Wang, Y.W.; Wang, G.M.; Zong, B.F. Directivity improvement of Vivaldi antenna using double-slot structure. *IEEE Antennas Wirel. Propag. Lett.* **2013**, *12*, 1380–1383. [CrossRef]
53. Finkenzeller, K. *RFID Handbook: Fundamentals and Applications in Contactless Smart Cards, Radio Frequency Identification and Near-Field Communication*, 3rd ed.; Wiley-Blackwell: Hoboken, NJ, USA, 2010.
54. Where Do You Find RFID Technology in Everyday Life? Available online: https://www.trace-id.com/where-do-you-find-rfidtechnology-in-everyday-life/ (accessed on 1 May 2024).
55. Athauda, T.; Karmakar, N. Chipped versus chipless RF identification: A comprehensive review. *IEEE Microw. Mag.* **2019**, *20*, 47–57. [CrossRef]
56. Herrojo, C.; Paredes, F.; Mata-Contreras, J.; Martín, F. Chipless-RFID: A review and recent developments. *Sensors* **2019**, *19*, 3385. [CrossRef] [PubMed]
57. Yeo, J.; Lee, J.-I.; Kwon, Y. Humidity-sensing chipless RFID tag with enhanced sensitivity using an interdigital capacitor structure. *Sensors* **2021**, *21*, 6550. [CrossRef]

58. Jha, A.K.; Akhter, Z.; Tiwari, N.; Muhammed Shafi, K.T.; Samant, H.; Jaleel Akhtar, M.; Cifra, M. Broadband wireless sensing system for non-invasive testing of biological samples. *IEEE J. Emerg. Sel. Top. Circuits Syst.* **2018**, *8*, 251–259. [CrossRef]
59. Electromagnetic Simulation Solvers, CST Studio Suite. Available online: https://www.3ds.com/products-services/simulia/products/cst-studio-suite/solvers/ (accessed on 1 May 2024).

sensors

MDPI

Article

Triple-Band Reconfigurable Monopole Antenna for Long-Range IoT Applications

Muhammad Sani Yahya [1,2,*], Socheatra Soeung [1], Narinderjit Singh Sawaran Singh [3], Zainab Yunusa [4], Francis Emmanuel Chinda [1], Sharul Kamal Abdul Rahim [5], Umar Musa [6], Nursyarizal B. M. Nor [1], Cheab Sovuthy [7] and Ghulam E. Mustafa Abro [1]

[1] Department of Electrical and Electronic Engineering, Universiti Teknologi PETRONAS, Bandar Seri Iskandar 32610, Perak, Malaysia
[2] Department of Electrical and Electronic Engineering, Abubakar Tafawa Balewa University, Bauchi 740272, Nigeria
[3] Faculty of Data Science and Information Technology (FDSIT), INTI International University, Persiaran Perdana BBN, Putra Nilai, Nilai 71800, Negeri Sembilan, Malaysia; narinderjits.sawaran@newinti.edu.my
[4] Department of Electrical Engineering, University of Hafr Al Batin, Hafr Al Batin 39524, Saudi Arabia
[5] Wireless Communication Centre, Universiti Teknologi Malaysia, Skudai 81310, Johor, Malaysia
[6] Faculty of Electrical and Electronic Engineering, University Tun Hussein Onn, Parit Raja 86400, Johor, Malaysia
[7] FILPAL (M) Sdn. Bhd., Bayan Lepas, George Town 11900, Penang, Malaysia
* Correspondence: muhammad_22000359@utp.edu.my

Abstract: In this study, a novel reconfigurable triple-band monopole antenna for LoRa IoT applications is fabricated on an FR-4 substrate. The proposed antenna is designed to function at three distinct LoRa frequency bands: 433 MHz, 868 MHz, and 915 MHz covering the LoRa bands in Europe, America, and Asia. The antenna is reconfigurable by using a PIN diode switching mechanism, which allows for the selection of the desired operating frequency band based on the state of the diodes. The antenna is designed using CST MWS® software 2019 and optimized for maximum gain, good radiation pattern and efficiency. The antenna with a total dimension of 80 mm × 50 mm × 0.6 mm ($0.12\lambda_0 \times 0.07\lambda_0 \times 0.001\lambda_0$ at 433 MHz) has a gain of 2 dBi, 1.9 dBi, and 1.9 dBi at 433 MHz, 868 MHz, and 915 MHz, respectively, with an omnidirectional H-plane radiation pattern and a radiation efficiency above 90% across the three frequency bands. The fabrication and measurement of the antenna have been carried out, and the results of simulation and measurements are compared. The agreement among the simulation and measurement results confirms the design's accuracy and the antenna's suitability for LoRa IoT applications, particularly in providing a compact, flexible , and energy efficient communication solution for different LoRa frequency bands.

Keywords: antenna; energy efficiency; IoT; LoRa; monopole; PIN diode; reconfigurable

1. Introduction

The Internet of Things (IoT) is a fast-growing network that globally interconnects objects, supporting various input/output devices, actuators, and sensors for real-time data collection, control, analysis, and sharing using standard communication protocols. The IoT has had a great influence on our daily lives and has evolved from machine-to-machine communication to connecting people, objects, data, and services. It is considered a key enabler of Cyberphysical Systems (CPSs), which use IoT to link the physical and virtual worlds [1].

One of the critical challenges in IoT is developing communication protocols that meet the energy efficiency, wide signal coverage, energy conservation, affordability, and prolonged battery duration requirements of IoT devices. Low-Power Wide-Area Network (LPWAN) technology is a solution that meets these requirements and has LoRa as one of its

major contenders. LoRa is a patented radio modulation technology that utilizes unlicensed frequency bands below 1 GHz and is suitable for IoT applications because of its availability globally and lower cost. The aim of LoRa is to enable IoT devices to communicate over long ranges with improved network capacity, secured data transmission, reduced device cost, and low power consumption [2–6].

Owing to regulatory requirements, the operating frequency bands for LoRa in the ISM bands differ according to regions and countries. For example, within the band of 410–441 MHz in China, about 32 channels were defined for LoRa applications [7]. In Europe, the designated frequencies for LoRa are 868 MHz and 433 MHz, while in America, the operating frequency is 915 MHz [8]. Also, the operating frequency for LoRa in India is 865 MHz [9].

Robust and sophisticated communication protocols and efficient hardware are vital to accomplishing an efficient communication network. Communication devices use antennas to transmit and receive signals; therefore, an antenna is an integral part of LoRa IoT devices [10–14]. Considering the operating frequencies of LoRa (below 1 GHz) and the ever-increasing need for IoT devices to be small and economically low-cost, it is incredibly challenging to design a miniaturized LoRa antenna that can be integrated alongside compact IoT devices [15].

Conventional LoRa modules are equipped with a single whip antenna operating at a fixed frequency. On the other hand, modern IoT devices communicate over multiple frequency bands. The device will be cumbersome if several single-frequency resonant antennas are used. Hence, there is a need for a single multiband antenna for IoT communication to extend network capacity [16]. It should be noted that wideband and multiband antennas operate at a wide/single frequency band. They cannot be changed to a particular frequency band based on the user's demand. Instead, they radiate energy in all their designed frequency bands leading to higher energy consumption and interference with other devices. This limitation can hinder the usage of such antennas in emerging IoT devices.

Reconfigurable antennas are a better choice to overcome these challenges. The concept of reconfigurability in antenna design refers to its capability to adjust its characteristics, such as polarization, radiation pattern or resonant frequency. A reconfigurable frequency antenna can switch its operating frequency to a chosen band. Therefore, the frequency spectrum can be efficiently utilized [17,18].

The modern printed circuit technology enables easy manufacture of Microstrip Patch Antennas (MPAs), which are also lightweight and mechanically robust. Moreover, these antennas can be integrated with both planar and non-planar surfaces [19–21]. It is, therefore, the best candidate to be used in LoRa IoT communications. Despite these advantages, it remains difficult to design a miniaturized antenna for LoRa IoT applications at frequencies below 1 GHz.

There have been a number of documented antenna designs [7,16,22–42] for LoRa applications over the last decade. The authors in [7] reported the design of a miniaturized antenna for LoRa sensor node IoT application on an FR-4 substrate. The antenna employs a Planar Inverted Antenna (PIFA) structure with additional resonance created by cutting slots on the ground plane. This results in a downward shift of the PIFA's resonance frequency from 450 MHz to 410 MHz. The antenna was designed to fit at the edge of the LoRa sensor node circuit board, covering an area of 125 mm × 20 mm × 1.6 mm. It achieved a realized gain greater than −6 dBi and a Voltage Standing Wave Ratio (VSWR) of less than 3.

In [16], a miniaturized dual-band antenna prototyped on an FR-4 material for LPWAN application was reported. The antenna operates at 433 MHz and 868 MHz and has an overall size of 90 mm × 30 mm × 1.6 mm. It used the geometry of the logo for the Université Cote d'Azur to achieve a maximum gain of −4.1 dB at 433 MHz and −2.2 dB at 868 MHz. However, the antenna is non-reconfigurable, and its gain is insufficient for long-range communication.

In [22], an FR-4 material was employed to develop a rectangular MPA for LoRaWAN application at 433 MHz. Cutting two (2) T-Shaped slots on its ground plane enhanced the

antenna's gain and efficiency. It has accomplished a gain of 2.194 dB with a total dimension of 210.82 mm × 164.79 mm × 5.5 mm. A novel LoRa antenna operating at 868 MHz for overwater and underwater surface communication was reported in [23]. With a footprint of 120 mm × 70 mm × 2.4 mm, the antenna has achieved a gain of 2.11 dB. An E-shaped dual-band energy harvesting antenna designed to operate in EGSM-900 and LoRaWAN mobile communication networks was presented in [28]. The antenna design was carried out on an FR-4 substrate and optimized to a total size of 102 × 81 × 1.6 mm^3 using HFSS and Grey Wolf Optimizer (GWO).

An IoT terminal with a dimension of 300 × 30 × 0.8 mm^3 designed to support three antennas operating at four frequency bands was presented in [33]. The terminal comprises: dual band GSS antenna at 1.57 GHz and 1.21 GHz for the Galileo L1 and L2 frequencies, respectively, 2.4 GHz LoRa antenna, and 868 MHz LoRa antenna. The realized maximum gain of the GSS antenna was 3.05 dBi for both L1 and L2 frequencies, 4.17 dBi at 2.4 GHz and 3.36 dBi at 868 MHz. Each of these antennas operates in one LoRa frequency and has a large footprint; hence, they are not suitable for compact IoT devices.

A reconfigurable pattern antenna at 868 MHz was reported in [41]. The antenna has a compact dimension of 80 × 55 mm^2 and is switched electronically to achieve four patterns. With a single-slot radiator, the antenna achieved a peak gain greater than 0.5 dB, whereas a gain of 1.6 dB was achieved in the monopole configuration. This antenna has compact and reconfigurable characteristics but is fixed to only one LoRa frequency.

A compact wideband double leaf-shaped MPA was reported in [42]. The antenna was prototyped on an FR-4 material and had a total size of 22 × 34 mm^2. It has covered all the LoRa bands in the sub-1 GHz: 915 MHz, 868 MHz, and 433 MHz, with a peak gain of 2.56 dB. This antenna is compact but cannot be tuned to suppress or select a particular LoRa frequency band.

This work presents a compact, novel, triple-band frequency reconfigurable monopole antenna for LoRa IoT applications on commercially available and cheaper FR-4 material. The antenna with a dimension of 80 mm × 50 mm × 0.6 mm can be tuned using two (2) RF (Radio Frequency) PIN diodes (D1 and D2) placed strategically in the branches of the antenna. Switching these diodes enables the antenna to operate at 915 MHz, 868 MHz, and 433 MHz, depending on the state of the diodes. These covered the LoRa frequencies across the globe. Meandered radiating monopoles and partial ground plane are employed to achieve compact size and impedance matching of the antenna. To the best of our knowledge, this is the first compact reconfigurable antenna that covered all the LoRa frequencies.

The subsequent sections of this paper have been organized as follows: Section 2 discusses the theory, structure, and reconfiguration mechanisms of the novel triple-band LoRa monopole antenna. Section 3 provides a detailed analysis of the comparison between measurement and simulation results for the antenna. Finally, Section 4 gives the conclusion of the work.

2. Design Methodology

The endless demand for compact and low-cost wireless IoT systems has increased the necessity for miniaturized, compact, and portable antennas. Such compact antennas should fit easily into every small space for IoT applications. Here, the proposed antenna's methodology, basic structure, theory, design, and reconfiguration mechanism are presented.

2.1. Theory and Geometry of the Antenna

The geometry of the proposed antenna is shown in Figure 1. It comprises two (2) branches of radiating elements each containing spirals of rectangular meandered monopoles on the top surface of the substrate and a partial copper ground plane on the bottom layer. Each branch has its specific resonance, which is controlled by RF switches. Meandered microstrip lines are considered a powerful miniaturization technique in antenna design. They are used to lengthen the path of current flow on an antenna's surface to produce lower frequencies resonance. Figure 1a depicts the top view of the triple band

LoRa monopole antenna designed on a 0.6 mm thick FR-4 substrate of dimensions 80 mm × 50 mm.

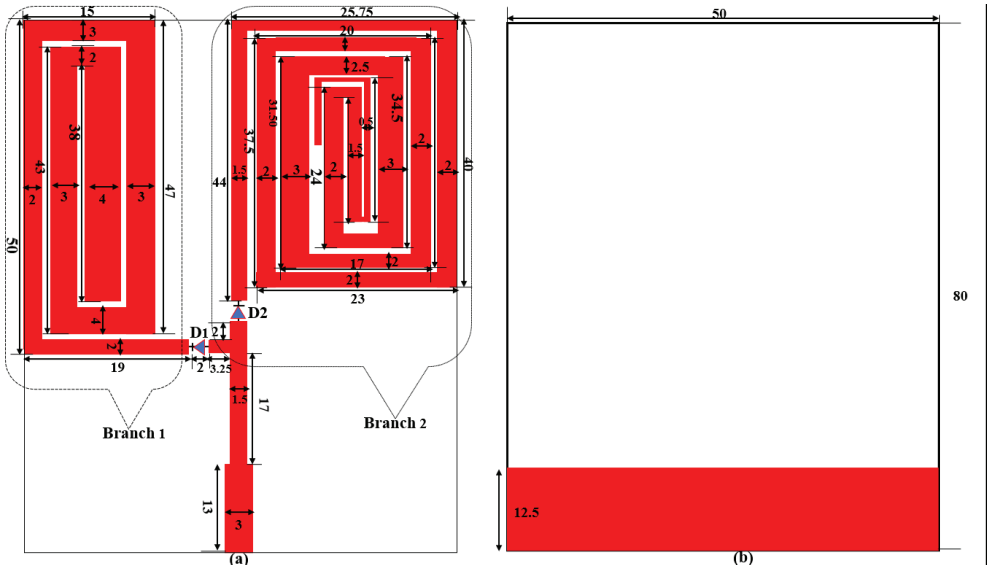

Figure 1. Geometry of the antenna (**a**) Front (**b**) Back.

To make the antenna integrable in emerging IoT devices, standard credit card dimensions of 85.6 mm × 53.98 mm are targeted to be the size of the proposed antenna. The type and characteristics of the substrate were chosen to make the antenna planar, cheaper, and easy to fabricate. The substrate has ε_r (relative permittivity) of 4.4 and tan δ (loss tangent) of 0.02. To improve the antenna's performance in terms of gain and efficiency, a partial copper ground plane (35 m) is used as shown in Figure 1b. A Microstrip line with a dimension of 3 mm is used to excite the antenna to achieve 50Ω impedance matching. Two slots of width 2 mm each are cut at appropriate positions on the branch 1 and branch 2 so that RF switches represented by D1 and D2 can be integrated into the antenna for switching among LoRa frequencies. The length (L) of the spiral meandered monopoles in each branch that will produce resonance at a specific frequency is determined using the Equations (1) and (2) as presented in [43,44]. A monopole antenna is theoretically a quarter wavelength antenna having its radiating elements and ground plane equal to 1/4th of the wavelength of the resonance frequency of the antenna. This concept is used to fold the monopoles into a spiral pattern to produce the required resonance at 433 MHz, 868 MHz, and 915 MHz. Then, PIN Diodes are used to select among these frequencies depending on the state of the diodes. The design, simulation, optimization, and antenna analysis are carried out in CST MWS® software environment. The detailed dimensions of the antenna parameters in millimetres are presented in Figure 1. In the simulation, the antenna is excited using a waveguide port. The efficiency of an antenna increases when it is excited at the correct position. This also reduces the reflection coefficient of the antenna (S_{11}).

$$L = \frac{\lambda}{4}, \tag{1}$$

where λ is the guided wavelength at each resonant frequency (f_r) and it is given by:

$$\lambda_{f_r} = \frac{c}{f_r\sqrt{\varepsilon_e}}, \tag{2}$$

c = speed of light in vacuum and ε_e is the effective permittivity

By folding the monopole conductors back and forth to form a meandered-line antenna as shown in branches 1 and 2 of Figure 1, a compact antenna is realised which is capable of operating at three distinct frequencies, 915 MHz, 868 MHz, and 433 MHz, depending on the status of the switching elements D1 and D2.

2.2. Frequency Switching Techniques

Frequency reconfigurability in an antenna refers to the ability to alter the path that current follows on the antenna's surface, thereby allowing for a shift in resonance to the desired frequency band. Instead of using multiple antennas operating at different frequencies, a reconfigurable frequency antenna can achieve the same function and simultaneously reduce cost and save space. Various techniques and methods are used to achieve frequency reconfiguration, including switches or slots on an antenna's radiating elements. Electronic switches used for reconfiguration in antenna include Field-Effect-Transistors (FET), Varactor diodes, Micro-Electromechanical Systems (MEMS), PIN diodes, etc. PIN diodes have received much attention for use as a switch in antenna due to their low cost, moderate isolation, less complicated biasing circuitry, and ease of integration with the antenna elements [45,46]. In this work, two PIN diodes D1 and D2 (BAR50-02V) from Infineon, are used to switch the antenna to operate at different LoRa frequencies. BAR50-02V is a silicon PIN diode with low forward resistance and extremely low harmonics distortions. It can operate from >10 MHz to 6 GHz. When both the diodes are ON, current flows from the feed to branch 1 and branch 2 of the antenna to produce an effective resonance at 915 MHz. When D1 is ON, and D2 is OFF, a resonance at 433 MHz is produced. The antenna operates at 868 MHz when D2 is ON, and D1 is OFF. The schematic for the equivalent circuits of the ON and OFF states of PIN diode are shown in Figure 2.

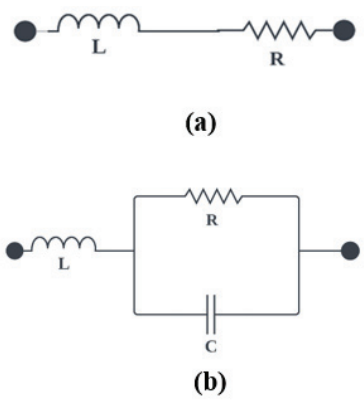

Figure 2. Equivalent circuit (**a**) ON state (**b**) OFF state.

It is evident from Figure 2 that, in the ON state, the PIN diode is represented by a series combination of a resistor (R) and an inductor (L). While in the OFF state, it is represented by an inductor (L) in series with a parallel combination of a resistor (R) and a capacitor (C), as shown in Figure 2b. The values of these parameters for the ON and OFF states are obtained from the diodes' technical data sheets. In the ON state, the values of R and L are small such that they behave as a short circuit to allow current to flow through the radiating loops. While in the OFF state, the values are selected such that the circuit blocks the current flow through the radiating loops. In the simulation, the ON state of the PIN diode is modelled using resistor of 1 Ω without taking the effects of the capacitor and inductor because in both the PIN diode model and the RLC lumped model, the ON-state of diode behaves as a short circuit to allow the flow of current to the radiating monopoles. In contrast, 20k Ω resistance is used to model the OFF state of the diode to block the flow of current to the radiating monopoles. Alternatively, touchstone files are used in CST to provide the S-Parameters of the diodes at ON and OFF states. This is considered the best method to get the response of the diodes at ON and OFF states for different ranges of frequencies. It is observed that the diodes behaved in a similar way using the two techniques. In the prototype antenna, the two PIN diodes are soldered appropriately on branch 1 and branch 2. The biasing voltage of the PIN diode is provided by 2-AAA batteries through jumper wires. Figure 3 depicts the biasing circuit of the PIN diode.

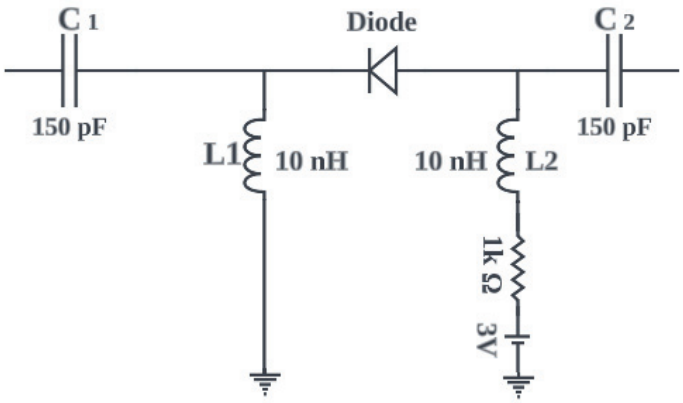

Figure 3. Biasing circuit of PIN Diode.

3. Results and Analysis

This section presents a discussion and analysis of the performance of the proposed antenna, with a focus on the return loss (S_{11}), distribution of surface currents, radiation patterns, gain, efficiency, etc. The results of simulations and measurements are compared in terms of these metrics. The fabricated antenna depicted in Figure 4 is fabricated on a cheaper substrate material (FR-4). The antenna's S_{11}, gain, and radiation pattern were measured using VNA (Vector Network Analyzer) and an anechoic chamber.

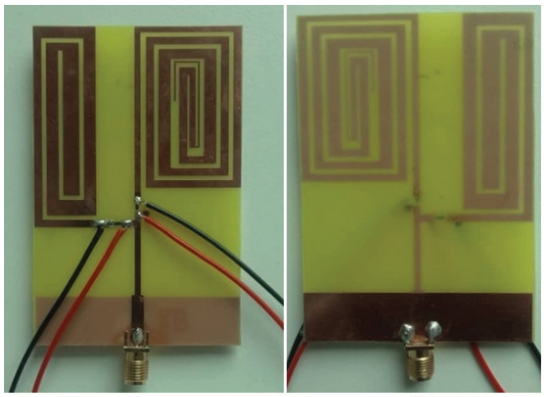

Figure 4. Prototype antenna (**a**) Front (**b**) Back.

3.1. Return Loss S_{11}

The simulated and measured S_{11} of the antenna at different switching conditions of the PIN diodes are shown in Figure 5. It is observed that, depending on the diode's state, the antenna operates at 433 MHz, 868 MHz, and 915 MHz. When D1 is ON and D2 is OFF, the antenna operates at 433 MHz with a magnitude of −35.8 dB and −19.9 dB for simulation and measurement, respectively. This is due to the fact that D2 is reversed biased; hence, current cannot flow through it to branch 2. During the OFF state of D1 and ON state of D2, the antenna operates at 868 MHz with a magnitude of −33.9 dB and −18.1 dB for simulation and measurements, respectively. This is due to the isolation of branch 1 as a result of D1 being in reverse bias. The proposed antenna operates at 915 MHz when both D1 and D2 are in the ON states. The current from the feed flows freely to branch 1 and branch 2, which results in a combined effect of producing a single band at 915 MHz. The magnitude of the return loss at 915 MHz is −45.9 dB and −18.9 dB for simulation and measurements, respectively. The summary of the functionality of the antenna at different states of the diode is presented in Table 1. In each case, the simulated and measured results agreed with each other. The proposed antenna covers all the LoRa bands (433 MHz, 868 MHz, and 915 MHz), making it the first single-solution reconfigurable antenna with

these characteristics. The antenna is well-matched in each case with very small return loss values.

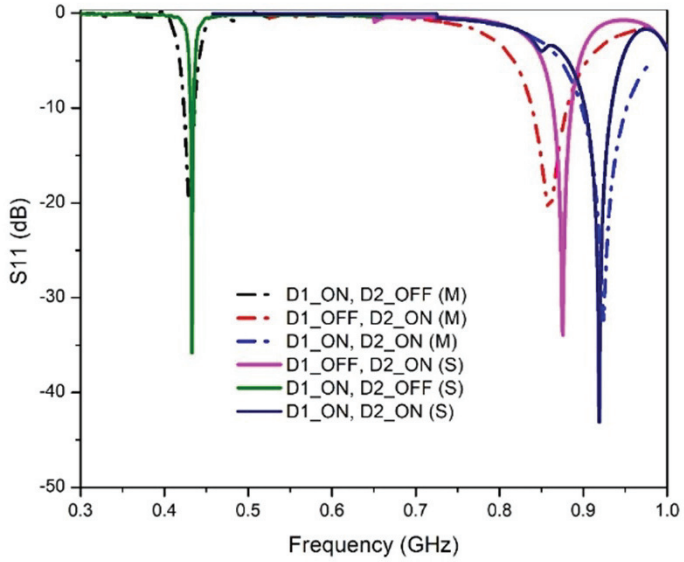

Figure 5. Comparison of S_{11} of the proposed antenna at different states of the diodes.

Table 1. Summary of the switching states of the diodes.

Diode	D1	D2	Frequency (MHz)	S_{11} (dB) Simulation	Measurement
State	ON	ON	915	−45.9	−18.9
	ON	OFF	433	−35.8	−19.9
	OFF	ON	868	−33.9	−18.1

3.1.1. Parametric Studies

In order to optimize the performance of the antenna design, parametric studies were conducted on some key parameters: the length of the feed (L_f) and its width (W_f) as well as the length of the ground plane (L_g) under different switching states of D1 and D2. The purpose of these studies is to identify the values of L_f, W_f, and L_g that would yield lower return loss and good matching at the desired frequencies of operation.

For the investigation of L_f, different lengths are considered: 13 mm, 20 mm, and 26 mm. The return loss and matching characteristics are analyzed for each length. The results indicated that the optimum length that provided the desired performance is 13 mm. At this length, the antenna exhibited lower return loss and achieved good matching.

Similarly, the study on the W_f is conducted using different widths: 3 mm, 4 mm, 5 mm, and 6 mm. The goal is to determine the width that would lead to improved performance in terms of return loss and matching. The analysis revealed that a width of 3 mm yielded good matching, and the antenna exhibited lower return loss at this width.

It is worth noting that as the L_f increased, the matching deteriorated, indicating a diminishing performance as the length deviated from the optimum value of 13 mm. Similarly, the W_f showed a similar trend, with an increase in width, resulting in a degradation of matching.

Figure 6 presents the variation of the L_f at 915 MHz, displaying the corresponding S_{11} and matching characteristics for the different lengths considered in the parametric study. The plot clearly illustrates that the performance is significantly improved when the feed length is set to 13 mm.

Figure 7 showcases the variation of W_f at 915 MHz, demonstrating the associated return loss and matching characteristics for the different widths examined. The plot demonstrates that a width of 3 mm offers superior matching compared to the other

widths tested, reinforcing the importance of selecting an appropriate width for achieving desired performance.

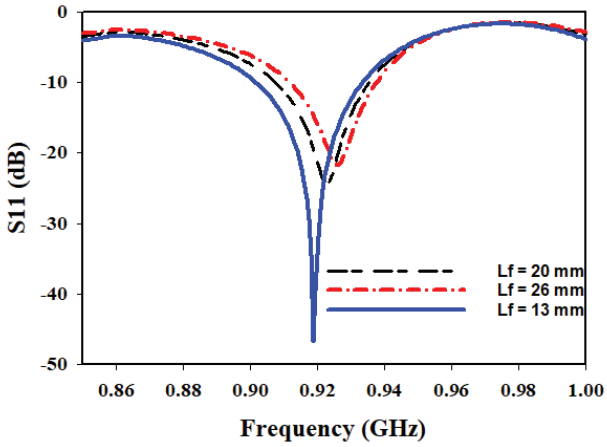

Figure 6. Variation of L_f.

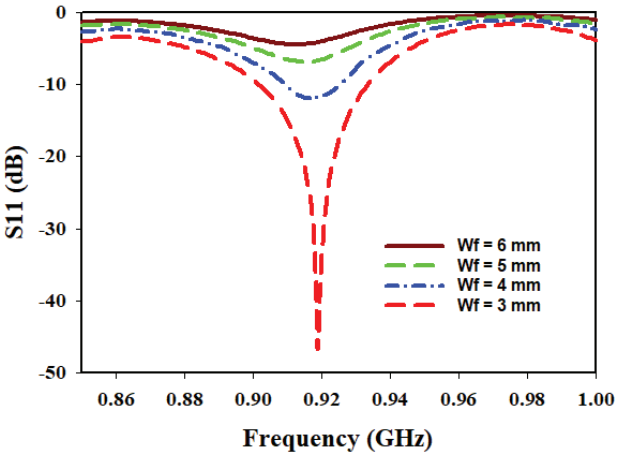

Figure 7. Variation of W_f.

These parametric studies play a crucial role in identifying the optimal values of the feed length and width, enabling the design of the antenna with lower return loss and improved matching at all the desired operating frequencies.

To further enhance the understanding and optimization of the antenna design, an additional parameter is investigated: the length of the ground plane L_g. The performance of the antenna is studied at different switching states of the diodes while considering two ground plane lengths: 12.5 mm and 25 mm. The analysis focused on the input impedance at three different frequencies: 433 MHz, 868 MHz, and 915 MHz. Figures 8–10 present the corresponding plots of Z1,1 (Re) and Z1,1 (Im) at 433 MHz, 868 MHz and 915 MHz.

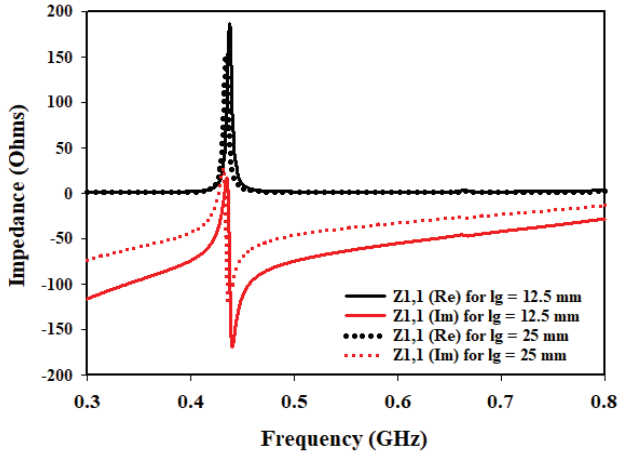

Figure 8. Effects of variation of L_g on input impedance at 433 MHz.

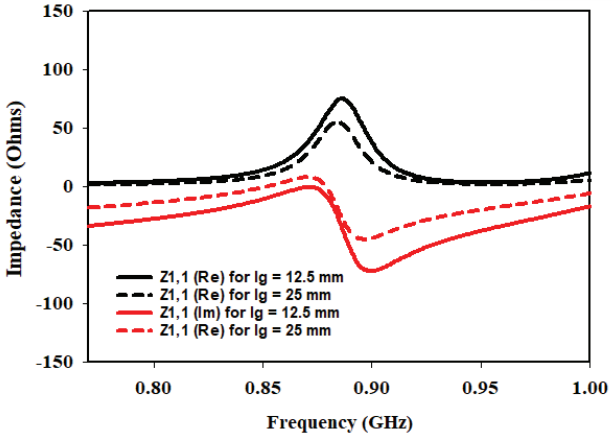

Figure 9. Effects of variation of L_g on input impedance at 868 MHz.

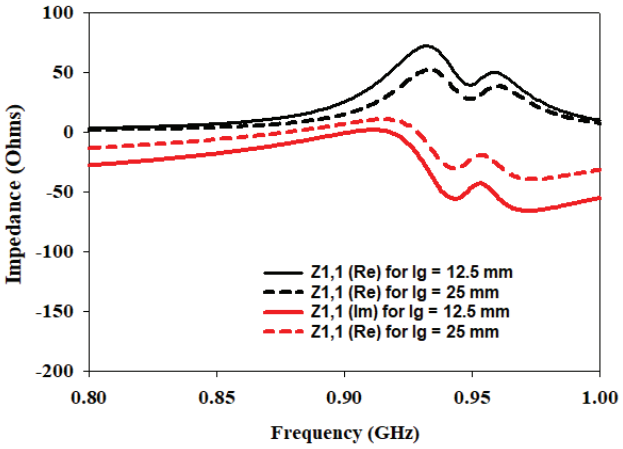

Figure 10. Effects of variation of L_g on input impedance at 915 MHz.

In the investigation of the L_g, it is observed that when the ground plane is set to 12.5 mm, the antenna exhibits favorable characteristics in terms of input impedance at the specified frequencies. Specifically, at each frequency, Z1,1 (Re) is found to be closer to the desired value of 50 Ω indicating good matching. Additionally, Z1,1 (Im) is also closer to zero, suggesting a better impedance balance.

However, as the L_g is doubled to 25 mm, the input impedance deviated significantly from the desired 50 Ω target. The values of Z1,1 (Re) and Z1,1 (Im) moved further away from the desired values, indicating a deterioration in matching and impedance balance.

These findings highlight the crucial role played by the L_g in achieving optimal antenna performance. When the ground plane length is set to 12.5 mm, the antenna demonstrated improved matching and impedance characteristics at the specified frequencies of 433 MHz, 868 MHz, and 915 MHz. This suggests that a shorter ground plane length helps in achieving a closer match to the desired impedance of 50 Ω, resulting in improved performance.

On the other hand, doubling the ground plane length to 25 mm led to a significant deviation from the desired impedance values. This indicates that an increase in the ground plane length adversely affects the matching and impedance balance, resulting in degraded performance.

The parametric studies involving the L_g, in addition to the L_f and W_f, have provided valuable insights into optimizing the antenna design. The results emphasize the importance of selecting appropriate values for these parameters to achieve lower return loss, improved matching, and closer adherence to the desired input impedance of 50 Ω at the specified frequencies.

3.1.2. Distribution of Surface Current

The performance of any antenna is greatly influenced by the distribution of surface current on its radiating elements. The surface current distribution on an antenna is crucial in determining its radiation pattern, gain, and directivity. By carefully controlling the current distribution on the radiating elements, the performance of an antenna can be optimized to resonate at specific frequencies for specific applications.

Here, the monopole elements on which the surface current density is maximum and responsible for producing resonance at a particular frequency are studied. The surface current distributions at distinct switching states of the diodes are illustrated in Figure 11. It is apparent from Figure 11a that all the elements in branch 1 and branch 2 produced the resonance at 915 MHz when both D1 and D2 are ON. This is due to the free flow of current to both the branches due to D1 and D2 being in a forward bias states. In contrast, when D1 is ON, and D2 is OFF, current does not flow to branch 2; consequently, only the elements of branch 1 radiate and produce a resonance at 433 MHz (Figure 11b). Additionally, when D1 is OFF, and D2 is ON, current does not flow to branch 1 because D1 is reversed-biased; hence, only the elements in branch 2 radiate and generate the resonance at 868 MHz (Figure 11c). In each case, the maximum current density is illustrated by the red colour, as can be visualized from the current density colour ramp.

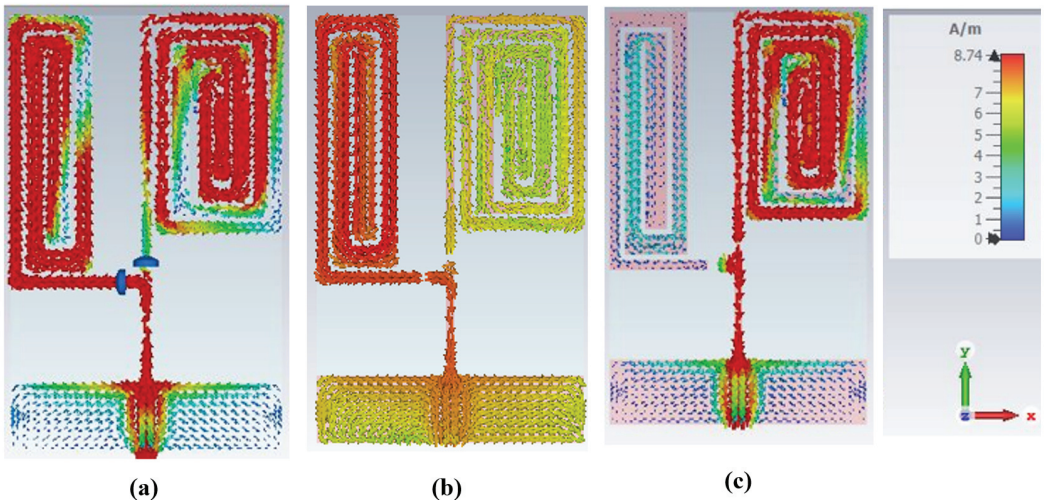

Figure 11. Surface current (**a**) D1: ON, D2: ON (**b**) D1: ON, D2: OFF (**c**) D1: OFF, D2: ON.

3.1.3. Radiation Pattern, Gain and Efficiency

The antenna's radiation pattern represents how the antenna radiates electromagnetic energy into space. It provides information about the antenna's directivity, which measures

how well it concentrates its energy in a particular direction. It also provides information about the antenna's gain, which measures the amount of power radiated by the antenna in a specific direction compared to an isotropic radiator. The proposed antenna's radiation pattern in E and H planes for simulation and measurements at 915 MHz, 868 MHz, and 433 MHz are shown in Figure 12. In Figure 12a, the antenna operates at 433 MHz (D1: ON, D2: OFF) with a peak directivity of 2 dBi. Figure 12b illustrates how the proposed antenna emits radio waves at 868 MHz (D1: OFF, D2: ON) with a peak gain of 1.9 dBi. In Figure 12c, the proposed antenna operates at 915 MHz when both diodes are ON with a gain of 1.9 dBi. In each case, for both simulation and measurement, the proposed antenna has an omnidirectional pattern in H-plane. While the radiation pattern in E-plane is bidirectional, as evidenced by the 'Eight' shape of the E-plane patterns with a null lobe at $\theta = 90°$ for each state of the diode. A bidirectional radiation pattern is often used in wireless communication systems, particularly in wireless sensor networks where the sensor node needs to communicate with two or more other nodes for IoT applications. The simulated and measured results in both planes (E and H) agree. The plots of gain and efficiency of the proposed antenna against frequency are shown in Figure 13. It can be seen that the antenna has almost uniform gain (1.9 dBi) in all its bands of operation with a maximum radiation efficiency of 93% at 915 MHz. This implied that the antenna could transmit and receive signals with relatively equal strength across all its three bands of operation.

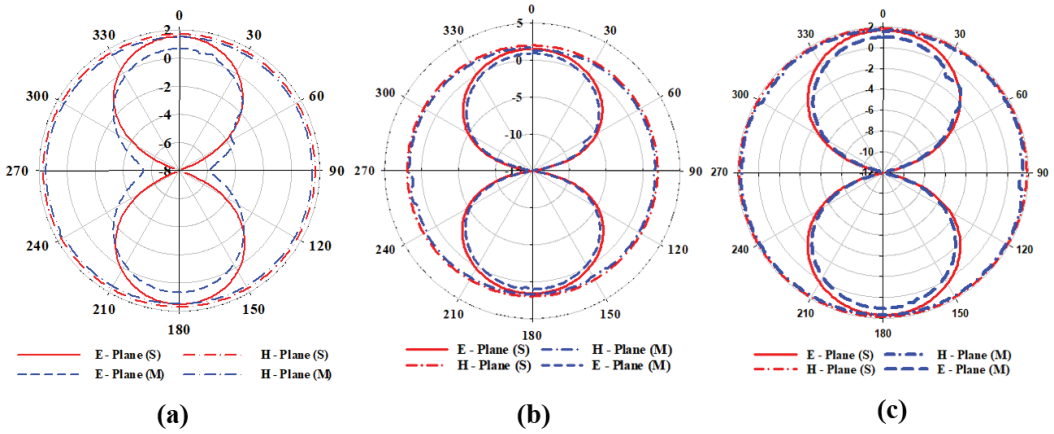

Figure 12. Comparison of radiation patterns of the proposed antenna (**a**) D1: ON, D2: OFF (**b**) D1: OFF, D2: ON (**c**) D1: ON, D2: ON.

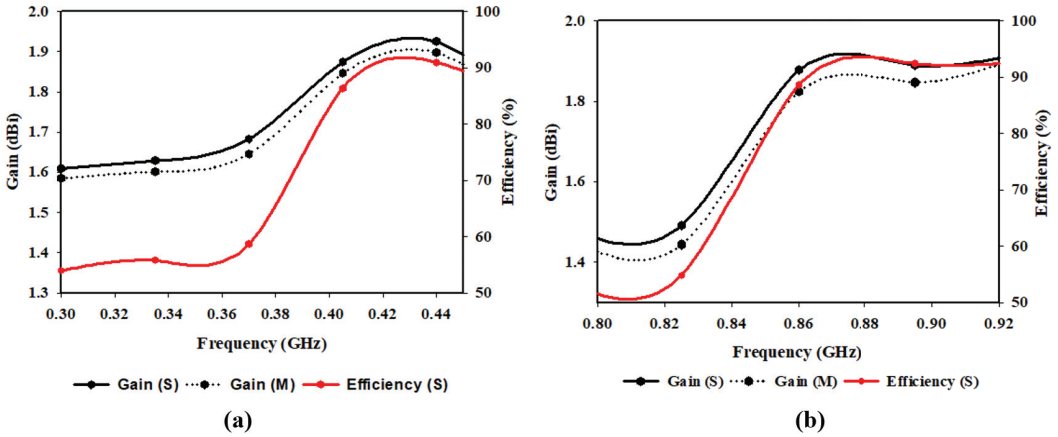

Figure 13. Comparison of gain and efficiency of the proposed antenna (**a**) 433 MHz (**b**) 868 MHz and 915 MHz.

A comparison of the performance of the proposed antenna with the existing literature is presented in Table 2. The comparison table provides a comprehensive evaluation of various antennas designed for LoRa applications. From the table, it is evident that the

proposed work, which is a monopole antenna, offers superior performance compared to the other works listed.

One of the key advantages of the proposed antenna is its multiband coverage, which spans across three frequency bands: 433 MHz, 868 MHz, and 915 MHz. This makes the antenna suitable for various applications where a multiband antenna is required. Additionally, the proposed antenna has a higher gain of 2 dBi at 433 MHz, which is desirable for long-range communication and signal reception in low signal strength environments.

Table 2. Comparison of the performance of the proposed antenna with available literatures

Ref.	Year	Bands	Frequency (MHz)	Substrate Material	Conductor Material	Gain (dBi)	Reconfi-Gurable?	All LoRa Frequencies?	Size (mm^2)
[7]	2018	1	402.4–441.6	FR-4 (NA *)	Copper	−6	NO	YES	125 × 20
[23]	2021	1	868	FR-4 (4.3)	Copper	2.11	NO	YES	120 × 70
[25]	2020	1	871	FR-4 (4.4)	Copper	0.58	NO	YES	67.7 × 55
[27]	2019	1	848–950	FR-4 (4.4)	Copper	2.1	NO	YES	40 × 26
[29]	2019	2	868 2400	FR-4 (4.4)	Copper	1.92 4.2	NO	NO	100 × 40
[30]	2021	2	400 900.2	FR-4 (NA)	Copper	−5	NO	YES	160 × 170
[34]	2021	3	401 466 868	FR-4 (4.7)	Copper	−8.5 −5.2 −2.8	NO	YES	78 × 88
[41]	2021	1	868	FR-4 (4.4)	Copper	1.6	YES	YES	80 × 55
[42]	2022	Wide band	151.9–1080	FR-4 (4.4)	Copper	2.56	NO	YES	22 × 34
This work	**2023**	**3**	**433** **868** **915**	**FR-4 (4.4)**	**Copper**	**2** **1.9** **1.9**	**YES**	**YES**	**80 × 50**

* NA = No information available.

Another significant advantage of the proposed antenna is its reconfigurability, which allows it to change its operating frequency. This feature enables the antenna to adapt to different communication protocols and environments, improving its performance significantly. Furthermore, the antenna's compact size of 80 mm × 50 mm × 0.6 mm^3 makes it suitable for integration into small devices. The monopole technique used in the proposed antenna is well-established and widely used in various applications. This technique is known for its simplicity and ease of design, which makes it attractive for antenna design in various applications.

4. Conclusions

In this paper, a novel compact (80 × 50 × 0.6 mm^3), triple band reconfigurable monopole antenna for LoRa IoT applications was presented. By utilizing two PIN diodes (D1 and D2) to switch the antenna to different modes, resonance at 433 MHz, 868 MHz, and 915 MHz was achieved, depending on the states of the diodes. When D1 is turned ON, and D2 is turned OFF, the antenna operates in the 433 MHz band, which is the designated frequency for LoRa in Europe. Conversely, when D1 is turned OFF, and D2 is turned ON, the antenna operates in the 868 MHz band, which is also used in Europe for LoRa applications. When both diodes are turned ON, the antenna operates in the 915 MHz band, the designated frequency band for LoRa in North America and some Asian countries. To keep the cost of the antenna low for LoRa IoT applications, the substrate and reconfiguration mechanisms chosen were cost-effective. Additionally, the antenna was miniaturized to have a dimension smaller than the size of a standard "credit card". With a peak gain of 2 dBi and a radiation efficiency above 90%, this proposed antenna is novel in terms of size and performance for LoRa IoT applications. The antenna was prototyped and tested to validate its performance, and the results of measurements are in good agreement with those of simulation.

Author Contributions: M.S.Y. conceptualized the idea, conducted the simulations and experiments, and prepared the manuscript and visualizations. S.S., S.K.A.R., N.B.M.N. and C.S. provided supervision throughout the study. N.S.S.S., Z.Y., F.E.C., U.M. and G.E.M.A. contributed to the experimental

validation and reviewed the manuscript. All authors have read and agreed to the published version of the manuscript.

Funding: This research was funded by Petroleum Technology Development Fund (PTDF) and Unversiti Teknologi PETRONAS Malaysia under Graduate Assistantship (GA) Scheme Grant and YUTP-PRG (015PBC-007).

Institutional Review Board Statement: Not applicable.

Informed Consent Statement: Not applicable.

Data Availability Statement: Not applicable.

Acknowledgments: The authors express their sincere gratitude for the assistance of the Petroleum Technology Development Fund (PTDF), Centre of Graduate Studies, Universiti Teknologi PETRONAS, Malaysia, and the Faculty of Data Science and Information Technology, INTI International University, Malaysia for making available the latest research facilities that were necessary to conduct this study.

Conflicts of Interest: The authors declare no conflict of interest.

References

1. Huh, H.; Kim, J.Y. LoRa-based mesh network for IoT applications. In Proceedings of the 2019 IEEE 5th World Forum on Internet of Things (WF-IoT), Limerick, Ireland, 15–18 April 2019; pp. 524–527.
2. Ribeiro, L.E.; Tokikawa, D.W.; Rebelatto, J.L.; Brante, G. Comparison between LoRa and NB-IoT coverage in urban and rural Southern Brazil regions. *Ann. Telecommun.* **2019**, *75*, 755–766. [CrossRef]
3. Hammi, B.; Khatoun, R.; Zeadally, S.; Fayad, A.; Khoukhi, L. IoT technologies for smart cities. *IET Netw.* **2017**, *7*, 1–13.
4. Bouguera, T.; Diouris, J.F.; Chaillout, J.J.; Jaouadi, R.; Andrieux, G. Energy consumption model for sensor nodes based on LoRa and LoRaWAN. *Sensors* **2018**, *18*, 2104. [CrossRef] [PubMed]
5. Zourm, A.; Hing, A.L.K.; Hung, C.W.; AbdulRehman, M. Internet of things (IoT) using LoRa technology. In Proceedings of the 2019 IEEE International Conference on Automatic Control and Intelligent Systems (I2CACIS), Selangor, Malaysia, 29 June 2019; pp. 324–330.
6. Khutsoane, O.; Isong, B.; Abu-Mahfouz, A.M. IoT devices and applications based on LoRa/LoRaWAN. In Proceedings of the IECON 2017—43rd Annual Conference of the IEEE Industrial Electronics Society, Beijing, China, 29 October–1 November 2017; pp. 6107–6112.
7. Zhang, Q.; Gao, Y. Embedded antenna design on LoRa radio for IoT applications. In Proceedings of the 12th European Conference on Antennas and Propagation (EuCAP 2018), London, UK, 9–13 April 2018.
8. Trinh, L.H.; Nguyen, T.Q.K.; Tran, H.L.; Nguyen, P.C.; Truong, N.V.; Ferrero, F. Low-profile horizontal omni-directional antenna for LoRa wearable devices. In Proceedings of the 2017 International Conference on Advanced Technologies for Communications (ATC), Quy Nhon, Vietnam, 18–20 October 2017; pp. 136–139.
9. Chaudhari, P.; Tiwari, A.K.; Pattewar, S.; Shelke, S.N. Smart infrastructure monitoring using LoRaWAN technology. In Proceedings of the 2021 International Conference on System, Computation, Automation and Networking (ICSCAN), Puducherry, India, 30–31 July 2021; pp. 1–6.
10. Tyagi, D.; Kumar, S.; Kumar, R. Multifunctional Antenna Design for Internet of Things Applications. In Proceedings of the 2021 7th International Conference on Advanced Computing and Communication Systems (ICACCS), Coimbatore, India, 19–20 March 2021; Volume 1, pp. 557–560.
11. Haque, M.A.; Sarker, N.; Sawaran Singh, N.S.; Rahman, M.A.; Hasan, M.N.; Islam, M.; Zakariya, M.A.; Paul, L.C.; Sharker, A.H.; Abro, G.E.M.; et al. Dual Band Antenna Design and Prediction of Resonance Frequency Using Machine Learning Approaches. *Appl. Sci.* **2022**, *12*, 10505. [CrossRef]
12. Rahaman, I.; Jafor, M.S.; Singh, N.S.S.; Haque, M.A.; Biswas, A.K.; Rahman, M.A.; Zakariya, M.A.B.; Abro, G.E.M.; Sarker, N. Performance Investigation of Linearly Arranged Circular, Circular Planer, Rectangular, and Concentric Circular Antenna Arrays Using Robust NVL Techniques. *Appl. Sci.* **2022**, *12*, 11481. [CrossRef]
13. Yahya, M.S.; Dalyop, I.A.; Saleh, Y.; Aminu-Baba, M. Antenna for 5G mobile communications systems at 10 GHz. *Int. J. Eng. Technol.* **2018**, *7*, 13–15. [CrossRef]
14. Yahya, M.S.; Soeung, S.; Chinda, F.E.; Sovuthy, C.; Nor, N.B.; Rahim, S.K.A.; Musa, U. A Compact Dual Band Microstrip Patch Antenna for LoRa IoT Applications. In Proceedings of the 2022 IEEE International RF and Microwave Conference (RFM), Kuala Lumpur, Malaysia, 19–21 December 2022; pp. 1–4.
15. Roges, R.; Malik, P.K.; Sharma, S. A compact CPW-fed log-periodic antenna for IoT applications. In Proceedings of the 2021 International Conference on Communication, Control and Information Sciences (ICCISc), Idukki, India, 16–18 June 2021; Volume 1; pp. 1–5.
16. Ferrero, F.; Toure, M.B. Dual-band lora antenna: Design and experiments. In Proceedings of the 2019 IEEE Conference on Antenna Measurements & Applications (CAMA), Kuta, Bali, Indonesia, 23–25 October 2019; pp. 243–246.

17. Awan, W.A.; Naqvi, S.I.; Ali, W.A.E.; Hussain, N.; Iqbal, A.; Tran, H.H.; Alibakhshikenari, M.; Limiti, E. Design and realization of a frequency reconfigurable antenna with wide, dual, and single-band operations for compact sized wireless applications. *Electronics* **2021**, *10*, 1321. [CrossRef]
18. Ullah, S.; Hayat, S.; Umar, A.; Ali, U.; Tahir, F.A.; Flint, J.A. Design, fabrication and measurement of triple band frequency reconfigurable antennas for portable wireless communications. *AEU Int. J. Electron. Commun.* **2017**, *81*, 236–242. [CrossRef]
19. Balanis, C.A. *Antenna Theory: Analysis and Design*; John Wiley & Sons: Hoboken, NJ, USA, 2015.
20. Fang, D.G. *Antenna Theory and Microstrip Antennas*; CRC Press: Boca Raton, FL, USA, 2017.
21. Sani Yahya, M.; Rahim, S.K.A. 15 GHz grid array antenna for 5G mobile communications system. *Microw. Opt. Technol. Lett.* **2016**, *58*, 2977–2980. [CrossRef]
22. Mushtaq, A.; Gupta, S.H.; Rajawat, A. Design and performance analysis of LoRa LPWAN antenna for IoT applications. In Proceedings of the 2020 7th International Conference on Signal Processing and Integrated Networks (SPIN), Noida, India, 27–28 February 2020; pp. 1153–1156.
23. Dala, A.; Arslan, T. Design, implementation, and measurement procedure of underwater and water surface antenna for Lora communication. *Sensors* **2021**, *21*, 1337. [CrossRef] [PubMed]
24. Wanpare, W.; Paisal, A.; Chalermwisutkul, S. A Compact 923 MHz Monopole Antenna for LoRaWAN IoT Applications. In Proceedings of the 2020 International Conference on Power, Energy and Innovations (ICPEI), Chiangmai, Thailand, 14–16 October 2020; pp. 53–56.
25. Pandey, A.; Nair, M.D. Inset fed miniaturized antenna with defected ground plane for LoRa applications. *Procedia Comput. Sci.* **2020**, *171*, 2115–2120. [CrossRef]
26. Boursianis, A.D.; Papadopoulou, M.S.; Pierezan, J.; Mariani, V.C.; Coelho, L.S.; Sarigiannidis, P.; Koulouridis, S.; Goudos, S.K. Multiband patch antenna design using nature-inspired optimization method. *IEEE Open J. Antennas Propag.* **2020**, *2*, 151–162. [CrossRef]
27. Tarbouch, M.; Reha, A.; El Amri, A.; Mejdoub, Y. A Compact PIFA Antenna for Internet of Things Network LORAWAN at 900 Mhz Band. In *Colloque sur les Objets et Systèmes Connectés*; Institut Universitaire de Technologie d'Aix-Marseille: Casablanca, Morocco, 2019.
28. Boursianis, A.D.; Goudos, S.K.; Yioultsis, T.V.; Siakavara, K. Low-cost dual-band e-shaped patch antenna for energy harvesting applications using grey Wolf optimizer. In Proceedings of the 2019 13th European Conference on Antennas and Propagation (EuCAP), Krakow, Poland, 31 March–5 April 2019; pp. 1–5.
29. Reha, A.; Tarbouch, M.; El Amri, A. A Dual Band Compact PIFA Antenna For Internet Of Things Networks Sigfox, Lorawan And Zigbee. In *Proceedings of the Colloque sur les Objets et systèmes Connectés*; Institut Universitaire de Technologie d'Aix-Marseille: Casablanca, Morocco, 2019.
30. Krishna, M.V.; Raju, G.S.N. Triangle Shaped Antenna Design for IoT-based Lorawan Applications. *SAMRIDDHI J. Phys. Sci. Eng. Technol.* **2021**, *13*, 8–11. [CrossRef]
31. Trinh, L.H.; Nguyen, T.Q.K.; Phan, D.D.; Tran, V.Q.; Bui, V.X.; Truong, N.V.; Ferrero, F. Miniature antenna for IoT devices using LoRa technology. In Proceedings of the 2017 International Conference on Advanced Technologies for Communications (ATC), Quy Nhon, Vietnam, 18–20 October 2017; pp. 170–173.
32. Shin, G.; Park, T.R.; Park, J.; Lee, S.K.; Kim, G.; Yoon, I.J. Sustaining the Radiation Properties of a 900-MHz-Band Planar LoRa Antenna Using a 2-by-2 Thin EBG Ground Plane. *IEEE Access* **2020**, *8*, 145586–145592. [CrossRef]
33. Wang, Y.; Santamaria, L.; Ferrero, F.; Lizzi, L. Design of a Multi-Antenna Portable IoT Terminal. In Proceedings of the 2021 IEEE Conference on Antenna Measurements & Applications (CAMA), Antibes Juan-les-Pins, France, 15–17 November 2021; pp. 597–599.
34. Bouyedda, A.; Barelaud, B.; Gineste, L. Design and realization of an UHF frequency reconfigurable antenna for hybrid connectivity LPWAN and LEO satellite networks. *Sensors* **2021**, *21*, 5466. [CrossRef]
35. Ibrahim, N.F.; Dzabletey, P.A.; Kim, H.; Chung, J.Y. An All-Textile Dual-Band Antenna for BLE and LoRa Wireless Communications. *Electronics* **2021**, *10*, 2967. [CrossRef]
36. Ngamjanvaporn, P.; Phongcharoenpanich, C.; Krairiksh, M. A Beam-Scanning Array Antenna for LPWAN Base Station. In Proceedings of the 2018 IEEE International Symposium on Antennas and Propagation & USNC/URSI National Radio Science Meeting, Boston, MA, USA, 8–13 July 2018; pp. 473–474.
37. Putra, N.A.; Hasbi, W.; Manggala, M.P.; Kusmara, D.U.; Putri, W.M.; Triyogi, R.; Wirakusuma, M.P. Design of CubeSat Microstrip Antenna with Metamaterial Structure for LoRa Communication. In Proceedings of the 2021 IEEE International Conference on Aerospace Electronics and Remote Sensing Technology (ICARES), Bali, Indonesia, 3–4 November 2021; pp. 1–5.
38. Turkmen, C.; Bakirli, Y.; Secmen, M.; Altuntas, M. Printed quasi yagi antenna with closely spaced and thick directors for triple ISM-band/wideband applications at UHF. In Proceedings of the 2018 IEEE International Symposium on Antennas and Propagation & USNC/URSI National Radio Science Meeting, Boston, MA, USA, 8–13 July 2018; pp. 677–678.
39. Shin, G.; Park, J.; Park, T.R.; Yoon, I.J. Compact 900-MHz LoRa Band Antenna On a Low-Profile AMC Surface. In Proceedings of the 2019 International Symposium on Antennas and Propagation (ISAP), Xi'an, China, 27–30 October 2019; pp. 1–2.
40. Wang, X.; Xing, L.; Wang, H. A wearable textile antenna for lora applications. In Proceedings of the 2021 IEEE 4th International Conference on Electronic Information and Communication Technology (ICEICT), Xi'an, China, 18–20 August 2021; pp. 613–615.

41. Haydhah, S.A.; Ferrero, F.; Lizzi, L.; Sharawi, M.S.; Zerguine, A. A multifunctional compact pattern reconfigurable antenna with four radiation patterns for sub-GHz IoT applications. *IEEE Open J. Antennas Propag.* **2021**, *2*, 613–622. [CrossRef]
42. Roges, R.; Malik, P.K.; Sharma, S. A Compact Wideband Antenna with DGS for IoT Applications Using LoRa Technology. In Proceedings of the 2022 10th International Conference on Emerging Trends in Engineering and Technology-Signal and Information Processing (ICETET-SIP-22), Nagpur, India, 29–30 April 2022; pp. 1–4.
43. Sayidmarie, K.H.; Yahya, L.S. Design and analysis of dual band crescent shape monopole antenna for WLAN applications. *Int. J. Electromagn. Appl.* **2013**, *3*, 96–102.
44. Yahya, L.S.; Sayidmarie, K.H.; Elmegri, F.; Abd-Alhameed, R.A. Crescent-shaped double-monopole antennas with reduced coupling for WLAN and WIMAX applications. In Proceedings of the 2015 Internet Technologies and Applications (ITA), Wrexham, UK, 8–11 September 2015; pp. 393–398.
45. Nikam, P.B.; Kumar, J.; Baidya, A.; Ghosh, A. Low-profile bandwidth and E-plane radiation pattern reconfigurable patch antenna for sub-6 GHz 5G applications. *AEU Int. J. Electron. Commun.* **2022**, *157*, 154415. [CrossRef]
46. Musa, U.; Shah, S.M.; Majid, H.A.; Abidin, Z.Z.; Yahya, M.S.; Babani, S.; Yunusa, Z. Recent Advancement of Wearable Reconfigurable Antenna Technologies: A Review. *IEEE Access* **2022**, *10*, 121831–121863. [CrossRef]

sensors

MDPI

Article

Design of Wideband High-Gain Patch Antenna Array for High-Temperature Applications

Ruibo Li [1], Peng Li [1,*], Paolo Rocca [1,2], Aarón Ángel Salas Sánchez [2], Liwei Song [1], Xinghua Li [1], Wanye Xu [1] and Zijiao Fan [1]

[1] Key Laboratory of Electronic Equipment Structure Design, Xidian University, Xi'an 710071, China; paolo.rocca@xidian.edu.cn (P.R.)
[2] DICAM—Department of Civil, Environmental, and Mechanical Engineering, Trento University, 38123 Trento, Italy
* Correspondence: lipeng18@xidian.edu.cn

Abstract: A low-profile, wideband, and high-gain antenna array, based on a novel double-H-shaped slot microstrip patch radiating element and robust against high temperature variations, is proposed in this work. The antenna element was designed to operate in the frequency range between 12 GHz and 18.25 GHz, with a 41.3% fractional bandwidth (FBW) and an obtained peak gain equal to 10.2 dBi. The planar array, characterized by a feed network with a flexible 1 to 16 power divider, comprised 4×4 antenna elements and generated a pattern with a peak gain of 19.1 dBi at 15.5 GHz. An antenna array prototype was fabricated, and the measurements showed good agreement with the numerical simulations as the manufactured antenna operated in the range of 11.4–17 GHz, with a 39.4% FBW, and the peak gain at 15.5 GHz was 18.7 dBi. The high-temperature simulated and experimental results, performed in a temperature chamber, demonstrated that the array performance was stable in a wide temperature range, from −50 °C to 150 °C.

Keywords: antennas; patch array; wideband; high-gain; high-temperature

1. Introduction

An antenna is, by definition, a sensor of EM (electromagnetic) waves; it plays an extremely important role in radar sensor [1], biomedical sensors [2], satellite information detection [3–5], remote control [6], and navigation [7,8]. Patch array antenna technology has dramatically improved over the last few decades due to the development of modern antenna technology having a low cost, a low profile, high reliability, and multiple functions. The main drawbacks of ordinary patch antennas are the narrow bandwidth, the low gain, and the sensitivity to the material parameters [9,10]. Especially for high-temperature environments, the temperature change can have a non-negligible impact on the material properties, thus causing frequency shifts and gain losses [11,12]. In this framework, this work aims to design a novel planar high-gain and wideband patch antenna array that works in the Ku-band, is robust against high temperature variations, and is suitable for EM wave sensing in a large temperature range. Therefore, the antenna design's main challenge was achieving a suitable performance balance between antenna thickness, gain, and bandwidth.

Many effective methods have been proposed in the literature to increase the operation bandwidth of microstrip patch antennas. Among them, the use of parasitic patches has been considered as well as optimization of the antenna shape. More specifically, a patch antenna adopting a U-shaped slot-fed and stacked structure was proposed in [13], reaching a 2.58 GHz bandwidth (59.7% FBW) and a peak gain equal to 8 dBi. Other solutions have been considered using parasitic patches on the same substrate of the patch antenna [14,15]. Although this can effectively expand the bandwidth, a large 2D antenna aperture area is required. A different strategy considers the optimization of the shape of the slot used to feed

the patch antennas. In this context, antennas using U-shaped slots have been adopted to increase the bandwidth [16–18], but in these cases, the gain did not exceed 5 dBi. Alternatively, spline-shaped profiles have also been exploited to model the contours of the patch radiating elements [19] and their optimization, yielded by acting on a limited set of geometric degrees of freedom. This has been addressed using advanced optimization methods [19,20].

Other methods have been investigated to improve the gain of the antenna element. In [21–23], the introduction of multiple short-circuit probes allowed high gain values between 8 dBi and 12 dBi to be achieved, with a bandwidth close to 500 MHz (13.4% FBW). In [24], using a feed network with four pin-diode switches, multiple working modes were excited on the antenna, including the common mode and differential feed schemes. This solution allowed for pattern reconfiguration, and a high gain pattern was obtained with an antenna bandwidth of 200 MHz (7% FBW). In [25–27], combining a short-circuit probe and multiport dual-polarized patches enabled the improvement of the antenna gain and the bandwidth, reaching values of 800 MHz (22% FBW). In [28], a novel method for removing part of the dielectric substrate was proposed, and the designed antenna was shown to achieve a gain of 7 dBi and 400 MHz bandwidth (10% FBW). In addition, electrically longer patch antennas provide higher gain, but narrower bands. In this framework, a long rectangular patch antenna with a single feed was proposed in [29], the gain of which reached 10.5 dBi. In [30], a structurally compact rectified antenna was fabricated, combining the characteristics of long patches and coplanar waveguides. In [31], by short-circuiting both ends of a long patch, various modes were excited to obtain an antenna gain to 9.7 dBi, and, jointly, a bandwidth of 13.2%. In [32], an ultra-wideband, high-gain, circularly polarized antenna was proposed, with FBW and peak gain equal to 49.8% and 8.5 dBi, respectively. More recently, many studies have considered multiport-fed dipole antennas to improve the antenna bandwidth and gain by increasing the radiation area of the dipole. In this framework, the antenna proposed in [33], based on the radiation mechanism of dipole and microstrip patch antenna, achieved high gain (8.9 dBi) and wideband (48% FBW) performance, but at a low frequency for application in this work.

This study proposes a novel double-H-shaped slot microstrip patch antenna, robust against high temperature variations, as a radiating element of a low-profile, wideband, and high-gain patch antenna array. In order to test the effectiveness of the proposed design, the antenna was fabricated and the prototype measured for comparison with the numerical results. The analysis of the temperature resistance was performed in a temperature chamber between -50 °C and 150 °C.

Accordingly, the remainder of this article is as follows. The elements of the antenna and antenna array designs are presented in Section 2. The prototype and the measurement results, also considering the analysis at high temperatures, are reported in Section 3. Eventually, some conclusions are given in Section 4.

2. Antenna Model and Design

2.1. Antenna Element Geometry

The proposed antenna element is shown in Figure 1, and comprises three parts. The first part is a patch radiator, which includes a pair of patches, two dielectric substrates (i.e., substrate 1 and substrate 2) characterized by a Rogers 4350B material (ε_r = 3.66, tan δ = 0.004), and a ground plane (i.e., ground 1) with a double-H slot fed through a microstrip line. The second part is a coplanar radiator, which includes four parasitic patches, a ground plane (i.e., ground 2) connected with the ground plane of the first part by means of metallic pin columns, and a dielectric substrate (i.e., substrate 3). The third part, filling the space between the two radiators, consists of air (or foam).

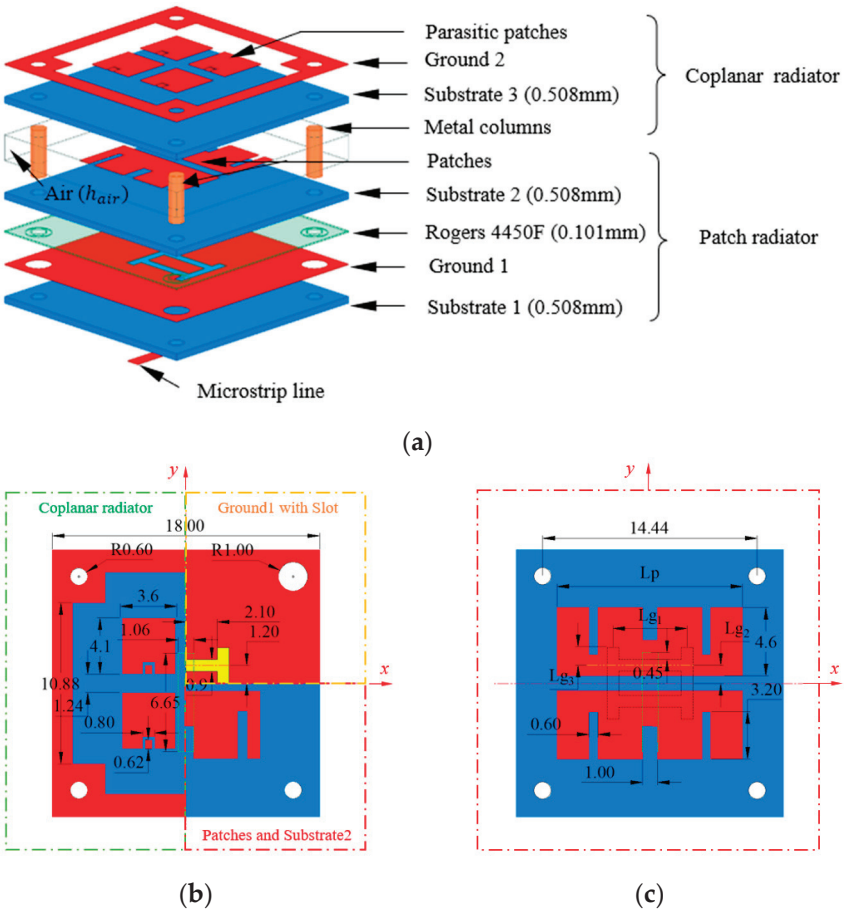

Figure 1. Antenna element structure: (**a**) 3D layout of the proposed antenna element; (**b**,**c**) parameter sizes, in millimeters, of the proposed antenna element (L_p = 12.5 mm, L_{g1} = 5 mm, L_{g2} = L_{g3} = 1.2 mm, h_{air} = 2 mm); (**b**) ground 1 patches (patch radiator) and parasitic patches (coplanar radiator); (**c**) patches (patch radiator).

2.2. Antenna Element Design

The antenna element proposed in this paper uses a novel double-H-shaped fed slot, which allows for the generation of multiple resonant modes thanks to the adopted double patch structure. More specifically, the coplanar parasitic radiator and the patch radiation structure form a resonant cavity, which reduces the Q-factor and increases the antenna's bandwidth. As shown in Figure 2, the design of the proposed antenna element was carried out in four stages. For each stage, the antenna performance, and, more precisely, the magnitude of the reflection coefficient and the pattern gain, were simulated to demonstrate the obtained improvements (Figure 3).

In the first stage (Stage I), a patch antenna with a single H-shaped slot was considered. The resonant frequency of the microstrip patch working in the TM_{10} mode was calculated as

$$f_{TM_{mn}} = \frac{c}{2\pi\sqrt{\varepsilon_r}}\sqrt{\left(\frac{m\pi}{W_p}\right)^2 + \left(\frac{m\pi}{L_p}\right)^2} \quad (1)$$

where W_p and L_p are the effective width and length, calculated according to [1]. The antenna bandwidth, computed as the frequency range for which the magnitude of the reflection coefficient is below −10 dB, is from 15.17 to 15.73 GHz, thus resulting in a 3.6% FBW and peak gain of 6.8 dBi at 15.5 GHz.

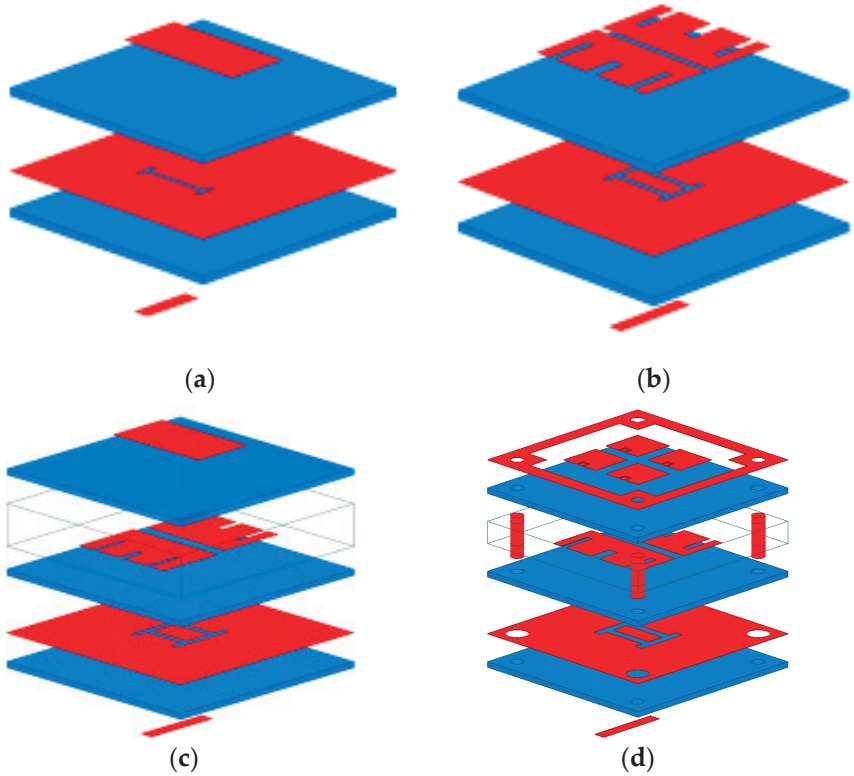

Figure 2. Design stages of the antenna element: (**a**) stage I, (**b**) stage II, (**c**) stage III, and (**d**) stage IV.

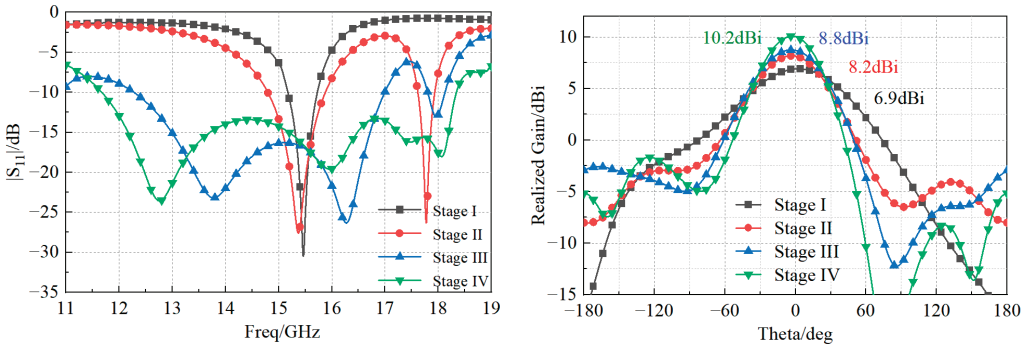

Figure 3. Simulated (**a**) magnitude of the reflection coefficient and (**b**) gain pattern at the four stages of the antenna design shown in Figure 2.

In the second stage (Stage II), two H-shaped feeding slots were considered in the ground plane. The geometrical parameters of the slot (Figure 1) satisfied the following condition:

$$L_{g1} + L_{g2} + L_{g3} \approx \lambda_g \tag{2}$$

where the parameters $L_{g1} \approx \frac{\lambda_g}{2}$, $L_{g3} \approx \frac{\lambda_g}{4}$, L_{g2} can be fine-tuned in order to optimize the impedance match. The antenna was characterized by two resonance frequencies at 15.5 GHz and 17.7 GHz (Figure 3a), with 7.1% FBW and 1.7% FBW, respectively. The peak gain of the pattern obtained at 15.5 GHz was 8.2 dBi (Figure 3b).

The third stage (Stage III) showed that the antenna's bandwidth was greatly improved by adopting a stacked structure. Moreover, the peak gain increased to 8.8 dBi. The distance h_{air} between the coplanar radiator and the patch radiator was calculated as

$$h_{air} = \frac{c}{4\pi f}(\varphi_1 + \varphi_2) + \frac{\lambda}{2}n, n = 1, 2, \ldots \quad (3)$$

where φ_1 and φ_2 are the reflection phase of the patch radiator and the coplanar radiator.

The last stage (Stage IV) consisted of the final design, with a bandwidth of 12 GHz to 18.25 GHz (41.3% FBW) and a peak gain of 10.2 dBi. Figure 4 shows that the operating bandwidth of the coplanar radiator excited by FloquetPort was 8.25–12.14 GHz (38.2% FBW). When the patch radiator was used as its feed source, the coplanar radiator received near-field electromagnetic wave excitation formed by the patch, causing changes in its impedance bandwidth.

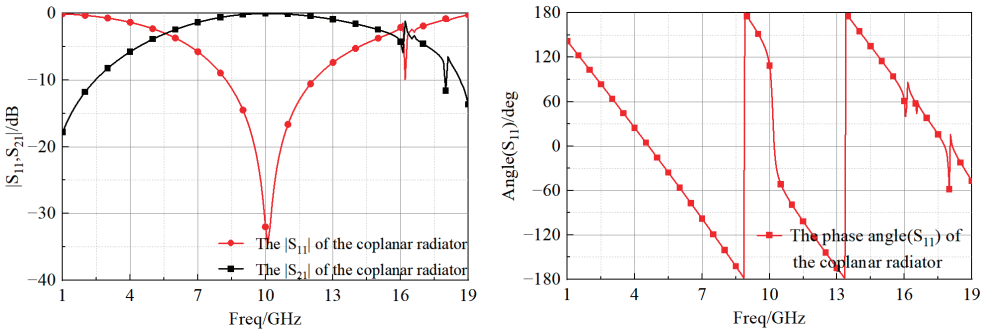

Figure 4. Values of the (**a**) magnitude and (**b**) phase of the reflection coefficient of the coplanar radiator.

To maintain high gain over a wide bandwidth, the characteristic mode of the coplanar radiator was analyzed using HFSS to exploit the mode in order to generate a pattern with high gain. Figure 5 shows that the coplanar radiator was able to generate 7 modes, with corresponding mode significance |MS| > 0.707 in the range between 11 GHz and 20 GHz. The characteristic current corresponding to each mode is shown in Figure 6. The current of modes 1 and 2 was distributed unidirectionally along the *x*-axis and worked at different frequency bands. For Mode 1, the bandwidth of |MS| > 0.707 was between 12 GHz to 14.7 GHz, which can be considered as the lowest frequency part of the bandwidth in combination with the operating frequency band of the previous feed antenna. For Mode 2, the bandwidth of |MS| > 0.707 was 14.7 GHz to 20 GHz. By stimulating these two modes, the antenna can achieve a high gain in a wide band. In mode 3, the bandwidth of |MS| > 0.707 was between 14.5–20 GHz. The current of the parasitic patches and ground 2 was in the opposite direction along the x-axis and in the offset state. When using this mode, one needs to enhance or weaken a certain mode according to the mode of the patch radiator. The current components of the parasitic patch in mode 4 along the x and y axes were in the offset state, and it could not be used as the main radiation mode. Modes 5, 6, and 7 were unsuitable for linear polarization and high gain. The combination of modes 1, 2, and 3 of the coplanar radiator and the patch radiator enabled the overall structure to obtain a high gain and a high bandwidth.

Indeed, the antenna resonated in the frequency range between 12 GHz and 18.25 GHz, with a 41.3% FBW, and the peak gain was equal to 10.2 dBi at 15.5 GHz. In order to achieve such a performance, the value of the parameter *Lp* (i.e., the length of radiation patches) was properly tuned. As is evident from Figure 7, the antenna element reached the widest bandwidth when *Lp* = 12.5 mm.

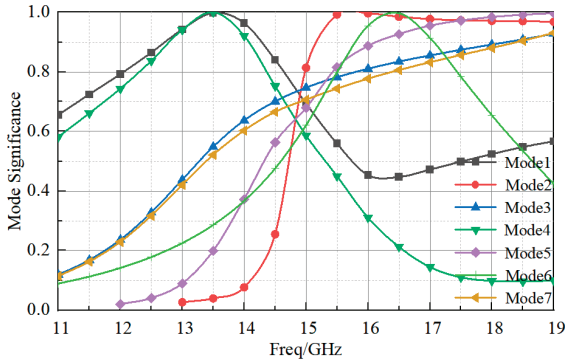

Figure 5. The mode significance of the coplanar radiator.

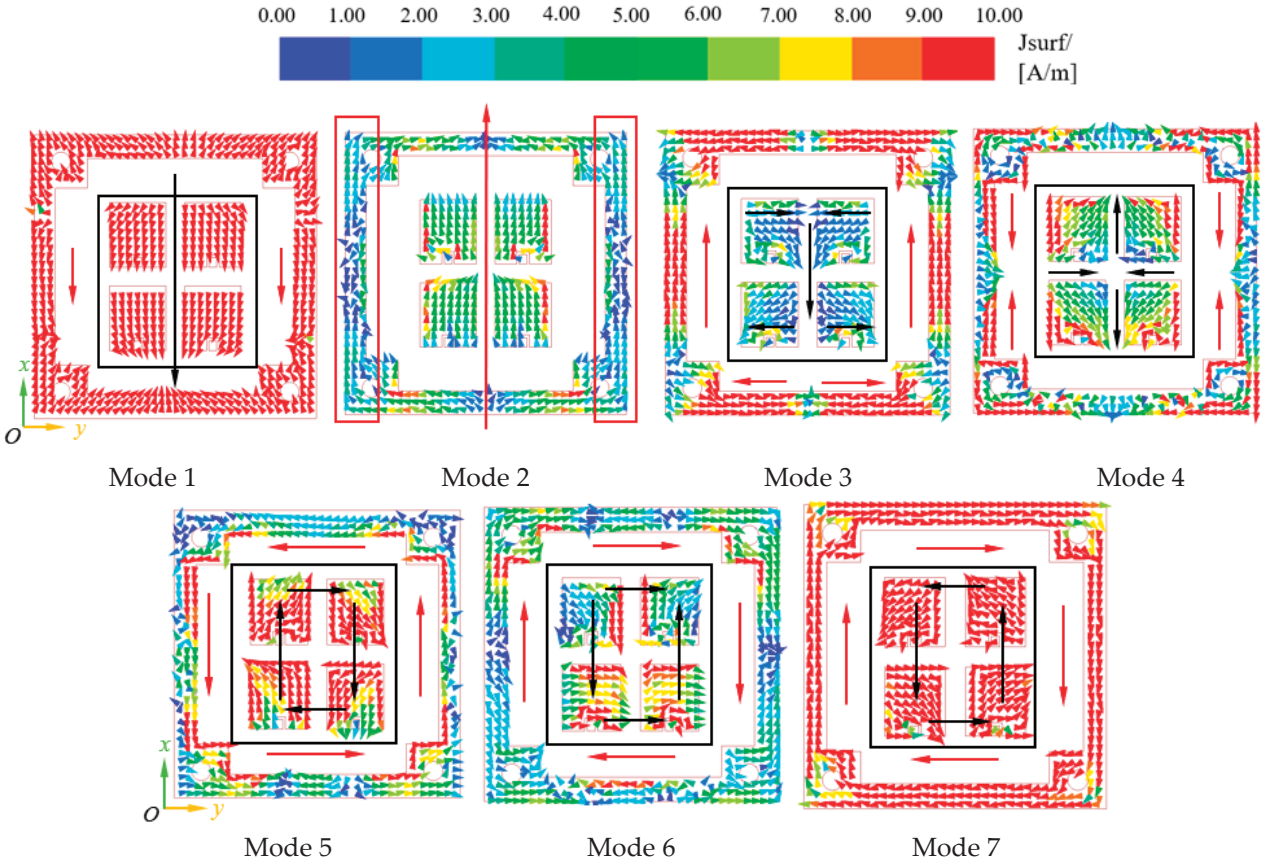

Figure 6. The current mode distribution of the coplanar radiator.

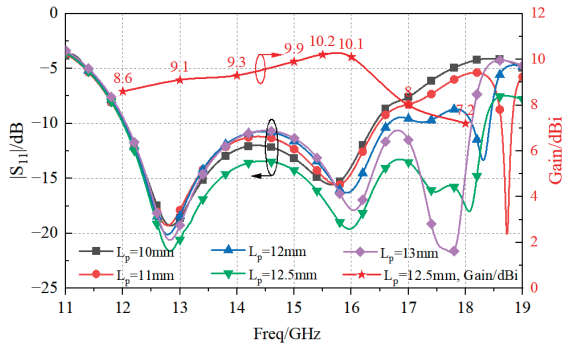

Figure 7. Numerical analysis of the magnitude of the reflection coefficient and peak gain versus *Lp*.

The working principle of the proposed antenna element can be described as follows. At the frequency f = 13 GHz, the radiation patch worked as shown in Figure 8a, and an overall downward current was induced on the metallic patches. The edge of the ground plane in the coplanar radiator (ground 2) supported a current induced in the same direction, thus resulting in the superposition of two radiation modes. The pattern gain, shown in Figure 9a, reached a peak value of 9.1 dBi. At f = 16 GHz, the radiation patch worked as shown in Figure 8b, and an overall upward current was induced on the patch. The parasitic patches and the ground plane in the coplanar radiator supported an induced current in the same direction. The corresponding pattern is shown, in this case, in Figure 9d, and the achieved peak gain was equal to 10.1 dBi. Differently, at f = 17.5 GHz, the current induced on the radiation patch was mainly concentrated near the gaps, as shown in Figure 8c. There was no current induced in the coplanar radiator, which became a transmission surface. The pattern obtained in this case is shown in Figure 9e. At f = 18 GHz, the current induced on the radiation patch was mainly concentrated at the narrow edge, as shown in Figure 8d, and the parasitic patches in the coplanar radiator also supported a current mode. The peak gain resulted to be equal to 7.2 dBi, and the corresponding pattern is reported in Figure 9d.

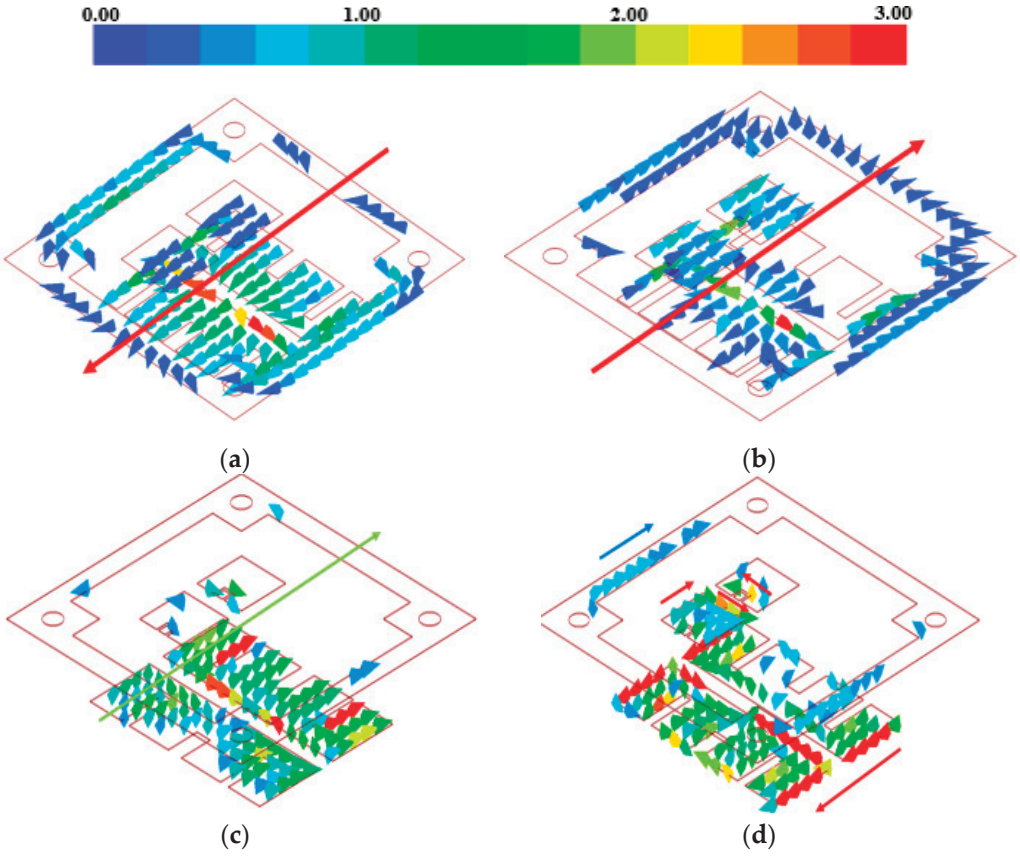

Figure 8. Current distribution on the antenna element at (**a**) 13 GHz, (**b**) 16 GHz, (**c**) 17.5 GHz, and (**d**) 18 GHz.

For the sake of comparison, Table 1 reports the principal geometrical and electrical features of the proposed antenna solution as compared to other patch antennas previously published in the literature. Compared with the antenna element in [1,2], which adopted a large number of FSS parasitic structures to improve its bandwidth and gain, our element reached a wider bandwidth, with smaller floor space and good performance in terms of gain. Compared with the element in [8], which was cavity-backed to improve the gain, our work achieved a wider bandwidth and a higher gain. Compared with the antenna element in [13], which had a traditional stacked structure, a single H-slot, and air dielectric substrates, our antenna element had a higher gain, although the FBW was smaller since

the substrate had higher permittivity. The antenna element in [32,33], which adopted a double-Y-shaped slot and microstrip dipole antenna, respectively, still had a wider FBW, but less peak gain. In addition, the antenna element in [34] needed to match a more complex feeding structure. As compared to the antennas in [31,34,35], characterized by a rectangular patch [31]; a single-slot, multilayer parasitic structure [34]; and a planar magneto-electric dipole stack structure [35], our solution achieved a wider bandwidth and a greater gain. Accordingly, in comparison with previous works, the antenna proposed in this paper guaranteed a good trade-off between bandwidth, gain, and antenna size.

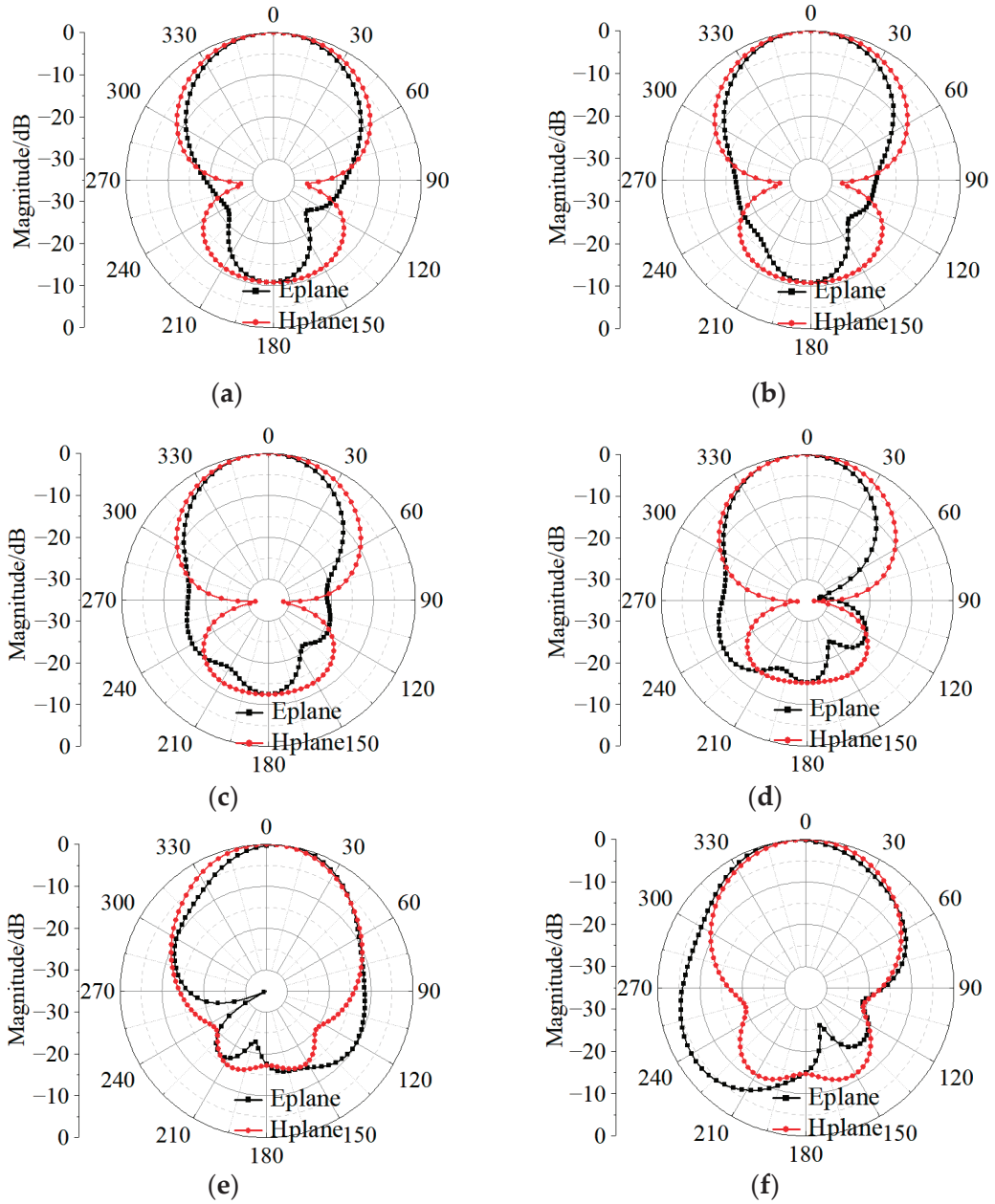

Figure 9. Radiation patterns of the proposed antenna at (**a**) 13 GHz, (**b**) 14 GHz, (**c**) 15 GHz, (**d**) 16 GHz, (**e**) 17.5 GHz, and (**f**) 18 GHz.

Table 1. Comparison with benchmark patch antennas.

Ref	Dimensions ($\lambda_0 \times \lambda_0 \times \lambda_0$)	Permittivity (ε_r)	Bandwidth, FBW (GHz, %)	Peak Gain (dBi)	Number of Ports
[3]	4.8 × 4.8 × 0.63	2.2	8.3–11.25, 29.5%	10.4	1
[4]	1.48 × 1.48 × 0.04	3	8.17–9.61, 16.2%	8.9	1
[8]	0.7 × 0.7 × 0.13	2.2	25.58–27.04, 5.2%	7.8	1
[13]	/	1.1	3.27–6, 59.7%	8	1
[31]	1.3 × 0.7 × 0.04	2.2	5.13–5.85, 13.1%	9.7	1
[32]	0.4 × 0.4 × 0.23	2.65	3.6–6, 49.8%	8.5	1
[33]	0.78 × 0.78 × 0.18	4.4	1.68–2.75, 48%	8.9	2
[34]	0.5 × 0.5 × 0.25	3.2	6.5–10.2, 37%	7.8	1
[35]	0.96 × 0.96 × 0.14	2.5	5.2–5.9, 12.6%	9.6	1
Present	0.9 × 0.9 × 0.18	3.66	12–18.25, 41.3%	10.2	1

2.3. 4 × 4 Antenna Array Design

In addition to the antenna element, the design of a 4 × 4 antenna array, shown in Figure 10, was carried out in this work. Towards this end, the inter-element spacing was set according to the antenna element length ($0.9\lambda < \lambda$), and an equal power division (1 to 16 divider) in a corporate feed network was properly designed. Figure 11 illustrates the geometry of the feeding network and of the 1-to-16 power divider.

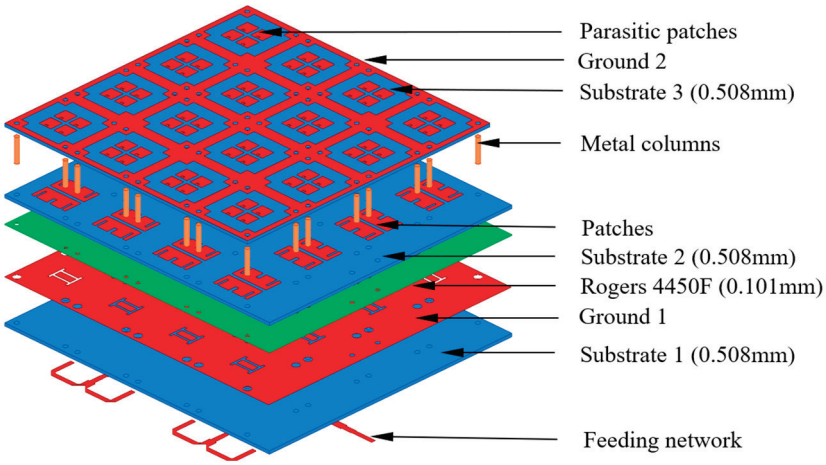

Figure 10. Structure of the proposed 4 × 4 antenna array.

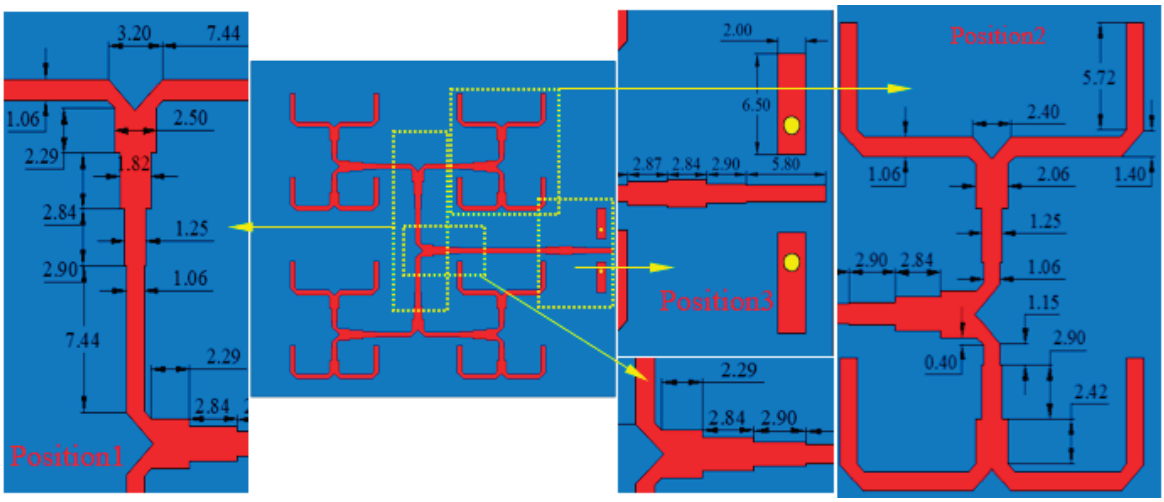

Figure 11. Structure of the corporate feeding network.

The simulated reflection and transmission coefficients at positions 1, 2, and 3 of Figure 11 are shown in Figures 12a and 12b, respectively. In the frequency range of [10–20] GHz, the reflection coefficient obtained in the three positions was lower than −25 dB. The transmission coefficients of the one-to-two T-type impedance transformation section at position 1 and 2 were higher than −3.1 dB, and the impedance compensation transformation section at position 3 was higher than −0.2 dB, thus implying reduced losses along the feeding line. The plot of the simulated reflection and transmission coefficients of the feed network, shown in Figure 12c, demonstrated a good matching ability with $|S_{11}|$ values below −15 dB from 9 to 20 GHz. As for the array, the values of the simulated reflection coefficient and of the peak gain given in Figure 12d show that the antenna operated (i.e., $|S_{11}| < -10$ dB) from 11.4 GHz to 17 GHz, and the maximum gain was 19.1 dBi.

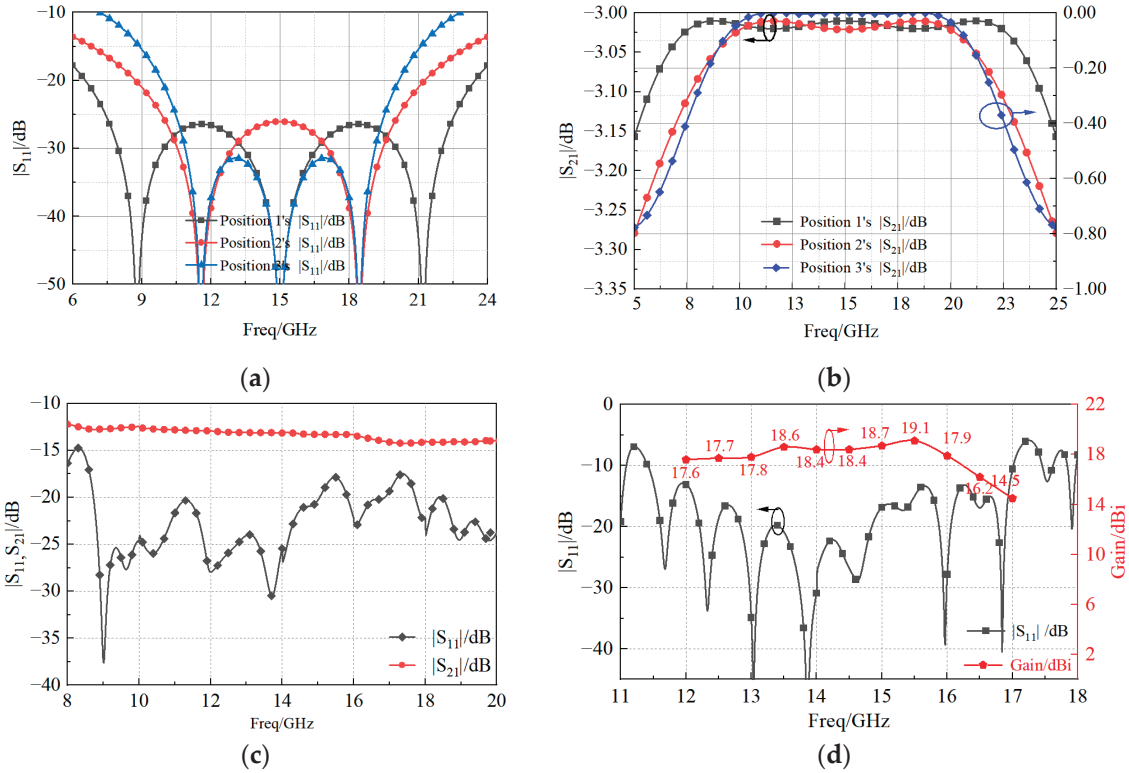

Figure 12. Simulated magnitude of the (**a**) reflection and (**b**) transmission coefficients of position 1, position 2, and position 3; the (**c**) whole $|S_{11}, S_{21}|$ of the feeding network; and the (**d**) reflection coefficient and gain of the proposed antenna array.

3. Experimental Measurements and Discussion

3.1. Measurement at Normal Temperature

The prototype of the proposed 4 × 4 patch antenna array is shown in Figure 13. The patch radiator and the coplanar radiator (Figure 1a) were assembled by stainless steel screws. The final dimensions of the fabricated prototype resulted as 78 × 78 × 3.7 mm^3. To measure the reflection coefficient, a ROHDE and SCHWARZ vector network analyzer was used. The radiation patterns were instead measured in an anechoic far-field chamber at Space Star Technology Co., Ltd., in Xi'an, China. The gain was measured using the gain comparison method with standard gain horns, and the gain measurement uncertainty ranged between ±0.5 dB according to the specification of the anechoic far-field chamber. The values of the simulated and measured magnitude of the reflection coefficient, as well as the peak gain, are shown in Figure 14. The operation bandwidth resulted to be almost 5.6 GHz, with a FBW = 39.4%, while the peak gain at 15.5 GHz was 18.7 dBi, only 0.4 dB below the simulated value. In addition, the gain measurements showed good agreement with the simulated values, since the deviation was smaller than 0.5 dB in the range of 13–

14 GHz and 15–17 GHz, and 1 dB in the range of 11.4–13 GHz and 14–15 GHz. Moreover, the power pattern measured in the E- and H-plane at 12.5, 13.5, 15.5, and 16.5 GHz agreed well with the simulated results, as shown in Figure 15. From the analysis of the pattern at 12.5, 13.5, and 15.5 GHz, it resulted that the relative sidelobe level was below −11 dB. As for the cross-polarization level, it was always below −15 dB, and below −20 dB in the angular range ± 20°. At 15.5 GHz, the mismatch between sidelobe levels in the E- and H-planes was about ±2 dB. At 16.5 GHz, the array antenna had obvious side radiation, which reduced its gain. In addition, the measured patterns had lower relative sidelobe levels as compared to the simulated results. We summarize the reasons for the differences between the simulation and the experiment as follows: First, it is difficult to avoid errors introduced during antenna processing. Furthermore, the antenna is affected by tools such as clamps during testing, which affects its side radiation. Moreover, errors in antenna sampling and turntable position during testing can also affect the antenna's performance. In addition, if the antenna needs to be used in situations with high sidelobe requirements, the operating frequency band should be controlled within the range of 12 GHz to 15.5 GHz.

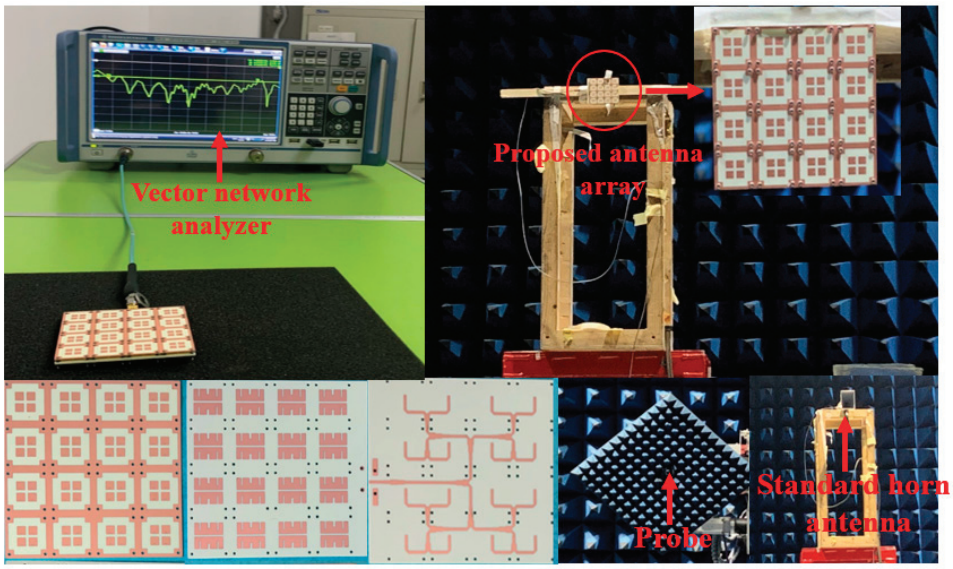

Figure 13. Photographs of the fabricated prototype and measurement setup.

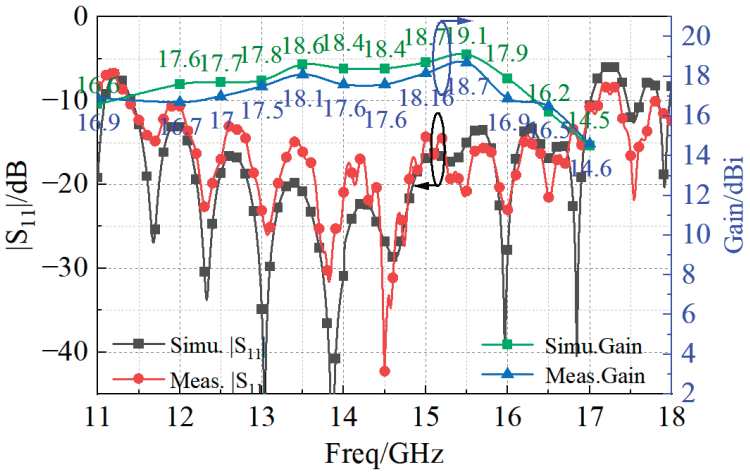

Figure 14. Comparison between simulated and measured reflection coefficient magnitude.

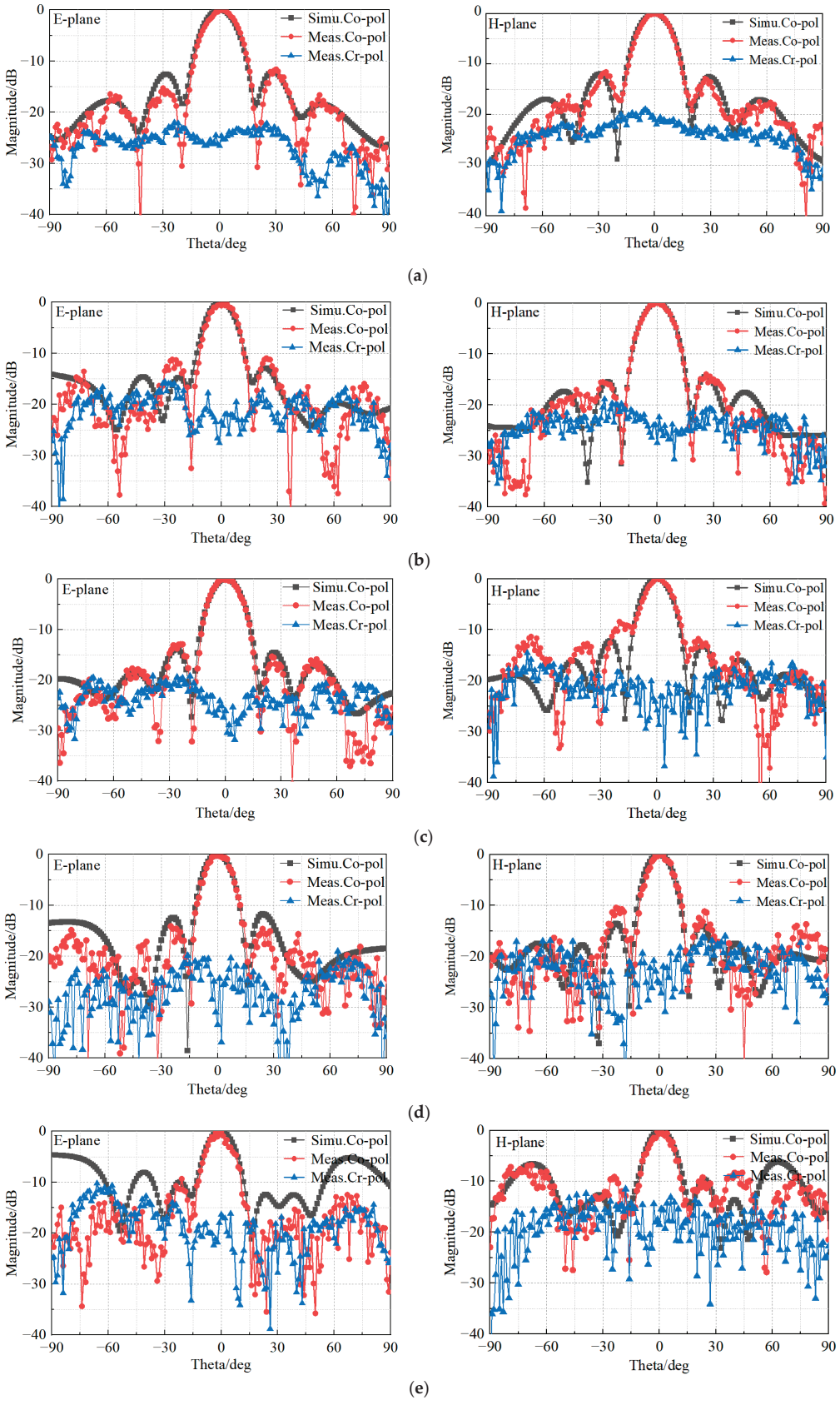

Figure 15. Measured and simulated radiation patterns of the proposed 4 × 4 wideband antenna array at (**a**) 12.5 GHz, (**b**) 13.5 GHz, (**c**) 14.5 GHz, (**d**) 15.5 GHz, and (**e**) 16.5 GHz.

3.2. Measurement in High-Low Temperature Chamber

In order to verify the performance of the proposed antenna in high-temperature environments, the measurement of the reflection coefficient was carried out in a high–low temperature chamber, as shown in Figure 16.

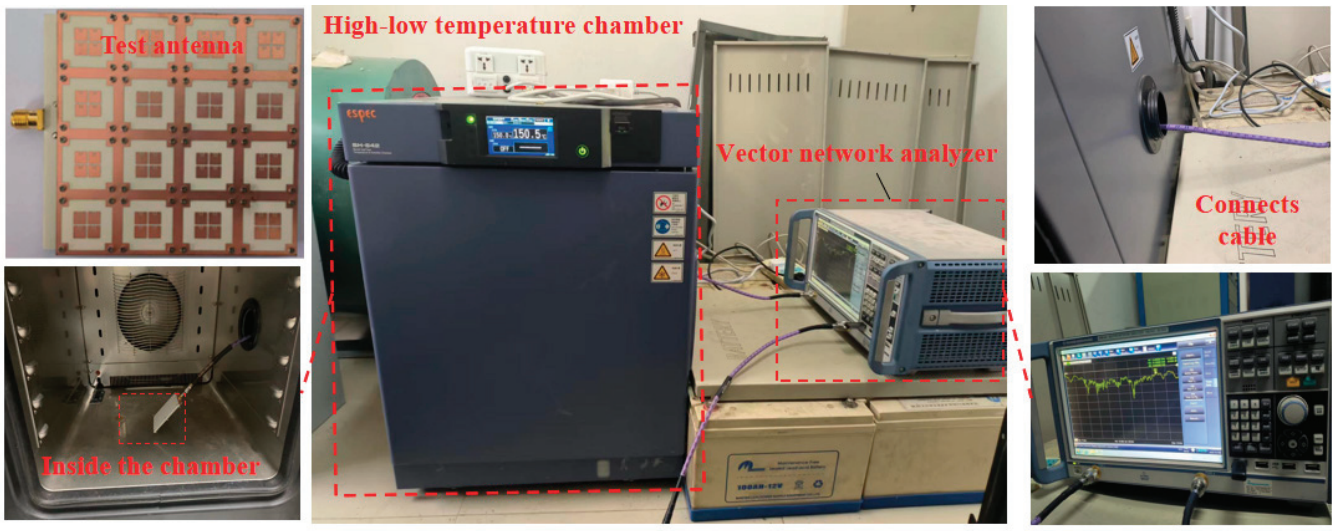

Figure 16. Measurement setup in the high–low temperature chamber.

More specifically, an ESPEC (SH-642) high–low temperature chamber and a vector network analyzer were used. The measurement considered nine different temperatures, namely, 20 °C, −20 °C, 0 °C, 40 °C, 60 °C, 80 °C, 100 °C, 130 °C, and 150 °C. The behavior of the magnitude of the reflection coefficient versus the frequency is shown in Figure 17.

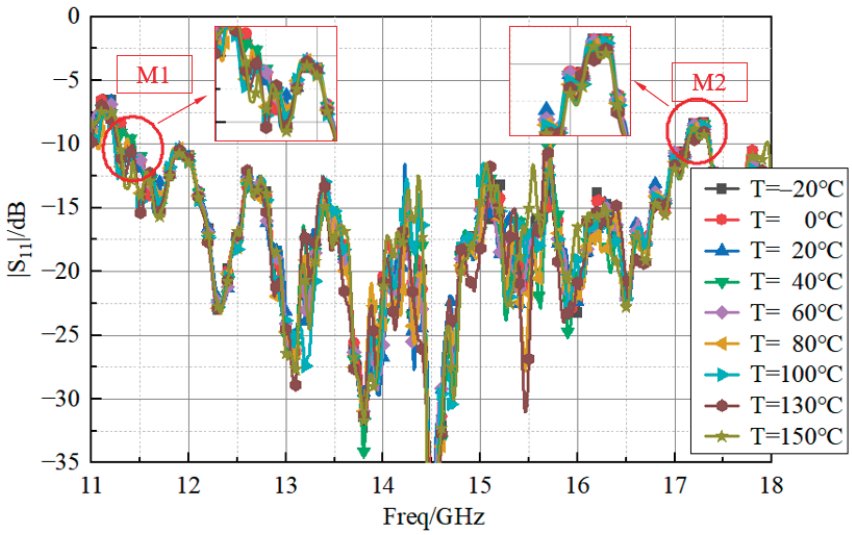

Figure 17. Measured reflection coefficient at nine different temperatures.

The values of the minimum frequency (M1), the maximum frequency (M2), and the bandwidth of the curves shown in Figure 17 are reported in Table 2. It is clear that the proposed antenna had good bandwidth stability in the temperature range from −20 °C to 150 °C, as the reflection coefficient showed marginal variations during the high–low temperature tests. For the sake of completeness, Figure 18 reports the values of the reflection coefficients, measured at a temperature of 20 °C, with the antenna in the chamber (curve "20 °C_in") and outside the chamber (curve "20 °C_out").

Table 2. Measurement of the antenna bandwidth at different temperatures.

Temperature (°C)	M1 (GHz)	M2 (GHz)	Bandwidth (GHz)
−20	11.39	17.04	5.65
0	11.38	17.02	5.64
20	11.27	17.01	5.74
40	11.44	17.12	5.68
60	11.46	17.10	5.64
80	11.38	17.12	5.74
100	11.40	17.12	5.72
130	11.44	17.10	5.66

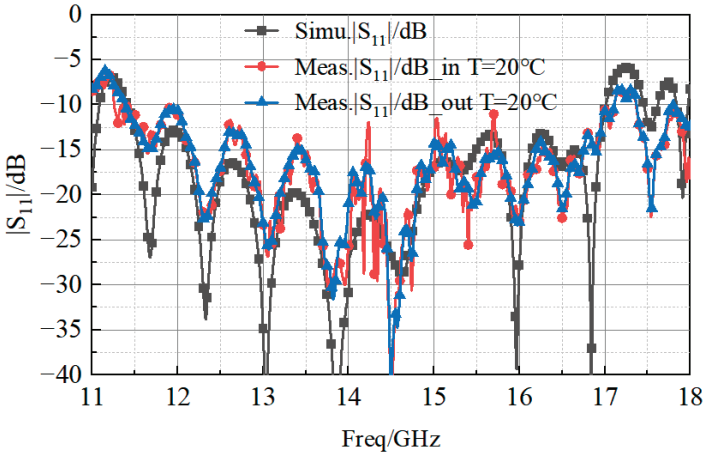

Figure 18. Measured reflection coefficient at a temperature of 20 °C inside and outside the high–low temperature chamber.

According to the datasheet on the substrate material, the expected variation of the permittivity in the temperature range between −50 °C and 150 °C was about 3.66 ± 0.05. Therefore, the impact on the magnitude of the reflection coefficients was also simulated (Figure 19). Like in Table 2, the corresponding values of the minimum frequency (M1), the maximum frequency (M2), and the bandwidth reported in Table 3 demonstrate that there was good agreement with the experimental measurements.

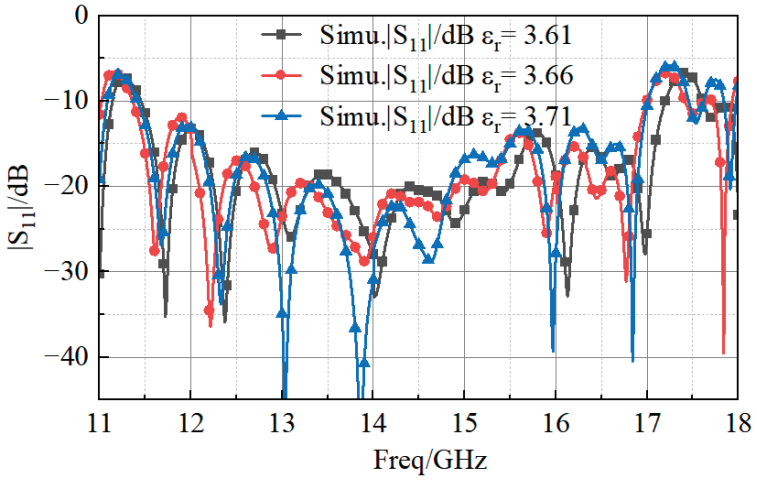

Figure 19. Simulated reflection coefficient magnitude values.

Table 3. Simulation of antenna bandwidth at high and low temperatures.

Permittivity	M1 (GHz)	M2 (GHz)	Bandwidth (GHz)
3.61	11.45	17.20	5.75
3.66	11.4	17	5.6
3.71	11.36	17	5.64

Moreover, although the power pattern could not be measured in the high–low temperature chamber, it has been simulated when changing the material property, and the results in Figure 20 confirm the expected stability of the pattern.

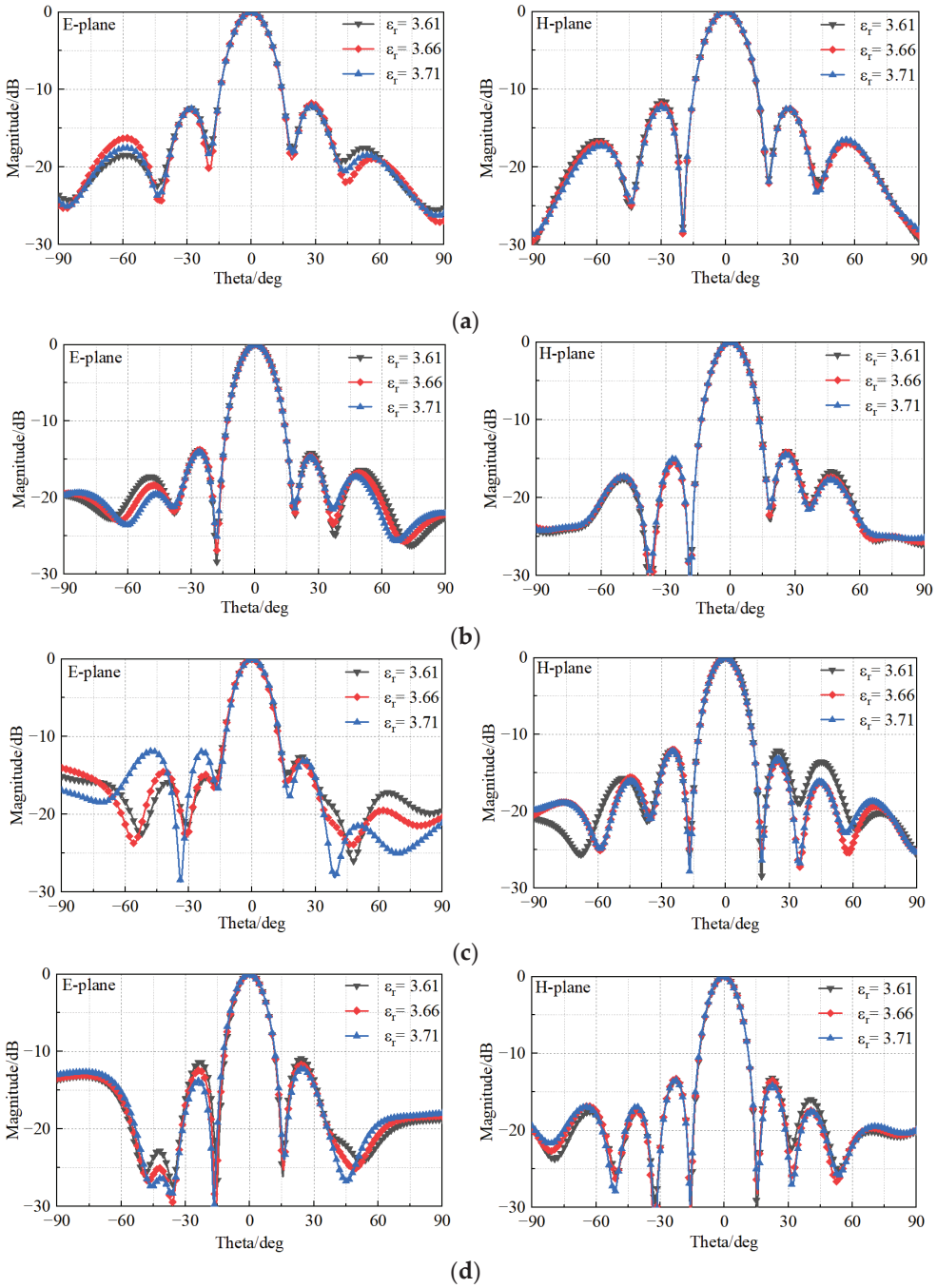

Figure 20. *Cont.*

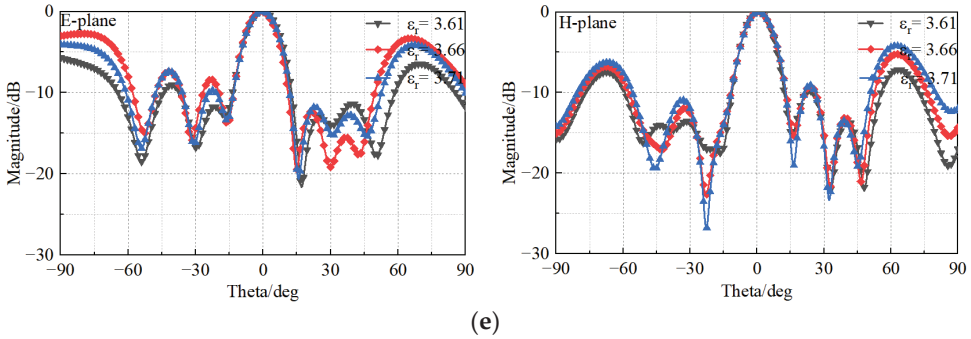

(**e**)

Figure 20. Simulated radiation patterns of the antenna in a high–low temperature chamber at (**a**) 12.5 GHz, (**b**) 13.5 GHz, (**c**) 14.5 GHz, (**d**) 15.5 GHz, and (**e**) 16.5 GHz.

4. Conclusions

The design of a low-profile, wide-band, and high-gain 4 × 4 antenna array based on a novel double-H-shaped slot microstrip patch radiating element, robust against high temperature variations, was presented. The corresponding prototype was fabricated, and the measurement results demonstrated that the antenna array reached a 5.6 GHz bandwidth (39.4% FBW, Ku-band) and a maximum gain of 18.7 dBi. The test and simulation results also indicate that the proposed antenna array had good stability in a temperature range from −50 °C to 150 °C, and that, therefore, the antenna has good potential to be applied in higher-temperature environments.

Author Contributions: All authors contributed equally to this work. Conceptualization, R.L. and P.L.; methodology, P.R. and A.Á.S.S.; validation, L.S., A.Á.S.S. and P.R.; software, R.L., X.L. and Z.F.; validation, R.L. and X.L.; writing—original draft preparation, R.L. and P.L.; writing—review and editing, P.L. and P.R.; project administration, P.L. and W.X.; funding acquisition, P.L. and P.R. All authors have read and agreed to the published version of the manuscript.

Funding: This work was supported by the National Natural Science Foundation of China (Grant No. 51875431 and No. 61971334) and the Natural Science Basic Research Plan in Shaanxi Province (Grant No. 2022-JC-33, and No. 2023-GHZD-35).

Institutional Review Board Statement: Not applicable.

Informed Consent Statement: Not applicable.

Data Availability Statement: Not applicable.

Conflicts of Interest: The authors declare no conflict of interest. The funders had no role in the design of the study; in the collection, analyses, or interpretation of data; in the writing of the manuscript; or in the decision to publish the results.

References

1. Nagy, L. Microstrip Antenna Development for Radar Sensor. *Sensors* **2023**, *23*, 909. [CrossRef] [PubMed]
2. Jain, P.; Chhabra, H.; Chauhan, U.; Prakash, K.; Gupta, A.; Soliman, M.S.; Islam, M.S.; Islam, M.T. Machine learning assisted hepta band THz metamaterial absorber for biomedical applications. *Sci. Rep.* **2023**, *13*, 1792. [CrossRef] [PubMed]
3. Sheng, X.; Lu, X.; Liu, N.; Liu, Y. Design of Broadband High-Gain Fabry–Pérot Antenna Using Frequency-Selective Surface. *Sensors* **2022**, *22*, 9698. [CrossRef] [PubMed]
4. Kim, S.-W.; Yu, H.-G.; Choi, D.-Y. Analysis of Patch Antenna with Broadband Using Octagon Parasitic Patch. *Sensors* **2021**, *21*, 4908. [CrossRef] [PubMed]
5. Anim, K.; Danuor, P.; Park, S.-O.; Jung, Y.-B. High-Efficiency Broadband Planar Array Antenna with Suspended Microstrip Slab for X-Band SAR Onboard Small Satellites. *Sensors* **2022**, *22*, 252. [CrossRef]
6. Ghimire, J.; Diba, F.D.; Kim, J.-H.; Choi, D.-Y. Vivaldi Antenna Arrays Feed by Frequency-Independent Phase Shifter for High Directivity and Gain Used in Microwave Sensing and Communication Applications. *Sensors* **2021**, *21*, 6091. [CrossRef]
7. Hehenberger, S.P.; Elmarissi, W.; Caizzone, S. Design and Installed Performance Analysis of a Miniaturized All-GNSS Bands Antenna Array for Robust Navigation on UAV Platforms. *Sensors* **2022**, *22*, 9645. [CrossRef]
8. Anim, K.; Lee, J.-N.; Jung, Y.-B. High-Gain Millimeter-Wave Patch Array Antenna for Unmanned Aerial Vehicle Application. *Sensors* **2021**, *21*, 3914. [CrossRef]

9. Zhong, S.S. *Microstrip Antenna Theory and Application*; Xidian University Press: Xi'an, China, 1991.
10. Li, P.; Wang, C.; Xu, W.; Song, L. Taylor Expansion and Matrix-Based Interval Analysis of Linear Arrays With Patch Element Pattern Tolerance. *IEEE Access* **2021**, *9*, 21004–21015. [CrossRef]
11. Wang, C.; Li, P.; Xu, W.; Song, L.; Huang, J. Tolerance analysis of 3D printed patch antennas based on interval arithmetic. *Microw. Opt. Technol. Lett.* **2021**, *63*, 516–524. [CrossRef]
12. Li, P.; Xu, W.Y.; Song, L.W. Power Pattern Tolerance Analysis of Radome with the Material Properties Error Based on Interval Arithmetic. *IEEE Antennas Wirel. Propag. Lett.* **2017**, *16*, 1321–1324. [CrossRef]
13. Matin, M.; Sharif, B.; Tsimenidis, C. Probe-fed stacked patch antenna for wideband applications. *IEEE Trans. Antennas Propag.* **2007**, *55*, 2385–2388. [CrossRef]
14. Sung, Y. Bandwidth enhancement of a microstrip line-fed printed wide slot antenna with a parasitic center patch. *IEEE Trans. Antennas Propag.* **2012**, *60*, 1712–1716. [CrossRef]
15. Wi, S.; Lee, Y.; Yook, J. Wideband microstrip patch antenna with U shaped parasitic elements. *IEEE Trans. Antennas Propag.* **2007**, *55*, 1196–1199. [CrossRef]
16. Lee, K.; Luk, K.; Tong, K.; Shum, S.; Huynh, T.; Lee, R. Experimental and simulation studies of the coaxially fed U-slot rectangular patch antenna. *IEE Proc. Microw. Antennas Propag.* **1997**, *144*, 354–358. [CrossRef]
17. Khidre, A.; Lee, K.; Elsherbeni, A.Z.; Yang, F. Wide band dualbeamU-slot microstrip antenna. *IEEE Trans. Antennas Propag.* **2013**, *61*, 1415–1418. [CrossRef]
18. Liu, W.; Yin, Y.; Xu, W.; Zuo, S. Compact open-slot antenna with bandwidth enhancement. *IEEE Antennas Wirel. Propag. Lett.* **2011**, *10*, 850–853.
19. Salucci, M.; Robol, F.; Anselmi, N.; Hannan, M.A.; Rocca, P.; Oliveri, G.; Donelli, M.; Massa, A. S-Band spline-shaped aperture-stacked patch antenna for air traffic control applications. *IEEE Trans. Antennas Propag.* **2018**, *66*, 4292–4297. [CrossRef]
20. Massa, A.; Salucci, M. On the design of complex EM devices and systems through the system-by-design paradigm—A framework for dealing with the computational complexity. *IEEE Trans. Antennas Propag.* **2018**, *70*, 1328–1343. [CrossRef]
21. Ou, J.-H.; Huang, J.; Liu, J.; Tang, J.; Zhang, X.Y. High-Gain Circular Patch Antenna and Array with Introduction of Multiple Shorting Pins. *IEEE Trans. Antennas Propag.* **2020**, *68*, 6506–6515. [CrossRef]
22. Liu, Z.; Zhu, L.; Zhang, X. A Low-Profile and High-Gain CP Patch Antenna with Improved AR Bandwidth Via Perturbed Ring Resonator. *IEEE Antennas Wirel. Propag. Lett.* **2019**, *18*, 397–401. [CrossRef]
23. Zhang, X.; Hong, K.-D.; Zhu, L.; Bi, X.-K.; Yuan, T. Wideband Differentially Fed Patch Antennas Under Dual High-Order Modes for Stable High Gain. *IEEE Trans. Antennas Propag.* **2021**, *69*, 508–513. [CrossRef]
24. Hong, K.-D.; Zhang, X.; Zhu, L.; Yuan, T. A High-Gain and Pattern-Reconfigurable Patch Antenna Under Operation of TM_{20} and TM_{21} Modes. *IEEE Open J. Antennas Propag.* **2021**, *2*, 646–653. [CrossRef]
25. Luo, Y.; Chen, Z.N.; Ma, K. A Single-Layer Dual-Polarized Differentially Fed Patch Antenna with Enhanced Gain and Bandwidth Operating at Dual Compressed High-Order Modes Using Characteristic Mode Analysis. *IEEE Trans. Antennas Propag.* **2020**, *68*, 4082–4087. [CrossRef]
26. Wang, X.; Tang, S.; Yang, L.; Chen, J. Differential-Fed Dual-Polarized Dielectric Patch Antenna with Gain Enhancement Based on Higher Order Modes. *IEEE Antennas Wirel. Propag. Lett.* **2020**, *19*, 502–506. [CrossRef]
27. Zhang, X.; Tan, T.-Y.; Wu, Q.-S.; Zhu, L.; Zhong, S.; Yuan, T. Pin-Loaded Patch Antenna Fed with a Dual-Mode SIW Resonator for Bandwidth Enhancement and Stable High Gain. *IEEE Antennas Wirel. Propag. Lett.* **2021**, *20*, 279–283. [CrossRef]
28. Yeap, S.; Chen, Z. Microstrip patch antennas with enhanced gain by partial substrate removal. *IEEE Trans. Antennas Propag.* **2010**, *58*, 2811–2816. [CrossRef]
29. Bhattacharyya, A. Long rectangular patch antenna with a single feed. *IEEE Trans. Antennas Propag.* **1990**, *38*, 987–993. [CrossRef]
30. Chin, C.; Xue, Q.; Chan, C. Design of a 5.8-GHz rectenna incorporating a new patch antenna. *IEEE Antennas Wirel. Propag. Lett.* **2005**, *4*, 175–178. [CrossRef]
31. Wang, Z.; Liu, J.; Long, Y. A Simple Wide-Bandwidth and High-Gain Microstrip Patch Antenna with Both Sides Shorted. *IEEE Antennas Wirel. Propag. Lett.* **2019**, *18*, 1144–1148. [CrossRef]
32. Wei, J.; Jiang, X.; Peng, L. Ultrawideband and High-Gain Circularly Polarized Antenna with Double-Y-Shape Slot. *IEEE Antennas Wirel. Propag. Lett.* **2017**, *16*, 1508–1511. [CrossRef]
33. Zhou, Z.; Wei, Z.; Tang, Z.; Yin, Y. Design and Analysis of a Wideband Multiple-Microstrip Dipole Antenna with High Isolation. *IEEE Antennas Wirel. Propag. Lett.* **2019**, *18*, 722–726. [CrossRef]
34. Pavuluri, S.K.; Wang, C.; Sangster, A.J. High Efficiency Wideband Aperture-Coupled Stacked Patch Antennas Assembled Using Millimeter Thick Micromachined Polymer Structures. *IEEE Trans. Antennas Propag.* **2010**, *58*, 3616–3621. [CrossRef]
35. Dong, H.-J.; Kim, Y.-B.; Joung, J.; Lee, H.L. High Gain and Low-Profile Stacked Magneto-Electric Dipole Antenna for Phased Array Beamforming. *IEEE Access* **2020**, *8*, 180295–180304. [CrossRef]

sensors

MDPI

Article

Miniaturized On-Ground 2.4 GHz IoT LTCC Chip Antenna and Its Positioning on a Ground Plane

Jaime Molins-Benlliure, Marta Cabedo-Fabrés, Eva Antonino-Daviu and Miguel Ferrando-Bataller *

Antennas and Propagation Lab (APL), Instituto de Telecomunicaciones y Aplicaciones Multimedia (iTEAM), Universitat Politècnica de València (UPV), C/ Camí de Vera s/n, 46022 Valencia, Spain; jaimoben@iteam.upv.es (J.M.-B.); marcafab@dcom.upv.es (M.C.-F.); evanda@upvnet.upv.es (E.A.-D.)
* Correspondence: mferrand@dcom.upv.es

Abstract: This paper presents a very low-profile on-ground chip antenna with a total volume of $0.075\lambda_0 \times 0.056\lambda_0 \times 0.019\lambda_0$ (at f_0 = 2.4 GHz). The proposed design is a corrugated (accordion-like) planar inverted F antenna (PIFA) embedded in low-loss glass ceramic material (DuPont GreenTape 9k7 with ϵ_r = 7.1 and $\tan\delta$ = 0.0009) fabricated with LTCC technology. The antenna does not require a clearance area on the ground plane where the antenna is located, and it is proposed for 2.4 GHz IoT applications for extreme size-limited devices. It shows a 25 MHz impedance bandwidth (for $S_{11} < -6$ dB), which means a relative bandwidth of 1%). A study in terms of matching and total efficiency is performed for several size ground planes with the antenna installed at different positions. The use of characteristic modes analysis (CMA) and the correlation between modal and total radiated fields is performed to demonstrate the optimum position of the antenna. Results show high-frequency stability and a total efficiency difference of up to 5.3 dB if the antenna is not placed at the optimum position.

Keywords: chip antenna; LTCC; small antennas; IoT antenna; bluetooth; Wi-Fi; 2.4 GHz

1. Introduction

Internet of Things (IoT) introduces a new scenario comprising all connected devices that require RF capabilities for their connection at 2.4 GHz ISM band for WLAN/Wi-Fi/Sensors (Bluetooth, Zigbee, RFID, and NFC) applications. The 2.4–2.48 GHz band is widely used in machine-to-machine (M2M) communications, and often, the wavelength at that frequency (λ_0 = 125 mm) poses a challenge for designing resonating antennas to be installed in size-limited devices. In the past decade, the interest in miniaturizing antennas [1] increased as a consequence of the inclusion of antennas in all kinds of IoT devices, even in ones with extremely limited space which required highly miniaturized antennas. These reduced-size antennas are widely known as small antennas (ESAs), and by definition, they satisfy $ka < 1$ (where k is the wavenumber and a is the smallest radius of a sphere containing the antenna). Miniaturization techniques enable the installation of antennas in such constrained scenarios, but in general, reducing the size of an antenna leads to a reduction in bandwidth and efficiency, and compromises its radiation properties. The Chu/Wheeler limit [2,3] is widely used to evaluate the radiation limitations of ESAs in terms of impedance bandwidth and efficiency. Miniaturization increases the Q-factor [4–7] and the sensitivity to the scenario where the antennas are installed [8]. It is important to note that reducing the antenna volume also reduces its bandwidth and efficiency.

Multiple single-band miniaturized antenna solutions have been presented for the 2.4 GHz ISM band for WLAN/Wi-Fi/Sensors applications. A folded strip and a slot are combined in [9] in a compact FR4 board, resulting in an antenna with a size of $0.073 \times 0.052 \times 0.008\lambda_0^3$ and obtaining a bandwidth of 5.09% for WLAN applications. In addition, a planar quasi-isotropic antenna with a folded dipole, two loaded loops, and a coplanar stripline on a PCB is analyzed in [10], obtaining an antenna with a total

size of $0.165 \times 0.164 \times 0.006\lambda_0^3$ and an impedance bandwidth of 0.99%. Furthermore, a modified meander line microstrip patch antenna is presented in [11] with a total size of $40 \times 10 \times 1.6$ mm^3 and a 12.5% impedance bandwidth for IoT applications. Lastly, a compact microstrip filter antenna is proposed in [12] for ISM band and 4G applications with a $45 \times 42 \times 0.81$ mm^3 volume and a 50% impedance bandwidth.

Regarding dual-band solutions [13–16], several antennas have been proposed to cover two ISM/Wi-Fi/WLAN bands. In [13], a textile PIFA antenna is analyzed with a $140 \times 80 \times 6$ mm^3 size covering the 433 MHZ and 2.4 GHz ISM bands. A reconfigurable FR4 microstrip-based solution is presented in [14], covering the 2.4 GHz and 2.8 GHz ISM bands for IoT applications. Yet, another dual-band solution is proposed in [15] for ISM/Wi-Fi/WLAN applications with a coplanar waveguide antenna working at the 2.45 GHz and 5.65 GHz bands with a total size of $23 \times 23 \times 0.79$ mm^3. Triple-band solutions [17,18] have been also investigated. In [17], a conformal and electronically reconfigurable antenna is presented for portable devices covering the 2.45 GHz (ISM, Wi-Fi, and WLAN), 3.3/3.5/3.9 GHz (WiMAX), and 4.1/4.9 GHz (4G/5G) bands with the use of a modified triangular patch radiator, two open-ended stubs, and PIN diodes with a total size of $30 \times 25 \times 0.254$ mm^3. In addition, in [18], a miniaturized antenna based on a square split-ring resonator that operates at the 2.4 GHz, 3.7 GHz, and 5.8 GHz WLAN/WiMAX is proposed, with a volume of $33 \times 22 \times 1.6$ mm^3.

Antennas for wearable applications are receiving more attention due to the increasing presence of wireless devices for health and sports tracking, including flexible [19,20] and textile [21] based solutions. Two solutions for earphone integration are presented in [22,23]: one with a chip antenna and another with a wideband loop antenna. Additionally, a planar solution on a semiflexible substrate is proposed in [24], featuring an I-shaped monopole and an inverted L-shaped slit with a size of $0.016 \times 0.1 \times 0.004\lambda_0^3$ and a 5.7% bandwidth.

Reconfigurable antennas [17,25–27] are also used in 2.4 GHz IoT applications. In [25], a planar complementary reconfigurable antenna with the combination of electric/magnetic dipoles is analyzed with a size of $0.285 \times 0.31 \times 0.065\lambda_0^3$, and in [26], a reconfigurable microstrip antenna with a slot and a ground plane modification is studied obtaining an impedance bandwidth of 8.7% and a size of $0.016 \times 0.016 \times 0.007\lambda_0^3$. In addition, a $25 \times 25 \times 1.6$ mm^3 five-band reconfigurable patch antenna is presented in [27] for WLAN/WiMAX applications.

Miniaturized implantable antennas are necessary for biomedical applications [28,29]. Several solutions have been proposed recently. Another application that is gaining more attention is RFID with the miniaturization of RFID tag antennas [30–33]. RFID tag antennas are used in many devices to identify tagged objects.

In the early 2000s, there was a surge of interest in miniaturized antennas embedded in ceramic substrates to address the size limitations of traditional solutions such as monopoles and PIFAs. These antennas are commonly known as chip antennas [34–39] and have since become primarily commercial solutions due to their low cost when produced in mass quantities. However, there are also low-cost non-ceramic options available, such as the multilayer PCB antenna analyzed in [40], with a size of $0.026 \times 0.013 \times 0.007\lambda_0^3$. It is worth noting that while there were many miniaturized antennas proposed in the past, chip antennas have become the predominant solution in the market today.

The use of Low-Temperature Cofired Ceramic (LTCC) technology is prevalent in the manufacturing of chip antennas. LTCC technology involves stacking ceramic layers with high electric permittivity and low loss tangent, along with metallic sheets and vias with high precision. This technology allows for a high degree of design freedom in creating multilayer antennas, owing to the availability of layers with different thicknesses. However, strict guidelines must be followed during the manufacturing process, such as maintaining proper via separation, adhering to stacking limitations, and accounting for the shrinkage factor that occurs after placing the layers in the oven.

Chip antenna manufacturers provide guidelines for appropriate antenna placement in different scenarios. This is because the contribution of the connected ground plane to small antennas is crucial, and small antennas are particularly sensitive to their surrounding envi-

ronment. Studies have shown that a significant percentage of the total radiated power of an antenna is produced by the ground plane [41]. Therefore, careful attention must be paid to the size and shape of the ground plane, as well as the placement of the antenna [42,43], in order to avoid degradation of the radiation properties of the device.

The Theory of Characteristic Modes (TCM) [44,45] is widely used for the analysis of metallic structures. Characteristic modes correspond to natural resonances of the structure and provide a great advance in getting information about how to properly feed the structure to excite the desired characteristic modes and enhance the radiation properties. As stated above, the radiation properties of ground planes play a really important role in the radiated fields of a small antenna. Investing effort to analyze ground plane modes [46–50] provides suitable information to place the small antenna properly and, in consequence, excite the desired ground plane modes enhancing the radiation properties of a device.

The Characteristic modes analysis (CMA) of ground planes with different geometries is well documented in the literature, and it is straightforwardly calculated in several electromagnetic simulators. On the contrary, when the antenna is placed on the ground plane, the analysis becomes more complex. When the antenna has a narrowband resonant behavior and a complex structure, such as the proposed antenna, fine meshing is required, which leads to time-demanding simulations and the emergence of issues such as crossing avoidance and modal tracking. In addition, the theoretical background of TCM is well established for lossless structures; hence, dielectric materials can not be easily included. To address this issue, in this paper, we only use CMA to analyze the connected ground plane and then correlate the modal radiated field of each mode to the total radiated field of the antenna+ground plane. With this strategy, high-complexity modal analysis is avoided, and the correlation of modal and total fields is used to approximate which modes of the ground plane are excited. The electromagnetic simulator utilized for the CMA is Feko software.

All the cited antennas require a clearance area (area free of metal dedicated to the antenna) on the PCB or substrate where they are installed. Some of them show a low radiation efficiency and narrow bandwidth due to their reduced size, which is, however, sufficient for the high sensitivity (<-100 dBm) that some receivers exhibit for IoT applications. The proposed LTCC antenna (designed in the CST Studio simulator) does not require a clearance area, and in Table 1, antennas with similar features are summarized. All of them show a higher impedance bandwidth, but the proposed antenna is unique in clearance area requirements (clearance-free), and it can be placed straight away on a ground plane and be operative with limited bandwidth and radiation efficiency. In addition, its resonance frequency remains stable independent of the ground plane size. The proposed antenna is highly suitable for installation in extremely size-limited devices which can not provide a dedicated area for the antenna installation.

Table 1. Comparison Table.

Ref.	BW (GHz)	BW (%)	Size (mm^3)	Size (λ_0^3)	Clearance-Free
[9]	2.362–2.492	5.36%	$9.2 \times 6.5 \times 1$	$0.073 \times 0.052 \times 0.008$	No
[11]	2.35–2.65	12.5%	$40 \times 10 \times 1.6$	$0.32 \times 0.08 \times 0.013$	No
[16]	2.4–2.5	4%	$30 \times 30 \times 2$	$0.24 \times 0.24 \times 0.016$	No
[22]	≈2.4–2.5	≈ 4%	$13 \times 4.9 \times 2$	$0.1 \times 0.04 \times 0.016$	No
[24]	2.4–2.54	5.7%	$19 \times 12 \times 0.508$	$0.15 \times 0.1 \times 0.004$	No
[40]	2.4–2.56	7.6%	$3.2 \times 1.6 \times 0.83$	$0.025 \times 0.013 \times 0.007$	No
[51]	≈2.4–2.45	≈ 2%	$7.5 \times 4 \times 1$	$0.06 \times 0.032 \times 0.008$	No
Prop.	2.4-2.425	1%	$9.3 \times 7 \times 2.45$	$0.075 \times 0.056 \times 0.019$	Yes

Furthermore, manufacturers of chip antennas provide guidelines for placing the antenna on the optimum position of a PCB, but only in general, without a clear understanding of the physical mechanisms involved. In this paper, the proposed antenna is used to analyze the degradation of the radiating performance of the device (antenna+ground plane) depending on the size of the ground plane and the position of the antenna using the CMA and the correlation of total and modal radiation patterns to demonstrate which is the

optimum position of the antenna. The paper is organized as follows: Section 2 describes the LTCC antenna geometry, and in Section 3, the analysis in terms of matching and total efficiency depending on the position of the antenna on ground planes of different sizes is performed. Characteristic modes analysis of the ground plane and correlation between total and modal fields are used to support the findings. Finally, in Section 4, the conclusions are presented.

2. Proposed LTCC Chip Antenna

The proposed miniaturized design is a corrugated (accordion-like) planar inverted F antenna (PIFA) embedded in a ceramic substrate and fabricated with LTCC technology, with a total size of $9.3 \times 7 \times 2.45$ mm^3 ($0.075 \times 0.056 \times 0.019\lambda_0^3$). The antenna geometry is depicted in Figure 1, and its dimensions are detailed in Table 2. The antenna is meant to be installed on a metallic ground plane with no clearance area requirement. Due to its reduced size and the absence of clearance, the bandwidth (25 MHz for $S_{11} < -6$ dB, which means a relative bandwidth of 1%) is compromised. However, it shows large frequency stability when the antenna is displaced on different-sized planes.

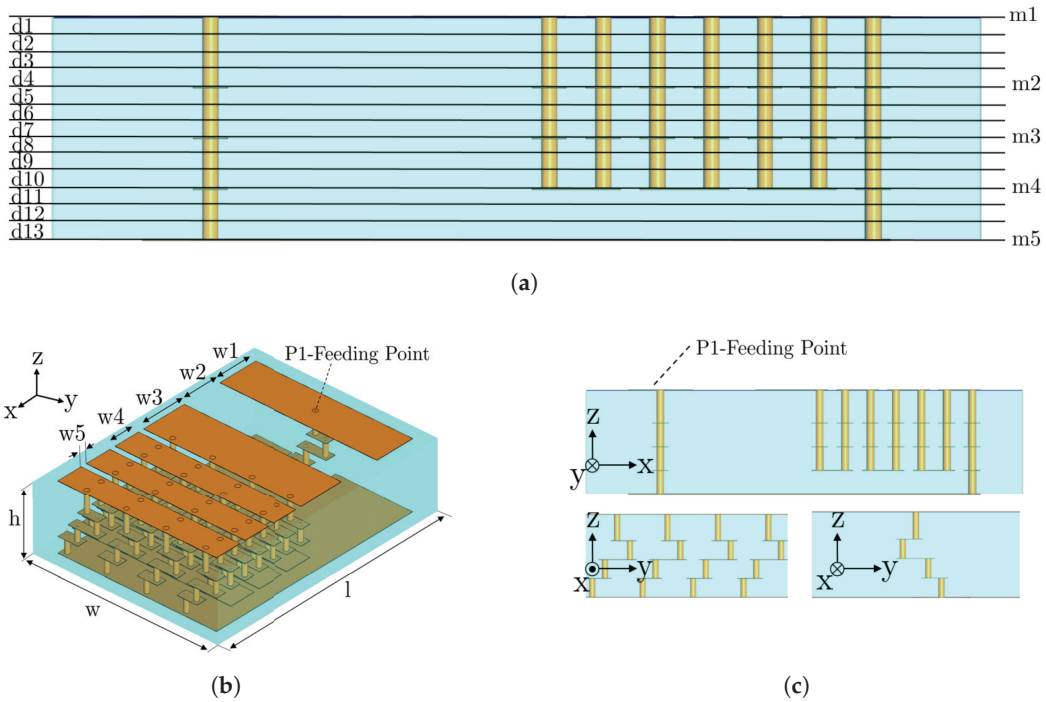

Figure 1. Geometry of the proposed low-profile LTCC chip antenna. Blue color represents the ceramic substrate, and orange color is the metallic layers and vias. (**a**) Side view with all LTCC layers specified, (**b**) overall view of the antenna (dimensions in Table 2), and (**c**) side views of the antenna.

Table 2. Dimensions of the proposed chip antenna (unit: mm).

l	w	h	w1	w2	w3	w4	w5
9.3	7	2.45	1.5	1.5	1.7	1	0.2

LTCC fabrication consists of stacking glass–ceramic sheet layers, including metallic sheets, vias, and components in between. The proposed antenna is fabricated using DuPont GreenTape 9k7 (DuPont (U.K.) Ltd., Bristol, UK) ($\epsilon_r = 7.1$, $\tan\delta = 0.0009$) low-loss glass ceramic dielectric tape, silver sheets, and silver vias. Figure 1a describes the 13 stacked ceramics layers (d1–d13) with 112 µm or 224 µm thickness. Figure 1b,c show the overall view and side views of the antenna with the grooves/ridges creating the accordion shape, respectively.

Miniaturization is obtained with the use of a high permittivity ceramic substrate and the inclusion of four ridges and three grooves to increase the electric length of the antenna and reduce its size. The design process for the proposed antenna is depicted in Figure 2a.

The first analyzed antenna is a capacitively fed PIFA of 4 mm height (Design 1 of Figure 2a). PIFA antennas are low-profile, and they can be placed on a ground plane without the need for a clearance area. In addition, the fact of feeding the antenna at the furthest point from the short circuit simplifies the future fabrication of a chip antenna, which will be welded to a PCB. The first size reduction applied to the PIFA antenna is its height reduction to 2.4 mm (Design 2 of Figure 2a), which comes with a reduction in impedance bandwidth (see Figure 2c). The following step to compact the low-profile PIFA is to embed the antenna in a ceramic substrate (Design 3 of Figure 2a). As observed, the size of the PIFA antenna is considerably reduced thanks to the use of a high-permittivity substrate. In this case, although the resonance frequency is preserved, the impedance bandwidth is decreased.

To further reduce the size of Design 3, the antenna is corrugated to increase its electrical length (Design 4 of Figure 2a), and lastly, in Design 5 (final design), the vertical walls created by the corrugation of Design 3 are replaced by vias, creating an additional reactive effect which shifts the resonance to lower frequencies and permits the extremely reduced size of the proposed design. The inclusion of so many vias in such a limited space spurs the use of LTCC technology to fabricate the antenna. The last design accounts for the restrictions of the LTCC fabrication process, where the vias must be meandered (see Figure 2b,c) because no more than four layers with vias at the same point can be stacked. Otherwise, bulge effects may appear.

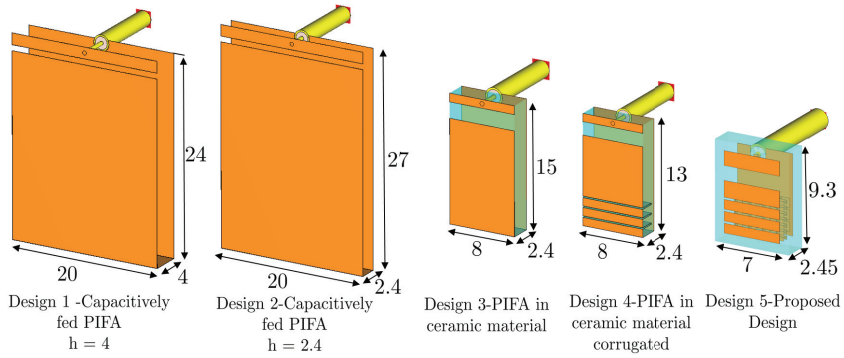

(**a**)

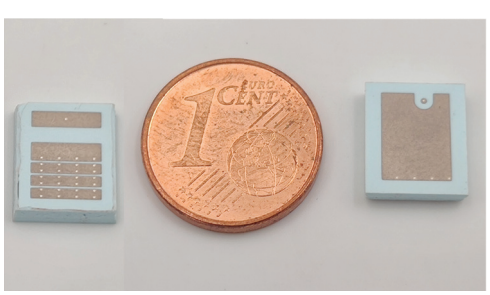

(**b**)

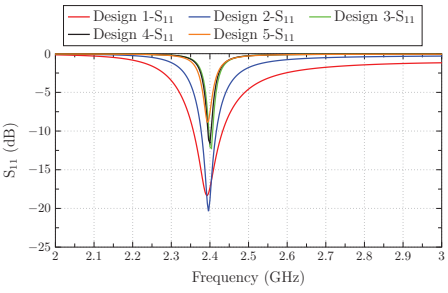

(**c**)

Figure 2. (**a**) Miniaturization process for obtaining the proposed antenna (from Design 1 to the proposed design (Design 5)) with dimensions in mm, (**b**) front and bottom view of the fabricated antenna, and (**c**) reflection coefficients (S_{11}) from Design 1 to Design 5.

In Figure 2c, it can be observed that the impedance bandwidth decreases with the antenna miniaturization, mainly when the antenna height is reduced and when a high-permittivity substrate is used. The height reduction produces a decrease in $\Re(Z_{11})$ close to 0 Ω, except a sudden high-impedance peak at the frequency where the antenna anti-

resonates. The imaginary part also shows a high slope change at the anti-resonance frequency. This behavior produces a decrease in the impedance bandwidth when the antenna height is reduced. In addition, the high-permittivity substrate permits the size reduction in the antenna, but increases its stored energy (Q-factor) and decreases its impedance bandwidth. The extreme miniaturization and the low-profile characteristics of the antenna, which can be placed straightforwardly on a ground plane with no clearance area, produce the narrow bandwidth and low-efficiency features of the antenna.

A really compact chip antenna is then obtained with clearance-free capabilities, showing a $9.3 \times 7 \times 2.45$ mm^3 ($0.075 \times 0.056 \times 0.019\lambda_0^3$) size. In Figure 2b, the front and back sides of the fabricated antenna are depicted next to a 1 Euro cent coin in order to show its reduced size.

3. Ground Plane Study

In this section, the radiation properties of the antenna in terms of matching and total efficiency are studied depending on the location of the proposed design at different-sized ground planes. The analysis quantifies the degradation of the radiation properties when an antenna is not placed in a proper place.

As mentioned in the introduction, the total radiated power of a small antenna is greatly affected by the environment surrounding the antenna. In addition, a great percentage of the total radiated power is produced by the induced currents on the ground plane where the antenna is placed. This is well known by the small antenna manufacturers, and generally, they provide guidelines for their antenna products' installation. In this paper, we provide both a theoretical and experimental study based on a characteristic modes analysis (CMA) to obtain which modes of the ground plane are excited.

Three ground plane sizes are studied: an electrically large (a = b = 100 mm $> \lambda/2$), an electrically small (a = b = 30 mm $< \lambda/4$), and a thin (a = 100 mm and b = 20 mm) ground plane. In Figure 3a, the three copper ground planes with the proposed antenna used for the experimental analysis are depicted. In addition, the connectorized antenna is depicted in Figure 3b inserted in different ground plane positions where different holes were drilled to connect the antenna. In Figure 3c, the set-up to measure the radiation patterns in the anechoic chamber is depicted.

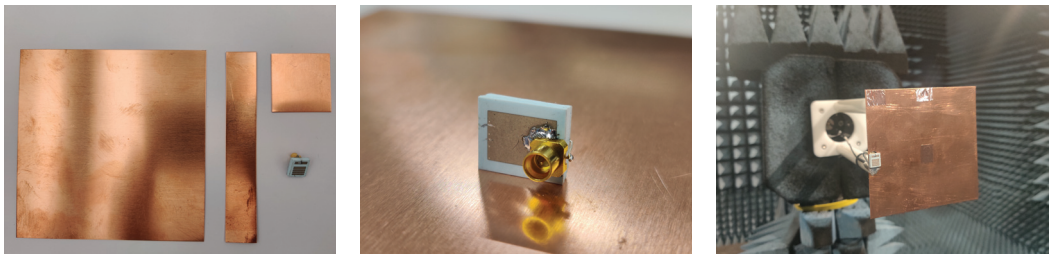

(**a**) (**b**) (**c**)

Figure 3. Pictures of the (**a**) analyzed ground planes manufactured with copper sheets and the fabricated antenna, (**b**) antenna with connector, (**c**) measurement set-up in the anechoic chamber.

3.1. Characteristic Modes Analysis (CMA)

The Theory of Characteristic Modes (TCM) [44,45] decomposes the total current of an arbitrary structure in a set of currents (modes) with orthogonal radiation properties. The modal subdivision provides visual and suitable information to properly excite the structure. Furthermore, it helps with the understanding of the radiation mechanism of the analyzed antenna. Characteristic modes are obtained from the generalized impedance matrix of a structure [Z], which is calculated with the method of moments (MoM), and then characteristic modes or eigenvectors (J_n) and eigenvalues (λ_n) are obtained with the following equation:

$$[X]\vec{J_n} = \lambda_n[R]\vec{J_n} \quad (1)$$

where [X] and [R] are the imaginary and real parts of the generalized impedance matrix of the structure [Z], respectively.

Eigenvalues (λ_n) are frequency-dependent and provide information about the radiation properties of the associated current mode (J_n). The mode is considered capacitive and stores electric energy when λ_n is negative, and inductive and stores magnetic energy when λ_n is positive. When $\lambda_n = 0$, the mode is at resonance. Different modal attributes for the physical interpretation of the eigenvalues have been proposed [52], such as the modal significance (MS), the variation with frequency of the Eigenvalues, the characteristic angle, or the modal quality factor. In this paper, the characteristic angle (α_n) is used for the analysis, and it is defined by the following:

$$\alpha_n = 180^\circ - \tan^{-1}(\lambda_n) \tag{2}$$

When the mode is at resonance, $\lambda_n = 0$ and $\alpha_n = 180^\circ$.

The CMA of different square plates is well detailed in the literature. The decomposition of the total current into modal currents or characteristic modes (J_n) provides a visual perspective of the radiation mechanism of the analyzed plate. It helps to determine which modes are good candidates to be excited and, consequently, which is the optimum position of the feeding. However, the CMA of the ground plane, including the small antenna, requires an extremely detailed meshing which is accompanied by time-demanding simulations, along with modal tracking and crossing avoidance issues. Furthermore, the antenna includes a lossy ceramic substrate, which complicates the analysis because the CMA is only well established for lossless structures, and commercial simulators do not analyze any lossy substrate. To face this problem, we analyze the isolated ground plane with the CMA, and then we correlate the radiated fields of each mode with the total radiated fields of the ground plane, including the chip antenna, at different positions. The correlation is then used as a metric to quantify approximately which mode of the ground plane is excited.

The correlation is detailed in (3), where g_n is the radiation pattern associated with mode J_n of the analyzed ground plane, and $g_{T(x,y)}$ is the total radiation pattern of the antenna + ground plane when the antenna is placed at (x,y). The superscript ^{H} denotes Hermitian, and $\Omega = (\theta, \phi)$ is the solid angle.

$$\rho_{n,T(x,y)} = \frac{\iint\limits_{4\pi} g_n^H(\Omega) g_{T(x,y)}(\Omega)\, d\Omega}{\sqrt{\iint\limits_{4\pi} g_n^H(\Omega) g_n(\Omega)\, d\Omega \cdot \iint\limits_{4\pi} g_{T(x,y)}^H(\Omega) g_{T(x,y)}(\Omega)\, d\Omega}} \tag{3}$$

Thanks to the correlation, we can analytically approximate which modes are excited. For a proper mode excitation, the antenna must be placed in a current maximum, and the currents of the antenna must flow in the same direction as the modal currents. These two requirements are critical for the proper excitation of any mode and for the enhancement of the radiation properties of the system.

3.2. Large Ground Plane (a = b = 100 mm)

The first analysis consists of an electrically large square ground plane with dimensions a = b = 100 mm, which correspond to a $> \lambda/2$. For this study, four positions of the antenna are considered, top-left corner P1(x,y) = (0,0), top-middle P2(x,y) = (45,0), left-middle P3(x,y) = (0,45), and center P4(x,y) = (45,45). In Figure 4a, the evaluation set-up is detailed.

The initial step focuses on the CMA of the isolated square ground plane. In Figure 4b,c, the characteristic angle and the current distribution of each mode are depicted, respectively. The gray bar represented in Figure 4b indicates the band where the proposed antenna is working. At that band, modes J_1/J_1', which are the fundamental modes (vertical/horizontal modes), have already resonated and have values close to 180°, and they have the potential to be excited. Mode J_2 also resonates before the operating band and also has characteristic

angle values close to 180°. This is a mode with four nulls at the corners of the plane and a maximum in the middle of the edges, and it is also a potential candidate to be excited. Mode J_3 is considered the loop mode, which does not resonate. Mode J_4 and J_5 resonate at higher frequencies, but they may be excited because they are not far from resonance, and the capacitive behavior that they show at the operating band can be compensated. Mode J_4 has four current nulls in the middle of the four edges, and mode J_5 has the same four nulls, along with four nulls at the corners. Since the ground plane is considered electrically big, all the mentioned modes can be potentially considered to be excited due to their relative proximity to resonance.

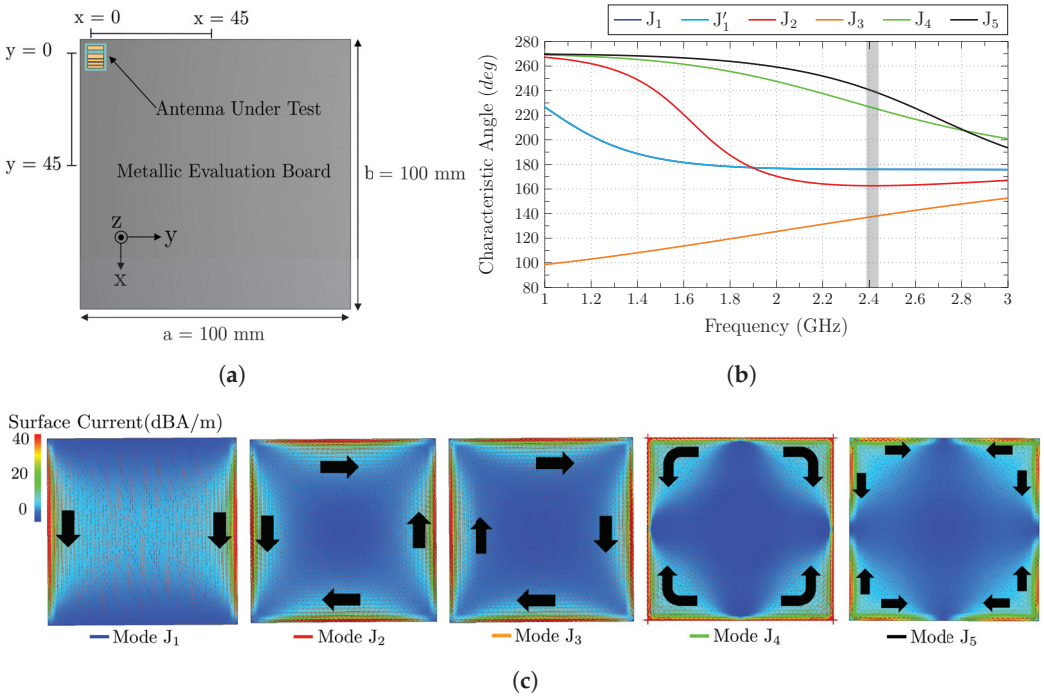

Figure 4. (**a**) Analyzed ground plane of 100 × 100 mm^2 with the antenna at four different positions, (**b**) characteristic angles of the isolated ground plane modes (J_1–J_5) with the operating frequency band colored in gray, and (**c**) current distribution of the isolated ground plane modes (J_1–J_5). J'_1 is equivalent to J_1, but rotated 90° (degenerated mode). Black arrows describe the direction of the currents.

Once the ground plane is analyzed, the antenna is placed at the four analyzed positions, and the reflection coefficient (S_{11}) and the total efficiency are calculated and depicted together in Figure 5a. The result for the S_{11} parameter shows a very narrow bandwidth for the operating band (25 MHz for $S_{11} < -6$ dB), and high stability with no detuning nor bandwidth degradation when the antenna is displaced. The measured S_{11} results show a slight frequency shift due to fabrication tolerances, but show high stability with the antenna displacement. The total measured efficiency is also measured, with good agreement with the simulated results.

As observed, the total efficiency is greatly affected by the position of the antenna. The highest value of total efficiency (−8.5 dB) is obtained when the antenna is placed at P3(x,y) = (0,45). In Figure 1b, the correlation between the total fields and each modal field is depicted, and in the case of (x,y) = (0,45), modes J_1, J_2, and J_4 are excited. The first two present higher correlation because the antenna is placed at a current maximum of both modes and for mode J_4 at a minimum. The second higher value (−10.2 dB) is obtained when the antenna is placed at P1(x,y) = (0,0), where only mode (J_4) is properly excited because only mode J_4 has a current maximum in the corner of the ground plane. Lastly, for positions P2(x,y) = (45,0) and P4(x,y) = (45,45), the lowest total efficiency value (−12 dB) is obtained. For P2(x,y) = (45,0), only mode J_5 is excited and at a low level because it has a current minimum at the excitation point. All the other modes are not excited because the

current flow of the antenna is orthogonal to the current flow of all the modal fields. For P4(x,y) = (45,45), the antenna is placed at a position where most of the modes have a null. Only mode J_1 can be excited because its current flow has the same direction as the antenna, but the antenna is not placed at the current maximum.

The total current of the ground plane with the antenna placed at the four positions is depicted in Figure 5c for its visual comparison with the modes. The radiation patterns (Directivity) for planes $\phi = 0°$ and $\phi = 90°$ are also depicted for all the analyzed positions (Figure 5d–g), and the measured radiation pattern for the best total efficiency position is also added. The measured radiation patterns differ from the simulated ones at $\theta = 180°$ for both planes due to the blocking effect of the positioner of the anechoic chamber.

As a first conclusion, the best position for the antenna is the middle-left position P3(x,y) = (0,45) because most of the first analyzed modes of the ground plane, which are close to resonance, exhibit a current maximum in the perimeter of the ground plane and especially in the middle of each side. In addition, the current flow of the antenna has the same direction as the modal currents.

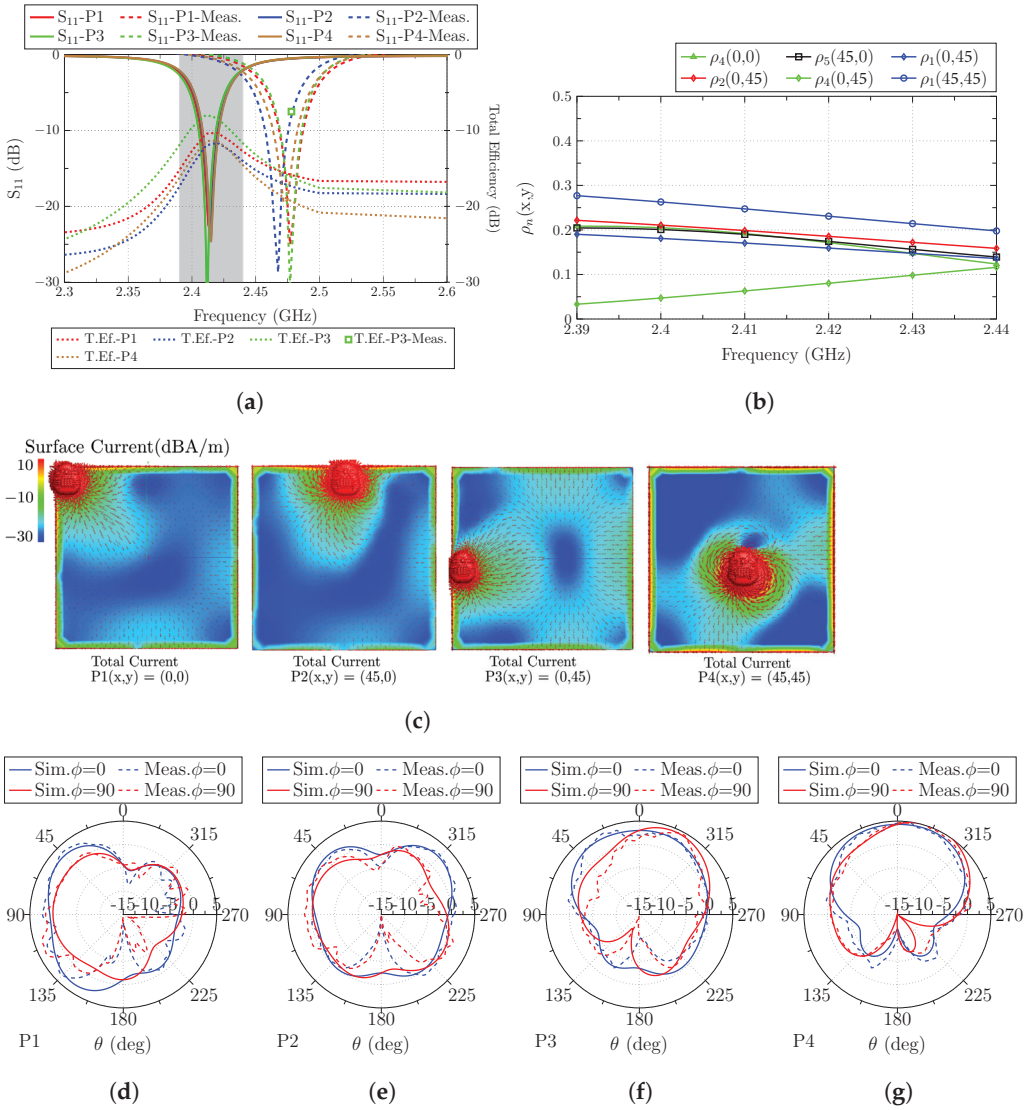

Figure 5. (**a**) Reflection coefficient (S_{11}) and total efficiency (dB) of the antenna located at the four analyzed positions (the frequency band colored in gray corresponds to the operating band analyzed with the correlation), (**b**) correlation (detailed in Equation (3)) of total and modal fields, (**c**) total current distribution of the antenna at the four positions, and radiation patterns at resonance when the antenna is placed at (**d**) P1(x,y) = (0,0), (**e**) P2(x,y) = (45,0), (**f**) P3(x,y) = (0,45), and (**g**) P4(x,y) = (45,45).

3.3. Small Ground Plane (a = b = 30 mm)

The second subsection analyzes an electrically small square ground plane with the dimensions a = b = 30 mm, which correspond to a $< \lambda/4$. As in the previous subsection, the same four positions of the antenna are considered: top-left corner P1(x,y) = (0,0), top-middle P2(x,y) = (12,0), left-middle P3(x,y) = (0,12) and center P4(x,y) = (12,12), detailed in Figure 6a.

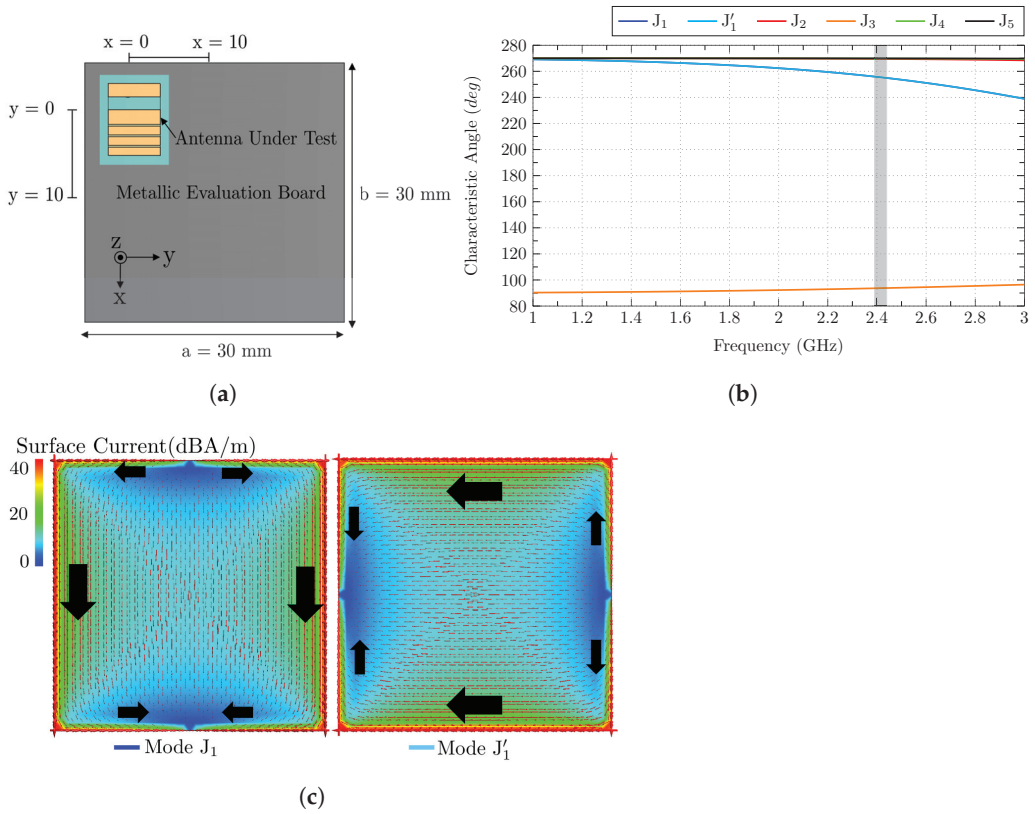

Figure 6. (**a**) Analyzed ground plane of 30 × 30 mm^2 with the antenna at four different positions on the ground plane, (**b**) characteristic angles of the isolated ground plane modes (J_1–J_5) with the operating frequency band colored in gray, and (**c**) current distribution of mode J_1 and J'_1 of the isolated ground plane. Black arrows describe the direction of the currents.

The CMA of the isolated plane shows that at the operating band (gray band of Figure 6b), all the modes have not resonated yet due to the limited size of the plane. Only modes J_1 and J'_1 have a lower value of characteristic angle, and they will be the only modes that will be excited. In Figure 6c, the current distribution of modes J_1 and J'_1 at 2.4 GHz is represented. Since the modes are far from resonance, it can be observed that currents are not only flowing vertically or horizontally (like at resonance), but they have an external path beginning in the current minimum (at the middle of one of the edges) and flowing throw the edge of the perimeter (C-shape path) until the middle of the other edge.

After the ground plane analysis, the antenna is analyzed at the four ground plane positions. The reflection coefficient (S_{11}) and the total efficiency are depicted together in Figure 7a. The result for the S_{11} parameter shows the same narrow bandwidth operating band (25 MHz for $S_{11} < -6$ dB) as in the electrically large ground plane and high stability with no detuning nor bandwidth degradation even when the antenna is displaced in such a limited ground plane.

The total efficiency is also affected by the position of the antenna. With a simple inspection of the two modes of the isolated ground plane J_1/J'_1, it is possible to anticipate which position is more suitable to obtain the highest total efficiency. Position P3(x,y) = (0,12) provides the highest efficiency value (−9.5 dB) because the antenna is placed in the middle

of the current maximum associated with mode J_1, and also, the current flow of the antenna follows the current flow of the mode. In addition, mode J_1' is excited with a lower level because it has a current null in that position, but the prolongation of intense currents in the C-shape distribution from the middle-top to middle-bottom point (which appears at such low frequencies) creates an additional current path in phase with the current flow of the antenna. The following efficiency values are −11.4 dB and −11.5 for positions P1(x,y) = (0,0) and P4(x,y) = (12,12), respectively. For P1(x,y) = (0,0), the antenna is placed not in a current minimum nor a maximum for mode J_1 and J_1'. Both modes are excited at a low level, because the antenna current flow has the same direction as the modes, but it is not placed in any of the current maximums. In the case of P4(x,y) = (12,12), only mode J_1 is excited with medium level because even though it has the same current flow as the mode, it is not placed in the exact current maximum (edge). The worst result for the total efficiency (−13.5 dB) is obtained at P2(x,y) = (12,0), with a current minimum for mode J_1 (with antenna current flow in phase) and a maximum of J_1' (but with the current flow orthogonal to the mode). Only mode J_1 is then excited in this case, but with a poor level.

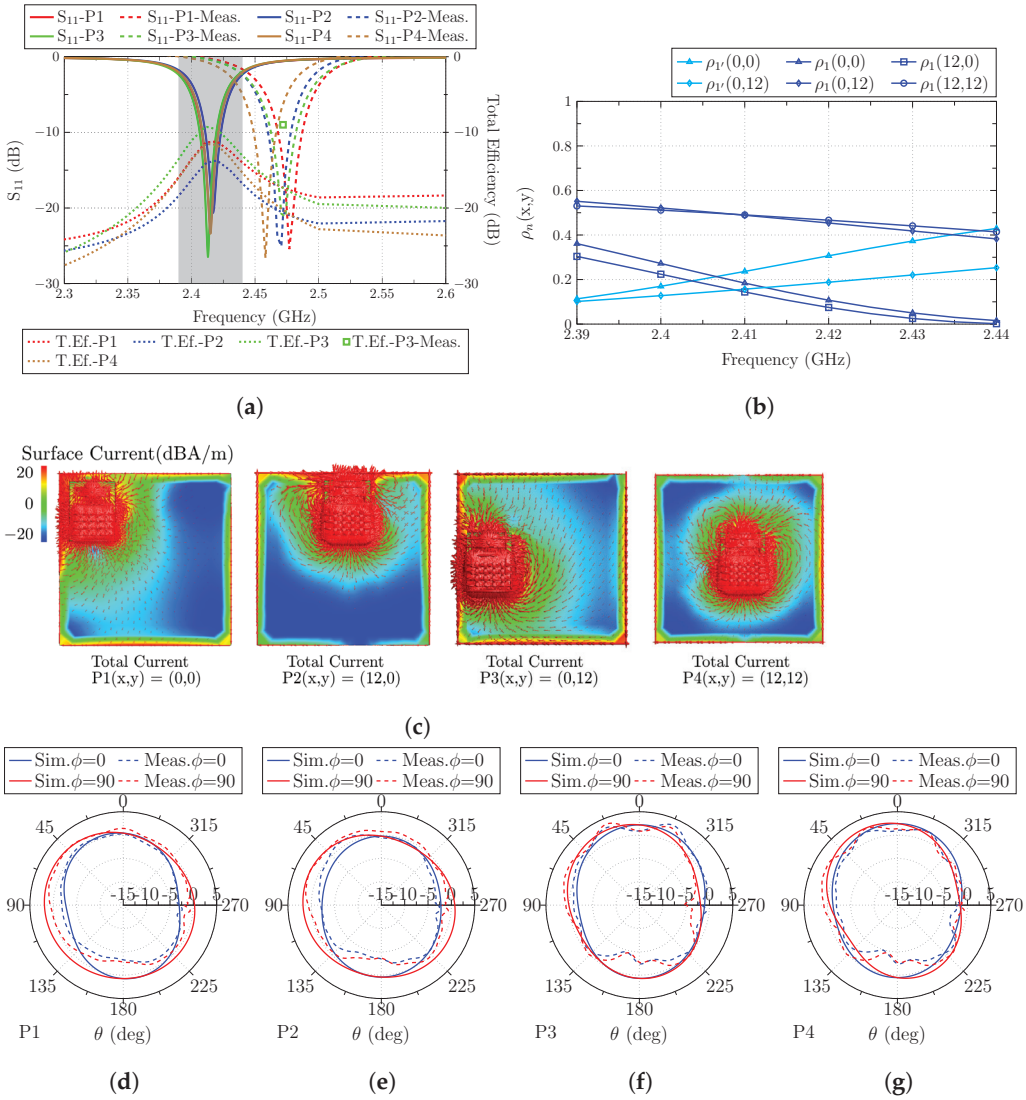

Figure 7. (**a**) Reflection coefficient (S_{11}) and total efficiency (dB) of the antenna located at the four analyzed positions (the frequency band colored in gray corresponds to the operating band analyzed with the correlation), (**b**) correlation (detailed in Equation (3)) of total and modal fields, (**c**) total current distribution of the antenna at the four positions, and radiation patterns at resonance when the antenna is placed at (**d**) P1(x,y) = (0,0), (**e**) P2(x,y) = (12,0), (**f**) P3(x,y) = (0,12), and (**g**) P4(x,y) = (12,12).

Total currents with the antenna placed at the four positions are depicted in Figure 7c for its visual comparison with the modal currents. The radiation patterns (directivity) for planes $\phi = 0°$ and $\phi = 90°$ are also depicted in Figure 7 for all the analyzed positions.

After the second analysis, it can be stated that, again, the best position for the antenna placement is the middle-left position, because the antenna is placed in the current maximum of mode J_1, and the current flow of the antenna is parallel to the current flow in the maximum of the mode. The worst position is the top-middle P2(x,y) = (12,0) because either the current flow is orthogonal to the current maximum flow of J_1' or, in the case of J_1, it is in a current minimum.

3.4. Long Ground Plane (a = 15 mm and b = 100 mm)

The last subsection provides the analysis of an electrically long ground plane with dimensions a = 15 mm and b = 100 mm. In this study, due to the reduced width (a) of the ground plane, only two positions are analyzed: Top P1(x,y) = (0,0) and middle P2(x,y) = (0,45). At each position, the antenna is placed in two orthogonal ways (see Figure 8a).

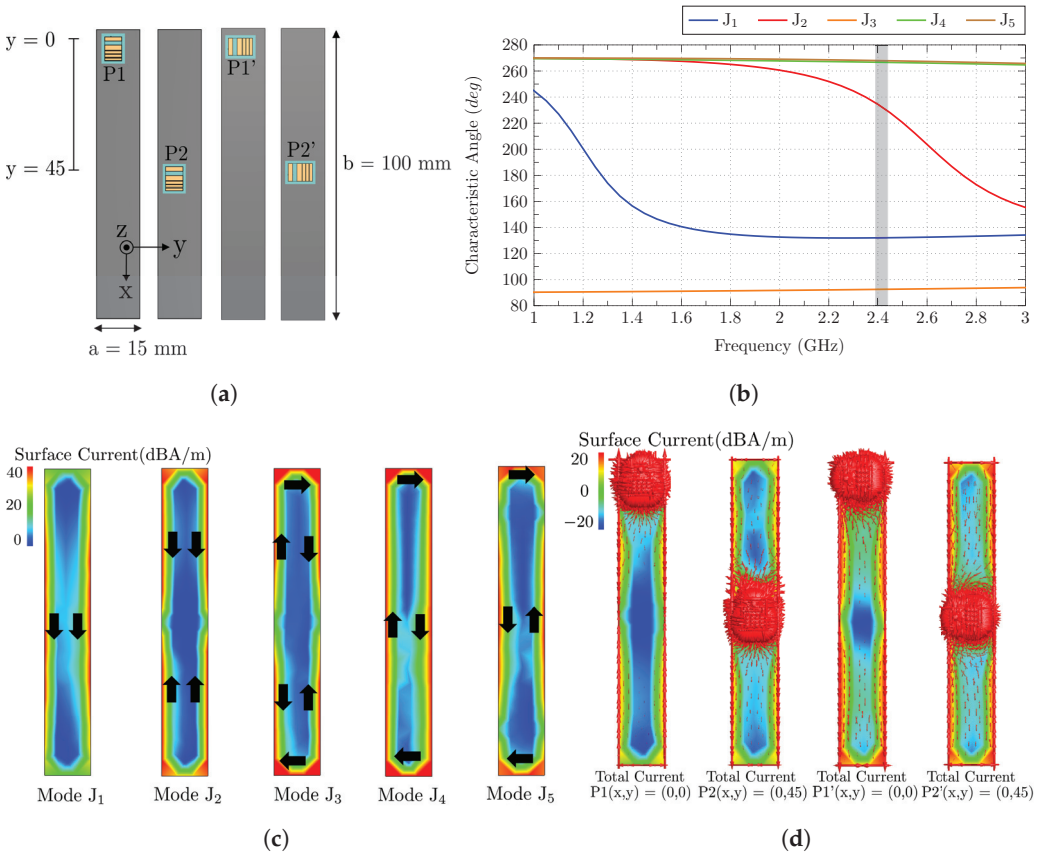

Figure 8. (**a**) Analyzed ground plane of 15 × 100 mm^2, with the antenna at two different positions and two polarizations, (**b**) characteristic angles of the isolated ground plane modes (J_1–J_5) with the operating frequency band colored in gray, (**c**) current distribution of modes J_1–J_5 of the isolated ground plane (black arrows describe the direction of the currents), and (**d**) total current distribution of the antenna at the four positions.

With an inspection of the characteristic angles associated with the modes of the long ground plane (Figure 8b), it can be observed that mode J_1 is resonant before the operating band (remarked in gray color), and mode J_2 is close to resonance. The other modes resonate at higher frequencies, and by a first impression, it can be stated that only modes J_1 and J_2 will be present in the analysis. Mode J_1 has the current distribution of the vertical mode (see Figure 8c), with nulls at the top and bottom edges and maximums in the middle of the left

and right sides. Mode J_2 presents a current minimum in the middle of the right/left sides and a current maximum at the top and bottom edges. Mode J_3 corresponds to the loop mode, and mode J_4 is a higher-order mode, with four current nulls and four maximums. The total currents, including the antenna, are depicted in Figure 8d for a visual comparison between modal and total currents.

Regarding the matching of the antenna (see Figure 9a), results show the same stability as in previous studies, with no detuning observed when the antenna is displaced, or the polarization is changed.

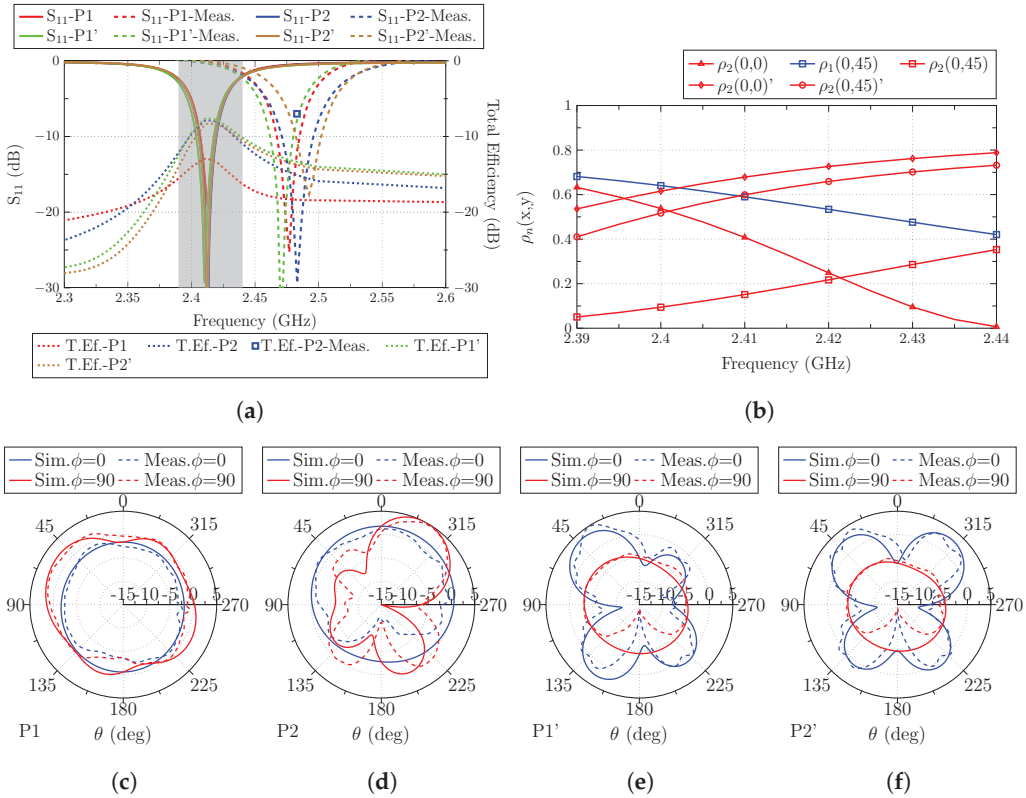

Figure 9. (**a**) Reflection coefficient (S_{11}) and total efficiency (dB) of the antenna located at the four analyzed positions (the frequency band colored in gray corresponds to the operating band analyzed with the correlation), (**b**) Correlation (detailed in Equation (3)) of total and modal fields, and radiation patterns at (**c**) P1(x,y) = (0,0), (**d**) P2(x,y) = (0,45), (**e**) P1′(x,y) = (0,0) and, (**f**) P2′(x,y) = (0,45).

The total efficiency (Figure 9a) exhibits the highest dynamic range among all the performed studies. On the one hand, the best total efficiency results (−7.6 dB and −7.8 dB) observed in Figure 9a are obtained at positions P1′(x,y) = (0,0) and P2(x,y) = (0,45). By analyzing the correlation (Figure 9b), it can be observed that for P1′(x,y) = (0,0), mode J_2 is perfectly excited because the antenna is placed parallel to the top edge, and there is a current maximum flowing in the same direction of the currents of the antenna. For P2(x,y) = (0,45) position, the antenna is clearly exciting mode J_1 og the ground plane, because it is placed in the middle of the left and right sides, and since the plane is very thin, both maximums are excited. The next highest value for the total efficiency is obtained for P2′(x,y)= (0,45), where mode J_2 is excited but not at the same level, because the antenna is placed in the current minimum. Although it is placed in the maximum for J_1, the current flow of the antenna is orthogonal to the currents of this mode. The worst total efficiency value (−12.9 dB) is observed for P1(x,y) = (0,0) positions. The reason for such a low level is that mode J_1 has a current minimum and mode J_2 has its maximum on the top edge, but it is orthogonal to the current flow of the antenna.

Radiation patterns (directivity) for planes $\phi = 0°$ and $\phi = 90°$ are also depicted for all the analyzed positions in Figure 9.

The information gathered in the last analysis shows that for narrow ground planes, the antenna position has a big impact on the total efficiency. Really high correlation and efficiency values are obtained if the antenna is placed in the correct position, always taking into consideration the current distribution of the modes close to resonance and taking also into consideration the current flow of the antenna.

4. Conclusions

A low-profile on-ground LTCC chip antenna resonating at 2.41 GHz has been presented. The antenna exhibits a total volume of $0.067 \times 0.048 \times 0.019\lambda_0^3$ and does not require a clearance area on the ground plane where it is installed. Characteristic modes analysis of ground planes with different sizes, and the correlation between the total radiated fields (antenna + ground plane) and modal radiated fields (ground plane) were successfully performed, justifying the best position for the antenna location in terms of total efficiency. This study shows that the antenna is really stable to detuning effects and shows a considerable difference in terms of efficiency from the best to the worst position (5.3 dB difference), as described in Table 3. The best results are obtained when the antenna is placed in the middle of the left side of the ground plane, and the reason is demonstrated by the modal analysis. Due to the size of the antenna and the lack of clearance area requirement, this antenna is a great candidate to be installed in extremely size-limited devices working for 2.4 GHz IoT applications. As further work, once the on-ground (no clearance) chip antenna concept has been presented and the CMA and correlation study to find the optimum location of the antenna in a ground plane has been performed, the impedance bandwidth enhancement of the proposed antenna will be investigated. A comparison between classical chip antennas with clearance area and on-ground chip antennas will be carried out.

Table 3. Summary of the results. Red cell: Antenna in a wrong location, Orange cell: Antenna in an intermediate location, Green cell: Antenna in the optimum location

Ground P. Size	Antenna Position	T.Eff.	Ground P. Size	Antenna Position	T.Eff.
100×100 mm^2	P1(0,0)	−10.2 dB	100×100 mm^2	P2(45,0)	−12 dB
100×100 mm^2	P3(0,45)	−8.5 dB	100×100 mm^2	P4(45,45)	−12 dB
30×30 mm^2	P1(0,0)	−11.4 dB	30×30 mm^2	P2(12,0)	−13.5 dB
30×30 mm^2	P3(0,12)	−9.5 dB	30×30 mm^2	P4(12,12)	−11.5 dB
15×100 mm^2	P1(0,0)	−12.9 dB	15×100 mm^2	P2(0,45)	−7.8 dB
15×100 mm^2	P1′(0,0)	−7.6 dB	15×100 mm^2	P2′(0,45)	−8.3 dB

Author Contributions: Conceptualization, J.M.-B., M.C.-F., E.A.-D. and M.F.-B.; methodology, J.M.-B.; software, J.M.-B.; validation, J.M.-B.; formal analysis, J.M.-B., M.C.-F., E.A.-D. and M.F.-B.; investigation, J.M.-B., M.C.-F., E.A.-D. and M.F.-B.; resources, J.M.-B., M.C.-F., E.A.-D. and M.F.-B.; data curation, J.M.-B.; writing—original draft preparation, J.M.-B.; writing—review and editing, J.M.-B., M.C.-F., E.A.-D. and M.F.-B.; visualization, J.M.-B., M.C.-F., E.A.-D. and M.F.-B.; supervision, M.C.-F., E.A.-D. and M.F.-B.; project administration, M.C.-F., E.A.-D. and M.F.-B.; funding acquisition, M.C.-F., E.A.-D. and M.F.-B. All authors have read and agreed to the published version of the manuscript.

Funding: This work has been supported by the Spanish Ministry of Science and Innovation (Ministerio de Ciencia e Innovación) under project PID2019-107885GB-C32.

Institutional Review Board Statement: Not applicable.

Informed Consent Statement: Not applicable.

Data Availability Statement: Not applicable.

Conflicts of Interest: The authors declare no conflicts of interest.

References

1. Fallahpour, M.; Zoughi, R. Antenna miniaturization techniques: A review of topology-and material-based methods. *IEEE Antennas Propag. Mag.* **2017**, *60*, 38–50. [CrossRef]
2. Chu, L.J. Physical limitations of omni-directional antennas. *J. Appl. Phys.* **1948**, *19*, 1163–1175. [CrossRef]

3. Wheeler, H.A. Fundamental limitations of small antennas. *Proc. IRE* **1947**, *35*, 1479–1484. [CrossRef]
4. Fante, R. Quality factor of general ideal antennas. *IEEE Trans. Antennas Propag.* **1969**, *17*, 151–155. [CrossRef]
5. Hansen, R.C. Fundamental limitations in antennas. *Proc. IEEE* **1981**, *69*, 170–182. [CrossRef]
6. McLean, J.S. A re-examination of the fundamental limits on the radiation Q of electrically small antennas. *IEEE Trans. Antennas Propag.* **1996**, *44*, 672. [CrossRef]
7. Pozar, D.M. New results for minimum Q, maximum gain, and polarization properties of electrically small arbitrary antennas. In Proceedings of the 2009 3rd European Conference on Antennas and Propagation, Berlin, Germany, 23–27 March 2009; pp. 1993–1996.
8. Lizzi, L.; Ferrero, F. Use of ultra-narrow band miniature antennas for internet-of-things applications. *Electron. Lett.* **2015**, *51*, 1964–1966. [CrossRef]
9. Dong, Y.; Choi, J.; Itoh, T. Folded strip/slot antenna with extended bandwidth for WLAN application. *IEEE Antennas Wirel. Propag. Lett.* **2016**, *16*, 673–676. [CrossRef]
10. Ouyang, J.; Pan, Y.M.; Zheng, S.Y.; Hu, P.F. An Electrically Small Planar Quasi-Isotropic Antenna. *IEEE Antennas Wirel. Propag. Lett.* **2018**, *17*, 303–306. [CrossRef]
11. Islam, M.S.; Islam, M.T.; Ullah, M.A.; Beng, G.K.; Amin, N.; Misran, N. A modified meander line microstrip patch antenna with enhanced bandwidth for 2.4 GHz ISM-band Internet of Things (IoT) applications. *IEEE Access* **2019**, *7*, 127850–127861. [CrossRef]
12. Al-Yasir, Y.I.; Alkhafaji, M.K.; Alhamadani, H.A.; Ojaroudi Parchin, N.; Elfergani, I.; Saleh, A.L.; Rodriguez, J.; Abd-Alhameed, R.A. A new and compact wide-band microstrip filter-antenna design for 2.4 GHz ISM band and 4G applications. *Electronics* **2020**, *9*, 1084. [CrossRef]
13. Yan, S.; Volskiy, V.; Vandenbosch, G.A.E. Compact Dual-Band Textile PIFA for 433-MHz/2.4-GHz ISM Bands. *IEEE Antennas Wirel. Propag. Lett.* **2017**, *16*, 2436–2439. [CrossRef]
14. Abdulkawi, W.M.; Sheta, A.F.A.; Elshafiey, I.; Alkanhal, M.A. Design of low-profile single-and dual-band antennas for IoT applications. *Electronics* **2021**, *10*, 2766. [CrossRef]
15. Jarchavi, S.M.R.; Hussain, M.; Gardezi, S.H.H.; Alibakhshikenari, M.; Falcone, F.; Limiti, E. A Compact and Simple Prototype CPW-Fed Dual Band Antenna for ISM, Wi-Fi, and WLAN Applications. In Proceedings of the 2022 United States National Committee of URSI National Radio Science Meeting (USNC-URSI NRSM), Boulder, CO, USA, 4–8 January 2022; pp. 30–31.
16. Morales-Centla, N.; Torrealba-Melendez, R.; Tamariz-Flores, E.I.; López-López, M.; Arriaga-Arriaga, C.A.; Munoz-Pacheco, J.M.; Gonzalez-Diaz, V.R. Dual-Band CPW Graphene Antenna for Smart Cities and IoT Applications. *Sensors* **2022**, *22*, 5634. [CrossRef]
17. Hussain, M.; Ali, E.M.; Awan, W.A.; Hussain, N.; Alibakhshikenari, M.; Virdee, B.S.; Falcone, F. Electronically reconfigurable and conformal triband antenna for wireless communications systems and portable devices. *PLoS ONE* **2022**, *17*, e0276922. [CrossRef]
18. Abdulzahra, D.H.; Alnahwi, F.; Abdullah, A.S.; Al-Yasir, Y.I.; Abd-Alhameed, R.A. A Miniaturized Triple-Band Antenna Based on Square Split Ring for IoT Applications. *Electronics* **2022**, *11*, 2818. [CrossRef]
19. Kirtania, S.G.; Elger, A.W.; Hasan, M.R.; Wisniewska, A.; Sekhar, K.; Karacolak, T.; Sekhar, P.K. Flexible antennas: A review. *Micromachines* **2020**, *11*, 847. [CrossRef]
20. de Cos Gómez, M.E.; Fernández Álvarez, H.; Puerto Valcarce, B.; García González, C.; Olenick, J.; Las-Heras Andrés, F. Zirconia-based ultra-thin compact flexible CPW-fed slot antenna for IoT. *Sensors* **2019**, *19*, 3134. [CrossRef]
21. Varma, S.; Sharma, S.; John, M.; Bharadwaj, R.; Dhawan, A.; Koul, S.K. Design and performance analysis of compact wearable textile antennas for IoT and body-centric communication applications. *Int. J. Antennas Propag.* **2021**, *2021*, 1–12. [CrossRef]
22. Seo, Y.; Cho, J.; Lee, Y.; Jang, J.; Kwon, H.W.; Kahng, S. A Chip Antenna for Bluetooth Earphones with Cross-Head Interference Tested from Received-Signal Sensing. *Sensors* **2022**, *22*, 3969. [CrossRef]
23. Woo, T.; Kim, D.; Park, C.Y.; Yoon, Y.J. Compact Wideband Loop Antenna for Earbuds. *IEEE Access* **2022**, *10*, 47340–47347. [CrossRef]
24. Le, T.T.; Yun, T.Y. Miniaturization of a Dual-Band Wearable Antenna for WBAN Applications. *IEEE Antennas Wirel. Propag. Lett.* **2020**, *19*, 1452–1456. [CrossRef]
25. Hu, P.F.; Pan, Y.M.; Hu, B.J. Electrically small, planar, complementary antenna with reconfigurable frequency. *IEEE Trans. Antennas Propag.* **2019**, *67*, 5176–5184. [CrossRef]
26. Borhani, M.; Rezaei, P.; Valizade, A. Design of a reconfigurable miniaturized microstrip antenna for switchable multiband systems. *IEEE Antennas Wirel. Propag. Lett.* **2015**, *15*, 822–825. [CrossRef]
27. Singh, P.P.; Goswami, P.K.; Sharma, S.K.; Goswami, G. Frequency reconfigurable multiband antenna for IoT applications in WLAN, Wi-Max, and C-band. *Prog. Electromagn. Res. C* **2020**, *102*, 149–162. [CrossRef]
28. Xia, Z.; Li, H.; Lee, Z.; Xiao, S.; Shao, W.; Ding, X.; Yang, X. A wideband circularly polarized implantable patch antenna for ISM band biomedical applications. *IEEE Trans. Antennas Propag.* **2019**, *68*, 2399–2404. [CrossRef]
29. Wang, G.B.; Xuan, X.W.; Jiang, D.L.; Li, K.; Wang, W. A miniaturized implantable antenna sensor for wireless capsule endoscopy system. *AEU-Int. J. Electron. Commun.* **2022**, *143*, 154022. [CrossRef]
30. Singh, R.K.; Michel, A.; Nepa, P.; Salvatore, A. Wearable dual-band quasi-yagi antenna for UHF-RFID and 2.4 GHz applications. *IEEE J. Radio Freq. Identif.* **2020**, *4*, 420–427. [CrossRef]
31. Corchia, L.; Monti, G.; Tarricone, L. A frequency signature RFID chipless tag for wearable applications. *Sensors* **2019**, *19*, 494. [CrossRef]

32. Abdulghafor, R.; Turaev, S.; Almohamedh, H.; Alabdan, R.; Almutairi, B.; Almutairi, A.; Almotairi, S. Recent advances in passive UHF-RFID tag antenna design for improved read range in product packaging applications: A comprehensive review. *IEEE Access* **2021**, *9*, 63611–63635. [CrossRef]
33. Behera, S.K.; Karmakar, N.C. Wearable chipless radio-frequency identification tags for biomedical applications: A review [antenna applications corner]. *IEEE Antennas Propag. Mag.* **2020**, *62*, 94–104. [CrossRef]
34. Asakura, K.; Oida, T.; Mandai, H. Chip-Antenna. U.S. Patent 6,028,568, 22 February 2000.
35. Watanabe, K.; Tsuru, T.; Kanba, S.; Suesada, T.; Dakeya, Y. Chip Antenna and Radio Equipment Including the Same. U.S. Patent 6,271,803, 6 August 2001.
36. Kim, H.J.; Yoon, S.J.; Choi, J.W.; Kang, C.Y.; Sim, S.H. Ceramic Chip Antenna. U.S. Patent 6,650,303, 18 November 2003.
37. de Rochemont, L.P. Ceramic Antenna Module and Methods of Manufacture Thereof. U.S. Patent 7,405,698, 29 July 2008.
38. Słobodzian, P.M. Challenges of design and practical application of LTCC chip antennas. In Proceedings of the 2015 12th International Conference on Telecommunication in Modern Satellite, Cable and Broadcasting Services (TELSIKS), Alsace, France, 21–23 July 2015; pp. 147–155.
39. Peng, Y.x.; Dong, Y.l.; Du, M.; Saito, K. Compact microstrip-fed LTCC chip antenna by capacitive coupling. *IEICE Commun. Express* **2017**, *6*, 242–247. [CrossRef]
40. Lee, M.W.; Leung, K.; Chow, Y. Low cost meander line chip monopole antenna. *IEEE Trans. Antennas Propag.* **2013**, *62*, 442–445. [CrossRef]
41. Vainikainen, P.; Ollikainen, J.; Kivekas, O.; Kelander, K. Resonator-based analysis of the combination of mobile handset antenna and chassis. *IEEE Trans. Antennas Propag.* **2002**, *50*, 1433–1444. [CrossRef]
42. Molins-Benlliure, J.; Cabedo-Fabrés, M.; Antonino-Daviu, E.; Ferrando-Bataller, M. Effect of the ground plane in UHF Chip antenna efficiency. In Proceedings of the 2020 14th European Conference on Antennas and Propagation (EuCAP), Copenhagen, Denmark, 15–20 March 2020; pp. 1–5.
43. Molins-Benlliure, J.; Cabedo-Fabrés, M.; Antonino-Daviu, E.; Ferrando-Bataller, M. Effect of the Size and Shape of the Ground Plane in Small Antennas Efficiency. In Proceedings of the 2020 International Workshop on Antenna Technology (iWAT), Bucharest, Romania, 25–28 February 2020; pp. 1–4.
44. Harrington, R.; Mautz, J. Theory of characteristic modes for conducting bodies. *IEEE Trans. Antennas Propag.* **1971**, *19*, 622–628. [CrossRef]
45. Harrington, R.; Mautz, J. Computation of characteristic modes for conducting bodies. *IEEE Trans. Antennas Propag.* **1971**, *19*, 629–639. [CrossRef]
46. Cabedo-Fabres, M.; Valero-Nogueira, A.; Antonino-Daviu, E.; Ferrando-Bataller, M. Modal analysis of a radiating slotted PCB for mobile handsets. In Proceedings of the 2006 First European Conference on Antennas and Propagation, Nice, France, 6–10 November 2006; pp. 1–6.
47. Antonino-Daviu, E.; Cabedo-Fabres, M.; Ferrando-Bataller, M.; Herranz-Herruzo, J. Analysis of the coupled chassis-antenna modes in mobile handsets. In Proceedings of the IEEE Antennas and Propagation Society Symposium, Monterey, CA, USA, 20–25 June 2004; Volume 3, pp. 2751–2754.
48. Cabedo-Fabres, M.; Antonino-Daviu, E.; Valero-Nogueira, A.; Bataller, M.F. The theory of characteristic modes revisited: A contribution to the design of antennas for modern applications. *IEEE Antennas Propag. Mag.* **2007**, *49*, 52–68. [CrossRef]
49. Antonino-Daviu, E.; Suarez-Fajardo, C.; Cabedo-Fabrés, M.; Ferrando-Bataller, M. Wideband antenna for mobile terminals based on the handset PCB resonance. *Microw. Opt. Technol. Lett.* **2006**, *48*, 1408–1411. [CrossRef]
50. Martens, R.; Safin, E.; Manteuffel, D. Inductive and capacitive excitation of the characteristic modes of small terminals. In Proceedings of the 2011 Loughborough Antennas & Propagation Conference, Loughborough, UK, 14–15 November 2011; pp. 1–4.
51. Santos, H.M.; Pinho, P.; Silva, R.P.; Pinheiro, M.; Salgado, H.M. Meander-Line Monopole Antenna with Compact Ground Plane for a Bluetooth System-in-Package. *IEEE Antennas Wirel. Propag. Lett.* **2019**, *18*, 2379–2383. [CrossRef]
52. Cabedo-Fabrés, M. Systematic Design of Antennas Using the Theory of Characteristic Modes. Ph.D. Thesis, Universitat Politècnica de València, València, Spain 2008.

sensors

MDPI

Article

Coherently Radiating Periodic Structures for Feeding Concentric Rings Array with Reduced Number of Phase Shifters

Brian Sanchez [1], Marco A. Panduro [1,*], David H. Covarrubias [1], Alberto Reyna [2] and Elizvan Juárez [1]

[1] CICESE Research Center, Electronics and Telecommunications Department, Carretera Ensenada-Tijuana No. 3918, Zona Playitas, Ensenada 22860, Baja California, Mexico
[2] Universidad Autónoma de Tamaulipas, UAMRR-R, Carretera Reynosa-San Fernando, Reynosa 88779, Tamaulipas, Mexico
* Correspondence: mpanduro@cicese.mx

Abstract: This paper presents the application of CORPS (coherently radiating periodic structures) for feeding CRA (concentric rings array) with a reduced number of phase shifters. The proposed design technique for the structure of concentric rings provides a better scanning capability with respect to other existing configurations. This design technique utilizes 2×3 or 4×7 CORPS networks depending on the configuration or the number of antenna elements in the phased array system. These CORPS networks are set strategically in the feeding network to provide several advantages with respect to others in the scanning capability and the reduction of the number of phase shifters of the array system. The contribution of this paper is the full antenna system design of phased CRA for analyzing scanning and the reduction of phase shifters. The proposed phased array reduces the number of phase shifter devices in CRA for a scanning range of $\pm 25^{\circ}$ in the elevation plane. Differential evolution (DE) was applied to optimize the amplitudes of the proposed system. Several design cases were analyzed using full-wave simulation results to verify the phased array model and to take mutual coupling into account. Full-wave simulation results provide radiation patterns with low SLL in all scanning directions. The proposed phased array was validated by experimental measurements of the full antenna system prototype.

Keywords: phased array; CORPS network; concentric rings; beam-scanning; side lobe level

1. Introduction

There is great interest about minimizing the number of electronic devices used in the feeding network of the antenna system while maximizing the radiation pattern quality [1]. Two of the main components of phased array systems are the array architecture and the beam-forming network (BFN). The first one determines the spatial distribution of each antenna element, and the BFN is a crucial component for feeding each antenna element of the system with adequate amplitudes and phases. An adequate BFN design allows us to generate radiation patterns with desirable properties such as a wide range of beam-scanning and low side lobe level (SLL) [2,3].

The complexity and cost of phased array systems depend strongly on the BFN. This complexity is high for a high number of electronic devices (phase shifters, amplifiers, switches, etc.) [4]. It is crucial to find out different antenna arrays geometries and BFN configurations for minimizing the number of electronic devices [5–7] in applications of wide range scanning and low SLL. There are several recent techniques in the state of art such as: checkered networks [8], minimal redundancy [9], hybrid beamforming [10], rotated elements [11], directional modulation [12], and coherently radiating periodic structures (CORPS) [13], among others.

The techniques based on CORPS have been studied for reducing the number of phase shifters in the BFN. Several CORPS network configurations have been analyzed yielding a better scanning capability with respect to other BFN configurations [14–22].

The previously mentioned works have provided several design techniques for feeding different antenna array structures such as linear, planar, and concentric rings. In this sense, new design methodologies are needed to minimize the complexity of the feeding system of the antenna array. All these methodologies can set more design options for emerging systems based on antenna arrays.

Our manuscript illustrates the use of CORPS to feed antenna array systems with a geometry of concentric rings by using a minimum quantity of phase shifters. The phased antenna system using the proposed CRA uses cophasal excitation and provides an interesting option for feeding the antenna elements and diminishing the quantity of phase devices. This antenna system design using the geometry of CRA can achieve a wide scanning range. In this case, 2×3 or 4×7 CORPS networks are utilized in the proposed CRA to provide the required phase distribution. The proposed design methodology using these CORPS blocks achieves some benefits, such as a wide scanning of the main beam and the simplification of the BFN by diminishing the quantity of phase shifters of the antenna system. The differences with respect to our previous work published in [22] are the reduction of phase shifters for a configuration based on arrays of concentric rings and the analysis of the radiation performance for different configurations.

The contribution of this paper is the full antenna system design of phased CRA for analyzing scanning and the reduction of phase shifters. The proposed phased array reduces the number of phase shifter devices in CRA for a scanning range of $\pm 25^{\circ}$ in the elevation plane. Differential evolution (DE) [23] was applied to optimize the amplitudes of the proposed system. Several design cases are analyzed using different numbers of antenna elements with full-wave simulation results (using CST Microwave Studio) to verify the phased array model and to take mutual coupling into account. Full-wave simulation results provide radiation patterns with low SLL in all scanning directions. The proposed phased array was validated by experimental measurements of the full antenna system prototype.

2. Phased Array Model

2.1. Concentric Rings Array

The geometry of concentric rings is considered for the phased array model. We have selected this geometry because the behavior of the required cophasal excitation for this structure facilitates the application of CORPS.

Basically, this array geometry incorporates multiple rings with antenna elements in a circular layout, sharing a common center where each ring has its own radius [21]. This concentric ring geometry considers M rings with N_m antenna elements on the x-y plane, as shown in Figure 1. Thus, the array factor expression considering this structure can be written as follows [21,24]:

$$\mathrm{AF}(\theta, \phi) = \sum_{m=1}^{M} \sum_{i=1}^{N_m} W_m e^{jkr_m(\lambda)[\sin\theta\cos(\phi-\phi_{mi})+\sin\theta_0\cos(\phi_0-\phi_{mi})]} \quad (1)$$

Where M is the number of rings, N_m is the number of elements in ring m, W_m is the excitation current of elements on mth ring, k is the angular wavenumber with λ as the wavelength, $r_m(\lambda)$ is the radius of each circular ring with inter-element spacing between rings of d_m; $\theta \in [0, \pi]$ and $\phi \in [0, 2\pi]$ are the elevation and azimuth angles (from the positive *z-axis* and from the positive *x-axis*), respectively. The maximum radiation direction is defined by θ_0 and ϕ_0. The element angular separation ϕ_{mi} from the positive x-axis in each ring can be calculated as $\phi_{mi} = 2\pi(i-1)/N_m$.

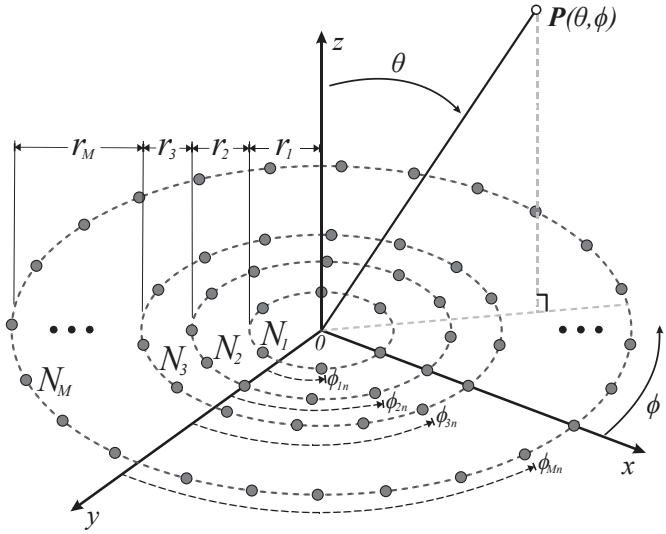

Figure 1. Geometry of the concentric rings array.

We analyzed the impact of the application of CORPS for reducing the number of phase shifter devices in this geometry of concentric rings. Two design configurations were proposed in order to take advantage of the CORPS properties for providing the required cophasal excitation for this structure and to consider the scanning possibilities.

Configuration 1, shown in Figure 2a, considers three rings with 10 antenna elements per ring. This kind of array configuration permits the control of blocks of three antenna elements. Each block had the same angular separation. Then, this configuration can utilize CN2×3 (2 × 3 CORPS networks) and take advantage of the phase interpolation property of CORPS networks [22] for generating the required cophasal excitation.

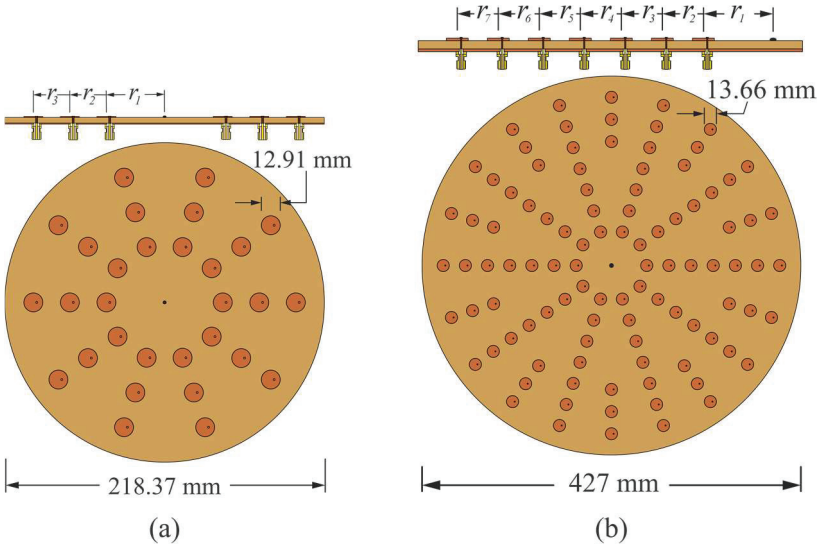

Figure 2. Array configurations: (**a**) Configuration 1 of three rings with 30 antenna elements, (**b**) Configuration 2 of seven rings with 100 antenna elements, both at 6 GHz.

The array configuration assumes the distance between antenna elements of the same ring to be 0.5λ, trying to avoid the effects of mutual coupling. Then, the corresponding radii for configuration 1 are: $r_1 = 0.7958\lambda$, $r_2 = 1.2958\lambda$, and $r_3 = 1.7958\lambda$. Figure 2a shows the antenna array using a circular patch with a central frequency of 6 GHz, diameter of 12.91 mm, $p' = 2.07$ [25], the FR4 substrate with a thickness of $h = 1.6$ mm, relative permittivity $e_r = 4.2$, and tangent loss $\delta = 0.025$.

The other interesting array configuration is illustrated in Figure 2b. As shown in Figure 2b, configuration 2 uses 100 antenna elements distributed over seven rings. This

configuration permits the control of blocks of seven antenna elements and blocks of three elements. Therefore, the array configuration can use CN4×7 (4 × 7 CORPS networks) and CN2×3 in order to generate the cophasal excitation for beam-scanning and reducing the number of phase shifter devices. As in configuration 1, the array configuration assumes the distance between antenna elements to be 0.5λ, having the next radii values: $r_1 = 0.7958\lambda$, $r_2 = 1.2958\lambda$, $r_3 = 1.7958\lambda$, $r_4 = 2.2958\lambda$, $r_5 = 2.7958\lambda$, $r_6 = 3.2958\lambda$, and $r_7 = 3.7958\lambda$.

2.2. CORPS Networks

The feeding networks are based on CORPS to be used as a beam-forming network of the concentric rings array. The CORPS networks take advantage of the wave propagation, splitting (S), and recombining (R) the waves or signals in basic nodes [14,15]. We applied the CORPS networks for taking advantage of the phase interpolation property of a CORPS network of one layer.

The C-BFN configurations were designed according to the CRA model structure. As commented previously, the CRA of configuration 1 utilizes CN2×3 and the CRA of the configuration 2 uses CN4×7 and CN2×3 in order to generate the cophasal excitation for beam-scanning. The CN2×3 uses 2 splitting nodes and 1 recombining node as shown in Figure 3a, and the CN4×7 is designed by interconnecting several CN2×3 [22] (Figure 3a). Unlike a CORPS conventional network (which has 15 splitting and 12 recombining nodes), this configuration uses only 6 splitting and 3 recombining nodes [22]. The theoretical power distribution is illustrated in Figure 3b.

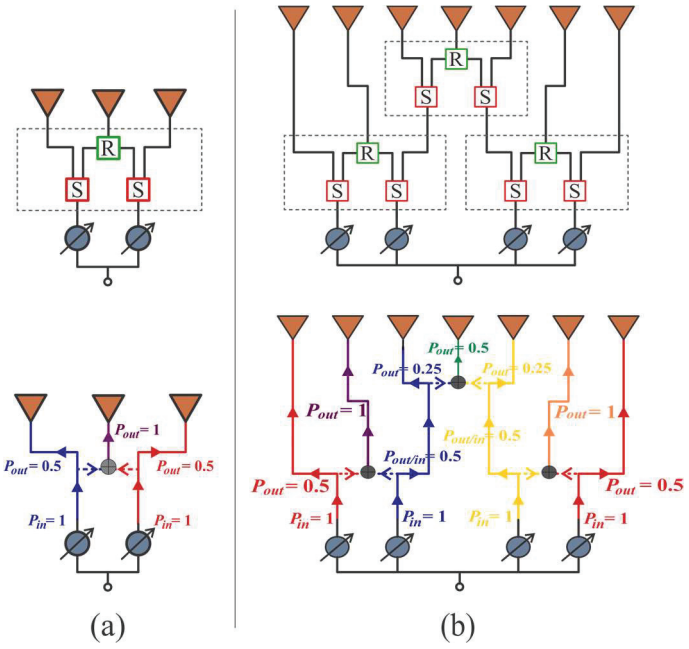

Figure 3. CORPS networks. (**a**) CN2×3, which uses 2 splitting uses and 1 recombining node, (**b**) CN4×7, which uses 6 splitting nodes and 3 recombining nodes.

Gysel power dividers [26] can perform the practical functions of the splitting and recombining nodes. Figures 4 and 5 illustrate the CN2×3 and CN4×7 using Gysel dividers. These configurations incorporate the FR4 substrate with a thickness of 1.6 mm, relative permittivity $e_r = 4.2$, and tangent loss $\delta = 0.025$. Gysel power dividers include chip resistors of 50 Ohms (FC0603-surface mount) and SMA connectors at each input and output port.

The power flow through the networks can be simulated. CN2×3 includes a combination of 3 Gysel power dividers that produce power attenuations (≈−3 dB per divider). Figure 6 shows the simulated power flow of the CN2×3 when the input ports are fed separately and simultaneously by a 6 GHz signal with the same phase value and a unitary amplitude. The Gysel power divider acts as a splitting or combining node of the network. In addition to this, Figure 7 shows a combination of 9 Gysel power dividers, which cor-

respond to 3 CN2×3 interconnected. Thus, this network reduces until 66%, the required Gysel power dividers with respect to the conventional CORPS network. Please note that the performance details of these networks (CN4×7 and CN2×3) such as reflection and transmission coefficients are explained and found in the references [20,22].

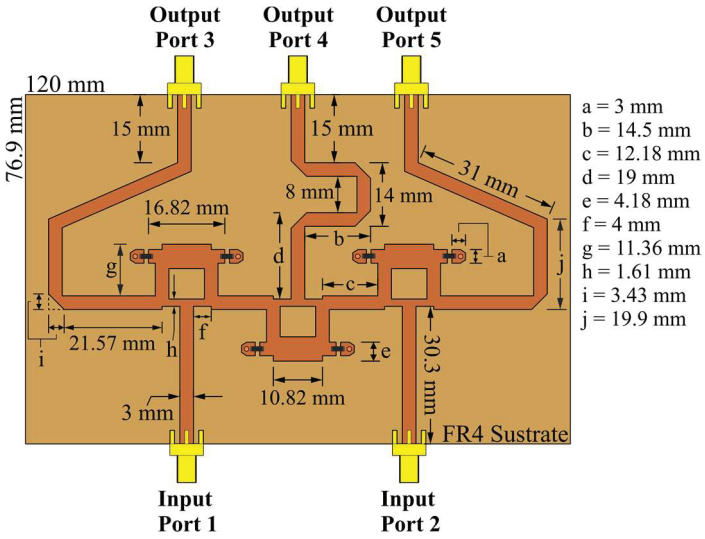

Figure 4. CN2×3, which uses 3 Gysel power dividers at 6 GHz in CST Studio Suite.

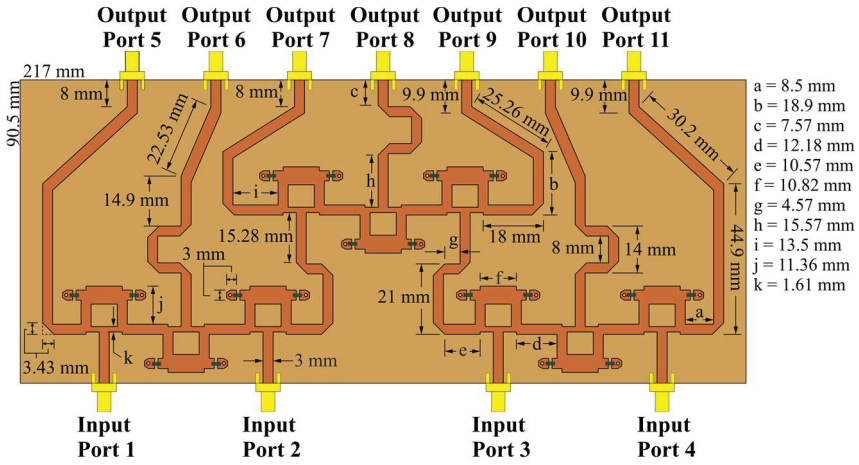

Figure 5. CN4×7, which uses 9 Gysel power dividers at 6 GHz in CST Studio Suite.

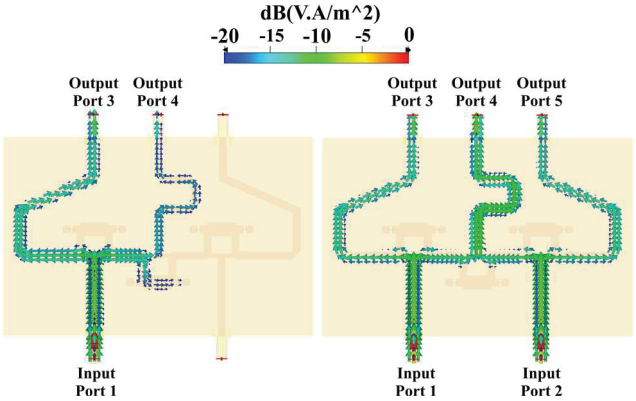

Figure 6. Power flow through the CN2×3.

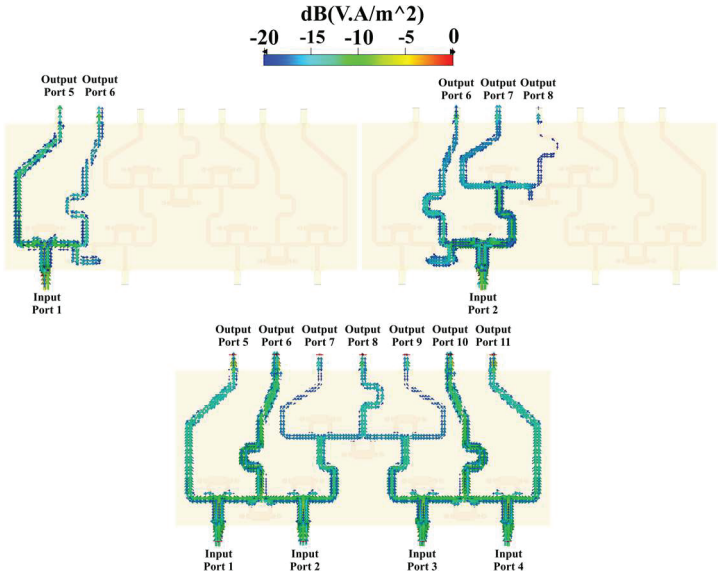

Figure 7. Power flow through the CN4×7.

Figure 7 shows the simulated power flow of the CN4×7 when the input ports are fed separately and simultaneously by a 6 GHz signal with the same phase value and a unitary amplitude. This configuration has a symmetric performance between the first two input ports and the last two input ports of the network, in which the power flow, attenuation, and phase shift are the same at the corresponding output ports. The maximum phase shift of the signal is found in the center. The phase shift can be adjusted at the ends of the network, generating longer lines.

The behavior of CN2×3 and CN4×7 can be studied using simulations and measurements. The S-parameters of CN2×3 and CN4×7 are illustrated in Figures 8 and 9 in terms of reflection and transmission coefficients and phase versus frequency. The CN2×3 shows a bandwidth of 3.9 GHz (as shown in Figure 8) with reflection coefficients of less than −20 dB and −18 dB in the simulated and measured results at 6 GHz, respectively. The transmission values are approximately −3.75 dB in the ports 3 and 5 and approximately −5.35 dB in the port 4.

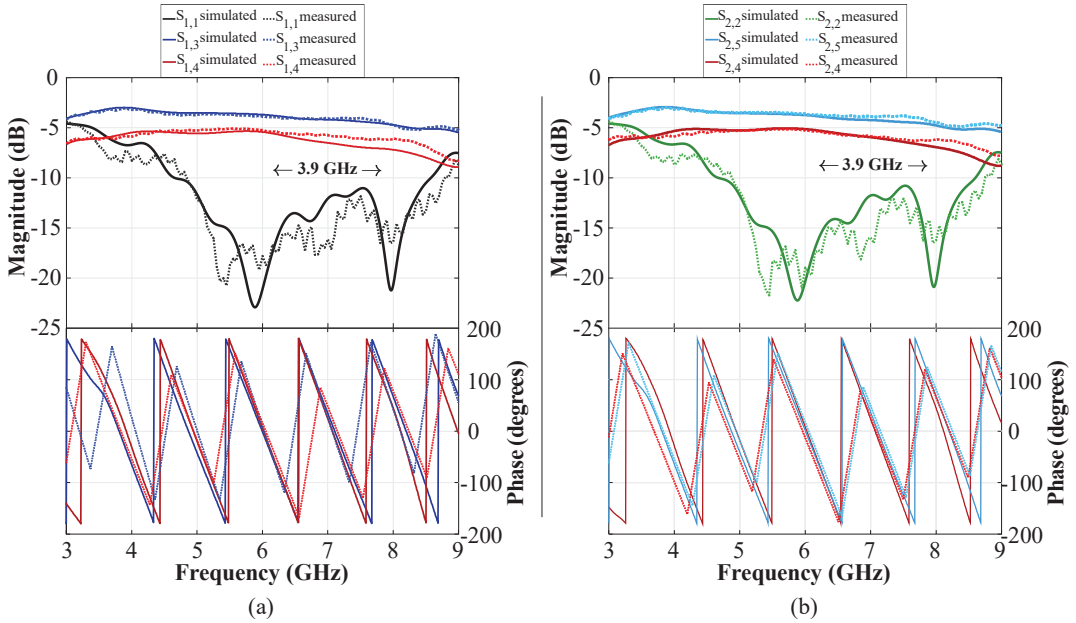

Figure 8. S-parameters of the CN2×3: (**a**) input 1 to outputs 3 and 4, (**b**) input 2 to outputs 4 and 5.

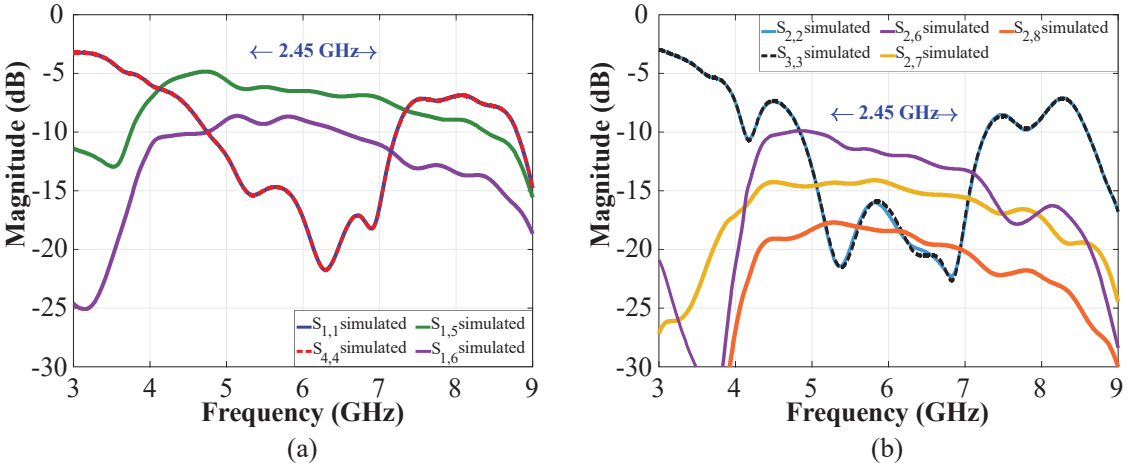

Figure 9. S-parameters of the CN4×7: (**a**) inputs 1 and 4, (**b**) inputs 2 and 3.

Figure 9 shows a reflection coefficient of −20 dB for the CN4×7 considering the input ports 1 and 4, and −15 dB for the ports 2 and 3 (6 GHz). This network presents a bandwidth of 2.45 GHz. The transmission values obtained are $S_{1,5\tilde{}4,11} = -7.52$ dB and $S_{1,6\tilde{}4,10} = -10.4$ dB for the input ports 1 and 4, and of approximately $S_{2,6\tilde{}3,10} = -11.1$ dB, $S_{2,7\tilde{}4,9} = -12$ dB, and $S_{2,8\tilde{}4,8} = -15.3$ dB for the ports 2 and 3.

2.3. Proposed Model for Phased Antenna Arrays

Each phased antenna array system (PAAS) was developed by the interconnection of the CORPS-BFN configuration with its corresponding CRA case. These interconnections are realized from the output of the network to each antenna element in the different rings of the array and the different array inputs are arranged or set as linear subsets. This simplifies the phased array system by a feeding network that uses a smaller number of phase shifters.

Figure 10 illustrates a schematic diagram for the PAAS of the CRA configuration 1, including 10 CN2×3. A layer of attenuators/amplifiers was set at the output of the feeding networks. These values of amplitude excitation can be optimized in order to yield radiation pattern characteristics with a low SLL for each main beam direction. These values of amplitude excitation are considered fixed, i.e., the same value of attenuation is used in each antenna element for each scanning direction.

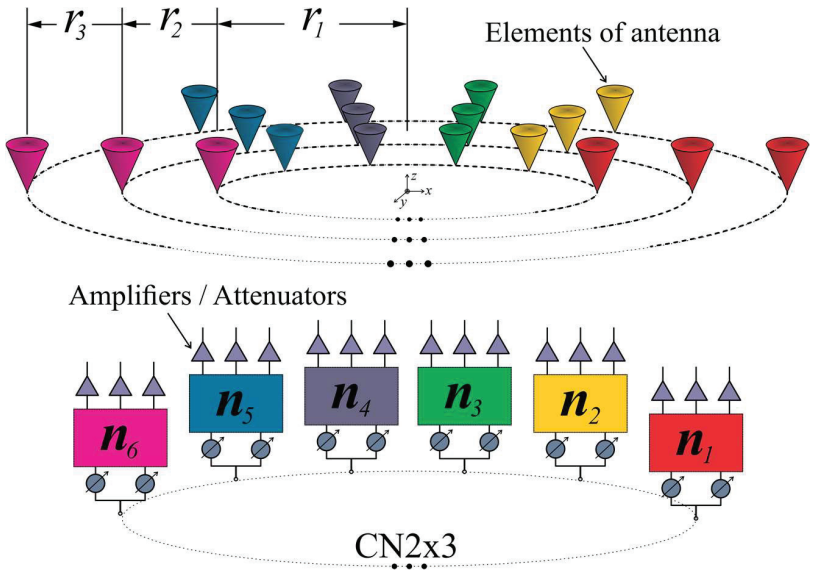

Figure 10. Schematic diagram for the phased antenna array system of configuration 1, including CN2×3.

As an example, Table 1 shows the different phase values generated by the CN2×3 at $\theta_0 = 25°$ in the cut of $\phi = 0°$. The computed phase value is illustrated for each antenna element of the CRA. Because of symmetry of the CRA geometry, the CN2×3 (the networks 2–10, 3–9, 4–8, and 5–7) generate the same phase values for each CN2×3 pair at the output of the feeding network. It is important to note that the input phase difference above 180° could generate power reflections at the input ports due the passive elements of the network. Therefore, phase differences above 180° (between input ports of CN2×3) must be absolutely avoided. This situation is not presented in this arrangement of antenna elements and CN2×3 for the CRA of configuration 1. This configuration provides a scanning range ±25°. Please, take note that this scanning performance is reached by controlling 30 elements of the CRA for this configuration with 20 phase shifters. There was a reduction of 33% in the number of phase shifters for phased arrays in a geometry of CRA.

Table 1. Phases values in each element of antenna grouped in each output port for CN2×3 of CRA of configuration 1.

CN2×3 No.	Element of Antenna	Phase Value (Rad)
1	1, 11, 21	−2.11, −3.44, −4.77
2; 10	2, 12, 22; 10, 20, 30	−1.71, −2.78, −3.86
3; 9	3, 13, 23; 9, 19, 29	−0.65, −1.1, −1.47
4; 8	4, 14, 24; 8, 18, 28	0.65, 1.1, 1.47
5; 7	5, 15, 25; 7, 17, 27	1.71, 2.78, 3.86
6	6, 16, 26	2.11, 3.44, 4.77

The schematic diagram for the PAAS of the CRA configuration 2 is shown in Figure 11. This configuration includes 10 CN2×3 and 10 CN4×7. Although 70 antenna elements could be controlled by the 10 CN4×7, 30 antenna elements are controlled by 10 CN2×3. These 30 elements set in 10 subarrays of 3 elements are added in order to provide better radiation characteristics. A layer of attenuators/amplifiers is set at the output of the feeding networks and these values of amplitude excitation are considered fixed, as previous configuration. Therefore, this configuration provides a scanning range ±25° by controlling 100 elements of the CRA for this configuration with 60 phase shifters. There was a reduction of 40% in the number of phase shifters.

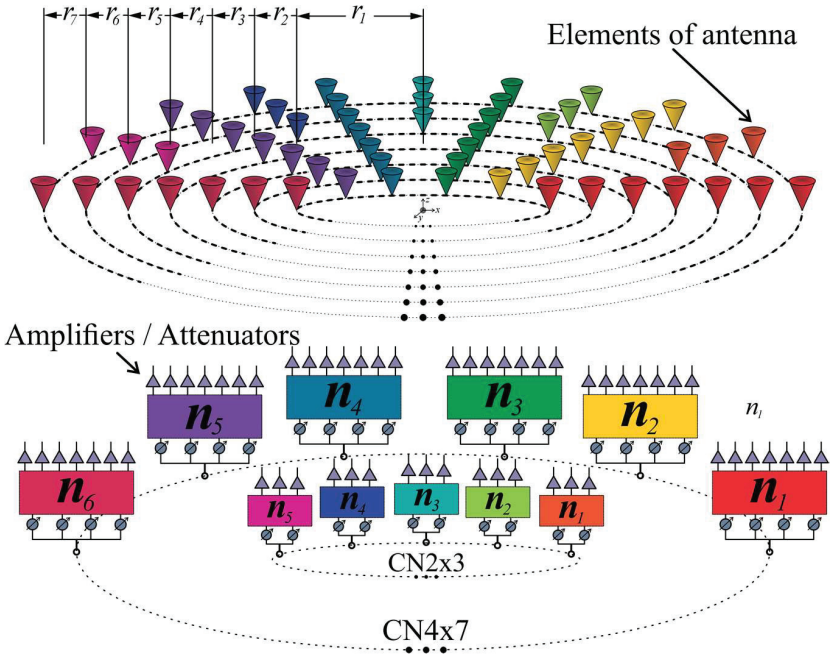

Figure 11. Schematic diagram for the phased antenna array of configuration 2, including CN4×7 and CN2×3.

Table 2 illustrates the different phase values generated by the 10 CN2×3 and the 10 CN4×7 at $\theta_0 = 25°$ in the cut of $\phi = 0°$. As in the previous configuration, the CN4×7 (networks 2–10, 3–9, 4–8, and 5–7) and the CN2×3 (networks 1–10, 2–9, 3–8, 4–7, and 5–6) generate the same phase values (for each networks pair mentioned previously) at the output of the feeding network. As shown in Table 2, the phase differences above 180° between input ports are avoided.

Table 2. Phases values in each element of antenna grouped in each output port for configuration 2.

Network No.	Antenna Element	Phase Value (Rad)
	CN4×7	
1	1, 11, 21, 31, 41, 61, 81	−2.11, −3.44, −4.77, −6.1, −7.42, −8.75, −10.08
2; 10	2, 12, 22, 32, 43, 63, 83; 10, 20, 30, 40, 59, 79, 99	−1.71, −2.78, −3.86, −4.93, −6, −7.1, −8.15
3; 9	3, 13, 23, 33, 45, 65, 85; 9, 19, 29, 39, 57, 77, 97	−0.65, −1.06, −1.47, −1.88, −2.3, −2.7, 3.11
4; 8	4, 14, 24, 34, 47, 67, 87; 8, 18, 28, 38, 55, 75, 95	0.65, 1.1, 1.47, 1.88, 2.3, 2.7, 3.11
5; 7	5, 15, 25, 35, 49, 69, 89; 7, 17, 27, 37, 53, 73, 93	1.71, 2.78, 3.86, 4.93, 6, 7.1, 8.15
6	6, 16, 26, 36, 51, 71, 91	2.11, 3.44, 4.77, 6.1, 7.42, 8.75, 10.08
	CN2×3	
1; 10	42, 62, 82; 60, 80, 100	−7.06, −8.32, −9.58
2; 9	44, 64, 84; 58, 78, 98	−4.36, −5.14, −6
3; 8	46, 66, 86; 56, 76, 96	0, 0, 0
4; 7	48, 68, 88; 54, 74, 94	4.36, 5.14, 6
5; 6	50, 70, 90; 52, 72, 92	7.06, 8.32, 9.58

3. Experimental Results

Simulation and experimental results were obtained for the PAAS of the CRA configurations. The full antenna system for the PAAS of the CRA configuration 1 was full wave simulated, fabricated, and measured for evaluating its performance. The PAAS of CRA configuration 2 was only evaluated by using full wave simulations due to the high complexity.

Figure 12a shows the full system design for the PAAS of the CRA configuration 1. The prototype was fabricated using the array design characteristics mentioned in Section 2.1 (Figure 12b). The design and the prototype illustrate the feeding network based on CN2×3, the attenuators, and the antenna elements of the CRA. All was constructed on FR4 substrate. More details are given in the next sections.

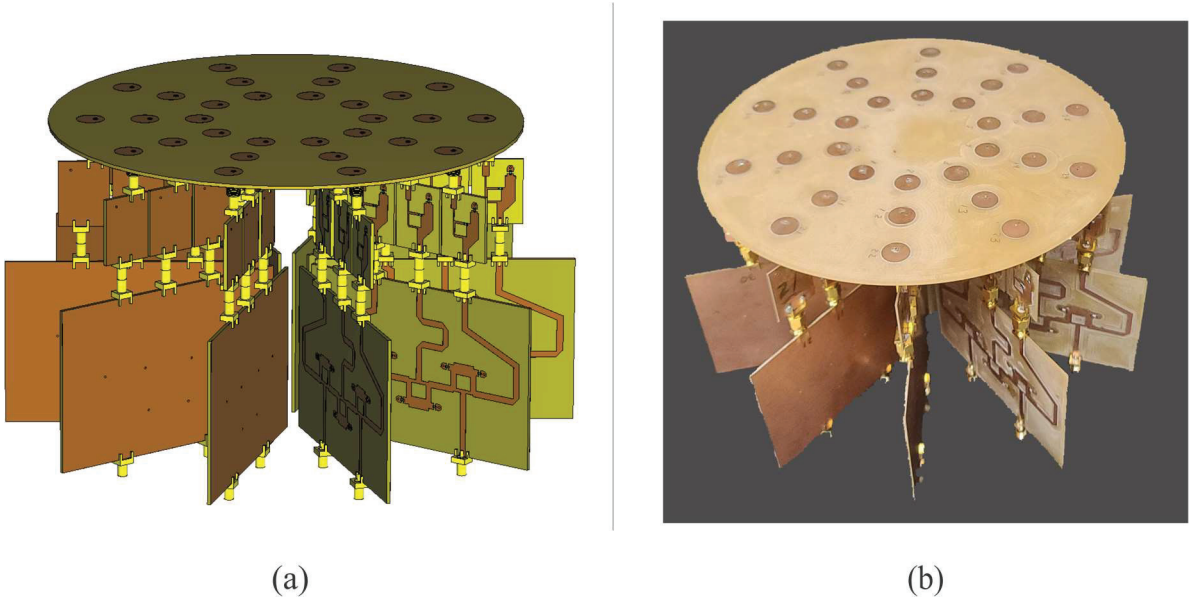

Figure 12. Full system design for the CRA configuration 1: (**a**) design and (**b**) prototype.

Figure 13 illustrates the active reflection coefficients for the CRA of configuration 1 and configuration 2 at $\theta_0 = 25°$. Every direction of the scanning range was examined, as this was the furthest scanning direction and the case of worst performance for active reflection coefficients. The reflection coefficients of all antenna elements remained below −10 dB at the design frequency of 6 GHz. The antenna elements show a good matching performance for the frequency of interest.

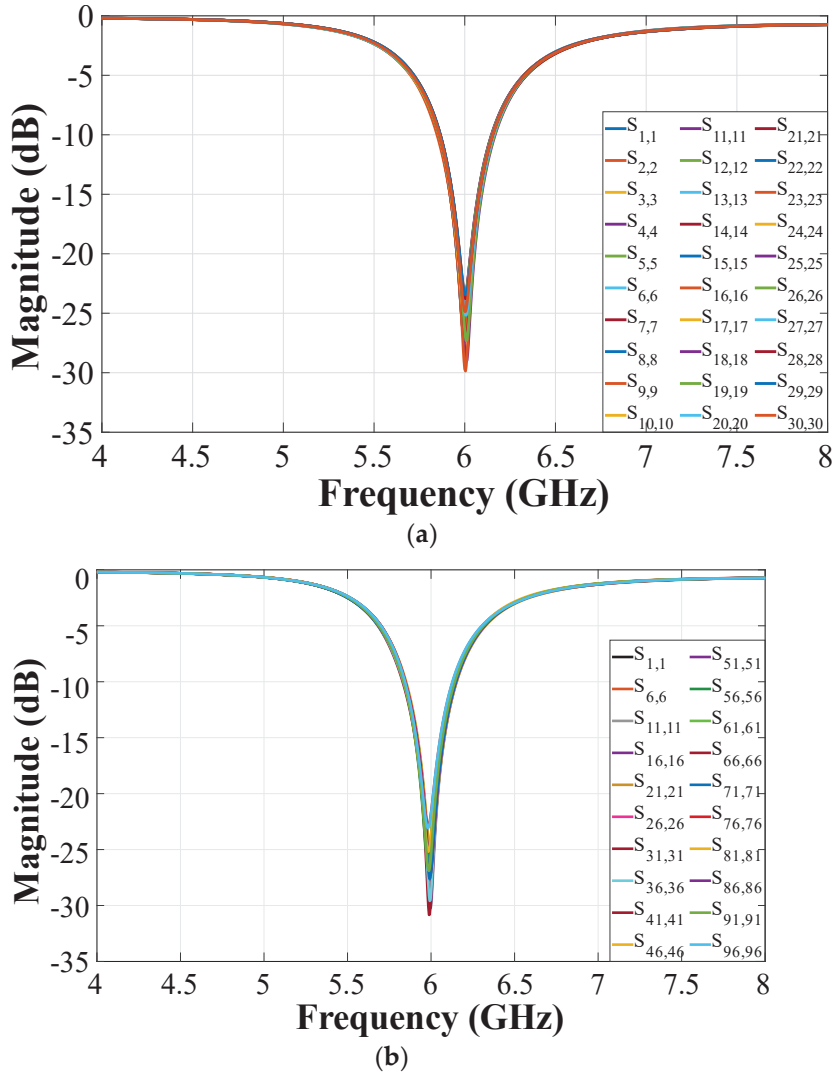

Figure 13. Active reflection coefficients for the CRA of (**a**) configuration 1 and (**b**) configuration 2 at $\theta_0 = 25°$ for a frequency of 6 GHz.

The amplitude excitations were optimized, intending to find radiation patterns with low SLL in all scanning directions for the PAAS of the two CRA configurations. The optimization process was made using a metaheuristic algorithm based in the DE [23]. The principal aim of this algorithm was to determine and select, from a random vector, the best combination of amplitudes for each CRA configuration. This algorithm has been applied extensively and successfully in the array design. Therefore, the details of this optimization algorithm can be found in [23]. We seek with this optimization to represent the use of a set of passive attenuators (due to the low cost of the fabrication). The DE algorithm was run with an initial population of 100 and a number of generations of 1000 iterations. Furthermore, the optimization process considers the next cost–function (*CF*), which evaluates the radiation parameters of SLL and Directivity (D):

$$CF = W_1 \mathrm{SLL}(\theta) - W_2/\mathrm{D}(\theta) \quad (2)$$

where W_1 and W_2 are weighting factors. The values of W_1 and W_2 can be set to give more importance to reduce the SLL or to improve directivity. Then, the values of SLL and directivity (used in the *CF*) are compared and evaluated by the DE algorithm trying to minimize the *CF* in Equation (2). The radiation pattern is considered to be scanned in the elevation plane in a range of $\theta_0 = \pm 25°$. Steps of 1° are considered to evaluate all the scanning range and the worst radiation characteristics (SLL and D) are obtained for the farthest direction. Table 3 presents the vectors of different amplitudes computed with DE algorithm for each CRA configuration.

Table 3. Optimized amplitudes for the PAAS of the two CRA.

Model	Amplitudes
Configuration 1	1.9998 0.3621 1.8963 1.9419 0.2094 1.9184 0.1059 1.6764 1.8317 0.3447 0.9966 0.4440 0.2555 0.1302 0.6474 0.4949 0.4979 0.1406 0.3137 0.5950 0.8243 0.5703 0.1405 0.3697 0.2117 0.2139 0.5985 0.3781 0.3781 0.3781
Configuration 2	0.4151 1.1743 1.2849 1.3340 0.5434 0.5843 1.3178 1.4168 1.1669 1.3718 1.3698 1.1058 1.4535 1.2601 0.7342 1.3838 1.3736 1.1524 1.3929 0.6461 0.8586 1.2891 1.2774 1.1981 1.4290 1.2180 1.4155 1.4239 1.1275 1.2777 0.6157 0.9340 0.4964 0.7554 0.8111 0.4849 0.7463 0.7183 0.9163 0.8420 0.5775 1.0298 0.8356 1.2533 0.5876 0.7050 0.6295 1.0512 0.8737 0.7361 0.5168 0.8362 0.7704 0.8781 0.7116 0.8127 0.5718 1.0242 0.5790 0.8141 0.6353 0.5105 0.5185 0.8109 1.0423 1.0958 0.4863 0.6007 0.5798 0.4462 0.4412 0.5110 0.6597 1.0407 0.8082 0.7466 0.7569 0.5486 0.4373 0.4019 0.5701 0.5093 0.5716 0.8326 1.2098 1.4269 1.1416 1.0053 0.4846 0.6187 0.6801 0.4758 0.5502 0.7493 0.7493 1.3071 1.3102 1.1493 0.4216 0.4216

Each attenuator of the prototype illustrated in Figure 14 was realized considering unequal Wilkinson power divider [27]. The split tee power divider consists in a common power divider with an isolated port. By this way, the output port has an attenuated signal from input [27]. The attenuation level is controlled by the different transmission lines width. Figure 14 illustrates the design of attenuators in CST Studio Suite with the split tee power dividers and (surface mount) resistors of 50 and 100 Ohms for attenuation levels of −1.86 dB and −8.13 dB of attenuation.

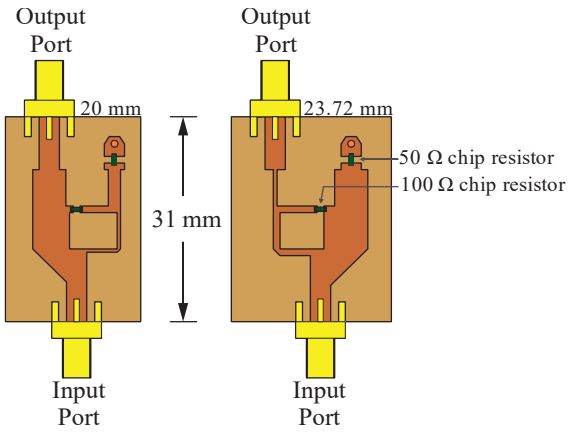

Figure 14. Design of attenuators in CST Studio Suite at 6 GHz.

All the attenuators were full wave simulated and measured to be integrated with the feeding network of CN2×3, i.e., the full system design for the PAAS of the CRA configuration 1 shown in Figure 12b. All the attenuation coefficients for the full system design (the simulation model in CST and the prototype illustrated in Figure 12a) are shown in Table 4. The attenuation values are given in dB.

Table 4. Attenuation coefficients of the full system design for the CRA configuration 1 shown in Figure 12.

Element of Antenna	Attenuation Coefficient	Element of Antenna	Attenuation Coefficient
1, 3, 4, 6, 8, 9	−1.86 dB	2, 10	−8.13 dB
5, 7	−8.16 dB	11	−7.74 dB
12, 20	−8.39 dB	13, 19	−9.28 dB
14, 18	−9.34 dB	15, 17	−8.5 dB
16	−7.92 dB	21	−8.15 dB
22, 30	−8.16 dB	23, 29	−8.07 dB
24, 28	−7.99 dB	25, 27	−7.88 dB
26	−7.91 dB		

Experimental measurements of the radiation pattern for the prototype of the PAAS for configuration 1 (Figure 12b) were performed in a far field anechoic chamber. It is important to note that this phased array design generates (or considers) a cophasal excitation across the antenna elements. More work and study could be done in the phase control in order to generate an optimal phase distribution, but this was outside the aim of our paper. In our case, the measurement system generates the phase shifts required at the input ports to generate a cophasal excitation across the CRA. These delays or transmission lines can be replaced by electronic phase shifters without change in the radiation pattern performance [6].

Figure 15 shows the radiation pattern obtained by full wave simulations (in CST) and experimental measurements, (a) $\theta_0 = -25^\circ$, (b) $\theta_0 = 0^\circ$, (c) $\theta_0 = 15^\circ$, and (d) $\theta_0 = 25^\circ$, for the system of the CRA configuration 1 (shown in Figure 12). These results illustrate that the design of the phased CRA (using the proposed technique) provides a reduction of phase shifters (33%) generating a radiation pattern with low SLL. This SLL performance remained in all scanning ranges. The radiation pattern obtained by the proposed design was compared (in Figure 15e) with respect to the case without amplitude excitations optimization and the uniform conventional CRA. The optimization of the amplitude coefficients generates a radiation pattern with a SLL value of −24 dB and a reduction of ≈11 dB in the SLL with respect to the other techniques. Furthermore, the radiation pattern obtained by the proposed optimized design with the reduction of phase shifters is compared with respect to the case of using 1 phase shifter by elements with optimized amplitudes (Figure 15f). Evidently, as shown in Figure 15f, there is a cost to having the reduction of phase shifters (1.5 dB of SLL with respect to the optimal case using 1 PS per element). The phased antenna system based on CRA configuration 1 was validated by experimental measurements as illustrated in Figure 15g). The radiation pattern results obtained by experimental measurements agree with the simulation results with a slight deviation in the SLL performance (−22.5 dB).

Furthermore, the scan-loss of the CRA configuration 1 is shown in Figure 16. The gain losses of the radiation pattern with respect to the natural response at the direction of $\theta_0 = 0^\circ$ (without beam steering) are approximately −0.51 dB and −0.36 dB at $\theta_0 = -25^\circ$ and $\theta_0 = 25^\circ$, respectively. The results demonstrate low losses in the gain values of the radiation pattern in the entire scan range, even when any phase shift is used (from $\theta_0 = 0^\circ$ to $\theta_0 = \pm 25^\circ$).

Figure 17 illustrates the radiation pattern obtained by full-wave simulations for the system of the CRA configuration 2 at (a) $\theta_0 = -25^\circ$, (b) $\theta_0 = 0^\circ$, (c) $\theta_0 = 15^\circ$, and (d) $\theta_0 = 25^\circ$, and a comparison is shown in Figure 17e (with respect to the uniform conventional CRA and without optimization). As shown in Figure 17, the radiation pattern obtained by the proposed design for this CRA configuration provides a SLL value of −27.9 dB, a significant reduction of SLL (≈11.2 dB) with respect to the conventional techniques. This SLL performance was reached by a reduction of 40% in the number of phase shifters in all scanning ranges.

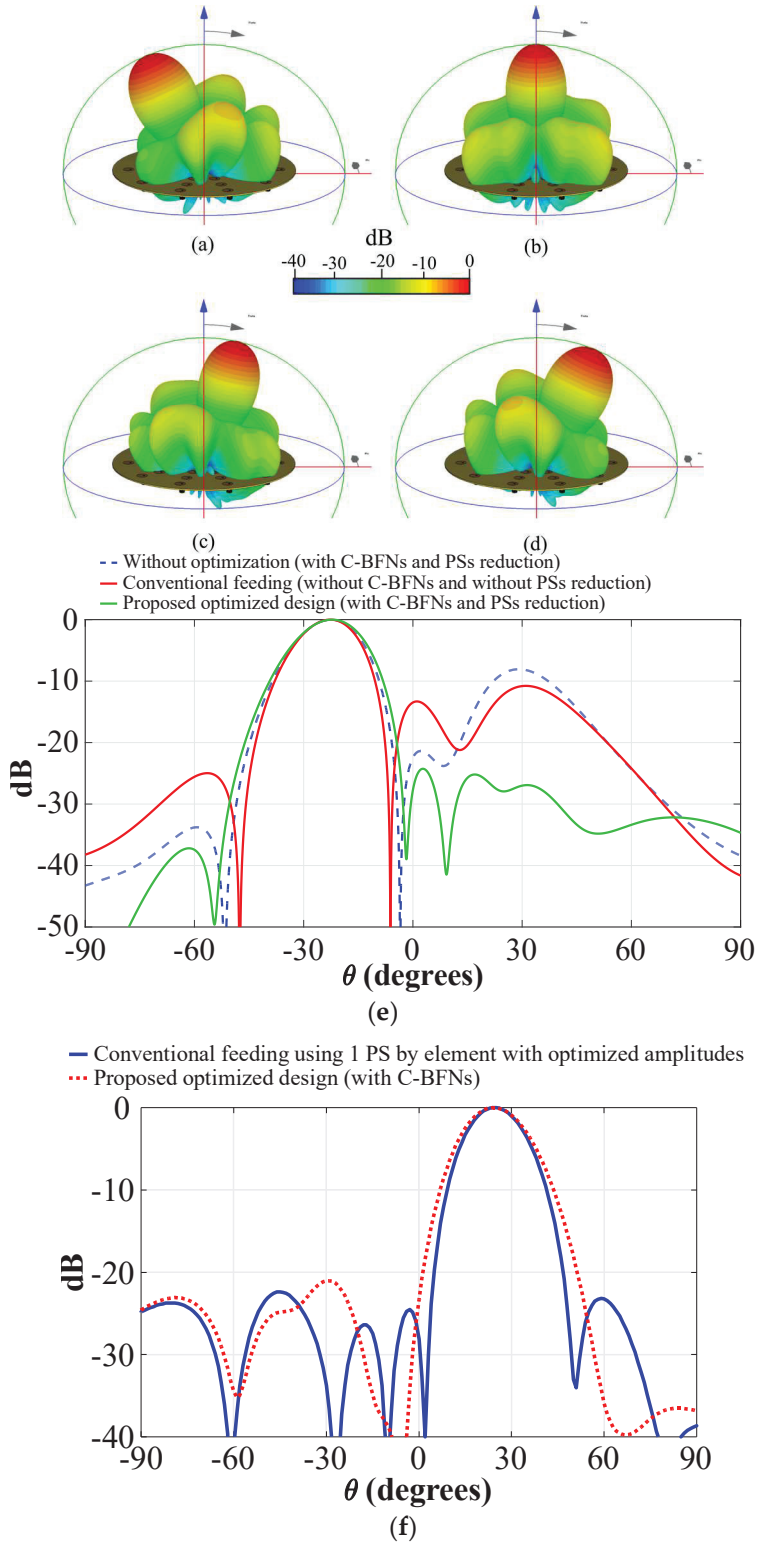

Figure 15. *Cont.*

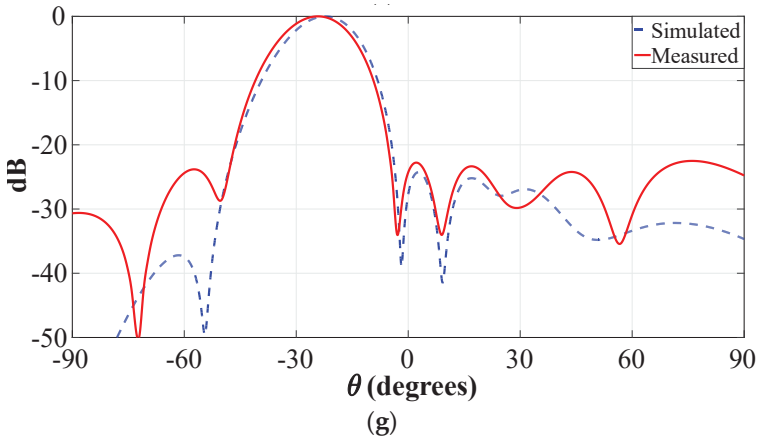

Figure 15. Radiation pattern obtained for the system of the CRA configuration 1 (Figure 12) by full-wave simulations (CST) (**a**) $\theta_0 = -25°$, (**b**) $\theta_0 = 0°$, (**c**) $\theta_0 = 15°$, (**d**) $\theta_0 = 25°$, (**e**) comparison of the radiation pattern with respect to conventional techniques, (**f**) comparison of the radiation pattern with respect to the case of using 1 PS by element (optimized amplitudes), and (**g**) experimental measurements.

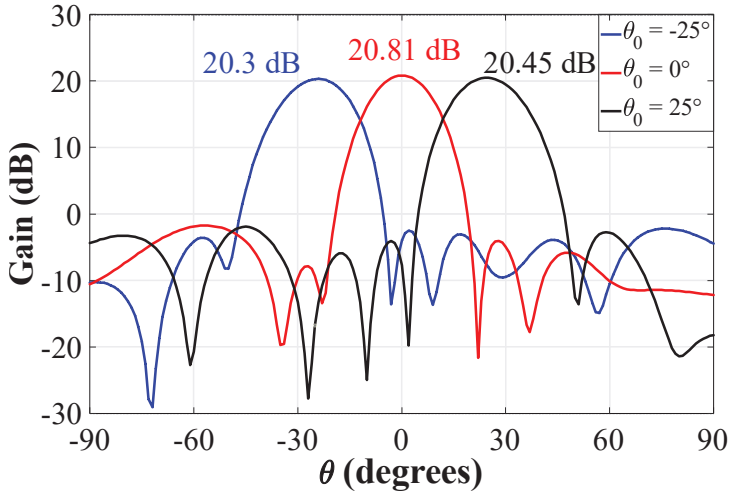

Figure 16. Gain values of the CRA configuration 1 considering beam-scanning.

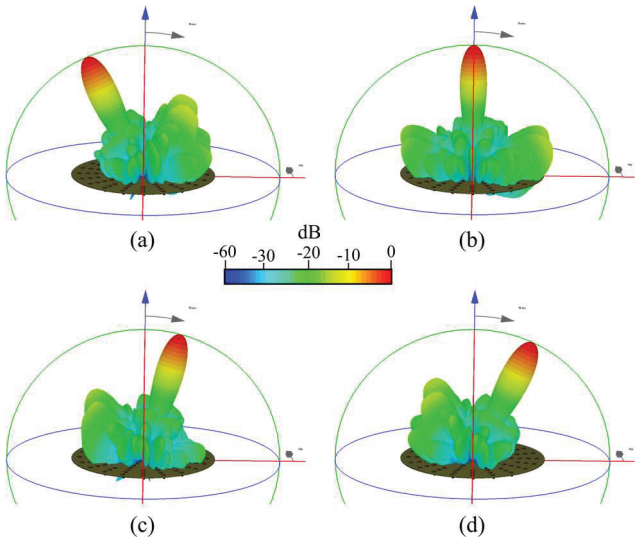

Figure 17. *Cont.*

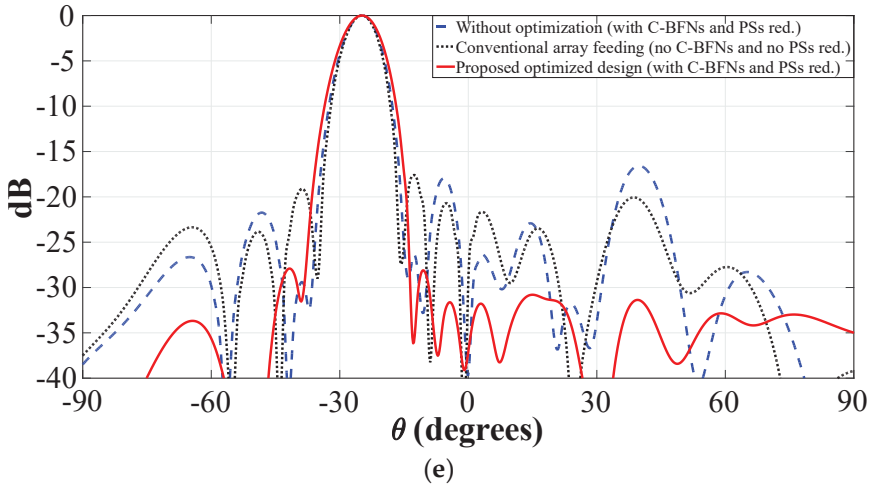

Figure 17. Radiation pattern obtained for the system of the CRA configuration 2 by full-wave simulations (CST) (**a**) $\theta_0 = -25°$, (**b**) $\theta_0 = 0°$, (**c**) $\theta_0 = 15°$, (**d**) $\theta_0 = 25°$, (**e**) comparison with respect to conventional techniques.

Table 5 illustrates a comparative analysis of the proposed design for PAAS of the CRA configurations with respect to other state of art techniques (for designing phased arrays in the geometry of CRA). This comparative analysis is made in terms of the SLL, reduction of phase shifters, number of antenna elements, and scanning range. The proposed design for the CRA configurations provides a reduction in phase shifters (of 33% for configuration 1 and 40% for configuration 2) for a scanning range of ±25° with a peak SLL of −24 dB (full-wave simulations) (−22.5 dB obtained with measurements) for configuration 1 and −27.9 dB (full-wave simulations) for configuration 2.

Table 5. Comparison between different works of concentric rings arrays with reduced phase shifters.

	Optimization	Number of Elements	Number of Phase Shifters	Reduction of Phase Shifters (%)	Scanning Range	Feeding Technique	Peak SLL (dB)
Conv. case	No	30	30	0%	±90°(θ)	Uniform	−10
This work: Conf. 1	Yes	30	20	33%	±25°(θ) Scan loss = 0.5 dB	C-BFN	−24 (sim.), −22.5 (Measured)
This work: Conf. 2	Yes	100	60	40%	±25°(θ)	C-BFN	−27.9 (Full-wave)
[18]	Yes	90	60	33%	Not specified	C-BFN	−25 (Array factor)
[21]	Yes	92	87	6%	Not specified	C-BFN	−23 (Array factor)
[28]	Yes	49	Not specif.	0%	Not specified	Uniform	−34 (Array factor)
[29]	Yes	201 142 134	Not specif.	0%	Not specified	Uniform	−29.03 −28 (Array factor) −29.07
[30]	Yes	18 30	Not specif.	0%	Not specified	Uniform	−36 (Array factor) −32.88

4. Conclusions

The proposed design technique for the structure of concentric rings provided a better scanning capability with respect to other existing configurations. CORPS networks were set strategically in the feeding network to provide several advantages with respect to others in the scanning capability and the reduction of the number of phase shifters of the array system. The proposed phased array reduced 33% and 40% of the phase shifters devices for CRA configuration 1 and configuration 2, respectively. DE was applied to optimize the amplitudes of the proposed system for both CRA configurations.

The proposed design for the CRA configurations provided a reduction in phase shifters for a scanning range of ±25° with a peak SLL of −24 dB (full-wave simulations)

(−22.5 dB obtained with measurements) for CRA configuration 1 and −27.9 dB (full-wave simulations) for CRA configuration 2. The proposed phased array achieves a good design compromise with respect to other techniques in the literature.

Author Contributions: Methodology, M.A.P. and B.S.; Software, A.R.; Validation, E.J. and B.S.; Formal analysis, B.S. and A.R.; Investigation, M.A.P. and B.S.; Resources, D.H.C. and A.R.; Data curation, B.S.; Visualization, E.J.; Supervision, A.R.; Project administration, D.H.C.; Funding acquisition, M.A.P. and A.R. All authors have read and agreed to the published version of the manuscript.

Funding: This research received no external funding.

Informed Consent Statement: Not applicable.

Data Availability Statement: Not applicable.

Conflicts of Interest: The authors declare no conflict of interest.

References

1. Laue, H.E.A.; Plessis, W.P.d. Numerical optimization of compressive array feed networks. *IEEE Trans. Antennas Propag.* **2018**, *66*, 3432–3440. [CrossRef]
2. Blake, J.; Nygren, E.; Shennum, G. *Beamforming Networks for Spacecraft Antennas*; International Symposium Antennas and Propagation Society: Boston, MA, USA, 1984.
3. Bhattacharyya, A.K. *Phased Array Antennas: Floquet Analysis, Synthesis, BFNs, and Active Array Systems*; John Wiley & Sons: Hoboken, NJ, USA, 2006.
4. Bevelacqua, P.J.; Balanis, C.A. Minimum sidelobe levels for linear arrays. *IEEE Trans. Antennas Propag.* **2007**, *55*, 3442–3449. [CrossRef]
5. Haupt, R.L. Optimized weighting of uniform subarrays of unequal sizes. *IEEE Trans. Antennas Propag.* **2007**, *55*, 1207–1210. [CrossRef]
6. Avser, B.; Frazita, R.F.; Rebeiz, G.M. Interwoven feeding networks with aperture sinc-distribution for limited-scan phased arrays and reduced number of phase shifters. *IEEE Trans. Antennas Propag.* **2018**, *66*, 2401–2413. [CrossRef]
7. Juarez, E.; Panduro, M.A.; Reyna, A.; Covarrubias, D.H.; Mendez, A.; Murillo, E. Design of concentric ring antenna arrays based on subarrays to simplify the feeding system. *Symmetry* **2020**, *12*, 970. [CrossRef]
8. Laue, H.E.A.; Plessis, W.P.d. Design and Analysis of a Proof-of-Concept Checkered-Network Compressive Array. *IEEE Trans. Antennas Propag.* **2022**, *70*, 7546–7555. [CrossRef]
9. Singh, S. Minimal Redundancy Linear Array and Uniform Linear Arrays Beamforming Applications in 5G Smart Devices. *Emerg. Sci. J.* **2021**, *4*, 70–84. [CrossRef]
10. Payami, S.; Ghoraishi, M.; Dianati, M.; Sellathurai, M. Hybrid Beamforming with a Reduced Number of Phase Shifters for Massive MIMO Systems. *IEEE Trans. Veh. Technol.* **2018**, *67*, 4843–4851. [CrossRef]
11. Yin, L.; Yang, P.; Gan, Y.; Yang, F.; Yang, S.; Nie, Z. A Low Cost, Low in-Band RCS Microstrip Phased-Array Antenna with Integrated 2-bit Phase Shifter. *IEEE Trans. Antennas Propag.* **2021**, *69*, 4517–4526. [CrossRef]
12. Dong, R.; Shi, B.; Zhang, X.; Shu, F.; Wang, J. Performance Analysis of Massive Hybrid Directional Modulation with Mixed Phase Shifters. *IEEE Trans. Veh. Technol.* **2022**, *71*, 5604–5608. [CrossRef]
13. Betancourt, D.; del Rio, C. Designing feeding networks with corps: Coherently radiating periodic structures. *Microw. Opt. Technol. Lett.* **2006**, *48*, 1599–1602. [CrossRef]
14. Garcia, R.; Betancourt, D.; Ibañez, A. Coherently radiating periodic structures (CORPS): A step towards high resolution imaging systems. In Proceedings of the 2005 IEEE Antennas and Propagation Society International Symposium, Washington, DC, USA, 3–8 July 2005; Volume 4B, pp. 347–350.
15. Ferrando, N.; Fonseca, N.J.G. Investigations on the efficiency of array fed coherently radiating periodic structure beam forming networks. *IEEE Trans. Antennas Propag.* **2011**, *59*, 493–502. [CrossRef]
16. Arce, A.; Cardenas-Juarez, M.; Pineda-Rico, U.; Covarrubias, D.H.; Stevens-Navarro, E. A multiple beamforming network for unequally spaced linear array based on CORPS. *Int. J. Antennas Propag.* **2015**, *2015*, 757989. [CrossRef]
17. Panduro, M.A.; del Rio-Bocio, C. Simplifying the feeding network for multi-beam circular antenna arrays by using CORPS. *Prog. Electromagn. Res. Lett.* **2011**, *21*, 119–128. [CrossRef]
18. Arce, A.; Panduro, M.A.; Covarrubias, D.H. An approach for simplifying a multiple beam-forming network for concentric ring arrays using CORPS. *J. Electromagn. Waves Appl.* **2014**, *28*, 430–441. [CrossRef]
19. Betancourt, D.; del Rio-Bocio, C. A novel methodology to feed phased array antennas. *IEEE Trans. Antennas Propag.* **2007**, *55*, 2489–2494. [CrossRef]
20. Juarez, E.; Panduro, M.A.; Covarrubias, D.H.; Reyna, A. Coherently radiating periodic structures to reduce the number of phase shifters in a 2-D phased array. *Sensors* **2021**, *21*, 6592. [CrossRef]
21. Arce, A.; Stevens-Navarro, E.; Cardenas-Juarez, M.; Pineda-Rico, U.; Simon, J.; Panduro, M.A. Design and Optimization of a Coherent Beamforming Network for an Aperiodic Concentric Ring Array. *Int. J. Antennas Propag.* **2019**, *2019*, 4601718. [CrossRef]

22. Juarez, E.; Panduro, M.A.; Covarrubias, D.H.; Reyna, A.; Sanchez, B.J. An innovative way of using CORPS for phased arrays with reduced number of phase shifters. *IEEE Trans. Antennas Propag.* **2022**, *70*, 307–316. [CrossRef]
23. Price, K.V.; Storn, R.M.; Lampinen, J.A. *Differential Evolution: A Practical Approach to Global Optimization*; Springer: Berlin/Heidelberg, Germany, 2005.
24. Stearns, C.O.; Stewart, A.C. An investigation of concentric ring antennas with low sidelobes. *IEEE Trans. Antennas Propag.* **1965**, *18*, 856–863. [CrossRef]
25. Balanis, C.A. *Antenna Theory: Analysis and Design*, 2nd ed.; Wiley: New York, NY, USA, 1997.
26. Ooi, B.L.; Palei, W.; Leong, M.S. Broad-banding technique for in-phase hybrid ring equal power divider. *IEEE Trans. Microw. Theory Technol.* **2002**, *50*, 1790–1794.
27. Parad, L.I.; Moynihan, R.L. Split-tee power divider. *IEEE Trans. Microw. Theory Technol.* **1965**, *13*, 91–95. [CrossRef]
28. Hamdi, B.; Liman, S.; Aguili, T. Uniform and Concentric Circular Antenna Arrays Synthesis for Smart Antenna Systems Using Artificial Neural Network Algorithm. *Prog. Electromagn. Res. B* **2016**, *67*, 91–105. [CrossRef]
29. Guo, Q.; Chen, C.; Jiang, Y. An Effective Approach for the Synthesis of Uniform Amplitude Concentric Ring Arrays. *IEEE Antennas Wirel. Propag. Lett.* **2017**, *16*, 2558–2561. [CrossRef]
30. Das, A.; Mandal, D.; Ghosal, S.P.; Kar, R. Concentric circular antenna array synthesis for side lobe suppression using moth flame optimization. *AEU Int. J. Electron. Commun.* **2018**, *86*, 177–184. [CrossRef]

sensors

MDPI

Article

A New Scheme of Applying CORPS and Crossovers to Reduce the Number of Phase Shifters in Antenna Arrays

Gilberto Calvillo [1], Marco A. Panduro [1,*], Brian Sanchez [1] and Alberto Reyna [2]

[1] CICESE Research Center, Electronics and Telecommunications Department, Carretera Ensenada-Tijuana No. 3918, Zona Playitas, Ensenada 22860, Baja California, Mexico
[2] Universidad Autónoma de Tamaulipas, UAMRR-R, Carretera Reynosa-San Fernando, Reynosa 88779, Tamaulipas, Mexico
* Correspondence: mpanduro@cicese.mx

Abstract: This paper presents a new scheme of applying CORPS (coherently radiating periodic structures) for reducing the number of phase shifters in linear antenna arrays. This scheme can be seen as a combination of the properties of two techniques: CORPS and butler. The proposed system applies an interleaving of several blocks of 2 × 3 CORPS networks. This interleaving of two stages of 2 × 3 CORPS networks is made in a convenient way to provide the required progressive phase for beam-scanning and the level of amplitude excitations necessary for achieving the radiation characteristics of low SLL. Interesting results are provided based on experimental measurements and full-wave simulations to analyze and evaluate the performance of the feeding network based on CORPS and the reduction capability of the number of phase shifters in the antenna system. The proposed design methodology achieves a reduction capability of 66% in the number of phase shifters used in linear antenna arrays. This reduction in the complexity of the antenna system is reached maintaining a peak SLL of −22 dB with scanning ranges of until ±25°. A good design option is provided to simplify the complexity of the feeding network in antenna array applications.

Keywords: linear array; scanning range; phase shifter; CORPS

1. Introduction

The new sensor technologies require novel radiating systems with better performance characteristics. Antenna arrays play a very important role as radiating systems in the new generation of communication systems. New communications systems can be possible with the application of different structures of antenna arrays based on beam-forming networks [1]. These beam-forming networks are responsible of generating different beams in certain directions of a scanning range with the desired characteristics of the side lobe level (SLL). The complexity of these beam-forming networks to generate desired patterns limit the application of antenna arrays in communication systems. The applications of antenna arrays will increase with key benefits for the system if the complexity of the beam-forming networks is decreased. Simpler, low-cost beam-forming networks that provide the required performance are required. One way of reducing the complexity of the beam-forming networks is to reduce the number of phase shifters used in the antenna system [2].

There are several design methodologies in the literature for generating beam-forming networks. There is an interesting study line from the traditional (or classical) networks such as the butler matrix [3], Blass [4], and Nolen [5] to the most recent feeding networks for reducing the number of active devices including the application of subarrays [6–13], overlapping techniques [14–18], interleaving schemes [19] and CORPS (coherently radiating periodic structures) networks [20–23].

The use of subarrays is the most used technique to reduce the number of phase shifters. The antenna array can be partitioned in groups of uniform subarrays [11,13] or non-uniform subarrays [1]. A high number of phase shifters can be reduced by using subarrays.

However, the radiation characteristics of array systems deteriorate substantially. So, the design problem complexity increases as the subarray size is increased. The overlapping [14] and interleaving [19] techniques could provide a reduction in the number of phase shifters and generate acceptable radiation characteristics. However, these techniques in general are complex and not easy to fabricate in the feeding network system.

It has been demonstrated recently that the CORPS technique reduces the number of phase shifters for linear [21] and planar [22] antenna arrays. Although these configurations of the previous work provide an interesting way of applying CORPS considering the cophasal excitation required for beam-scanning, the application of CORPS for reducing the number of phase shifters in the beam-forming network is really scarce in the literature. The CORPS concept can be considered to design new schemes or methodologies that simplify the complexity of the antenna system with the required radiation characteristics.

This paper introduces a new scheme of applying CORPS for reducing the number of phase shifters in linear antenna arrays. This new scheme applies an interleaving of several blocks of 2×3 CORPS networks. The outputs of a set of 2×3 CORPS networks are connected to the inputs of other set of 2×3 CORPS networks. This interleaving of two stages of 2×3 CORPS networks is made in a convenient way to provide the required progressive phase for beam-scanning and the level of amplitude excitations necessary for achieving the radiation characteristics of low SLL. In this case, a raised cosine amplitude distribution is applied to obtain low SLL. Interesting results are provided based on experimental measurements and full-wave simulations to analyze and evaluate the performance of the feeding network based on CORPS and the reduction capability of the number of phase shifters in the antenna system. The proposed design methodology achieves a reduction capability of 66% in the number of phase shifters used in linear antenna arrays. This reduction in the complexity of the antenna system is reached maintaining a low value of SLL with scanning ranges of until $\pm 25^{\circ}$. The feeding network and the full system using linear antenna arrays were validated using experimental measurements and electromagnetic simulations. This proposed technique provides several benefits with respect to other techniques in the literature.

2. Proposed Array Design Methodology

An interesting scheme to feed linear antenna arrays is proposed to achieve a reduction in the number of phase shifters in the system. So, the model and the proposed design configuration is described for this geometry. This new scheme can be seen as a combination of properties of two techniques: CORPS and crossovers.

2.1. Theoretical Aspects of CORPS

The feeding network systems based on CORPS have been introduced previously in [20–23]. The CORPS networks consist of the iteration of recombination and split nodes [23]. The key theoretical aspect of these networks is the power or energy propagation through the network using these nodes (split or recombination) [23]. Figure 1 illustrates this; it shows a linear antenna array using 9 elements and a CORPS feeding network of 5 layers and 4 input ports. Then, the signals set at the input ports are split and recombined in each layer delivering a phase and amplitude distribution at the output ports. Amplifiers and phase shifters can be used at the input ports to generate desirable characteristics of the phase and amplitude at the output ports. The basic case of Figure 1 reduces from 9 phase shifters (used in a traditional phased array) to 4. As set in [23], the design configuration of these networks must consider that the losses increases if the number of layers increases.

An interesting property of the CORPS networks was studied in [21,22]. This property considers that if 2 signals are fed to a CORPS network of 2×3, as shown in Figure 2, the phase average of the two signals is obtained at the output of the recombination node. This property is useful to generate the desirable progressive phase for linear antenna array configurations [21].

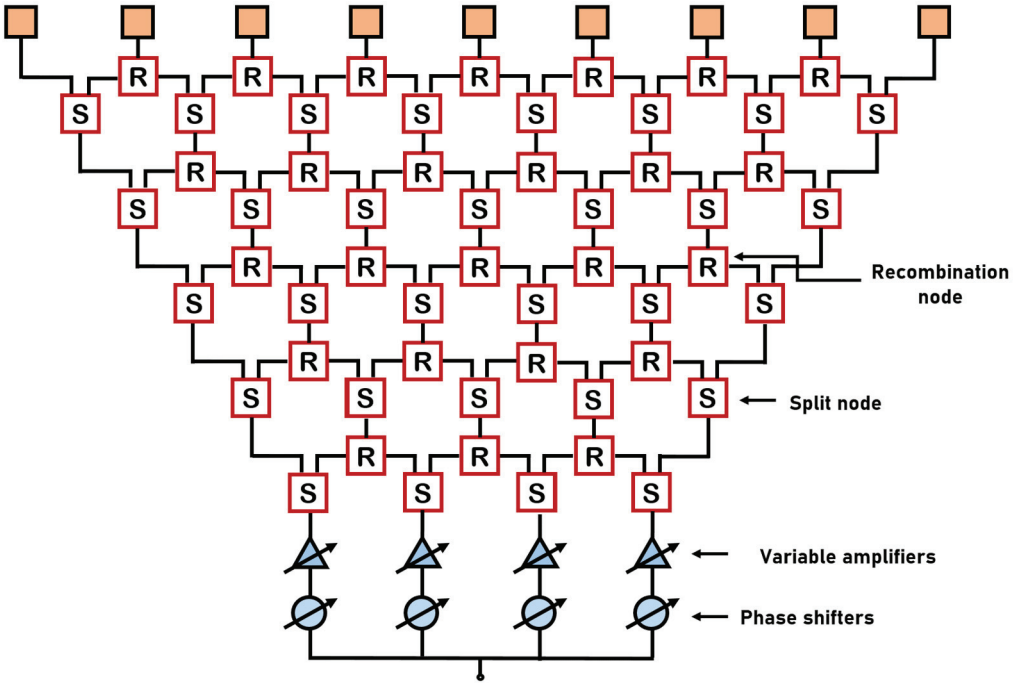

Figure 1. Standard scheme for a CORPS feeding network of 9 elements and 4 input ports.

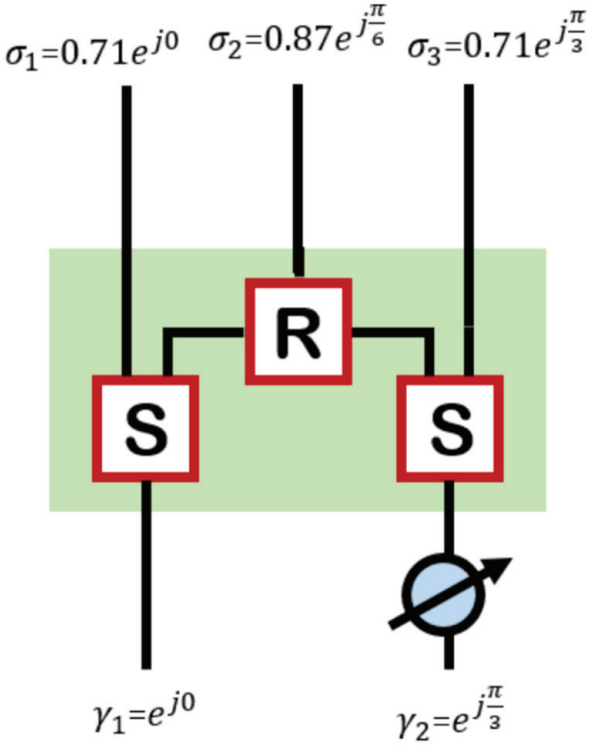

Figure 2. CORPS feeding network of 2 input ports and 3 output ports.

The proposed scheme takes advantage of using blocks of 2 × 3 CORPS networks and certain crossovers to interconnect two stages of 2 × 3 CORPS networks in a convenient way to provide the required progressive phase for beam-scanning. Though the crossovers in the design of antenna arrays could be undesirable, the crossovers can be useful to set new and different configurations by interconnecting different stages or blocks of 2 × 3 CORPS networks. The combination of these two properties helps to set a new configuration for reducing the number of phase shifters.

2.2. Design Configuration for Linear Antenna Arrays

The description of this proposed design scheme begins setting the array factor for the linear antenna array of 9 elements, as shown in Figure 3. The array factor is given as a function of θ using the next equation [24]:

$$AF(\theta) = \sum_{n=1}^{N} I_n e^{j(kd(n-1)sin(\theta)+\alpha_n)} \quad (1)$$

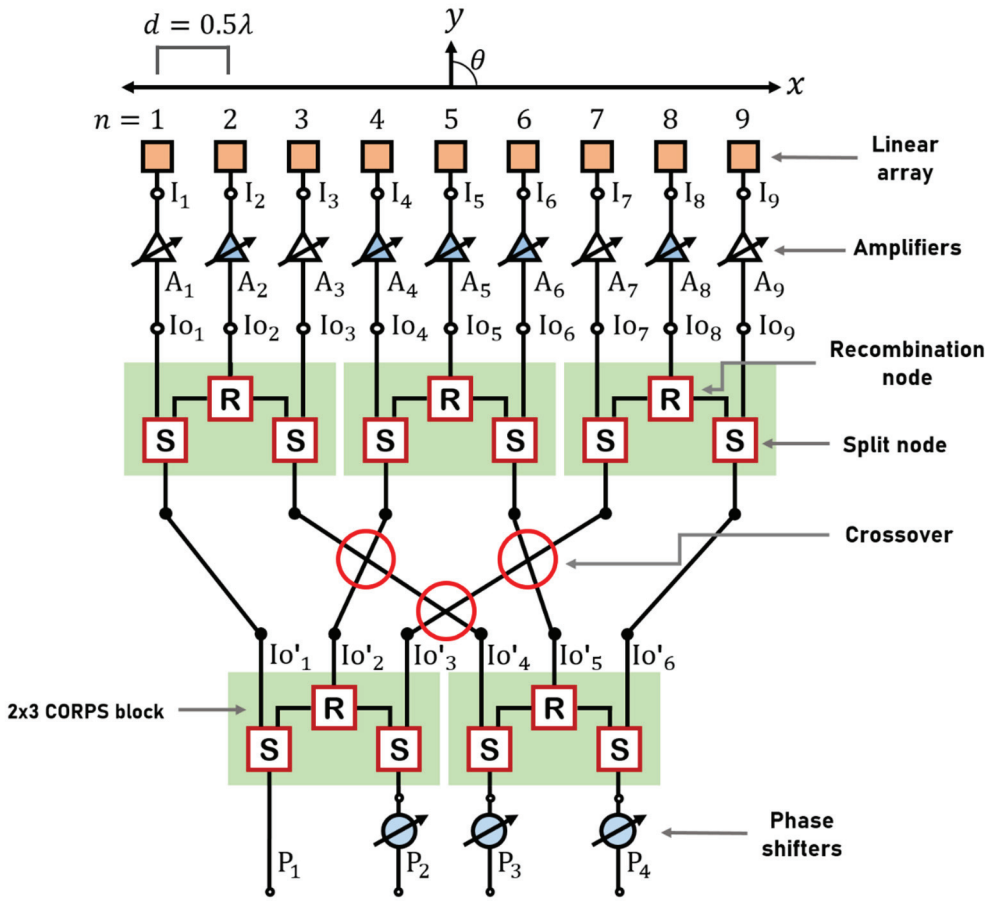

Figure 3. Proposed design scheme for a linear antenna array of 9 elements based on 2 × 3 CORPS networks and crossovers.

N is the number of antenna elements; each antenna element has an amplitude excitation using a fixed or variable amplifier and I_n is the nth amplitude excitation, d is given as the separation between antenna elements, k is the phase constant, and α_n is the progressive phase excitation for beam-steering at θ_0. The progressive phase excitation is calculated as:

$$\alpha_n = -kd(n-1)\sin(\theta_0)\ n = 1,\ 2,\ \ldots,\ N \quad (2)$$

Then, a progressive phase excitation is required at the antenna elements. Therefore, before the amplifiers stage, each group of three antenna elements is fed by a 2 × 3 CORPS network. As demonstrated in [21], one 2 × 3 CORPS network provides the average value of the phase values received at its two input ports. This network configuration applies an interleaving of two stages of 2 × 3 CORPS networks. The outputs of two 2 × 3 CORPS networks (first stage) are connected to the inputs of three 2 × 3 CORPS networks (second stage) to feed the 9 elements of the linear array (Figure 3). If we follow the phase values at each stage of the proposed network from input ports (P_1, P_2, P_3 and P_4), the required progressive phase for beam-scanning can be set at the antenna elements of the array system.

The phase values P_1, P_2, P_3, and P_4 are set at the input ports in a convenient way to consider the required phase values. These required phase values can be generated from Equation (2) for a desired value of θ_0. The input port 1 does not have a phase shifter. This is because the phase value $P_1 = 0$ for all scanning directions.

A raised cosine distribution is generated for the amplitude excitations at the antenna elements to obtain low SLL values. Variable amplifiers are considered at the outputs from a recombination node and fixed amplifiers from split nodes. The center of the linear array is the phase reference, and d_n can be set as the distance of the nth element to the antenna array center. The distribution of raised cosine for amplitude excitations can be calculated using the next equation [1]:

$$I_n = \frac{1 + \cos\left(\frac{d_n cos^{-1}(2a-1)}{0.5L}\right)}{2} \; n = 1,\ 2,\ \ldots,\ N \tag{3}$$

In the last expression, the value of a can be considered fixed and L as the array longitude. A value of $a = 0.35$ can be set to reach a desired SLL of -22 dB in a scanning range of $\pm 25^\circ$. The amplitude excitations values (I_n) must be determined considering the level of amplitude values at the output ports (IO_n) of the 4×9 CORPS network.

The required amplification values at the outputs of the feeding network ($A_1 \ldots A_9$) for different scanning directions are shown in Table 1. The required value at the output of a recombination node is higher for higher scanning values.

Table 1. Amplification values (at the outputs of the feeding system) that are required to obtain a raised cosine.

θ_0	A_1	A_2	A_3	A_4	A_5	A_6	A_7	A_8	A_9
-5°	0.71	0.85	1.59	1.83	1.42	1.34	1.59	0.85	0.71
0°	0.71	0.82	1.59	1.33	1.00	1.33	1.59	0.82	0.71
5°	0.71	0.85	1.59	1.83	1.42	1.34	1.59	0.85	0.71
10°	0.71	0.96	1.59	1.34	1.17	1.34	1.59	0.96	0.71
15°	0.71	1.20	1.59	1.75	1.91	1.75	1.59	1.20	0.71
20°	0.71	1.73	1.59	1.34	2.11	1.34	1.59	1.73	0.71
25°	0.71	3.42	1.59	2.01	6.23	2.01	1.59	3.42	0.71

The proposed scheme can be designed considering the higher value of antenna elements in the linear array by adding more input ports (and 2×3 CORPS networks). Table 2 shows a behavior of the numerical values (array factor performance) that could be reached as the number of antenna elements increases. Table 2 indicates that performance could be maintained in the reduction of phase shifters and SLL (below -20 dB).

Table 2. Numerical values as the number of antenna elements increases.

Number of Elements	Number of Phase Shifters	Number of Fixed Phase Shifters	Number of 2×3 CORPS	SLL [dB]	Maximum Beamwidth
9	3	4	5	-22.64	34.41°
18	7	8	10	-20.73	16.39°
27	11	12	15	-20.89	10.63°
36	15	16	20	-20.39	8.11°
45	19	20	25	-20.55	6.31°
54	23	24	30	-20.38	5.23°
63	27	28	35	-20.49	4.51°

2.3. Proposed Feeding System Based on 4 × 9 CORPS Network

As seen previously, the proposed scheme for linear phased arrays is based on a 4 × 9 CORPS network to provide the progressive phase for beam-scanning and to reduce the number of phase shifters. In comparison with a conventional CORPS [20], the proposed feeding system can achieve a good control of phase for beam-scanning and the number of recombination nodes (losses by energy dissipation) is lower, as observed in Figure 4. A total of 25 recombination nodes are used in a conventional CORPS network (a CORPS network of 4 inputs and 9 outputs with 5 layers), and 5 recombination nodes for the proposed feeding system. This means a reduction of 80% of recombination nodes. Fonseca et al. [25] advises a value of phase difference within the range 0° to 90° (between the two input ports of each 2 × 3 CORPS network) to avoid recombination losses. Therefore, we tried to avoid recombination losses by taking this consideration into account using fixed phase shifters of 90° and 180°, as indicated in Figure 4. Then, the use of these fixed phase shifters helps to set phase differences within the range 0° to 90° at the input ports of 2 × 3 CORPS networks of the first stage. The values of the fixed phase shifters compensate this phase difference, avoiding severe recombination losses. Furthermore, this is helpful to generate the amplitude excitation values of the raised cosine distribution. These amplitude excitation values are less attenuated by using the fixed phase shifters illustrated in Figure 4.

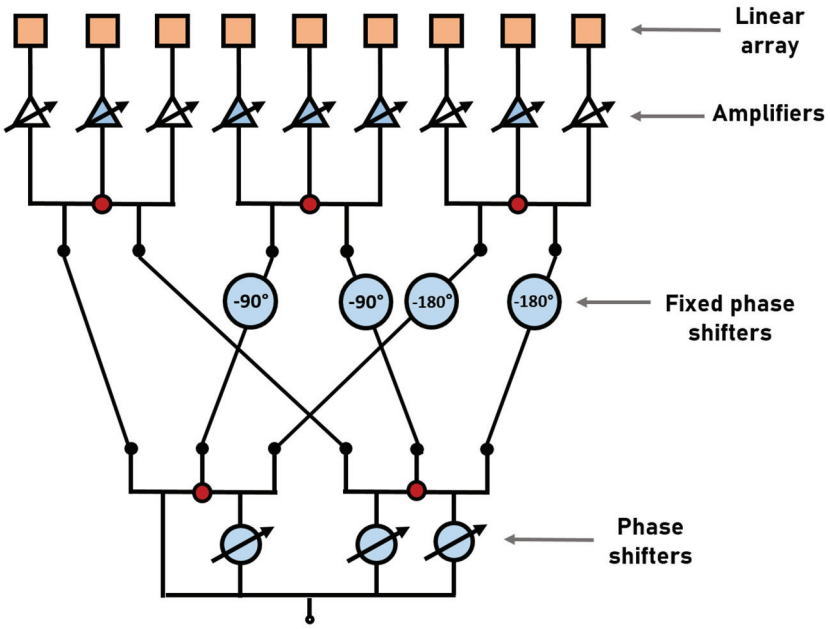

Figure 4. Scheme to illustrate the recombination nodes for the 4 × 9 CORPS network.

A mathematical description of the 4 × 9 CORPS network can be given by considering the next scattering matrix of each 2 × 3 CORPS network [20]:

$$[\mathbf{S}]^{NETWORK} = \begin{bmatrix} \frac{1}{\sqrt{2}} & 0 \\ \frac{1}{2} & \frac{1}{2} \\ 0 & \frac{1}{\sqrt{2}} \end{bmatrix} \tag{4}$$

Each 2 × 3 CORPS network has two inputs and three outputs. The complex inputs can be named as a_1 and a_2. The outputs (b_1 b_2 b_3) of each 2 × 3 CORPS network are generated by multiplying the complex inputs by the matrix of the Equation (4), and we have as a result $\frac{a_1}{\sqrt{2}}$, $a_1/2 + a_2/2$ and $\frac{a_2}{\sqrt{2}}$.

Therefore, we can follow each stage of the proposed feeding network to see the values of amplitude and phase generated by the complex inputs; Figure 3 illustrates this. The complex inputs are named P_1, P_2, P_3, and P_4. If we analyze the first stage, the first

2×3 CORPS network has the inputs P_1 and P_2, and the second 2×3 network has the inputs P_3 and P_4. Therefore, it is easy to determine that the outputs of the first stage are:

$$IO_{1'} = \frac{P_1}{\sqrt{2}} \tag{5}$$

$$IO_{2'} = P_1/2 + P_2/2 \tag{6}$$

$$IO_{3'} = \frac{P_2}{\sqrt{2}} \tag{7}$$

$$IO_{4'} = \frac{P_3}{\sqrt{2}} \tag{8}$$

$$IO_{5'} = P_3/2 + P_4/2 \tag{9}$$

$$IO_{6'} = \frac{P_4}{\sqrt{2}} \tag{10}$$

By following the structure of the proposed feeding network (Figure 3), the outputs of the first stage ($IO_{1'}$, $IO_{2'}$, $IO_{3'}$, $IO_{4'}$, $IO_{5'}$, and $IO_{6'}$) are the inputs of the second stage, i.e., the left 2×3 network has the inputs $IO_{1'}$ and $IO_{4'}$, the central 2×3 network has the inputs $IO_{2'}$ and $IO_{5'}$, and the right 2×3 CORPS network has $IO_{3'}$ and $IO_{6'}$ as inputs. Then, the outputs of the second layer are:

$$IO_1 = \frac{IO_{1'}}{\sqrt{2}} \tag{11}$$

$$IO_2 = IO_{1'}/2 + IO_{4'}/2 \tag{12}$$

$$IO_3 = \frac{IO_{4'}}{\sqrt{2}} \tag{13}$$

$$IO_4 = \frac{IO_{2'}}{\sqrt{2}} \tag{14}$$

$$IO_5 = IO_{2'}/2 + IO_{5'}/2 \tag{15}$$

$$IO_6 = \frac{IO_{5'}}{\sqrt{2}} \tag{16}$$

$$IO_7 = \frac{IO_{3'}}{\sqrt{2}} \tag{17}$$

$$IO_8 = IO_{3'}/2 + IO_{6'}/2 \tag{18}$$

$$IO_9 = \frac{IO_{6'}}{\sqrt{2}} \tag{19}$$

Then, the proposed feeding scheme can be designed for studying its behavior and performance. Figure 5 shows the design in CST Microwave Studio of the proposed feeding system. The feeding system in Figure 5 considers a frequency at 6 GHz using Gysel power dividers [26] and resistances of surface mount (50 Ohms-FC0603). The Gysel power dividers operate as split or recombination nodes. Furthermore, a substrate of 290×156 mm is considered with the next characteristics: FR4, thick = 1.6 mm, relative permittivity εr = 4.2, tangent loss = 0.025, and μ = 1.0. The values of length and width of the transmission line sections are illustrated in Figure 5a). Figure 5b) indicates where the components are located and the values of the characteristic impedances of all transmission line sections. The process of simulation (full-wave CST) takes the resistances and the SMA connectors into account.

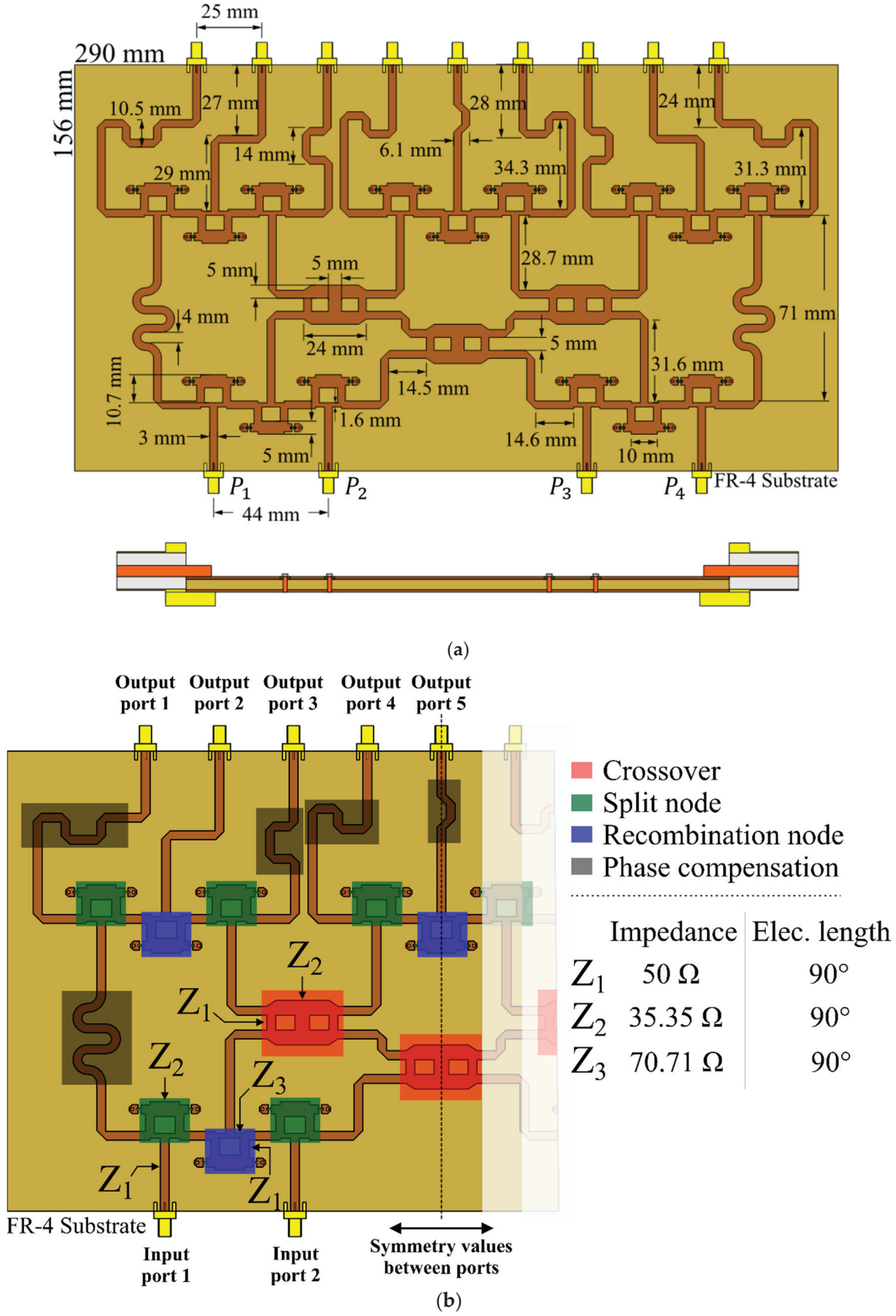

Figure 5. Design of the proposed feeding system based on 4 × 9 CORPS network: (**a**) Design in CST Microwave Studio, (**b**) components and values of the characteristic impedances of all transmission line sections.

The system of 9 antenna elements of the linear array are controlled with 3 input ports (or phase shifters), as illustrated in Figure 5. The nine phase values (generated by a conventional system of progressive phase excitation) are generated using only three control ports (3 phase shifters). The phase values at the input ports (P_1, P_2, P_3 and P_4) are set in according to the phase values required at the antenna elements: 1, 3, 7, and 9 (Equation (2)). Then, the blocks of 2 × 3 CORPS networks and the crossovers provide the phase values required at the antenna elements 2, 4, 5, 6, and 8. That is the key stone of the proposed feeding system. The crossovers are designed in a conventional way by considering line couplers as detailed in [27–29].

3. Results and Discussion

The antenna system of the linear phased array was evaluated considering the experimental measurements of the proposed feeding system based on 4 × 9 CORPS network. The details of the prototype and experimental measurements are given in the next sections.

3.1. Measurements of the Proposed Feeding System (4 × 9 CORPS Network)

The proposed feeding system of the 4 × 9 CORPS feeding network was fabricated and measured to evaluate its performance and its impact in feeding linear phased arrays. Figure 6 illustrates the fabricated prototype using the design values given in the previous section. Figure 7 illustrates the reflection coefficients simulated by CST and measured experimentally for the proposed feeding system of the 4 × 9 CORPS network. The measurement results gives a bandwidth of 2.6 GHz for the proposed feeding system, as shown in Figure 7. The measurement results show that the maximum value of the reflection coefficients is approximately −17 dB at 6 GHz (set as the design frequency). Figure 7 indicates that the behavior of the results of the reflection coefficients obtained by simulation and experimental measurements are very similar.

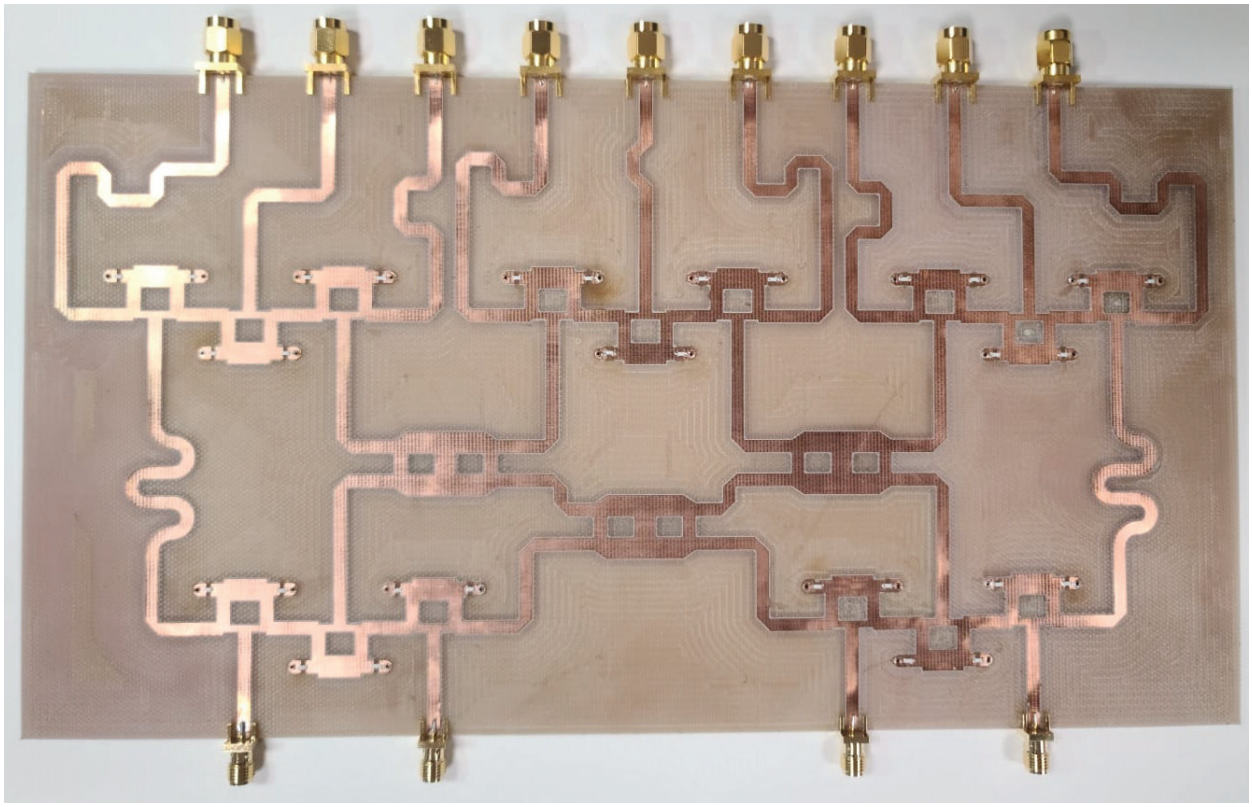

Figure 6. Fabricated prototype of the proposed feeding system.

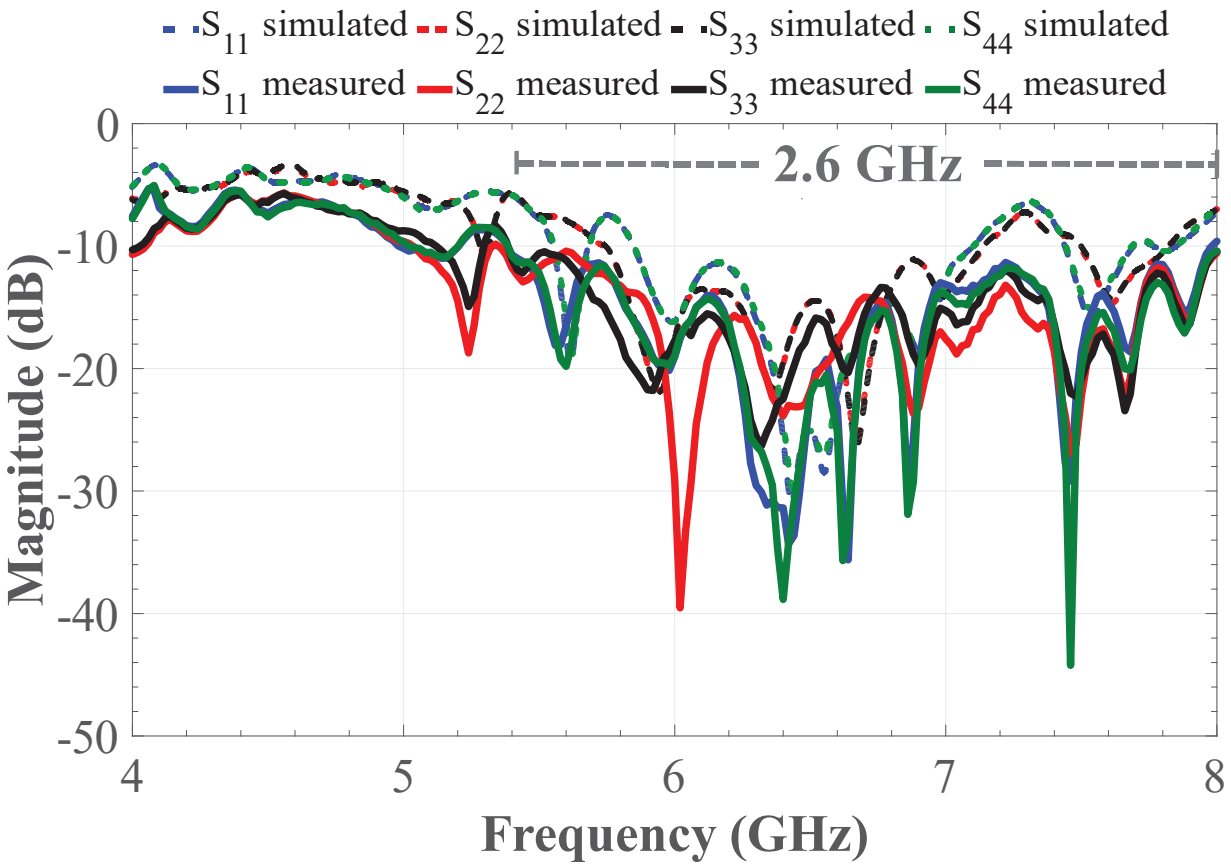

Figure 7. Reflection coefficients simulated and measured for the proposed feeding system.

Figure 8 illustrates the transmission coefficients simulated by CST and measured experimentally for the proposed feeding system. Power losses are generated by Gysel power dividers, SMA connectors, crossovers, and energy dissipation. However, the measurement results shows a good transmission considering the output ports of interest for each input port. The numbers 5, 6, 7, 8, 9, 10, 11, 12, and 13 indicate the output ports 1, 2, 3, 4, 5, 6, 7, 8, and 9 of the feeding system (4 × 9 CORPS network). As commented previously, a variable amplifier is considered at each output from a recombination node of the proposed feeding network [21]. The electromagnetic simulation results and the measurement results are very similar.

3.2. Experimental Evaluation of the Linear Phased Array

The measured CORPS feeding network (4 × 9) was used to feed the linear phased array considering the performance in the reduction of phase shifters and scanning capabilities. A separation of $d = 0.5\lambda$ is considered as uniform in the array system. The linear phased array was designed, simulated electromagnetically, and fabricated to analyze its performance considering the error of amplitude and phase of the proposed feeding system (4 × 9 CORPS network). A circular patch is considered at a central frequency of 6 GHz with the next design characteristics: r = 13.02 mm, h = 1.6 mm (FR4 substrate) and =2.07 [24]. The radiation efficiency is approximately 90% considering the FR4 substrate for the design frequency.

The fabricated prototype of the complete system for the linear phased array is illustrated in Figure 9. The complete array system includes the antenna elements (set as shown in Figure 9a), the stage of attenuators, the proposed feeding network (4 × 9), and the power division network. Every stage was fabricated on FR4. The reflection coefficient for the entire system was measured in a vector network analyzer, and its behavior is shown in Figure 10. As illustrated in this figure, each stage was designed and fabricated to match the design requisites. The system accomplishes the impedance requirements to operate

in a bandwidth of 975 MHz (considering 6 GHz as the design frequency). The stage of attenuators was designed and fabricated using the technique of unequal Wilkinson power division [30]. In this case, resistors of surface mount (50 and 100 Ohms) are considered as shown in Figure 11. Transmission lines (of different length) are employed as the phase shifts. The proposed feeding network is fed by the power divider. Then, the outputs of the proposed feeding network are connected to the stage of attenuators and antenna elements.

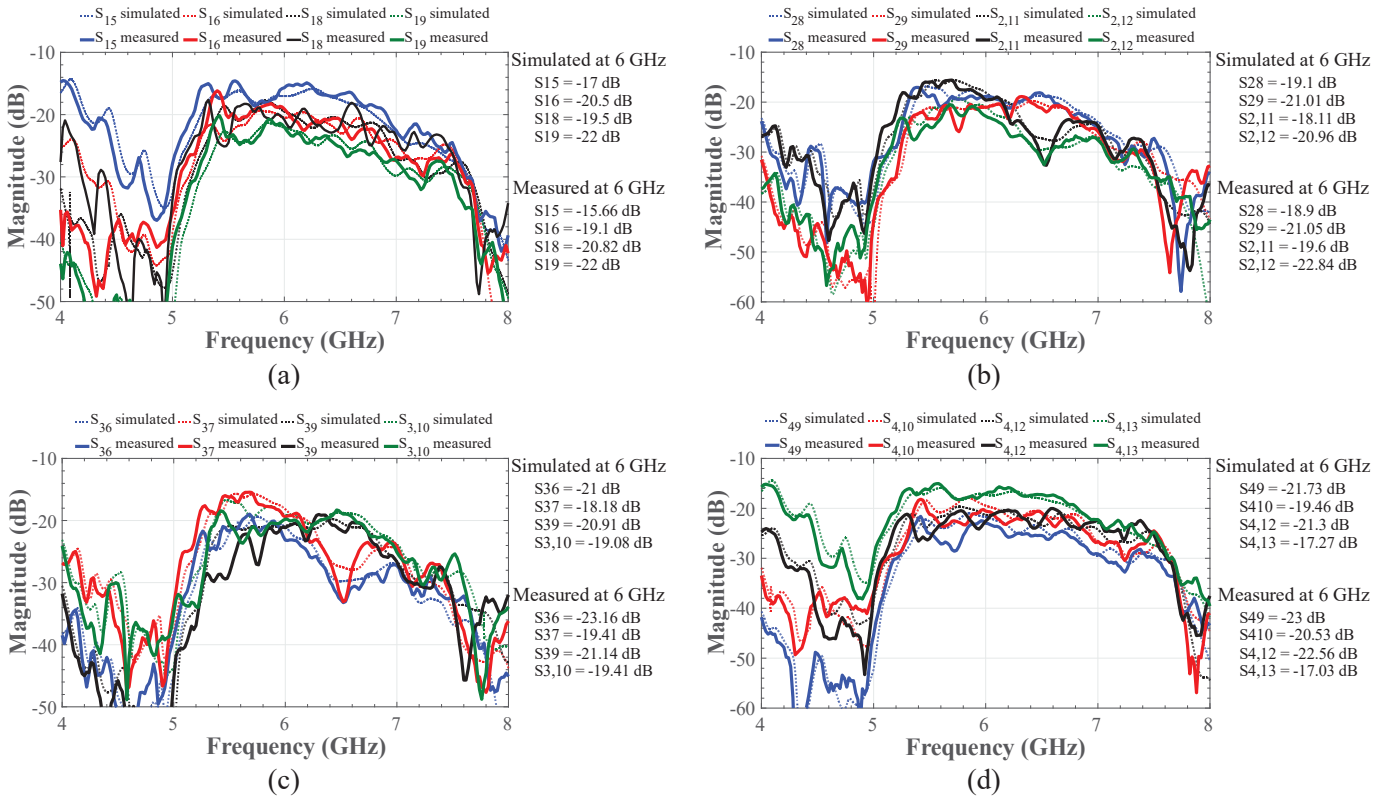

Figure 8. Transmission coefficients simulated and measured experimentally for the proposed feeding system (of 4 × 9 CORPS network) for each input port: (**a**) P1, (**b**) P2, (**c**) P3 and (**d**) P4.

The proposed feeding system using the linear phased array generates a reduction of phase shifters, providing a maximum SLL of approximately −22 dB for the range of $\theta_0 = \pm 25^\circ$. The SLL performance (−22 dB) is maintained during beam-scanning in $\theta_0 = \pm\ 25^\circ$.

The radiation pattern for the prototype of the full system was measured experimentally in an anechoic chamber (far field), as shown in Figure 12. Furthermore, the complete system based on the linear array was simulated using full wave software (CST) to study the behavior of the radiation pattern generated. Figure 13 shows the radiation pattern generated by electromagnetic simulations in CST for (a) $\theta_0 = -25^\circ$, (b) $\theta_0 = 0^\circ$, (c) $\theta_0 = 15^\circ$, and (d) $\theta_0 = 25^\circ$ and (e) measured experimentally for the complete system of the linear phased array. Figure 13e illustrates the behavior of the radiation pattern (normalized) for the frequency values of 5.6 GHz, 5.8 GHz, 6 GHz, 6.2 GHz, and 6.4 GHz. This figure shows the radiation pattern for the farthest scanning direction ($\theta_0 = -25^\circ$). There are some very slight changes in the radiation pattern for these frequency values. However, the radiation performance remains for these frequency changes. The use of the raised cosine distribution in the proposed design methodology generates low values of SLL (aprox. −19 dB) in the scanning range, as shown in the obtained results.

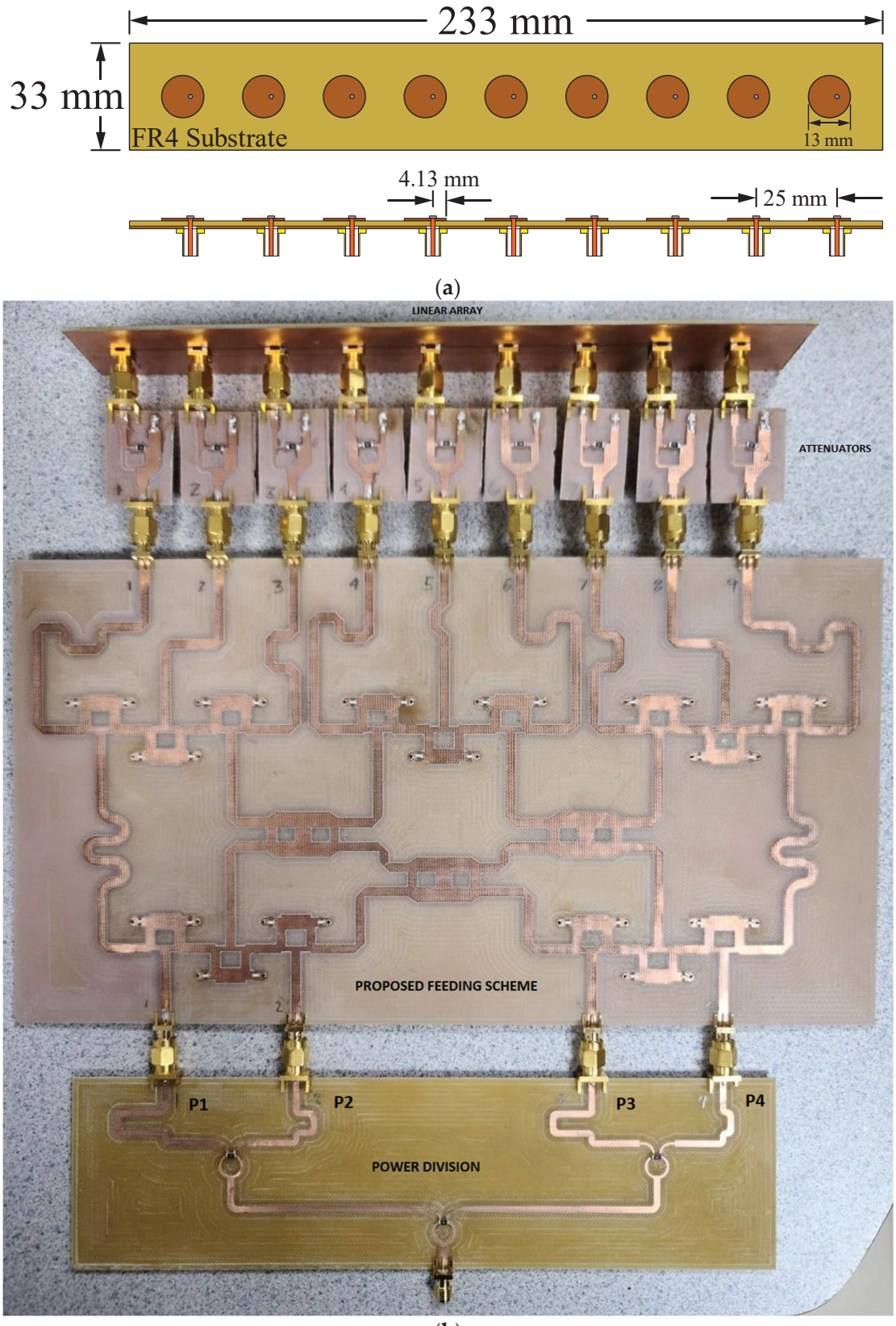

Figure 9. Linear phased array, (**a**) antenna elements configuration, and (**b**) the fabricated prototype of the complete system with power values of approximately 15 dBm, and phase shift values of (0°, 152.14°, 96.42°, 248.57°) for P_1, P_2, P_3 and P_4.

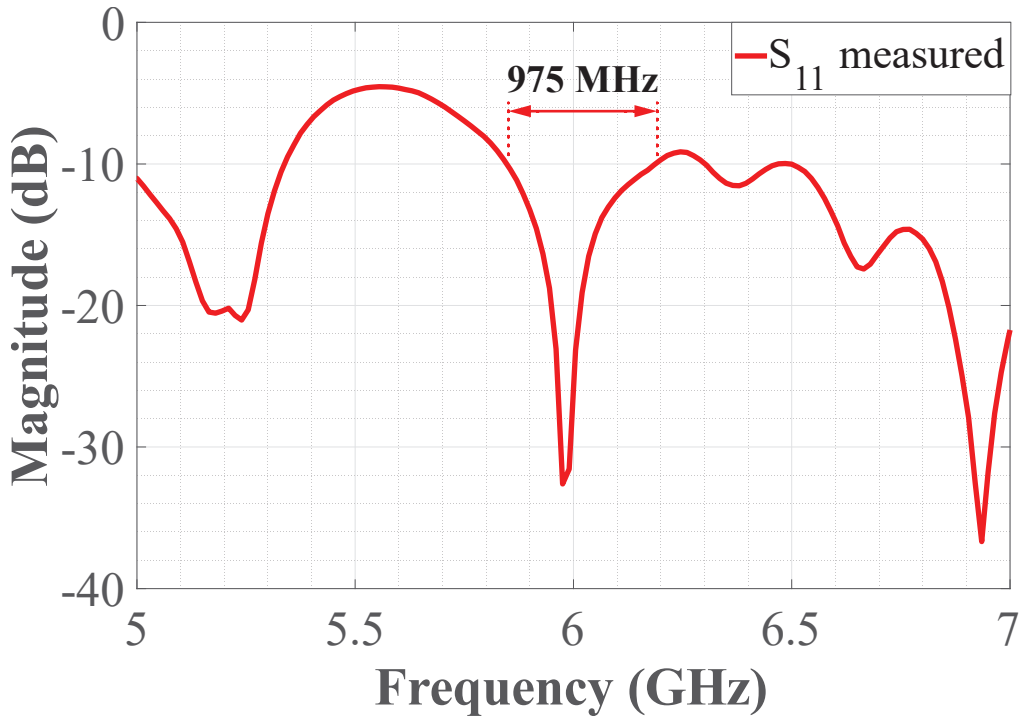

Figure 10. Reflection coefficient for the complete system measured by a vector network analyzer.

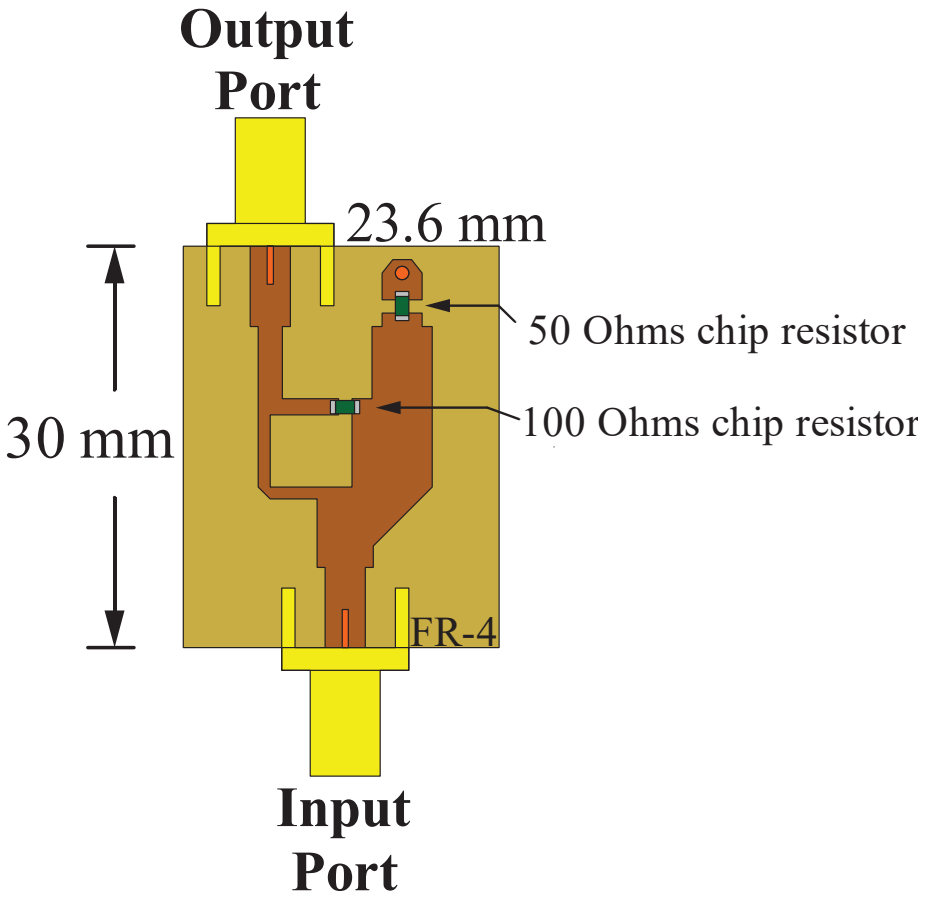

Figure 11. Example of the schematic diagram for the attenuators.

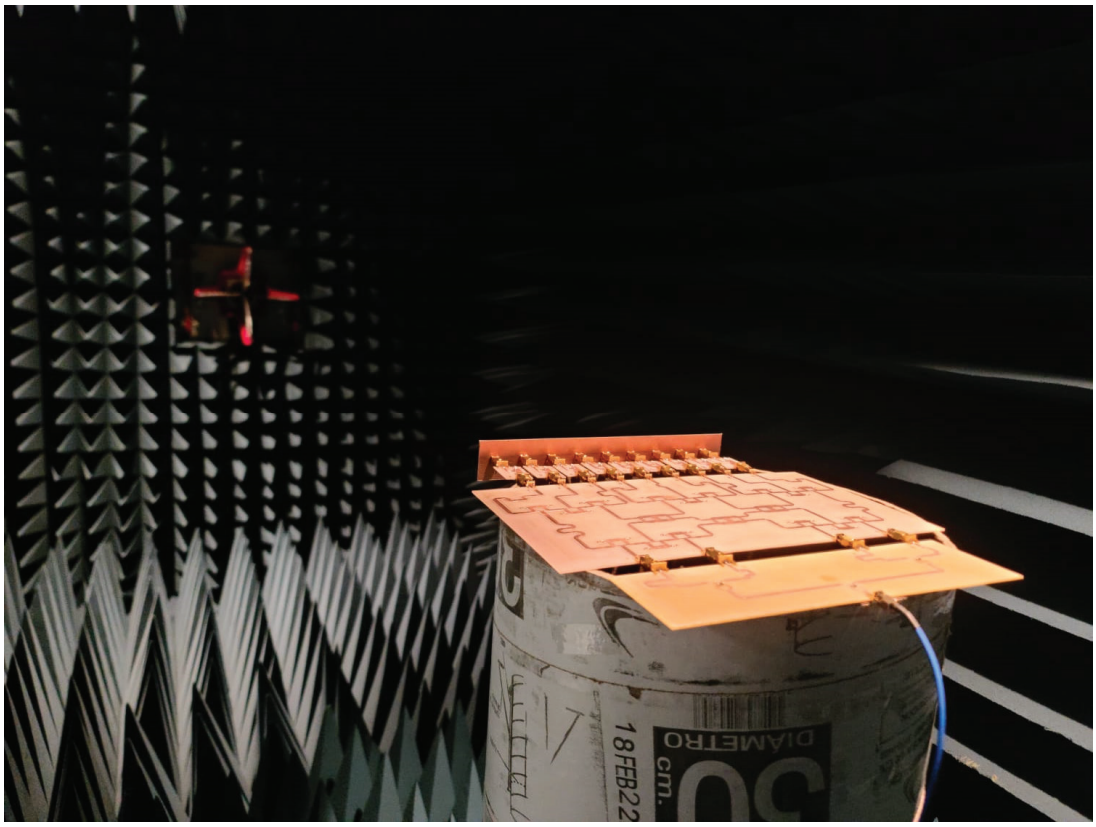

Figure 12. Prototype of the full system measured experimentally in a far field anechoic chamber.

Table 3 illustrates a comparative analysis of the proposed feeding system with respect to other design cases based on linear array geometries. The proposed design methodology reduces the number of phase shifters by 66%. The proposed technique outperforms to other techniques in the reduction of the number of phase shifters to be used in the antenna system. This reduction capability in the number of phase shifters is reached while maintaining a low SLL in the scanning range of $\pm 25^{\circ}$.

The values presented in Table 3 are based on the designs presented in each reference cited. Each paper or work provides the information of reduction of phase shifters, and we compared this information with that of our design case. This Table indicates the number of antenna elements used in the systems of each previous work. However, the reduction of phase shifters of each case in the table could be applicable if the number of elements is increased.

The technique presented in this paper can be considered a good design option to reduce the complexity of the feeding network in antenna array applications.

Table 3. A comparative analysis of the proposed feeding system with respect to other design cases based on linear array geometries.

	Number of Elements	Number of Phase Shifters	Reduction of Phase Shifters	Scanning Range	Peak Side Lobe Level	Number of Variable Amplifiers
This work	9	3	66%	$\pm 25^{\circ}$	-22 dB (sim.) -19 dB (mea.)	5
[21]	7	3	57%	$\pm 25^{\circ}$	-20 dB	3
[20]	10	8	20%	$\pm 30^{\circ}$	-19 dB	8
[1]	30	12	60%	$\pm 12^{\circ}$	-15 dB	12
[2]	28	14	50%	$\pm 24^{\circ}$	-15 dB	14

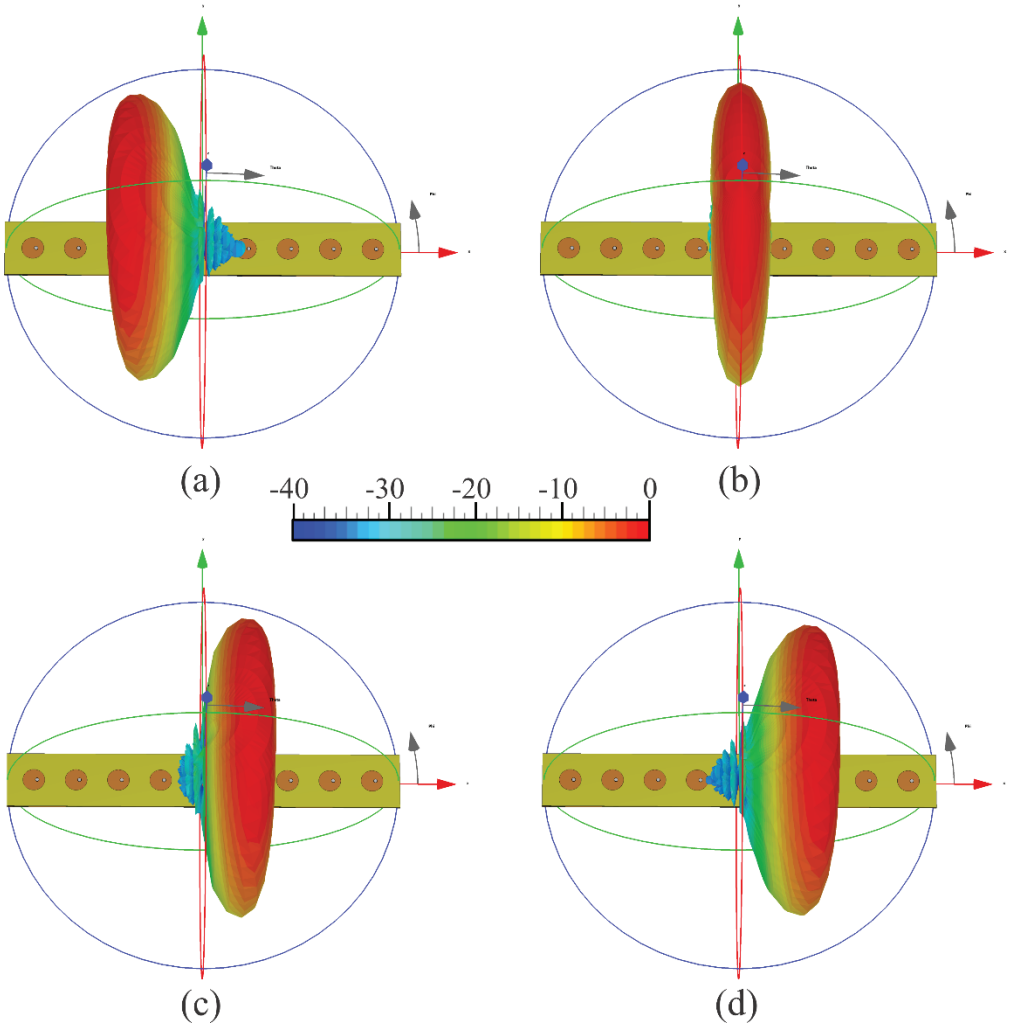

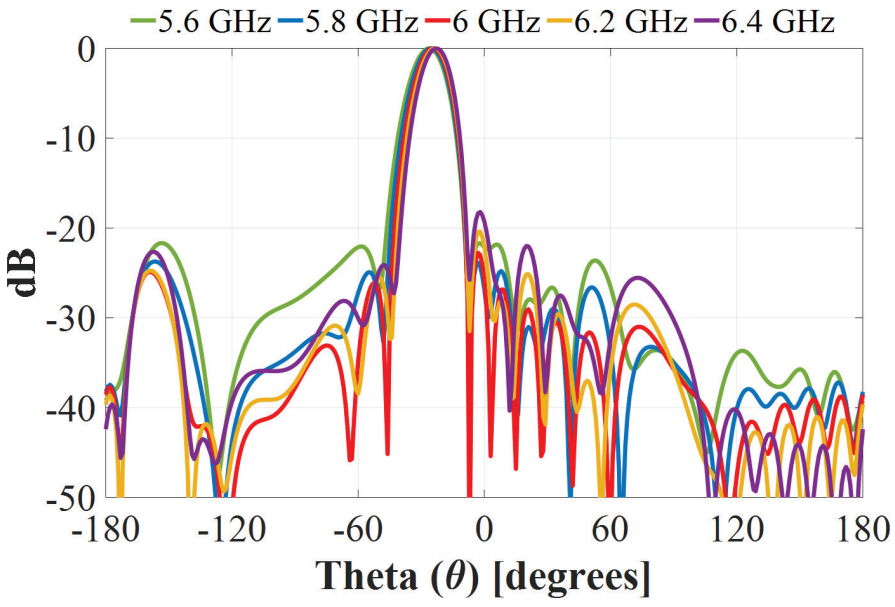

(e)

Figure 13. Radiation pattern obtained by CST simulations for (**a**) $\theta_0 = -25°$, (**b**) $\theta_0 = 0°$, (**c**) $\theta_0 = 15°$, and (**d**) $\theta_0 = 25°$ and (**e**) measured experimentally for the complete system.

4. Conclusions

This paper presented a design scheme to feed linear antenna arrays and achieve reduction capability in the number of phase shifters of the system. A feeding network (4 inputs and 9 outputs) based on CORPS technology and crossovers was proposed. This proposed feeding network was designed, simulated, and implemented. The proposed feeding system uses only 5 recombination nodes, i.e., a reduction of 80% of recombination nodes with respect to a conventional CORPS network. Experimental measurements showed that the proposed feeding network can operate in a wide bandwidth and provide the progressive phase for beam-scanning while obtaining a reduction in the number of phase shifters employed.

The proposed feeding system was analyzed and evaluated to feed linear phased arrays with respect to other techniques. The obtained benefits were a reduction capability of 66% in the number of phase shifters and a good SLL performance for beam-scanning using a raised cosine distribution. The electromagnetic simulation results for the full system generate a radiation pattern with a scanning range of $\pm 25^{\circ}$ maintaining a maximum SLL of -22 dB during beam-scanning. Furthermore, the linear phased array was validated by taking measurements obtaining a slight deviation in the SLL (approximately -19 dB) for different frequency values.

Author Contributions: Conceptualization, M.A.P. and G.C.; methodology, G.C. and B.S.; software, G.C. and B.S.; validation, A.R. and M.A.P.; formal analysis, G.C. and M.A.P.; investigation, A.R. and G.C.; resources, M.A.P. and A.R.; data curation, G.C. and B.S.; writing—original draft preparation, M.A.P. and G.C.; writing—review and editing, M.A.P. and G.C.; visualization, B.S. and G.C.; supervision, M.A.P.; project administration, M.A.P. and A.R.; funding acquisition, M.A.P. and A.R. All authors have read and agreed to the published version of the manuscript.

Funding: This research was funded by CONACYT grant number CF-2023-G-58 and The APC was funded by CICESE.

Institutional Review Board Statement: Not applicable.

Informed Consent Statement: Not applicable.

Data Availability Statement: Not applicable.

Conflicts of Interest: The authors declare no conflict of interest.

References

1. Avser, B.; Pierro, J.; Rebeiz, G.M. Random feeding networks for reducing the number of phase shifters in limited-scan arrays. *IEEE Trans. Antennas Propag.* **2016**, *64*, 4648–4658. [CrossRef]
2. Avser, B.; Frazita, R.F.; Rebeiz, G.M. Interwoven feeding networks with aperture sinc-distribution for limited-scan phased arrays and reduced number pf phase shifters. *IEEE Trans. Antennas Propag.* **2018**, *66*, 2401–2413. [CrossRef]
3. Butler, J.; Lowe, R. Beam-forming matrix simplifies design of electronically scanned antennas. *Electron. Des.* **1961**, *9*, 170–173.
4. Blass, J. Multidirectional antenna–a new approach of stacked beams. *Proc. IRE Int. Conv. Rec.* **1960**, *8*, 48–50.
5. Nolen, J. Synthesis of Multiple Beam Networks for Arbitrary Illuminations. Ph.D. Dissertation, Radio Division, Bendix Corp., Baltimore, MD, USA, 1965.
6. Rupakula, B.; Aljuhani, A.H.; Rebeiz, G.M. Limited Scan-Angle Phased Arrays Using Randomly Grouped Subarrays and Reduced Number of Phase Shifters. *IEEE Trans. Antennas Propag.* **2019**, *68*, 70–80. [CrossRef]
7. Toyama, N. Aperiodic array consisting of subarrays for use in small mobile Earth stations. *IEEE Trans. Antennas Propag.* **2005**, *53*, 2004–2010. [CrossRef]
8. Wang, D.; Hu, H.; Yang, Z. The pareto rank algorithm for the division of the subarrays for the phase array radar. In Proceedings of the CISP-BMEI, Datong, China, 15–17 October 2016; pp. 945–949.
9. Wang, H.; Fang, D.-G.; Chow, Y.L. Grating Lobe Reduction in a Phased Array of Limited Scanning. *IEEE Trans. Antennas Propag.* **2008**, *56*, 1581–1586. [CrossRef]
10. Krivosheev, Y.V.; Shishlov, A.V.; Denisenko, V.V. Grating lobe suppression in aperiodic phased array antennas composed of periodic subarrays with large element spacing. *IEEE Antennas Propag. Mag.* **2015**, *57*, 76–85. [CrossRef]
11. Haupt, R.L. Optimized weighting of uniform subarrays of unequal sizes. *IEEE Trans. Antennas Propag.* **2007**, *55*, 1207–1210. [CrossRef]

12. Mailloux, R.J.; Santarelli, S.G.; Roberts, T.M.; Luu, D. Irregular polyomino-shaped subarrays for space-based active arrays. *Int. J. Antennas Propag.* **2009**, *2009*, 956524. [CrossRef]
13. Rocca, P.; Haupt, R.L.; Massa, A. Sidelobe Reduction through Element Phase Control in Uniform Subarrayed Array Antennas. *IEEE Antennas Wirel. Propag. Lett.* **2009**, *8*, 437–440. [CrossRef]
14. Herd, J.S.; Duffy, S.M.; Steyskal, H. Design considerations and results for an overlapped subarray radar antenna. In Proceedings of the 2005 IEEE Aerospace Conference, Big Sky, MT, USA, 5–12 March 2005; pp. 1087–1092.
15. Duffy, S.M.; Santiago, D.D.; Herd, J.S. Design of overlapped subarrays using an RFIC beamformer. In Proceedings of the 2007 IEEE Antennas and Propagation Society International Symposium, Honolulu, HI, USA, 9–15 June 2007; pp. 1949–1952.
16. Azar, T. Overlapped subarrays: Review and update. *IEEE Antennas Propag. Mag.* **2013**, *55*, 228–234. [CrossRef]
17. Mailloux, R.J. An overlapped subarray for limited scan application. *IEEE Trans. Antennas Propag.* **1974**, *22*, 487–489. [CrossRef]
18. Mailloux, R.J. A low-sidelobe partially overlapped constrained feed network for time-delayed subarrays. *IEEE Trans. Antennas Propag.* **2001**, *49*, 280–291. [CrossRef]
19. Abbaspour-Tamijani, A.; Sarabandi, K. An affordable millimeter-wave beam-steerable antenna using interleaved planar subarrays. *IEEE Trans. Antennas Propag.* **2003**, *51*, 2193–2202. [CrossRef]
20. Panduro, M.A.; del Rio-Bocio, C. Design of beamforming networks using CORPS and evolutionary optimization. *AEU Int. J. Electron. Commun.* **2009**, *63*, 353–365. [CrossRef]
21. Juarez, E.; Panduro, M.A.; Covarrubias, D.H.; Reyna, A.; Sanchez, B.J. An innovative way of using CORPS for phased arrays with reduced number of phase shifters. *IEEE Trans. Antennas Propag.* **2022**, *70*, 307–316. [CrossRef]
22. Juarez, E.; Panduro, M.A.; Covarrubias, D.H.; Reyna, A. Coherently radiating periodic structures to reduce the number of phase shifters in a 2-D phased array. *Sensors* **2021**, *21*, 6592. [CrossRef]
23. Betancourt, D.; del Río Bocio, C. A novel methodology to feed phased array antennas. *IEEE Trans. Antennas Propag.* **2007**, *55*, 2489–2494. [CrossRef]
24. Balanis, C.A. *Antenna Theory: Analysis and Design*, 2nd ed.; Wiley: New York, NY, USA, 1997.
25. Ferrando, N.; Fonseca, N.J.G. Investigations on the efficiency of array fed coherently radiating periodic structure beam forming networks. *IEEE Trans. Antennas Propag.* **2011**, *59*, 493–502. [CrossRef]
26. Ooi, B.L.; Palei, W.; Leong, M.S. Broad-banding technique for in-phase hybrid ring equal power divider. *IEEE Trans. Microw. Theory Tech.* **2002**, *50*, 1790–1794.
27. Tang, C.; Lin, K.; Chen, W. Analysis and Design of Compact and Wide-Passband Planar Crossovers. *IEEE Trans. Microw. Theory Tech.* **2014**, *62*, 2975–2982. [CrossRef]
28. Maktoomi, M.A.; Maktoomi, M.H.; Zafar, Z.N.; Helaoui, M.; Ghannouchi, F.M. Simplified Analysis of Symmetrical RF Crossovers Extended with Arbitrary Complex Passive Two-Port Networks. *Prog. Electromagn. Res. Lett.* **2019**, *85*, 1–8. [CrossRef]
29. Tirado, J.V.; Bernaola, E.; de Paco, P. A Compact Microstrip Crossover Based on Capacitively-Loaded Artificial Transmission Lines Branch-Line Sections. *Prog. Electromagn. Res. Lett.* **2017**, *68*, 121–126. [CrossRef]
30. Parad, L.I.; Moynihan, R.L. Split-tee power divider. *IEEE Trans. Microw. Theory Tech.* **1965**, *13*, 91–95. [CrossRef]

sensors

MDPI

Review

Radar-Based Heart Cardiac Activity Measurements: A Review

Alvaro Frazao [1,*], Pedro Pinho [1] and Daniel Albuquerque [2]

[1] Department of Electronics Telecommunications and Informatics (DETI), Instituto de Telecomunicações, Universidade de Aveiro, 3810-193 Aveiro, Portugal; ptpinho@ua.pt
[2] Águeda School of Technology and Management (ESTGA), Instituto de Telecomunicações, Universidade de Aveiro, 3750-127 Águeda, Portugal; dfa@ua.pt
* Correspondence: alvarofrazao@ua.pt

Abstract: In recent years, with the increased interest in smart home technology and the increased need to remotely monitor patients due to the pandemic, demand for contactless systems for vital sign measurements has also been on the rise. One of these kinds of systems are Doppler radar systems. Their design is composed of several choices that could possibly have a significant impact on their overall performance, more specifically those focused on the measurement of cardiac activity. This review, conducted using works obtained from relevant scientific databases, aims to understand the impact of these design choices on the performance of systems measuring either heart rate (HR) or heart rate variability (HRV). To that end, an analysis of the performance based on hardware architecture, carrier frequency, and measurement distance was conducted for works focusing on both of the aforementioned cardiac parameters, and signal processing trends were discussed. What was found was that the system architecture and signal processing algorithms had the most impact on the performance, with FMCW being the best performing architecture, whereas factors like carrier frequency did not have an impact.This means that newer systems can focus on cheaper, lower-frequency systems without any performance degradation, which will make research easier.

Keywords: Doppler radar; HRV; remote vital signs; CW; FMCW; UWB

1. Introduction

Over the last few years, the need to remotely monitor the vital signs of people has been on the rise. Whether this is due to the possible appearance of another highly contagious disease, or the increasing interest in smart home technology to assist in providing healthcare for the elderly, this technology presents plenty of relevant use cases that justify giving attention to the topic. These systems are usually designed to measure certain physiological parameters, for example, respiratory and cardiac rates in a person or the variability of their heart rate. Traditionally, these measurements are performed either by direct observation of a patient, as is the case of respiratory rate measurements, or by direct contact through sensors placed on the patient's body for cardiac measurements. Despite providing the best results, these methods are sometimes not suitable due to requiring direct contact and or proximity to the patient, being impractical, being unusable (e.g., they cannot be used for infants and people with skin conditions or burns), and just being generally uncomfortable for the patient; this can also negatively affect the results. Remote measurement systems tackle these issues, since they are able to obtain results without causing any hindrance to the patients in question. Over the years, several different kinds of remote sensing systems have been developed, such as ones based on thermal or optical cameras that extract data from the changes in skin temperature or color [1,2], Doppler radar systems [3], ultrasonic systems [4], and systems that leverage the channel state information in Wi-Fi networks to extract physiological signals [5]. However, camera- and Wi-Fi-based systems present problems relative to privacy and light/temperature interference which make radar systems the better candidate for remote vital sign sensing. Radar still presents its own set of

challenges, but these can be more easily dealt with by employing the appropriate hardware and software implementations of the system, usually defined on a case-by-case basis. Due to this myriad of not only use cases but also system implementations, research on this topic is very widespread and, as such, several reviews have already been carried out on this topic; they are detailed below.

Obadi et al. [6] compared the implementations of these types of radar systems both from a hardware and signal processing perspective, concluding with an analysis of the existing implementations, which was performed using Field Programmable Gate Arrays (FPGAs); this required the consideration of points that are usually disregarded in the literature, such as power consumption and the computational complexity of the used algorithms. Zhang et al. [7] carried out a review on the state of the art of implementations based on the target objective of the given system, such as vital sign monitoring, activity detection, or noise mitigation. An analysis of the trends in radar hardware architecture and signal processing chains was also performed, the latter differentiating between each class of algorithms (spectrum and periodicity, among others), in order to assist in understanding which situations each architecture and algorithm are best suited to. A review of existing public datasets was performed, and lastly, a discussion about the current challenges that radar-based cardiac monitoring faces, as well possible future work to solve them, was carried out. Wu et al. [8] listed the main challenges that affect the several parts of the signal processing chain, such as data collection, feature extraction, and parameter estimates; they discussed possible solutions for these issues and concluded with a review of the deep learning approaches used in vital sign monitoring. Liebetruth et al. [9] reviewed the current state of the art, analyzing testing conditions, the reference measurement methods used, and the error metrics used in the literature, for the three main hardware architectures (continuous wave (CW), frequency-modulated continuous wave (FMCW)/linear frequency-modulated continuous wave (LFMCW), and ultra wideband (UWB)). In summary, most recent reviews focus on analyzing and comparing the several types of system implementations, from the architecture to the signal processing chain, but they mostly focus on their use in monitoring respiratory and cardiac rates. To the best of the authors' knowledge, no review has been conducted that analyzes implementations directed specifically towards the measurement of heart rate variability (HRV), nor has one been carried out that assesses the impact that the several parts of the system have on its performance. As such, in terms of the contribution made by this work, this review aims to fill that gap by providing an analysis of the current trends in HRV and HR monitoring and comparing them in order to understand what design choices have the biggest impact on the performance of the system and whether or not HRV monitoring requires a different approach in order to obtain quality measurements.

The rest of the work is organized as follows: Section 2 provides a short overview of the different radar hardware architectures that are more commonly used, as well as a brief definition of HRV; Section 3 contains the listing of the reviewed literature, alongside an explanation for their inclusion; in Section 4, the results of the review are discussed; in Section 5, conclusions are taken from the discussion, and future work is proposed for the challenges presented.

2. Background Overview

Radar refers to systems that, through sending and receiving electromagnetic waves into the environment, are able to detect and sense the range of objects therein. Although these systems were initially used to help prevent ship collisions and for aircraft detection, in more recent years, the use of radars has expanded to applications such as weather analysis and measuring vital signs. The measurement of vital signs using radar technology leverages the displacement of the chest wall to perform its measurements which, according to the Doppler effect, causes a shift in the frequency of the reflected radar signal that can also be interpreted as a phase shift [10]. It is by analyzing the phase shift in the signal that parameters like the respiratory and cardiac rate are extracted.

In the remainder of this section, an overview of the different types of radar architectures will be presented, followed by a general overview of the physiological components relevant to these measurements.

2.1. Radar Architectures

Although similar in principle, as illustrated in Figure 1, the several architectures are distinguished by the way with which they emit and receive the signals that are sent out into the environment. Based on what is said in [10], CW radars transmit a signal with a constant frequency, FMCW radars transmit a signal where the frequency is modulated over time according to a specific modulation type (linear, stepped), and UWB radars function by emitting pulses with a short duration and a wide-frequency bandwidth. The information regarding the vital signs of the subjects is extracted either from the phase of the reflected signal in the case of CW and FMCW systems, or from the propagation delay of the signal in the case of UWB systems.

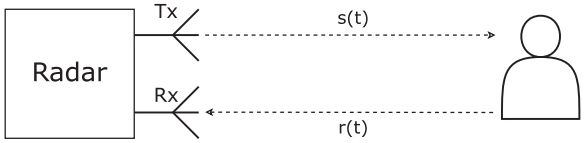

Figure 1. Basic radar architecture example.

Each use case has its unique requirements and as such, each architecture can be used properly if chosen for the right scenario; CW radars are simple in design, but since there is no modulation, it is impossible to measure the range of objects from the reflected signals [10,11]. This means that, if there are multiple targets in range, the signal will suffer distortion, and extra signal processing is required to extract the results. FMCW radars are capable of measuring this range, allowing for target separation and for the mitigation of noise due to reflections from surrounding objects. UWB radars allow for through-wall sensing and monitoring over long distances due to the wide frequency spectrum in its pulses. The downside is that this increases the hardware complexity of the system. However, this has gradually become of a less limiting factor due to the increased availability of hardware platforms that make it easier to implement these architectures [7].

Another important aspect of the design of these systems is the carrier frequency. This is because it not only affects the design of the antennas that are used with the radar, but it also affects the sensitivity to the phase changes and noise of the radar signal. As the carrier frequency increases, the phase changes resulting from smaller movements like the ones caused by cardiac activity also increase. However, this brings the downside of increased sensitivity to noise, meaning that while the phase change from cardiac movements is more noticeable in the reflected signal, so is the impact of random body movements by the subject. The distortion caused by these movements becomes greater as a consequence of this and requires more extensive signal processing to properly mitigate the resulting errors.

2.2. Heart Rate Variability

Heart rate variability (HRV) is defined as the variability of the intervals between consecutive heart beats, as seen in Figure 2 and as stated in [12]; this is caused by the autonomic nervous system and the interactions between the brain and the heart. Because of this, it can be used to infer something about a person's physiological and psychological state. There are a myriad of parameters that allow for the assessment of HRV, which are split between two domains: the frequency and time domain. For time domain measurements, the basis of all parameters is the beat-to-beat interval (BBI), which is then used to calculate parameters such as the standard deviation of N-N intervals (SDNN), the root mean square of successive interval differences (RMSSDs), and the percentage of intervals that differ by more than 50 ms (pNN50). The frequency domain parameters are obtained by analyzing the spectrum of the signal, usually an electrocardiogram, within specific frequency bands.

However, the frequency domain parameters are usually not calculated. This is because when using radars, the only phenomenon that is measured for the heart is the vibration it causes on the chest wall, as opposed to an ECG, where the measured signal contains information related to every single step of cardiac activity. As such, the recovered signals will not have enough information to properly calculate these parameters. With this in mind, these parameters will be disregarded in the reviewed works (whether they are measured or not).

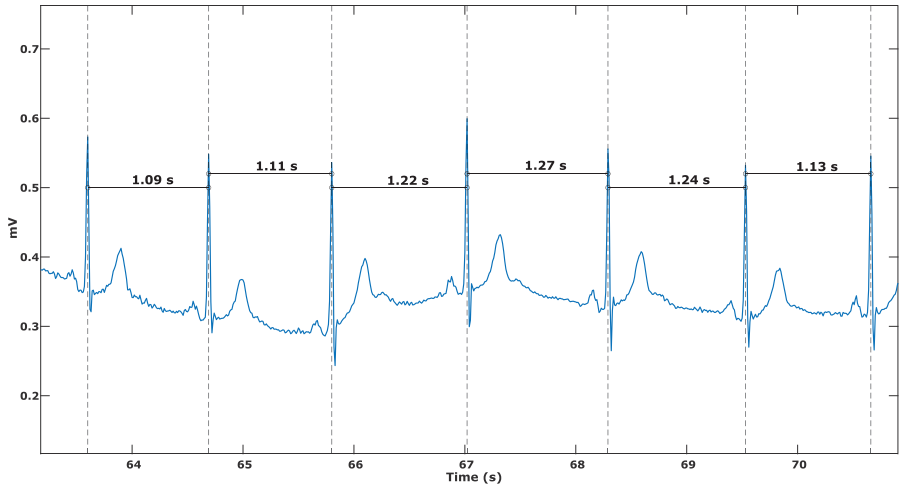

Figure 2. Beat-to-beat interval variation example.

3. Materials and Methods

In this section, the listing of the reviewed works is carried out. Since the review focused on the system design for both HR and HRV measurement systems, these are listed separately. Only information on the factors relevant to this review is listed, since others like measurement time and number of subjects under testing do not necessarily impact the performance of the system. These would serve only to assess the reliability of the results for any given work. However, since no information regarding the performance can be extracted from these factors, these will not be considered during the analysis for this review.

The works that were reviewed were obtained via Scopus (TITLE-ABS-KEY ("vital signs") AND TITLE-ABS-KEY (cardiac OR "heart rate variability" OR hrv OR bbi OR "Beat to Beat Intervals" OR "Heart Rate" OR hr) AND TITLE-ABS-KEY (radar OR "Doppler radar" OR "non-contact monitoring") AND PUBYEAR > 2017 AND PUBYEAR < 2025) and via IEEExplore ("All Metadata": "vital signs" AND ("All Metadata": cardiac OR "All Metadata": "Heart Rate Variability" OR "All Metadata": hrv OR "All Metadata": bbi OR "All Metadata": "beat to beat intervals" OR "All Metadata": "heart rate" OR "All Metadata": hr) AND ("All Metadata": radar OR "All Metadata": "doppler radar" OR "All Metadata": "non-contact monitoring")). The characteristics that were analyzed for similarities were the system architecture, carrier frequency, and measurement distance. While the first two are the most important, they are implementation-specific. The distance was also catalogued and analyzed in order to not only try and assess the impact it has on the measurements but also to assess the conditions in which the measurements are usually done, since, for a technology with such a wide range of possible uses, it is necessary to test it in an equal amount of varied scenarios. The number of subjects is also listed to provide some insight into how extensively each system is tested. With regard to the application scenarios in the reviewed works, most perform measurements in a laboratory environment with the subjects sitting upright and static during the experiments. As such, the scenarios are not specified in the tables. The results of this review are listed in Tables 1 and 2, and the yearly distribution of the reviewed works is displayed in Figure 3 where, based on the large number of works published in recent years, it is evident that cardiac activity measurement with radar is a relevant research topic that is attracting a lot of attention.

Table 1. Listing of HR-focused works.

Reference/Pub. Year	Architecture	Carrier Freq. (GHz)	N° of Subjects	Distance (m)	HR Error Metric
[13]/2023	CW FMCW	24/134	1	0.3	MAE < 0.5 bpm
[14]/2023	FMCW	[60.25,64]	10	0.5	Accuracy = 98%
[15]/2021	CW	24	10	0.5	MRE = [7.09–19.5%]
[16]/2019	UWB	[2.9,10.1]	4	0.65; 0.8; 0.95	Accuracy = 89%
[17]/2022	CW	24	12	0.05	Correlation Coeff. = 0.96
[18]/2023	FMCW	77	7	0.5; 0.6; 1.2; 1.3	MAE = 2.79 bpm
[19]/2019	UWB	7.29	10	0.1	MRE = 1.23%
[20]/2023	FMCW	[77,81]	10	0.5	Accuracy > 98%
[21]/2023	FMCW	60	10	0.3; 0.5; 0.8; 1.1	MAE = 4.91 bpm
[22]/2023	CW	24	5	0.5	MRE 2.26%
[23]/2014	CW	5.8	10	0.5	MRE 3.68%
[24]/2023	UWB	[3.2,5.4]	10	–	Accuracy = 94.16%
[25]/2019	CW	2.45	6	0.4	Accuracy > 95%
[26]/2024	FMCW	[60,63.6]	13	–	MAE = 3.82 bpm
[27]/2018	CW	5.8	2	–	Accuracy = 96.5%
[28]/2019	CW	10.525	–	–	MAE = 0.014 bpm
[29]/2023	FMCW	60	8	0.5; 1; 1.5; 2; 2.5; 3	Accuracy = [85.71–97.48%]
[30]/2023a	FMCW	60	10	–	MRE = 2.924%
[31]/2023b	FMCW	[77,81]	7	1	MAE = 1.18 bpm
[32]/2024	UWB	–	30	–	MAE = 1.23 bpm
[33]/2023	IR-UWB	–	3	6	MRE = 9.96%
[34]/2023	FMCW	76.4	10	0.5	MAE = 0.15 bpm
[35]/2023a	FMCW	[77,81]	1	0.4	MAE = 1.43 bpm
[36]/2023b	CW	2.4	1	1.3	MAE < 3 bpm
[37]/2023c	FMCW	24	10	0.75	MAE = 2.2 bpm

Table 1. *Cont.*

Reference/Pub. Year	Architecture	Carrier Freq. (GHz)	N° of Subjects	Distance (m)	HR Error Metric
[38]/2021	FMCW	[119.5,125.5]	10	1	Accuracy = 95.62%
[39]/2023	FMCW	[60,64]	3	[1.49–1.87]	MRE apporx 10%
[40]/2024	FMCW	[60,64]	6	[1.15–2.3]	MAE = 9 bpm
[41]/2020	LFMCW	[77,79]	2	1.1; 2.1	MRE = 2.56%
[42]/2024	FMCW	[77,79.6]	10	0.3; 1; 2	MRE = 1.4%
[43]/2018	CW	2.4	8	0.75; 1.5	Accuracy = 99%
[44]/2022	CW	77	2	0.3	MRE = 0.03%
[45]/2019	CW	2.45	1	0.3	MRE = 1.5%
[46]/2024	CW	24	7	0.6; 1	Accuracy = 95.25%
[47]/2023	FMCW	[77,81]	5	0.5; 1; 1.5; 2	MAE = 2.7 bpm
[48]/2023	IR-UWB	[5.9,10.3]	5	0.5; 1	Accuracy = [93–98]%
[49]/2022	CW	2.4	5	1	MAE = 2.6 bpm
[50]/2024	CW	2.4	4	–	MAE = 1.56 bpm
[51]/2022	CW	24	5	0.6	Poincare Comparison shows similarities
[52]/2023	QSIL	2.4	5	1	MRE = 5.6%
[53]/2023	FMCW	[58,64]	1	1	Accuracy = 74.4%
[54]/2024	FMCW	[77,81]	4	0.5; 1; 2; 3; 4	Accuracy = 100%
[55]/2022	CW	24	10	0.15	Correlation Coeff. = 0.998
[56]/2020	–	24	–	0.4	HR acc = 96%
[57]/2023	FMCW	[60,61]	2	0.3	MRE = 3.0%
[58]/2023a	UWB	7.3,1.4,23.328	13	1; 2	MAE = 0.9 bpm
[59]/2023c	UWB	[0.85,9.55]	5	0.5; 1; 1.5	MAE = 0.036 Hz
[60]/2023d	FMCW	[60,61]	3	–	Accuracy = 97.5%
[61]/2024	CW	24	30	0.4	PCC = 0.964
[62]/2020	FMCW	[8.15,8.65]	5	1.5	MRMSE ≈ 2 bpm

Table 1. *Cont.*

Reference/Pub. Year	Architecture	Carrier Freq. (GHz)	N° of Subjects	Distance (m)	HR Error Metric
[63]/2019	CW	24	5	0.3	MAE = 3.79 bpm
[64]/2023	UWB	[6.5,8.1]	7	–	MRE < 1%
[65]/2024	FMCW	[77,81]	3	0.7	HR acc = 95.65%
[7]/2023	FMCW	[77,81]	10	1	MAE = 1.03 bpm
[66]/2023	IR-UWB	[6.765,9.04]	5	[0.5-5]	MRE = 86.5%
[67]/2023a	FMCW	[77,81]	5	0.5	MRE = 1.29%

Table 2. Listing of HRV-focused works.

Reference/Pub. Year	Architecture	Carrier Freq. (GHz)	N° of Subjects	Distance (m)	HR Error Metric	HRV Error Metric
[13]/2023	CW LFMCW	24/134	1	0.3;0.5	–	MAE < 10 ms
[15]/2021	CW	24	10	0.5;1;1.5;2	MRE = [7.09–19.5%]	MRE = 5.26%
[68]/2023	CW	24	2	0.4	–	RMSE = 5.2 ms
[17]/2022	CW	24	12	0.05	Correlation Coeff. = 0.96	ANN = 0.99
[69]/2024	CW	5.8	20	0.5	–	RMSE = 51 ms
[19]/2019	UWB	7.29	10	0.1	MRE = 1.23%	MRE = 1.38%
[20]/2023	FMCW	[77,81]	10	0.5	Accuracy > 98%	MRE = 0.11%
[22]/2023	CW	24	5	0.5	MRE = 2.26%	MRE = 11.48%/4.87%
[23]/2014	CW	5.8	10	0.5	Accuracy > 97%	BBI RE—2.53–4.83%
[25]/2019	CW	2.45	6	0.4	Accuracy > 95%	Accuracy = 96.78%
[70]/2022	FMCW	60	5	0.6	–	RMSE = 100 ms
[71]/2019	IR-UWB	8.748	1	0.7	–	High Correlation with ECG
[72]/2023c	FMCW	[23.8,24.8]	3	1	–	MRE = 1.84%
[38]/2021	FMCW	[119.5,125.5]	10	1	Accuracy = 95.62 %	MAE = 6.4 ms
[43]/2018	CW	2.4	8	1.5	Accuracy = 99%	MRE = 2%
[73]/2016	CW	24	5	1	–	Mean RMSE < 100 ms

Table 2. *Cont.*

Reference/Pub. Year	Architecture	Carrier Freq. (GHz)	Nº of Subjects	Distance (m)	HR Error Metric	HRV Error Metric
[44]/2022	CW	77	2	0.3	MRE = 0.03%	MRE = 0.95%
[45]/2019	CW	2.45	1	0.3	MRE = 1.5%	MRE = 1.9%
[50]/2024	CW	2.4	4	–	MAE = 1.56 bpm	MAE = 9.31/12.42 ms
[74]/2023	CW	24	3	1.5	–	MRE = 3.61%
[75]/2022	CW	2.4	10	1	–	AAEP = 1.74%
[55]/2022	CW	24	10	0.15	Correlation Coeff. = 0.998	MRE = 3.68%
[76]/2021	FMCW	[76,81]	11	0.5	–	MAE = 3.89 ms
[77]/2024	CW	61	15	–	–	Accuracy = 93.8%
[78]/2021	CW	24	7	0.5	–	MRE = 1.15%
[62]/2020	FMCW	[8.15,8.65]	5	1.5	MRMSE $\approx$ 2 bpm	MAE < 5 ms
[79]/2018	CW	24	10	0.3	–	RMSE = 47.5 ms
[63]/2019	CW	24	5	0.3	AAEP < 5%	RMSE < 50 ms
[80]/2023	CW	24	18	0.2	–	MRE = 0.635%
[65]/2024	FMCW	[77,81]	3	0.7	Accuracy = 95.65%	AAEP = 0.86%

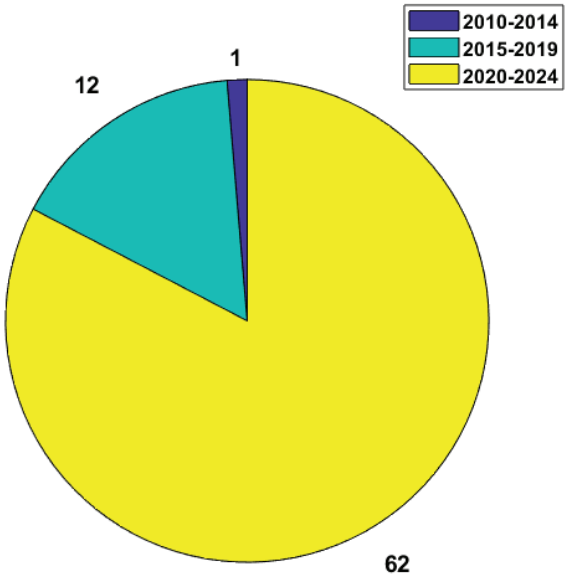

Figure 3. Number of works published per 5-year interval.

4. Results

In this section, the results of the analysis of the reviewed works are presented. Firstly, the works are split into two separate categories depending on whether they measure HRV or not. Within each category, the architectures and carrier frequencies are analysed and compared in order to establish any possible trends in system development and also to try to find a correlation between these parameters and the quality of the measurements made in their respective works, which is one of the main goals of this work. During the analysis of the works listed above, there was a noticeable lack of consistency in terms of the error metrics that researchers used to present their results, which makes a broader comparison of all works more difficult and makes it impossible to compare certain works within a category or subcategory. As such, when performing any sort of quantitative analysis of the reported error metrics, a criterion had to be established in order to be able to compare these results beyond a general qualitative assessment. The chosen criterion was to determine the most used type of error metric within each category and only consider works that reported this metric when performing comparisons. In the case of the two aforementioned categories, the metrics used were the mean absolute error (MAE) for HR-focused systems and the mean relative error (MRE) for HRV-focused systems. In order to increase the amount of data that could be analysed in the first category, the MRE of some works was converted into a corresponding MAE. However, due to some works not reporting a mean HR, a reference mean HR of 70 bpm was used to convert between the two metrics. For HRV focused works this was not possible to do since the second most reported error metric is the root mean square error (RMSE) of the intervals, which cannot be directly converted to a mean relative or absolute error. As a result, both categories will present numerical analyses and comparisons that do not consider all of the reviewed works for that respective category. As a final remark, it is important to note that for all the works that were reviewed, none of them provided an explanation as to why the architectures and carriers were chosen in favor of other options, which means that the conclusions drawn in this work regarding these points do not factor in the reasons that these design choices were made in the first place.

4.1. Works Measuring Heart Rate

Out of all the works listed in the previous section, 56 works are analyzed in this category. Based on the criteria established in the same section, and since 25 of these works do not report their metrics in the form of the MAE, they will not be considered for the quantitative analysis that follows. They will, however, be considered when discussing the number of works for any given parameter.

4.1.1. Hardware Architecture

For the works in this category, in terms of architecture usage, only one of the works did not specify which one they were implementing [56], and only one work reported using an architecture that differed from all the other ones that were mentioned [52]. As for the other architectures, the number of times that these are used is described in Figure 4.

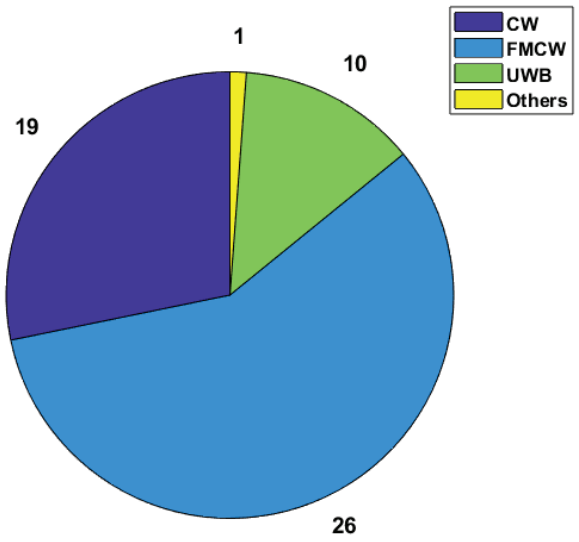

Figure 4. Architectures used in HR-focused works and the respective number of implementations.

As can be seen in the image, the FMCW architecture is used more times than both other architectures combined, while UWB is the one that is rarely used for this type of system. Based on the explanations provided in [10] regarding each of the architectures, certain points can be made. While CW radars are cheaper and easier to implement in terms of hardware, they are more heavily affected by forms of noise that do not affect these other two architectures because of their frequency modulation, such as multi-path noise. On the other side, UWB systems have much more complex hardware implementations and are harder to work with in terms of signal processing. FMCW radars strike a better balance with ease of use than UWB radars and have a more robust functionality than CW radars. With the recent increase in the availability of hardware platforms that allow for the implementation of more complex hardware platforms, FMCW radars have come to be the most researched and tested type of architecture in the field of radar-based heart rate monitoring.

As for the link between architecture and system performance, the boxplot displayed in Figure 5, which was made using the available data related to the MAE, was used to perform a comparisons and draw any possible conclusions.

As displayed in Figure 5, CW is the architecture with the higher median error when compared to both FMCW and UWB. It presents similar values to FMCW for maximum and minimum, but higher errors on average with regard to the other two. To compare FMCW and UWB, despite the significant difference in the number of works between the two architectures, it is still relevant to point out the similarities in their results. UWB shows a smaller interquartile range and a lower maximum value, therefore outperforming FMCW.

The results of this analysis point to a link between an improvement in system performance and the chosen system architecture, with FMCW being the better performing one when compared to CW. This is expected, given the fact that the architecture is inherently more robust to noise and signal interference due to how it functions. As for UWB, is is uncertain whether or not it definitively outperforms the other two architectures, and more research using UWB systems is needed to solidify this point.

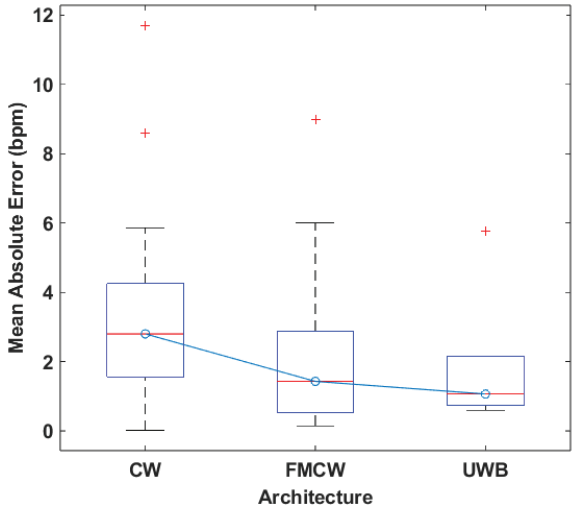

Figure 5. Boxplot of the MAE values for each architecture.

4.1.2. Carrier Frequency

For comparing the carrier frequencies that are used across the listed works in this category, they are separated into the following four frequency bands:

1. Below 20 GHz;
2. 20 to 40 GHz;
3. 60 to 80 GHz;
4. Above 120 GHz.

For the works in this category, only two did not specify the used carrier [32,33], and for the remaining works, the carriers used in each were split into the aforementioned bands based on their frequency for unmodulated systems and their corresponding center frequency for systems with frequency modulation. Their distribution across the bands is displayed in Figure 6.

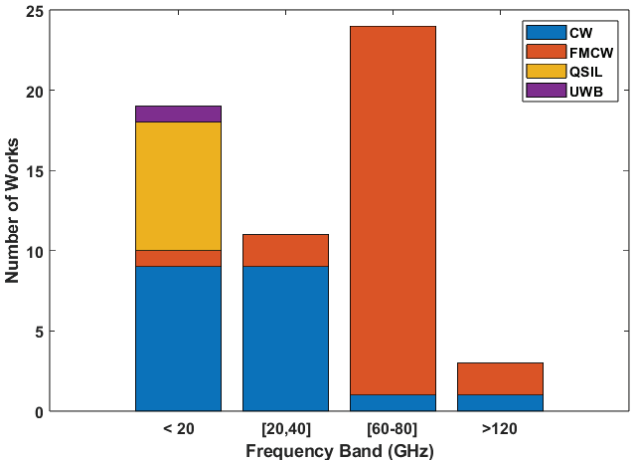

Figure 6. Number of works using carriers in each band based on their architecture in HR focused works.

As displayed in the image, carriers in the third band are the ones that are most used. This is directly related to the architecture usage trends, since most of the systems in this band use an FMCW radar, whereas for the first and second bands, the most predominant architecture is CW. All of the implemented UWB systems use carriers in the first band.

For the performance comparison of the carrier frequencies, a boxplot of the mean absolute error was made to analyze the distribution of errors across each individual bands, which is displayed in Figure 7. These results show that the second band, which is mostly

composed of works using a carrier of 24 GHz, is the one that achieves the worst results, displaying not only the highest maximum error but also a higher median error, while the other two bands present very similar median values. The fourth band was not included in this analysis due to there only being two works using a system with a carrier of this band, which means it is not possible to accurately compare it to the others. As for works that performed HR measurements on different carriers, only [13] performed these tests, meaning that the connection between the carrier frequency and system performance is not widely researched for these systems. Despite the fact that it is not possible to definitively say whether the performance differences between the bands is due to the carriers or the architectures predominantly used in each one, since both the first and third bands present similar results, we can confirm that there is no inherent loss of performance associated with lower carrier frequencies; therefore, there is no inherent performance gain to be achieved by increasing them.

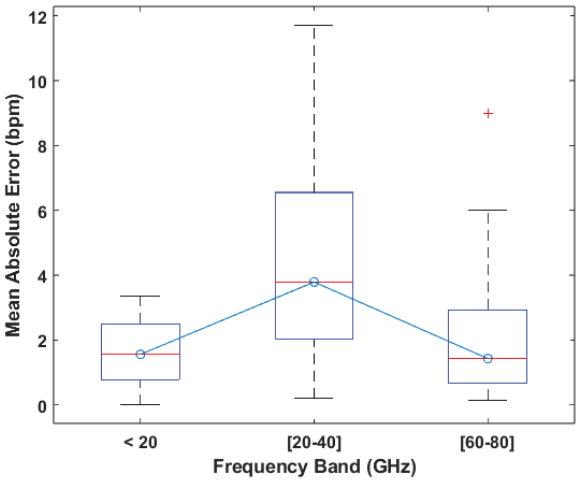

Figure 7. Boxplot of the MAE values reported per frequency band.

4.1.3. Measurement Distance

Measurement distance is important for these systems because it affects the performance of the system in several different ways, the foremost of which being its effect on the power of the reflected signal P_r in relation to the transmitted power P_t, as illustrated in the radar equation [10]:

$$P_r = \frac{P_t G^2 \sigma \lambda^2}{(4\pi)^3 R^4} = \frac{P_t G^2 \sigma c^2}{(4\pi)^3 f^2 R^4} \quad (1)$$

where G is the antenna gain, λ is the wavelength, and σ represents RCS. This equation establishes an inverse relation between the distance R and P_r and a similar relation between the carrier frequency and P_r. This relation is obviously extremely important because the more power the reflected signal has, the better the cardiac movement can be measured. The other effects that distance has are much less noticeable and apparent. Larger distances mean that there are more parts of the subject's body that reflect the signal, which in turn increases its distortion. Inversely, placing the antennas too close to the subject's body can also affect the reflected signal due to the differences between an antenna's near field and far fields resulting in uncertain behaviour and distortion for the reflected signal.

An important part of the design of these systems is the environment in which they are meant to be used. With this in mind, beyond trying to quantify the impact distance has on system performance, it is also pertinent to analyze the conditions in which these systems are commonly tested to see how similar they are to the radar's potential use cases. To that end, as displayed in Figure 8, the distances at which tests were performed across all works in this category were counted.

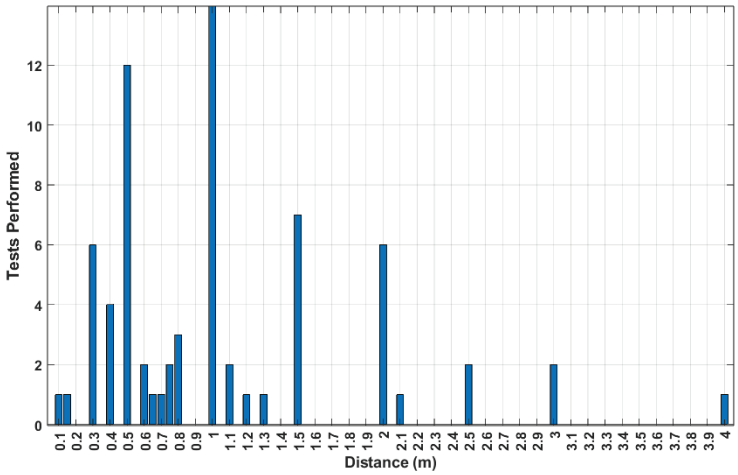

Figure 8. Number of HR-focused tests performed for each of the reported distances.

These distances lie mostly in the range below 1 m, with tests commonly being performed in increments of 0.5 m. As mentioned before, in an attempt to quantify the relation between distance and a performance metric, in this case the MAE, a linear regression was used to model the relation between distance and result error. The corresponding results are displayed in Figure 9, where there is a noticeable increase in the MAE as the distance also increases. Therefore, it is possible to link a variation in system performance based on the measurement distance, but no specific values could be determined.

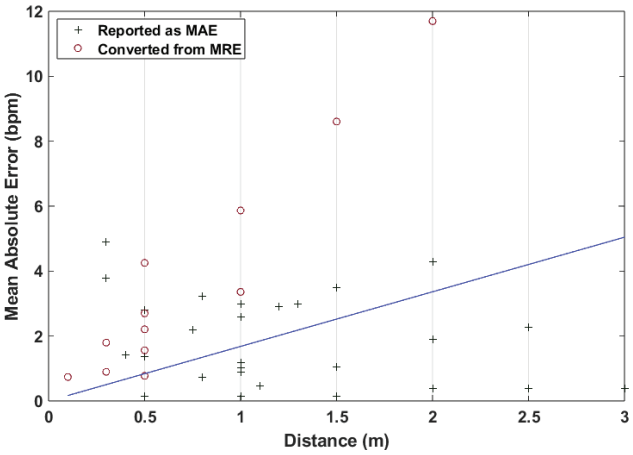

Figure 9. MAE distribution and linear regression with regards to distances tested in HR-focused works.

4.2. Works Measuring Heart Rate Variability

Out of all the works listed in the previous section, 30 works are analyzed in this category. Based on the criteria established in the same section, since 16 of these works do not report their metrics in the form of the MRE, they will not be considered for the quantitative analysis that follows. They will, however, be considered when discussing the number of works for any given parameter.

4.2.1. Hardware Architecture

The distribution of the architectures used across the works relevant to this category can be seen in Figure 10, where it is evident that both CW and FMCW see similar amounts of usage, whereas UWB is once again the least used type of system. As such, the UWB architecture cannot be accurately compared to the other two and will not be included in any comparison of results performed from this point forward. The remaining architectures still follow a similar usage pattern to the previous category, although CW systems are more

predominant in this category. Since the authors never give a reason as to why a specific architecture is chosen, it is difficult to explain this difference in usage. One possibility is that, despite the fact that FMCW radars are more robust to noise and interference than CW, they are more expensive to develop, making them less worthwhile to use in research.

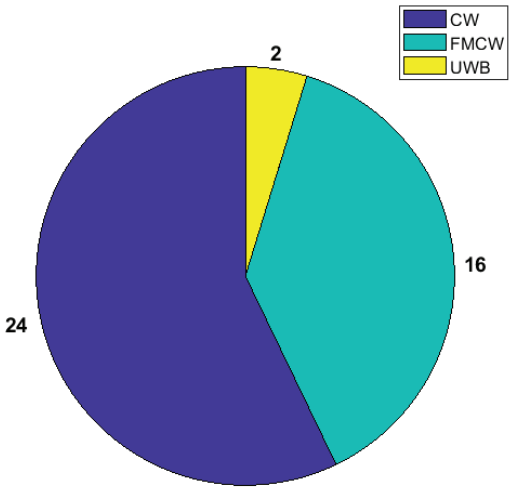

Figure 10. Architectures used in HRV-focused works and respective number of implementations.

Comparing the results using what is presented in Figure 11, FMCW systems present better performance, as evidenced by the lower median error and smaller values for maximum and minimum error. This means that, on a general level, it is possible to argue that using the FMCW architecture will produce better results. This is explained by the aforementioned robustness of the architecture, which leads to a smaller dispersion of the results when compared to CW. These results follow a similar trend to the one displayed in Figure 5, which means that there is a clearly better performing architecture, which is FMCW. Lastly, since UWB is not as widely tested for these scenarios when compared to the other two architectures, it is not possible to say if (similar to the results for HR measurements) UWB would outperform the other two architectures. More tests are required to verify this possibility.

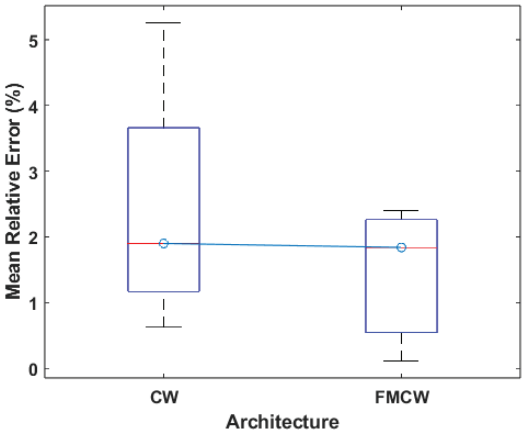

Figure 11. Boxplot of the MRE values for each architecture.

4.2.2. Carrier Frequency

The comparison of the results based on the used carrier frequencies follows the same categorization into bands as mentioned in Section 4.1.2. The distribution of this category of work across these bands is displayed in Figure 12, where it can be seen that all bands are used in a more or less equal capacity.

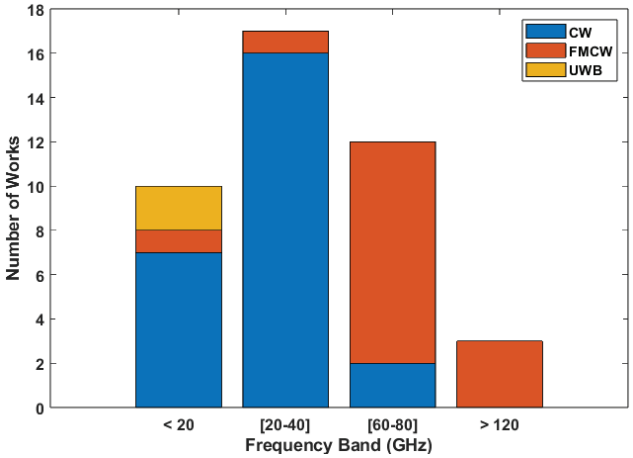

Figure 12. Number of works using carriers in each band based on their architecture in HRV focused works.

Based on the boxplot displayed in Figure 13, which was made from the mean relative errors of the works in this category, it is possible to say that the third frequency band of 60 to 80 GHz leads to better results, presenting not only the lowest median of 1% but also low values for the extremes. The 0 to 20 GHz band presents a similar distribution but exhibits a higher median value of 2%. With regard to the second band specifically, it could simply be due to the fact that all of the systems using carriers in this band use the CW architecture, which, as mentioned before, is more susceptible to interference. In fact, the boxplot for this band and the boxplot for the CW architecture shown in Figure 11 are extremely similar. The same applies to the third band and the FMCW architecture. For the first band, the performance can be explained in very much the same way as the second one, where the predominant architecture used in this band is CW; however, it is also due to the fact that these frequencies do not have enough sensitivity to achieve the same kind of results that are achievable using carriers in the third band. Lastly, considering the fact that the reasoning for choosing a specific carrier is never given, and based on the analysis performed, it is possible to say that the frequency of the carrier signal does not have an impact on the performance of the system.

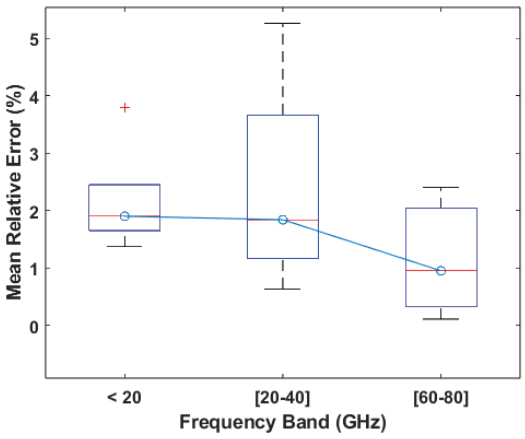

Figure 13. Boxplot of the MRE values reported per frequency band.

4.2.3. Measurement Distance

As mentioned in Section 4.1.3, the distance at which measurements are taken is extremely important because it will affect the energy of the reflected signal, making it more or less susceptible to noise relative to the radar's positioning. In the case of HRV measurements, this is important because there needs to be minimal loss of information regarding the cardiac activity in order to obtain reliable results. Despite this, the possible

effects due to close proximity of the antennas to the subject still apply, so one cannot simply place them as close as possible, and, depending on the overall system and use case, the proper positioning needs to be determined.

Regarding the tests conducted for the works in this category, their distribution in terms of range is displayed in Figure 14 where, much like what was displayed in Figure 8, most of the tests are conducted at distances lower than 1 m. As for systems tested across different ranges, only four of the works in this category performed measurements in different ranges [13,70,76,79], following the trend of HR-focused systems where there are few tests being performed at ranges larger than 1 m.

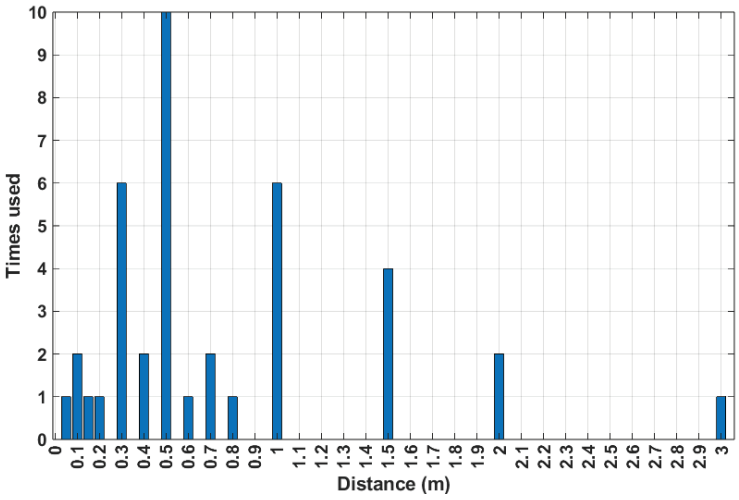

Figure 14. Number of HRV-focused tests performed for each of the reported distances.

Given the amount of works also presenting RMSE as an error metric, linear regression was also performed for this metric, alongside the one performed for MRE. The results of these regressions are presented in Figure 15, where it can be seen that there is an increase in the error values related to an increase in distance. This is effectively the same result as was achieved for the previous category of works.

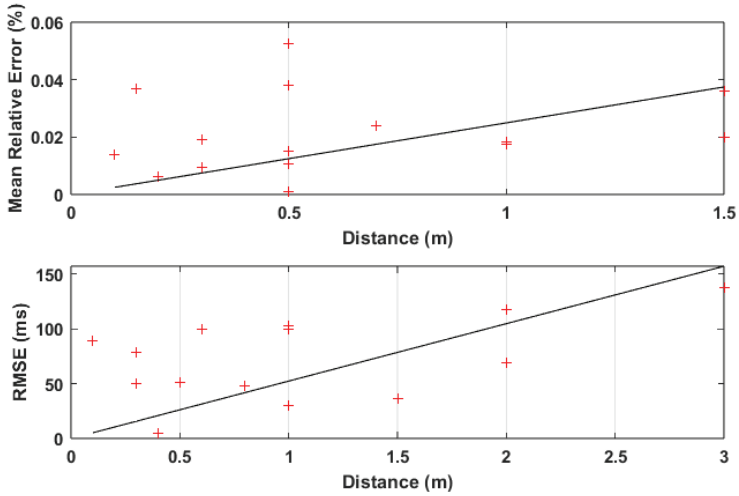

Figure 15. MRE/RMSE distribution and linear regression with regard to distances used in HRV tests.

4.3. Vital Sign Extraction Algorithms

Given the fact that HRV measurements rely on the measurement of the interval between consecutive signal peaks and HR measurement is performed either by measuring the number of peaks in a signal or by performing some form of frequency domain analysis, the algorithms used for signal processing will not be analyzed in separate categories. The

algorithms used in each work were not listed in Section 3 for the sake of clarity. Lastly, all algorithms mentioned in this section are ones that have reported uses in radar-based systems, and it is in the context of these systems that they are analyzed.

The algorithms (not the full signal processing chain) used across the reviewed works can be split into several different classes based on their functionality (not all algorithms are listed):

- Digital Filtering, e.g., Bandpass, Moving Average;
- Spectral Analysis, e.g., Fourier Transform, Cossine Transform, CZT, FTPR;
- Mode Decomposition, e.g., EMD, EEMD, VMD, ICA;
- Wavelet Transform, e.g., DWT, MODWT, CWT, WPT;
- Deep Learning;
- Uncategorized, e.g., Autocorrelation, Differential Enhancement.

For almost all of the reviewed works, the signal processing chains use either zero-crossing detection or peak detection in order to detect the data points relevant for HR/HRV parameter calculation. However, some resort to more complex forms of event detection to avoid false positives and improve results such as the Viterbi Algorithm or HSMM [73,78] or the Decoding Peak Detection and Template Matching Algorithms [20,50,78]. As for the usage distribution of each of the aforementioned algorithm classes, it is difficult to tally them individually, since most of the time, they are used as parts of a larger signal processing chain, in which case there is no reason to count individual uses of the algorithm. Instead, it would make more sense to try and count the times a specific algorithm chain is used (for example, how many times mode decomposition is used in tandem with a wavelet transform), but that is also not reasonable because there are different pairings of mode decomposition and of the wavelet transform, which can lead to different results or even applications of the same algorithms that lead to different results due to different parametrization. This means that when comparing the results obtained in the works that were reviewed, the only outcome is a general idea of which algorithms might perform better in general. It is important to note that since there are works in which the details of the algorithms implemented are not disclosed, for example, exact data for the filters designed in [81] or which type of wavelet transform is used and the criteria used to choose the correct IMFs in [15,23], attempting to replicate the algorithms used in some of these works might lead to results that are different from what was expected.

Despite these constraints, it is still an important analysis to perform, since it allows us to obtain a general idea of which classes of algorithm are used more frequently, and how these classes are used together. In terms of performance in HR measurements, most algorithms can achieve good results (considering a minimum accuracy of over 95%), with mode decomposition, wavelets and digital filtering being the most used, either combined or individually. Although several types of the wavelet transform are used, none present a clear advantage when considering only the results. For mode decomposition, improvements on existing algorithms have been presented, but since no single improvement sees frequent use, it is hard to assert which one is better. FTPR also stands out with highly accurate results ($\geq$99%), but as it is not frequently tested [43,44], it is uncertain whether this accuracy would be maintained with further testing. Signal processing methods using deep learning algorithms or other forms of neural network or machine learning are also used, albeit rarely in the reviewed works; however, they present good results. For HRV measurements, the algorithms that are used more frequently follow the trend for HR measurements, but works relying mostly on digital filtering and the simpler forms of mode decomposition tend to display higher error values. Signal processing chains that properly implement several algorithms in tandem [68,78] or improved/more complex versions of pre-existing algorithms [63,76] tend to be the ones that obtain the best results. Deep learning was also used in one work for HR measurements [60] and in one work for HRV measurements [65], with both achieving good results. Overall, there is a large overlap in terms of the algorithms used for measuring HR and HRV; however, systems measuring the latter tend to present more complex signal processing.

5. Discussion

The goal of this review is to assess, in terms of hardware architecture, carrier frequency and the signal processing chain, the choices of which tend to lead to the best possible performance based on the work that has already been performed for this kind of system. However, when comparing systems based on each of these categories individually, the impact of other categories cannot be separated. Because of this, the points made for each of the categories are not meant to be definitive, but more so guidelines to help researchers to make their decisions when designing their own systems.

With regard to the impact that the used architecture has on the performance of the system, if comparing based solely on the values for the median error metrics that were presented, then FMCW is the better choice for this kind of system. However, when considering other factors like cost and hardware complexity, then CW is still a viable alternative despite the fact that the architecture suffers from more interference than FMCW. With regard to the UWB architecture, given the performance displayed for HR measurements, it is still a viable choice presenting good performance. However, further testing and experiments for HRV measurements are required to truly determine how much better or worse it might perform when compared to the other two architectures. IRegarding the impact of the carrier frequency, systems with carriers in the range below 20 GHz and carriers above 60 GHz present better results for both categories. However in the context of this work, it is important to note that it is not possible to say for certain that the results presented are solely due to the used carrier frequency or if they are in part or solely due to the architectures that are used, since most systems using higher carrier frequencies tend to use FMCW, whereas systems with lower frequencies use mostly CW. Based on the relationship between the carrier frequency and the sensitivity to the chest wall displacement mentioned in Section 2.1, it was expected that systems with higher carrier frequencies would perform better than ones with lower frequencies. However, as can be seen in the results of the reviewed works, this is not the case. With this in mind, it is not possible to establish a definitive link between the used carrier frequency and the overall performance of the system. For the measurement distance, the decrease in performance due to larger distances was to be expected, not only due to the mathematical relation between distance and received signal power described by the radar equation but also due to the fact that larger distances mean that the signal will be reflected off of a larger surface of the subject's body, which can cause significant amounts of interference. Apart from analyzing the extent of the impact on performance, analyzing the number of tests per distance also provided some insight into the current state of research on these systems. When analyzing this distribution, it became apparent that the number of experiments that were conducted at distances greater than 1 m is extremely low; for HR-focused works, out of 86 total tests, only 23 tests were performed at distances greater than 1 m. For HRV-focused works, out of 40 total tests, only 7 were performed at distances greater than 1 m. Since most of the reviewed works focus on studying the performance of specific signal processing methods, performing tests at distances that minimize interference and the impact of confounding variables is desirable. However, it is also important to perform tests in scenarios closer to the ones encountered in real-world applications. As such, an increase in testing performed in non-ideal scenarios is recommended. As for the signal processing performed, there is no singularly defined approach that is considered ideal. What is used is mostly dependent on what parameter the system is meant to be extracting: measuring HR only requires the preservation of the number of peaks within the measured signal, whilst HRV measurements also require the preservation of the position of the peaks with respect to time. This means that algorithms that measure HR through any form of spectral analysis, like the Fourier Transform, are not recommend for use in HRV measurements. Since there is not one individual signal processing chain/algorithm that is used frequently, it is not possible to determine which one would categorically lead to better results.

Lastly, in the closing of this review, based on the points made regarding the current state of the research on these systems, certain trends were seen that are worth trying to

change. First, the standardization of the reported performance metrics is recommended in order to be able to properly judge different works on the same level. While certain works, for both HR- and HRV-focused systems, provide clear listings of the results per subject, there are still some that choose to report the metrics as an average of all subjects or use a different error metric. Some works report their performance solely in metrics that are not part of the norm, such as a correlation coefficient, or report their performance using only one type of metric. This makes a proper analysis of system performance significantly more difficult, since results can only be compared qualitatively (MRE and RMSE cannot be directly compared). Secondly, clearer explanations of the parameters necessary for some of the used signal processing algorithms are encouraged in order to improve replicability. This makes the testing of certain algorithms across different systems easier and opens up a path for research focused on comparing the most well performing algorithms and analyzing in which systems they perform better, if at all. Lastly, an increase in experiments conducted in non-ideal scenarios is recommended, in order to test the technology in conditions closer to the ones it will face if and when it becomes widely adopted.

As for recommendations for future work, although an assessment of which architecture/carrier frequency presents the best results is not really necessary, an assessment of which algorithm presents the best results by default for the widest variety of systems is a promising idea. Establishing a baseline system from which, if necessary, more specific implementations can be designed is a good step forward for a technology that is intended for use in the medical field and therefore needs to cover a variety of use cases.

6. Conclusions

Cardiac activity measurement using radar is a promising solution to the increased interest in the remote measurement of vital signs in smart-home environments and other scenarios in which contact is not possible. This review focuses on analyzing the performance of recent implementations of radar systems for cardiac activity measurement to try and link changes in performance to changes in several aspects of the overall system: hardware architecture, carrier frequency, and measurement distance. A general overview of the signal processing methods used in these systems was also carried out to establish possible usage trends. Based on the results of the performed analysis, it is possible to conclude that the hardware architecture and the signal processing methods used in the system are the aspects with the most significant impact, whereas the impact that the carrier frequency has is unclear. From this review, several recommendations are also given and mostly relate to the standardization of the reporting of results and the ease of replicating pre-existing systems. As more research is carried out on this topic, the focus should be on trying to find a baseline from which more specific systems can be designed.

Author Contributions: Conceptualization, D.A. and A.F.; methodology, D.A. and A.F.; validation, A.F., D.A. and P.P.; formal analysis, A.F.; investigation, A.F., D.A. and P.P.; data curation, A.F.; writing—original draft preparation, A.F.; writing—review and editing, A.F., D.A. and P.P.; supervision, D.A. and P.P.; funding acquisition, A.F., D.A. and P.P. All authors have read and agreed to the published version of the manuscript.

Funding: This work is funded by FCT/Ministério da Ciência, Tecnologia e Ensino Superior (MCTES) through national funds and, when applicable, co-funded by the European Union (EU) fund under the project 2022.05005.PTDC and the project UIDB/50008/2020-UIDP/50008/2020 with DOI https://doi.org/10.54499/UIDB/50008/2020 (IT).

Institutional Review Board Statement: Not applicable.

Informed Consent Statement: Not applicable.

Data Availability Statement: All data relevant to this study is included in the article in Tables 1 and 2. Further inquiries can be directed to the corresponding author.

Conflicts of Interest: Authors declare no conflicts of interest.

Abbreviations

The following abbreviations are used in this manuscript:

FPGA	Field Programmable Gate Array
CW	Continuous Wave
FMCW	Frequency Modulated Continuous Wave
LFMCW	Linear Frequency Modulated Continuous Wave
UWB	Ultra Wideband
HR	Heart Rate
HRV	Heart Rate Variability
BBI	Beat to Beat Interval
SDNN	Standard Deviation of N-N Intervals
RMSSD	Root Mean Square of Sucessive Differences
MAE	Mean Absolute Error
MRE	Mean Relative Error
RMSE	Root Mean Square Error
RCS	Radar Cross Section
PCC	Pearson Correlation Coefficient
QSIL	Quadrature Self Injection Locked
AAEP	Absolute Average Error Percentage

References

1. Chen, X.; Cheng, J.; Song, R.; Liu, Y.; Ward, R.; Wang, Z.J. Video-Based Heart Rate Measurement: Recent Advances and Future Prospects. *IEEE Trans. Instrum. Meas.* **2019**, *68*, 3600–3615. [CrossRef]
2. Liao, W.; Zhang, C.; Alić, B.; Wildenauer, A.; Dietz-Terjung, S.; Ortiz Sucre, J.G.; Weinreich, G.; Viga, R.; Sutharsan, S.; Schöbel, C.; et al. Advancing Sleep Diagnostics: Contactless Multi-Vital Signs Continuous Monitoring with a Multimodal Camera System in Clinical Environment. In Proceedings of the 2024 IEEE International Symposium on Medical Measurements and Applications (MeMeA), Eindhoven, The Netherlands, 26–28 June 2024; pp. 1–6. [CrossRef]
3. Wang, P.; Ma, X.; Zheng, R.; Chen, L.; Zhang, X.; Zeghlache, D.; Zhang, D. SlpRoF: Improving the Temporal Coverage and Robustness of RF-based Vital Sign Monitoring during Sleep. *IEEE Trans. Mob. Comput.* **2023**, *23*, 7848–7864. [CrossRef]
4. Al-Naji, A.; Al-Askery, A.J.; Gharghan, S.K.; Chahl, J. A System for Monitoring Breathing Activity Using an Ultrasonic Radar Detection with Low Power Consumption. *J. Sens. Actuator Netw.* **2019**, *8*, 32. [CrossRef]
5. Jia, W.; Peng, H.; Ruan, N.; Tang, Z.; Zhao, W. WiFind: Driver Fatigue Detection with Fine-Grained Wi-Fi Signal Features. *IEEE Trans. Big Data* **2020**, *6*, 269–282. [CrossRef]
6. Bin Obadi, A.; Soh, P.J.; Aldayel, O.; Al-Doori, M.H.; Mercuri, M.; Schreurs, D. A Survey on Vital Signs Detection Using Radar Techniques and Processing with FPGA Implementation. *IEEE Circuits Syst. Mag.* **2021**, *21*, 41–74. [CrossRef]
7. Zhang, Y.; Yang, R.; Yue, Y.; Lim, E.G.; Wang, Z. An Overview of Algorithms for Contactless Cardiac Feature Extraction From Radar Signals: Advances and Challenges. *IEEE Trans. Instrum. Meas.* **2023**, *72*,4009520. [CrossRef]
8. Wu, Y.; Ni, H.; Mao, C.; Han, J.; Xu, W. Non-intrusive Human Vital Sign Detection Using mmWave Sensing Technologies: A Review. *ACM Trans. Sens. Netw.* **2023**, *20*, 1–36. [CrossRef]
9. Liebetruth, M.; Kehe, K.; Steinritz, D.; Sammito, S. Systematic Literature Review Regarding Heart Rate and Respiratory Rate Measurement by Means of Radar Technology. *Sensors* **2024**, *24*, 1003. [CrossRef]
10. Boric-Lubecke, O.; Lubecke, V.; Droitcour, A.; Park, B.; Singh, A. *Doppler Radar Physiological Sensing*; Wiley Series in Biomedical Engineering and Multi-Disciplinary Integrated Systems; Wiley: Hoboken, NJ, USA, 2015; pp. 28–32. 39–53.
11. Eder, Y.; Eldar, Y.C. Sparsity-Based Multi-Person Non-Contact Vital Signs Monitoring via FMCW Radar. *IEEE J. Biomed. Health Inform.* **2023**, *27*, 2806–2817. [CrossRef]
12. Shaffer, F.; Ginsberg, J.P. An Overview of Heart Rate Variability Metrics and Norms. *Front. Public Health* **2017**, *5*, 258. [CrossRef]
13. Antolinos, E.; Grajal, J. Comprehensive Comparison of Continuous-Wave and Linear-Frequency-Modulated Continuous-Wave Radars for Short-Range Vital Sign Monitoring. *IEEE Trans. Biomed. Circuits Syst.* **2023**, *17*, 229–245. [CrossRef] [PubMed]
14. Cao, L.; Wei, R.; Zhao, Z.; Wang, D.; Fu, C. A Novel Frequency-Tracking Algorithm for Noncontact Vital Sign Monitoring. *IEEE Sens. J.* **2023**, *23*, 23044–23057. [CrossRef]
15. Cruz, J.C.; Ibera, J.C.; Cabarios, P.M.R.; Cruz, J.B.P. Non-contact Determination of Heart Rate Variability Using 24 GHz Doppler Radar. In Proceedings of the 2021 11th International Conference on Biomedical Engineering and Technology, New York, NY, USA, 17–20 March 2021; pp. 80–86. [CrossRef]
16. Duan, Z.; Liang, J. Non-Contact Detection of Vital Signs Using a UWB Radar Sensor. *IEEE Access* **2019**, *7*, 36888–36895. [CrossRef]
17. Edanami, K.; Kurosawa, M.; Yen, H.T.; Kanazawa, T.; Abe, Y.; Kirimoto, T.; Yao, Y.; Matsui, T.; Sun, G. Remote sensing of vital signs by medical radar time-series signal using cardiac peak extraction and adaptive peak detection algorithm: Performance validation on healthy adults and application to neonatal monitoring at an NICU. *Comput. Methods Programs Biomed.* **2022**, *226*, 107163. [CrossRef]

18. Fu, Y.; Sun, L.; Guo, J.; Han, C.; Wang, S. EEMD-MICA Based Heart Rate Extraction Algorithm for Radar Signals. In Proceedings of the 2023 35th Chinese Control and Decision Conference (CCDC), Yichang, China, 20–22 May 2023; pp. 1649–1655. [CrossRef]
19. Han, Y.; Lauteslager, T.; Lande, T.S.; Constandinou, T.G. UWB Radar for Non-contact Heart Rate Variability Monitoring and Mental State Classification. In Proceedings of the 2019 41st Annual International Conference of the IEEE Engineering in Medicine and Biology Society (EMBC), Berlin, Germany, 23–27 July 2019; pp. 6578–6582. [CrossRef]
20. Han, X.; Zhai, Q.; Zhang, N.; Zhang, X.; He, L.; Pan, M.; Zhang, B.; Liu, T. A Real-Time Evaluation Algorithm for Noncontact Heart Rate Variability Monitoring. *Sensors* **2023**, *23*, 6681. [CrossRef]
21. Hazra, S.; Fusco, A.; Kiprit, G.N.; Stadelmayer, T.; Habib, S.; Servadei, L.; Wille, R.; Weigel, R.; Santra, A. Robust Radar-Based Vital Sensing with Adaptive Sinc Filtering and Random Body Motion Rejections. *IEEE Sens. Lett.* **2023**, *7*,7001604. [CrossRef]
22. Hossain, M.S.; Uddin, S.D.; Islam, S.M.M. Heart Rate Variability Assessment Using Single Channel CW Doppler Radar. In Proceedings of the 2023 IEEE Microwaves, Antennas, and Propagation Conference (MAPCON), Ahmedabad, India, 11–14 December 2023; pp. 1–6. [CrossRef]
23. Hu, W.; Zhao, Z.; Wang, Y.; Zhang, H.; Lin, F. Noncontact Accurate Measurement of Cardiopulmonary Activity Using a Compact Quadrature Doppler Radar Sensor. *IEEE Trans. Biomed. Eng.* **2014**, *61*, 725–735. [CrossRef]
24. Jing, F.; Liang, J.; Wang, Y.; Chen, P. Harmonics and intermodulation products-based fuzzy logic (HIPBFL) algorithm for vital sign frequency estimation using a UWB radar. *Expert Syst. Appl.* **2023**, *228*, 120294. [CrossRef]
25. Kim, J.Y.; Park, J.H.; Jang, S.Y.; Yang, J.R. Peak detection algorithm for vital sign detection using doppler radar sensors. *Sensors* **2019**, *19*, 1575. [CrossRef]
26. Kim, D.; Choi, J.; Yoon, J.; Cheon, S.; Kim, B. HeartBeatNet: Enhancing Fast and Accurate Heart Rate Estimation with FMCW Radar and Lightweight Deep Learning. *IEEE Sens. Lett.* **2024**, *8*, 6004004. [CrossRef]
27. Li, M.; Lin, J. Wavelet-Transform-Based Data-Length-Variation Technique for Fast Heart Rate Detection Using 5.8-GHz CW Doppler Radar. *IEEE Trans. Microw. Theory Tech.* **2018**, *66*, 568–576. [CrossRef]
28. Li, X.; Liu, B.; Liu, Y.; Li, J.; Lai, J.; Zheng, Z. A novel signal separation and de-noising technique for doppler radar vital signal detection. *Sensors* **2019**, *19*, 4751. [CrossRef] [PubMed]
29. Li, J.F.; Yang, C.L. High-Accuracy Cardiac Activity Extraction Using RLMD-Based Frequency Envelogram in FMCW Radar Systems. In Proceedings of the 2023 IEEE/MTT-S International Microwave Symposium—IMS 2023, San Diego, CA, USA, 11–16 June 2023; pp. 1097–1100. [CrossRef]
30. Li, J.; Guo, S.; Cui, G.; Zhou, X.; Shi, L.; Kong, L.; Yang, X. Multidomain Separation for Human Vital Signs Detection with FMCW Radar in Interference Environment. *IEEE Trans. Microw. Theory Tech.* **2023**, *72*, 4278–4293. [CrossRef]
31. Li, T.; Shou, H.; Deng, Y.; Zhou, Y.; Shi, C.; Chen, P. A Novel Heart Rate Estimation Method Exploiting Heartbeat Second Harmonic Reconstruction Via Millimeter Wave Radar. In Proceedings of the ICASSP 2023—2023 IEEE International Conference on Acoustics, Speech and Signal Processing (ICASSP), Rhodes Island, Greece, 4–10 June 2023; Volume 2023-June. [CrossRef]
32. Li, Q.; Liu, J.; Gravina, R.; Zang, W.; Li, Y.; Fortino, G. A UWB-Radar-Based Adaptive Method for In-Home Monitoring of Elderly. *IEEE Internet Things J.* **2024**, *11*, 6241–6252. [CrossRef]
33. Liang, Z.; Xiong, M.; Chen, J.; Zhao, D.; Yang, D.; Liang, B.; Mo, J. A combined algorithm for non-contact human vital signs monitoring using IR-UWB radar. In Proceedings of the 2023 International Conference on Microwave and Millimeter Wave Technology (ICMMT), Qingdao, China, 14–17 May 2023. [CrossRef]
34. Liu, L.; Zhang, J.; Qu, Y.; Zhang, S.; Xiao, W. mmRH: Noncontact Vital Sign Detection with an FMCW mm-Wave Radar. *IEEE Sens. J.* **2023**, *23*, 8856–8866. [CrossRef]
35. Liu, W.; Zhang, S.; Yang, J.; Wang, M. Human Vital Signs Detection Based on Millimeter Wave Radar and Digital Filtering. In Proceedings of the 2023 IEEE International Conference on Image Processing and Computer Applications (ICIPCA), Changchun, China, 11–13 August 2023; pp. 569–574. [CrossRef]
36. Liu, Y.; Sweeney, C.; Mayeda, J.C.; Lopez, J.; Lie, P.E.; Nguyen, T.Q.; Lie, D.Y.C. A Feasibility Study of Remote Non-Contact Vital Signs (NCVS) Monitoring in a Clinic Using a Novel Sensor Realized by Software-Defined Radio (SDR). *Biosensors* **2023**, *13*, 191. [CrossRef]
37. Liu, Y.; Li, N.; Zhang, Y.; Cheng, J.; Ma, T.; Yue, W. Research on non-contact vital sign detection based on 24 GHz FMCW radar. In Proceedings of the 2023 International Conference on Microwave and Millimeter Wave Technology (ICMMT), Qingdao, China, 14–17 May 2023. [CrossRef]
38. Lv, W.; Zhao, Y.; Zhang, W.; Liu, W.; Hu, A.; Miao, J. Remote Measurement of Short-Term Heart Rate with Narrow Beam Millimeter Wave Radar. *IEEE Access* **2021**, *9*, 165049–165058. [CrossRef]
39. Mehrjouseresht, P.; Babarinde, O.J.; Hail, R.E.; Schreurs, D.M.M.P. Wide-Angle Vital Signs Measurements by Adaptive FMCW Radar. In Proceedings of the 2023 IEEE MTT-S International Microwave Biomedical Conference (IMBioC), Leuven, Belgium, 11–13 September 2023; pp. 91–93. [CrossRef]
40. Mehrjouseresht, P.; Hail, R.E.; Karsmakers, P.; Schreurs, D.M.M.P. Respiration and Heart Rate Monitoring in Smart Homes: An Angular-Free Approach with an FMCW Radar. *Sensors* **2024**, *24*, 2448. [CrossRef]
41. Mei, Z.; Wu, Q.; Hu, Z.; Tao, J. A Fast Non-Contact Vital Signs Detection Method Based on Regional Hidden Markov Model in A 77ghz Lfmcw Radar System. In Proceedings of the ICASSP 2020—2020 IEEE International Conference on Acoustics, Speech and Signal Processing (ICASSP), Barcelona, Spain, 4–8 May 2020; pp. 1145–1149. [CrossRef]

42. Ni, C.; Pan, J.; Du, D.; Yang, X.; Shi, C.; Chen, S.; Yang, D.; Liu, S. Accurate Heart Rate Measurement Across Various Body Postures Using FMCW Radar. *IEEE Trans. Instrum. Meas.* **2024**, *73*,4006013. [CrossRef]
43. Nosrati, M.; Tavassolian, N. High-Accuracy Heart Rate Variability Monitoring Using Doppler Radar Based on Gaussian Pulse Train Modeling and FTPR Algorithm. *IEEE Trans. Microw. Theory Tech.* **2018**, *66*, 556–567. [CrossRef]
44. Pan, H.; Zou, Y.; Gu, M. A spectrum estimation approach for accurate heartbeat detection using Doppler radar based on combination of FTPR and TWV. *EURASIP J. Adv. Signal Process.* **2022**, *2022*, 67. [CrossRef]
45. Phuong Nguyen, N.T.; Lyu, P.Y.; Lin, M.H.; Chang, C.C.; Chang, S.F. A Short-Time Autocorrelation Method for Noncontact Detection of Heart Rate Variability Using CW Doppler Radar. In Proceedings of the 2019 IEEE MTT-S International Microwave Biomedical Conference (IMBioC), Nanjing, China, 6–8 May 2019; Volume 1, pp. 1–4. [CrossRef]
46. Pramanik, S.K.; Islam, S.M.M. Through the wall human heart beat detection using single channel CW radar. *Front. Physiol.* **2024**, *15*, 1344221. [CrossRef] [PubMed]
47. Qu, L.; Liu, C.; Yang, T.; Sun, Y. Vital Sign Detection of FMCW Radar Based on Improved Adaptive Parameter Variational Mode Decomposition. *IEEE Sens. J.* **2023**, *23*, 25048–25060. [CrossRef]
48. Raheel, M.S.; Tubbal, F.; Coyte, J.; Iranmanesh, S.; Ogunbon, P.; Odeh, N.; Raad, R.; Theoharis, P.I. Non-Invasive Monitoring System of Vital Signs using IR-UWB Radar: A Short Review and Feasibility Study. In Proceedings of the 2023 17th International Conference on Telecommunication Systems, Services, and Applications (TSSA), Lombok, Indonesia, 12–13 October 2023. [CrossRef]
49. Sameera, J.N.; Droitcour, A.D.; Boric-Lubecke, O. Heart rate detection using single-channel Doppler radar system. In Proceedings of the 2022 44th Annual International Conference of the IEEE Engineering in Medicine and Biology Society (EMBC), Glasgow, UK, 11–15 July 2022; pp. 1953–1956. [CrossRef]
50. Sameera, J.N.; Ishrak, M.S.; Lubecke, V.M.; Boric-Lubecke, O. Enhancing Beat-to-Beat Analysis of Heart Signals with Respiration Harmonics Reduction Through Demodulation and Template Matching. *IEEE Trans. Microw. Theory Tech.* **2024**, *72*, 750–758. [CrossRef]
51. Shi, Q.; Hu, B.; Tian, F.; Zhao, Q. Noncontact Doppler Radar-based Heart Rate Detection on the SVD and ANC. In Proceedings of the 2022 IEEE International Conference on Bioinformatics and Biomedicine (BIBM), Las Vegas, NV, USA, 6–8 December 2022; pp. 1710–1713. [CrossRef]
52. Shih, J.Y.; Zhong, J.X.; Wang, F.K. Cosine Transform with Frequency-Domain Correction Technique for Radar-Based Short-Time Vital Sign Monitoring. In Proceedings of the 2023 IEEE/MTT-S International Microwave Symposium—IMS 2023, San Diego, CA, USA, 11–16 June 2023; Volume 2023-June, pp. 855–858. [CrossRef]
53. Shin, M.; Jung, Y.; Kim, J.; Choi, K.; Lee, K.; Ju, H.; Cho, K.I.; Lee, S. FMCW Radar-based Vital Signal Monitoring Technique Using Adaptive Range-bin Selection. In Proceedings of the 2023 IEEE Radar Conference (RadarConf23), San Antonio, TX, USA, 1–5 May 2023; Volume 2023-May. [CrossRef]
54. Singh, A.; Rehman, S.U.; Yongchareon, S.; Chong, P.H.J. Human Vital Signs Estimation Using Resonance Sparse Spectrum Decomposition. *IEEE Trans.-Hum.-Mach. Syst.* **2024**, *54*, 304–316. [CrossRef]
55. Son, N.H.; Yen, H.T.; Sun, G.; Ishibashi, K. High-Accuracy Heart Rate Estimation By Half/Double BBI Moving Average and Data Recovery Algorithm of 24GHz CW-Doppler Radar. In Proceedings of the 2022 International Conference on Advanced Technologies for Communications (ATC), Ha Noi, Vietnam, 20–22 October 2022; pp. 360–363. [CrossRef]
56. Tsai, Y.C.; Lai, S.H.; Ho, C.J.; Wu, F.M.; Henrickson, L.; Wei, C.C.; Chen, I.; Wu, V.; Chen, J. High Accuracy Respiration and Heart Rate Detection Based on Artificial Neural Network Regression. In Proceedings of the 2020 42nd Annual International Conference of the IEEE Engineering in Medicine and Biology Society (EMBC), Montreal, QC, Canada, 20–24 July 2020; pp. 232–235. [CrossRef]
57. Wang, Y.; Liang, J. Noncontact Vital Signs Extraction using an Impulse-radio UWB Radar. In Proceedings of the IGARSS 2023—2023 IEEE International Geoscience and Remote Sensing Symposium, Pasadena, CA, USA, 16–21 July 2023; Volume 2023-July, pp. 5403–5406. [CrossRef]
58. Wang, H.; Du, F.; Zhu, H.; Zhu, X.; Cao, Q. Heart rate measurement method based on wavelet transform noise reduction for low power millimeter wave radar platform. *J. Phys. Conf. Sers.* **2023**, *2469*, 012026. [CrossRef]
59. Wang, Y.; Yang, Z.; Han, L.; Li, Y.; Zhang, C. Extraction of Vital Sign Based on Improved Complete Ensemble Empirical Mode Decomposition with Adaptive Noise for UWB radar. In Proceedings of the 2023 IEEE 6th International Electrical and Energy Conference (CIEEC), Hefei, China, 12–14 May 2023; pp. 2829–2834. [CrossRef]
60. Wang, H.; Du, F.; Zhu, H.; Zhang, Z.; Wang, Y.; Cao, Q.; Zhu, X. HeRe: Heartbeat Signal Reconstruction for Low-Power Millimeter-Wave Radar Based on Deep Learning. *IEEE Trans. Instrum. Meas.* **2023**, *72*, 4004515. [CrossRef]
61. Wu, Y.; Ni, H.; Mao, C.; Han, J. Contactless Reconstruction of ECG and Respiration Signals with mmWave Radar Based on RSSRnet. *IEEE Sens. J.* **2024**, *24*, 6358–6368. [CrossRef]
62. Xiong, Y.; Peng, Z.; Gu, C.; Li, S.; Wang, D.; Zhang, W. Differential Enhancement Method for Robust and Accurate Heart Rate Monitoring via Microwave Vital Sign Sensing. *IEEE Trans. Instrum. Meas.* **2020**, *69*, 7108–7118. [CrossRef]
63. Ye, C.; Toyoda, K.; Ohtsuki, T. A Stochastic Gradient Approach for Robust Heartbeat Detection with Doppler Radar Using Time-Window-Variation Technique. *IEEE Trans. Biomed. Eng.* **2019**, *66*, 1730–1741. [CrossRef]
64. Yuan, Z.; Lu, S.; He, Y.; Liu, X.; Fang, J. Nmr-VSM: Non-Touch Motion-Robust Vital Sign Monitoring via UWB Radar Based on Deep Learning. *Micromachines* **2023**, *14*, 1479. [CrossRef] [PubMed]

65. Yuan, S.; Fan, S.; Deng, Z.; Pan, P. Heart Rate Variability Monitoring Based on Doppler Radar Using Deep Learning. *Sensors* **2024**, *24*, 2026. [CrossRef] [PubMed]
66. Zhou, J. MVSM: Motional Vital Signs Monitoring with IR-UWB Radar and Attention-Based CNN-LSTM Network. In Proceedings of the 2023 8th International Conference on Intelligent Computing and Signal Processing (ICSP), Xi'an, China, 21–23 April 2023; pp. 679–683. [CrossRef]
67. Zhou, M.; Liu, Y.; Wu, S.; Wang, C.; Chen, Z.; Li, H. A Novel Scheme of High-Precision Heart Rate Detection with a mm-Wave FMCW Radar. *IEEE Access* **2023**, *11*, 85118–85136. [CrossRef]
68. Dong, S.; Li, Y.; Lu, J.; Zhang, Z.; Gu, C.; Mao, J. Accurate Detection of Doppler Cardiograms with a Parameterized Respiratory Filter Technique Using a K-Band Radar Sensor. *IEEE Trans. Microw. Theory Tech.* **2023**, *71*, 71–82. [CrossRef]
69. Gouveia, C.; Soares, B.; Albuquerque, D.; Barros, F.; Soares, S.C.; Pinho, P.; Vieira, J.; Brás, S. Remote Emotion Recognition Using Continuous-Wave Bio-Radar System. *Sensors* **2024**, *24*, 1420. [CrossRef]
70. Kitagawa, T.; Yamamoto, K.; Endo, K.; Ohtsuki, T. Multibeam Doppler Sensor-Based Non-Contact Heartbeat Detection Using Beam Diversity. *IEEE Access* **2022**, *10*, 16242–16253. [CrossRef]
71. Lee, W.H.; Yoon Na, J.; Lee, H.J.; Hyun Kim, S.; Lim, Y.H.; Cho, S.H.; Park, H.K.; Cho, S.H. Analysis of Heart Rate Variability Using Impulse Radio Ultra-wideband Radar in Neonatal Intensive Care Unit. In Proceedings of the 2019 IEEE SENSORS, Montreal, QC, Canada, 27–30 October 2019; pp. 1–4. [CrossRef]
72. Li, H.; Liu, Y.; Zhou, M.; Cao, Z.; Zhai, X.; Zhang, Y. Non-Contact Heart Rate Detection Technology Based on Deep Learning. In Proceedings of the 2023 International Seminar on Computer Science and Engineering Technology (SCSET), New York, NY, USA, 29–30 April 2023; pp. 272–277. [CrossRef]
73. Ohtsuki, T.; Mogi, E. Heartbeat detection with Doppler radar based on estimation of average R-R interval using Viterbi algorithm. In Proceedings of the 2016 IEEE 27th Annual International Symposium on Personal, Indoor, and Mobile Radio Communications (PIMRC), Valencia, Spain, 4–8 September 2016; pp. 1–5. [CrossRef]
74. Shi, H.; Yang, Z.; Shi, J. An improved real-time detection algorithm based on frequency interpolation. *EURASIP J. Wirel. Commun. Netw.* **2023**, *2023*, 68. [CrossRef]
75. Shih, J.Y.; Wang, F.K. Quadrature Cosine Transform (QCT) with Varying Window Length (VWL) Technique for Noncontact Vital Sign Monitoring Using a Continuous-Wave (CW) Radar. *IEEE Trans. Microw. Theory Tech.* **2022**, *70*, 1639–1650. [CrossRef]
76. Wang, F.; Zeng, X.; Wu, C.; Wang, B.; Liu, K.R. mmHRV: Contactless Heart Rate Variability Monitoring Using Millimeter-Wave Radio. *IEEE Internet Things J.* **2021**, *8*, 16623–16636. [CrossRef]
77. Wenzel, M.; Langer, D.; Koelpin, A.; Lurz, F. A Modular 61 GHz Vital Sign Sensing Radar System for Long-term Clinical Studies. In Proceedings of the 2024 IEEE Topical Conference on Wireless Sensors and Sensor Networks (WiSNeT), San Antonio, TX, USA, 21–24 January 2024; pp. 18–21. [CrossRef]
78. Xia, W.; Li, Y.; Dong, S. Radar-Based High-Accuracy Cardiac Activity Sensing. *IEEE Trans. Instrum. Meas.* **2021**, *70*, 4003213. [CrossRef]
79. Yamamoto, K.; Toyoda, K.; Ohtsuki, T. Spectrogram-Based Non-Contact RRI Estimation by Accurate Peak Detection Algorithm. *IEEE Access* **2018**, *6*, 60369–60379. [CrossRef]
80. Yen, H.T.; Kurosawa, M.; Kirimoto, T.; Hakozaki, Y.; Matsui, T.; Sun, G. Non-Contact Estimation of Cardiac Inter-Beat Interval and Heart Rate Variability Using Time-Frequency Domain Analysis for CW Radar. *IEEE J. Electromagn. Microwaves Med. Biol.* **2023**, *7*, 457–467. [CrossRef]
81. Petrović, V.L.; Janković, M.M.; Lupšić, A.V.; Mihajlović, V.R.; Popović-Božović, J.S. High-Accuracy Real-Time Monitoring of Heart Rate Variability Using 24 GHz Continuous-Wave Doppler Radar. *IEEE Access* **2019**, *7*, 74721–74733. [CrossRef]

MDPI AG
Grosspeteranlage 5
4052 Basel
Switzerland
Tel.: +41 61 683 77 34

Sensors Editorial Office
E-mail: sensors@mdpi.com
www.mdpi.com/journal/sensors

Academic Open
Access Publishing

mdpi.com

ISBN 978-3-7258-4734-1